SERS-active peptide nanoparticles for investigating protein allostery and bionanoassembly

Anna Robson

August 2012

This thesis is the result of the author's original research. It has been composed by the author and has not been previously submitted for examination which has lead to the award of a degree.

The copyright of this thesis belongs to the author under the terms of the United Kingdon Copyrights Acts as qualified by University of Strathclyde Regulation 3.50. Due acknowledgement must always be made of the use of any material contained in, or derived from, this thesis.

Signed: Date:

<u>Acknowledgements</u>

Abstract

The tumour suppressor protein, p53, is either mutated or absent in over 50 % of cancers and is negatively regulated by the mouse double minute two protein, MDM2. This thesis presents a novel nanosensing approach to investigate full-length MDM2 interactions with p53, thus providing an allosteric assay for identifying novel binding ligands. SERS (Surface enhanced Raman scattering) - active nanoparticles, functionalized with a p53 peptide mimic, peptide 12.1, display biologically specific aggregation following addition of MDM2. The extent of nanoparticle assembly is altered following the introduction of various MDM2 binding ligands. This is the first study to report nanoparticle assembly through specific protein-peptide interactions which can be followed by SERS. This approach lends itself to the development of a screening assay for identifying new MDM2 inhibitory molecules and a pilot screen of natural products is completed.

Owing to their biocompatibility, peptide functionalized nanoparticles have attracted increasing interest over the last decade for use in numerous biological applications applications. Controlling the assembly of peptide nanoparticles is of particular interest in the development of biocompatible nanomaterials. Coiled coil peptides have demonstrate highly specific binding activity in a variety of cellular functions and their structure is well understood. Work presented in chapter 4 of this thesis documents pH sensitive nanoparticle assembly driven by coiled coil heterodimer formation. SERS-active nanoparticles were functionalized with glutamic acid and lysine rich coiled coil peptides and assembly was observed, monitored using SERS, in heterogeneous solutions. This is the first instance of coiled coil directed assembly of silver nanoparticles followed by SERS.

Abbreviations

aa – amino acids

2-NPT – 2-Naphthalenethiol

α-cyano – α-cyano-4-hydroxycinnamic acid

AFM – Atomic force microscopy

AGIP – Amyloid growth inhibitor peptide

AgEDTA – EDTA-reduced silver nanoparticle

Ag-IR – near-IR linker functionalised AgEDTA

Ag-MBA – MBA functionalised AgEDTA

$AgNO_3$ – Silver nitrate

AgNP – Citrate-reduced silver nanoparticle

Ala – Alanine

ALPHAScreen – Amplified luminescence proximity binding assay

Ar+ - Argon

Asn – Asparagine

AU – Arbitrary unit

$AuCl_4^-$ - Gold (III) chloride

AuNP – Citrate-reduced gold nanoparticle

Au-TA – Thioctic acid functionalised AuNP

BT – Benzotriazole-PEG_3

BN - Bombesin

BRET – Bioluminescent resonance energy transfer

BSA – Bovine serum albumin

CAD – Central acidic domain (MDM2 protein)

CD – Circular dichroism

CFM – Confocal Fluorescence Microscopy

CRM – Confocal Raman microscopy

CFR – Curved field reflectron

CLIO – cross-linked iron oxide

Cys – cysteine

Da – Dalton

DAB – *p*-dimethylaminoazobenzene

DEE – Diethyl ether

ddH_2O – distilled and deionised water

DIPEA – Diisopropylethylamine

DLS – Dynamic light scattering

DMF – Dimethylformamide

DNA – Deoxyribose nucleic acid

DSNB – 5,5'-Dithiobis(succinimidyl-2-nitrobenzoate)

DTT – Dithiothrietol

EDTA – Ethylenediamine tetraacetic acid

EIA – Enzyme immunoassay

ELISA – Enzyme-linked immunosorbent assay

ERL – Extrinsic Raman label

Eu^{3+} - Europium (III)

FDA – Food and drug administration

FEM – Field emission electron microscope

FITC – Fluorescein isothiocyanate

FRET – Fluorescent resonance energy transfer

FWHM – Full width to half max

g – acceleration

Glu – Glutamic acid

GRPr – Gastrin-releasing peptide receptors

HATU – *O*-(7-Azabenzotriazol-1-lyl)-*N,N,N,N*-tetramethyluronium hexafluorophosphate

HCl – Hydrochloric acid

HeNe – Helium-Neon

HEPES – N-(2-Hydroxyethyl)piperazine-1-ethanesulfonic acid

His – Histidine

HIV – Human immunodeficiency virus

HPPS – High performance particle sizer

HS-PEG – thiol polyethylene glycol

IC50 – Half maximal inhibitory concentration

Ile – Isoleucine

KCl – Potassium chloride

L-CPL – Left handed circularly polarised light

Leu – Leucine

LSPR – localised surface plasmon resonance

LUT – Look up table (contrast scale)

Lys – Lysine

M – molar

MALDI-MS – Matrix-assisted laser desorption ionisation mass spectrometry

MBA – Mercaptobenzoic acid

MDM2 – Mouse double minute 2 protein

MeCN – Acetonitrile

mg – milligram

$MgSO_4$ – Magnesium sulphate

mL – millilitre

mM – millimolar

μL – microlitre

μM – micromolar

11-MUAM – 11-mercaptoundecanoic acid

m/z – mass to charge ratio

$NaAuCl_4$ – Sodium tetrachloroaurate

NaCl – Sodium chloride

NaOH – Sodium hydroxide

nM – nanomolar

nm – nanometre

NMR – Nuclear magnetic resonance

NP – nanoparticle

PDDA – poly(diallyldimethylammonium)

PEG – polyethylene glycol

PGN – peptide gold nanoparticle

PFTE – Polytetrafluoroethylene

pI – isoelectric point

pM – picomolar

pRb1 – Retinoblastoma protein

PSA – Prostate Specific Antigen

PSN – peptide silver nanoparticle

PNP – peptide functionalized nanoparticles

R-CPL – Right handed circularly polarised light

RIA - Radioimmunoassay

RING – Really interesting new gene

SAM – self-assembled monolayer

SEM – Scanning electron microscopy

SE(R)RS – Surface-enhanced (resonance) Raman scattering

SPR – Surface plasmon resonance

TA – Thioctic acid

TAT – Trans-acting transcriptional factor

TFA – Trifluoroacetic acid

TFE – 2,2,2-Trifluoroethanol

TIS – Triisopropylsilane

TNFα – Tumour necrosis factor alpha

TR-LRET – Time-resolved luminescence resonance energy transfer

TSH – Thyroid stimulating hormone

UV – Ultra violet

__Contents__

Chapter 1 – Introduction

Organism function, on a cellular level, is governed primarily by complex molecular processes involving proteins. Investigating how proteins interact and how these interactions may be altered during disease pathogenesis lends to the discovery of novel targets for disease therapeutics. New developments in the engineering of synthetic bionanomaterials can also be greatly enhanced through observing protein assembly.

1.1 – Proteins and peptides

Proteins are complex biological macromolecules whose intricate interaction networks are indispensable for controlling cellular function. DNA (deoxyribonucleic acid) is transcribed into mRNA (messenger ribonucleic acid), which in turn is translated into specific amino acid sequences that fold in various ways to produce conformations essential for protein function. Unveiling protein structures and interactions within signalling pathways is therefore critical to understanding disease pathogenesis. The elucidation of specific protein interactions involved in disease progression can lend to novel targets for drug development.

Since the evolution of solid phase peptide synthesis and owing to their biological compatibility, peptides have been increasingly investigated for use in numerous biological applications. Coiled coil peptides have been particularly explored for their assembly properties.[1, 2]

1.1.1 – Protein structure

Primary structure

The primary structure of a macromolecule is defined as the sequence of monomeric units making up a chain. In proteins this structure is composed of amino acids connected to each other via peptide bonds, often referred to as amide linkages. Figure 1.1 outlines the general amino acid structure and the formation of an amide bond through the loss of one water molecule. These reactions are commonly described as condensation reactions in reference to protein synthesis.
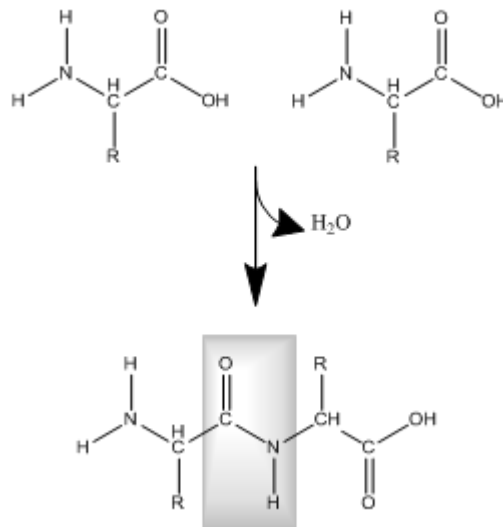
Figure 1.1 – Formation of a di-peptide by a condensation reaction.

The peptide theory came under much scrutiny when it was first proposed in 1902 by Emil Fischer and Franz Hofmeister and was not fully accepted until well into the twentieth century.[3] There are now known to be twenty amino acids occurring regularly

in proteins, fifteen of which were identified by Fischer as early as 1906.[3] Amino acids can be grouped according to their chemical properties arising from different side chain structures. Such groupings include: Hydrophobic, hydrophilic acidic, hydrophilic basic, hydrophilic amide, small, nucleophilic and aromatic. Structures of the twenty commonly occurring amino acids are reported in appendix A. Just as proteins can be built from individual amino acids, they can also be degraded by the breakage of peptide bonds in the primary structure resulting in shorter polypeptide chains.[3]

Secondary structure

Secondary structure of a macromolecule refers to the conformation arising from local interactions of the primary polymer. In proteins this is dependent on intramolecular hydrogen bonds between amide and carbonyl groups in the polypeptide backbone chain. Individual hydrogen bonding interactions are inherently weak, however numerous bonds can cumulatively create well defined structures. A number of different secondary protein conformations have been characterized. Organized structures predominantly take the form of α-helices and β-pleated sheets which were first described in 1951 (figure 1.2).[4] Most proteins contain a mixture of these helices and sheets, linked to each other via more flexible regions commonly referred to as loops and turns. The α-helix structure contains approximately 3.6 residues per helical turn and hydrogen bonding occurs, parallel to the helical axis, between main chain amide and carbonyl groups situated four amino acid residues apart.[4] β-sheets are composed of interacting individual β-strands in which the polypeptide backbone structure is almost fully extended. Stabilization of β-sheet formations results from hydrogen bonding between backbone amide and carbonyl groups on every second residue in individual β-strands, positioned in either a parallel or antiparallel orientation (figure 1.2).[4]
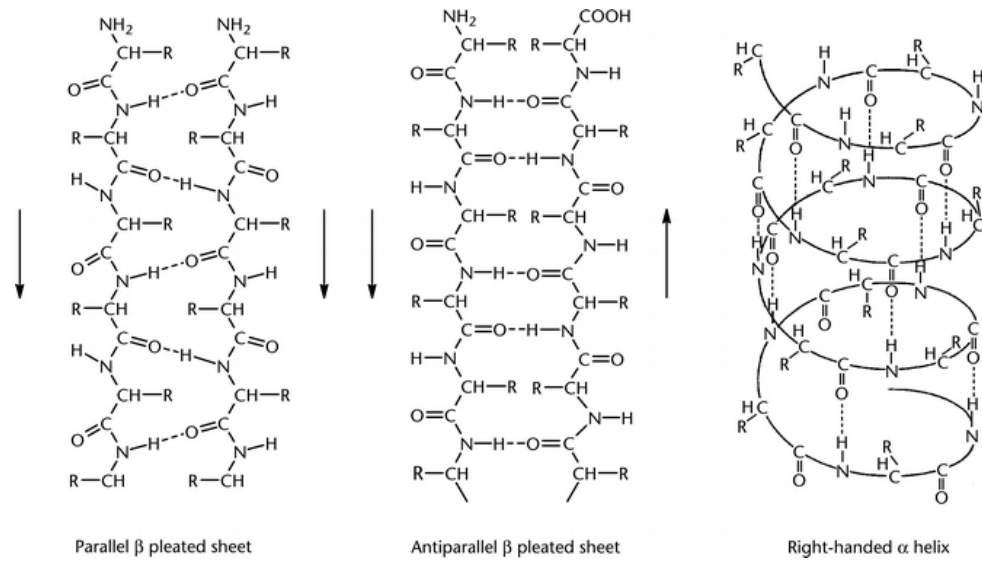
Figure 1.2 – Illustration of three commonly occurring secondary protein structures[4]

Studies into the refolding process of ribonuclease A were the first to indicate a role for the primary amino-acid sequence in secondary structure formation.[5, 6] Since then a phenomenal amount of research has focused on relating primary structure to protein folding.[6] Statistical studies have demonstrated certain residue patterns,[6] for instance the presence of polar residues in the flanking regions of helices can stabilize specific conformations.[6] Specific inter-strand pairing preferences have also been illustrated in β-sheets.[6] Secondary structure is lost during protein denaturation, where hydrogen bonding along the polypeptide chain backbone is disrupted.[6] Various interactions between amino-acid side chains also result in folding of secondary structure architecture into an overall globular structure, defined as the tertiary protein structure.

Tertiary structure

Tertiary protein folding is driven by the aqueous environment of the cell, which is responsible for the globular nature of most soluble proteins. Formation of hydrophobic pockets is shown to be of primary importance in protein folding and these are often found in the protein core due to clustering of non-polar residues.[6] Once formed, hydrophobic pockets are stabilized by Van der Waals interactions.[6] Hydrogen bonding between polar side chains and ionic interactions between positive and negatively charged side chains also play a role in the shaping of tertiary protein conformation. Finally, disulphide bond formation between cysteine residues bind parts of the protein structure together.[5] All of these interactions are essential in maintaining the native protein conformation and are disrupted during protein denaturation. Figure 1.3 depicts the tertiary structure of the hydrophobic pocket of a regulatory protein investigated in chapter 3, MDM2, containing a mixture of secondary architecture.
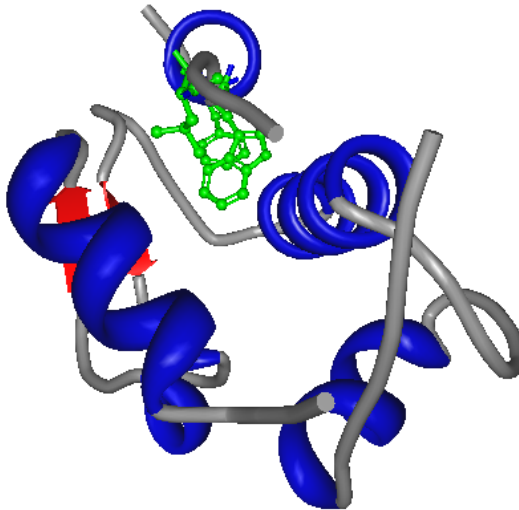
Figure 1.3 – Tertiary structure of the MDM2 hydrophobic cleft bound to a p53 peptide. Helices are depicted in blue, β-sheets in red and amino acid residues (Phe[19], Trp[23], Leu[26]) in green. Flexible loops and coils are shown in grey. PDB ID: 1YCR[7-9]

Quaternary structure

Many proteins comprise of more than one polypeptide chain (sub-unit) which are associated primarily via non-covalent interactions.[10, 11] Quaternary protein structure, elucidated in the late 1950s, refers to the spatial architecture of sub-units in an oligomer.[11] Proteins comprised of identical and non-identical sub-units are known as homo-oligomers and hetero-oligomers respectively.[10, 11] Multisubunit proteins are reported to be evolutionarily favoured since few proteins exist naturally as monomers.[10] This is proposed to be partly due to ease of sub-unit replacement compared with protein translation with respect to protein repair.[10] Integrity of the quaternary structure of proteins is vital for protein interactions and therefore functionality within cellular processes.[10, 11] Figure 1.4 illustrates the multisubunit structures of two well studied homo-oligomeric and hetero-oligomeric proteins.
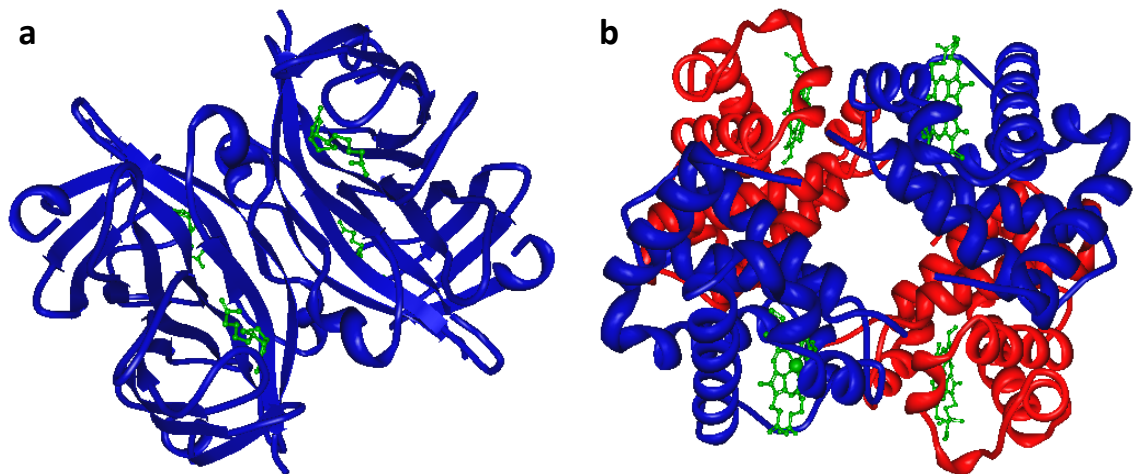
Figure 1.4 – a) Homo-oligomeric structure of streptavidin (blue) bound to four molecules of biotin (green). PDB ID: 1STP.[7, 9, 12] b) Hetero-oligomeric structure of haemoglobin bound to four haem molecules (green) with α and β subunits shown in blue and red respectively. PDB ID: 2DN2.[7, 9, 13]

1.1.2 – Protein-protein interactions

Understanding the interface of protein – protein interactions aids in the precise mapping of biochemical pathways, and elucidation of disease processes. Protein interactions are extensively studied in the development of novel therapeutic molecules designed to disrupt binding events which are crucial to disease progression. Protein interactions can be described as allosteric when the binding activity of one domain in a protein results in a conformational change in protein structure, which subsequently affects the binding activity of a separate domain on the same protein. This section describes two proteins, of which their interactions are central to cancer pathogenesis. Interactions between these two proteins, p53 and MDM2, are investigated using a novel nanoparticle-based assay in chapter 3.

1.1.2.1 – p53

The p53 tumour suppressor protein is central to a number of cancer progression pathways.[14-16] Predominantly known for its involvement in cell cycle regulation, p53 has been referred to as the 'guardian of the genome'.[14-16] The anti-proliferative action of p53 arises from the induction of cell cycle arrest and apoptosis in cells subjected to DNA damage in response to various metabolic and genotoxic stresses.[14-16] As such, p53 activity is critical to protecting cells from uncontrolled growth and malignant transformation. Inactivation or mutation of p53 is detected in over 50 % of human cancers.[14-16] The p53 structure is 393 amino acids in length, exhibits a non-globular conformation and consists of two separate oligomerization domains.[17] Oligomerization is essential for tumour suppressor activity in which p53 interacts with DNA as a dimer of dimers through a central DNA-binding domain (figure 1.5).[18] Alternative domain regions are involved in interactions with other cellular components.[19] Due to its clear

importance, characterization of p53 and its interactions are of utmost importance in medical research.
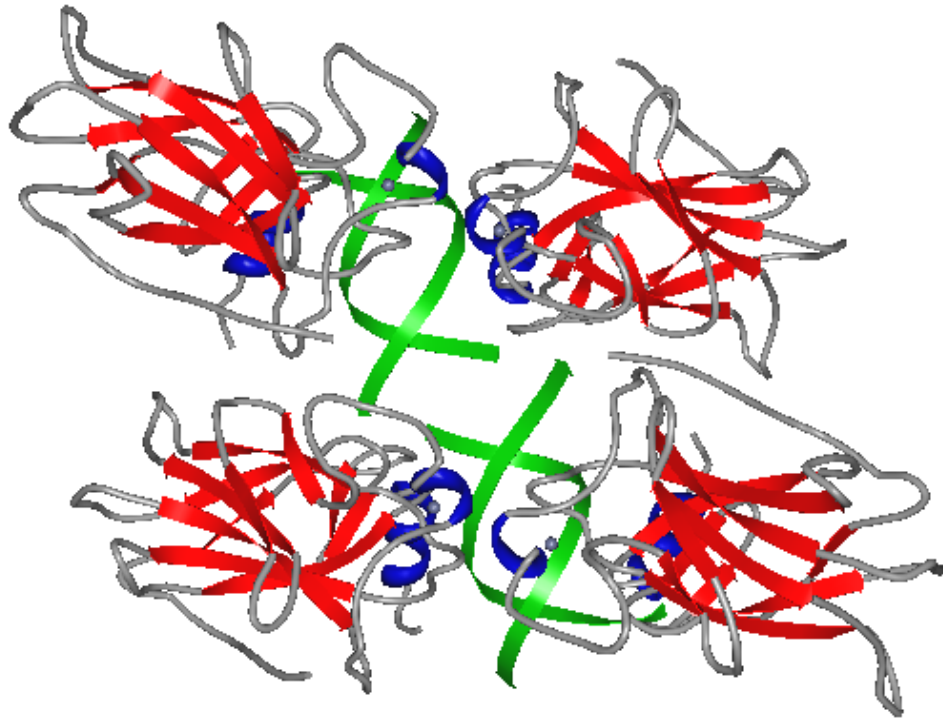
Figure 1.5 – Structure of the p53 core domain tetramer bound to DNA. Helices, β-strands and flexible loops and coils of p53 are depicted in blue, red and grey respectively. The DNA backbone is shown in green. PDB ID: 2ADY.[7, 9, 20]

1.1.2.2 – MDM2

The *MDM2* gene was first identified in 1991 by Fakharzedeh *et al.*, who reported the development of tumourogenic properties in cell lines which over-expressed this gene.[21] MDM2 binding and subsequent inactivation of p53 was demonstrated in 1992,[22, 23] since when the p53-MDM2 interaction has been extensively studied as a target for cancer therapeutics.

Structure of MDM2

Murine double minute (MDM2) is a 491 amino acid protein with a flexible conformation containing three distinct functional domains.[24] The N-terminal domain, often referred to as the hydrophobic pocket / cleft, contains a binding site for the p53 BOX-1 domain (figure 1.6a).[8, 25] Structural elucidation of this binding event has shown that the p53 BOX-1 domain forms an amphipathic helix in binding the hydrophobic pocket of MDM2 via specific aromatic – aromatic interactions.[8, 26, 27] Owing to the therapeutic potential, a number of small molecule and peptide inhibitors have been designed to efficiently block this p53-MDM2 binding event.[28-33] The central acidic domain (CAD) of MDM2 is known to bind the p53 BOX-V domain (S9-S10 region).[34] This secondary p53-MDM2 binding event is not as well defined as BOX-1 interactions with the hydrophobic cleft, however it is required for MDM2-directed ubiquitination of p53.[25, 34] A number of other proteins have also been found to bind the CAD of MDM2.[35, 36] Finally, the MDM2 C-terminal consists of an ATP binding site and a RING finger domain which plays a regulatory role in enzymatic activity (figure 1.6b).[24] The RING finger domain contains two Zn^{2+} coordination sites and incorporation of Zn^{2+} is shown to be essential for maintaining domain structure.[37] Recent work has also shown that certain RING finger domain interactions may positively influence CAD binding.[24]
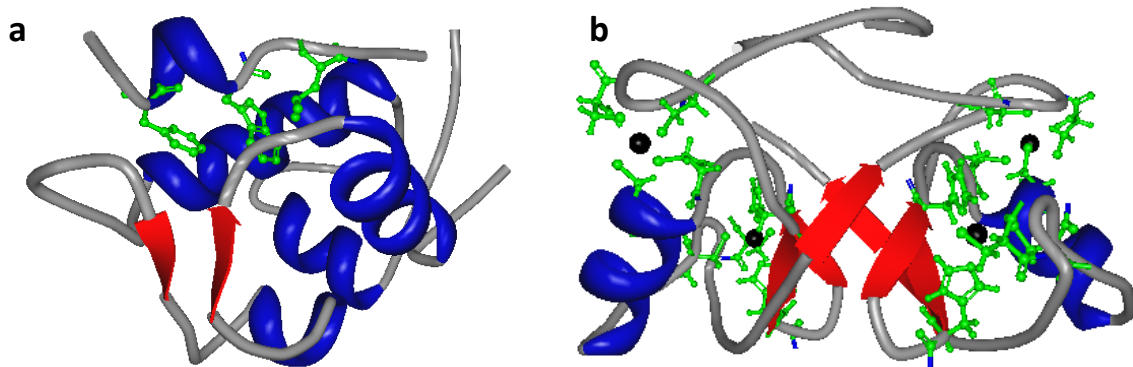
Figure 1.6 – a) Structure of the MDM2 hydrophobic cleft interacting with a helical p53 peptide (unattached) showing the romatic sidechains Phe19, Trp23 and Leu26 (PDB ID: 1YCR[7-9]). b) Structure of the HDM2 RING domain homodimer incorporating four molecules of Zn^{2+} (PDB ID: 2HDP[7, 9, 37]). Side chains from zinc – binding site C4 (Cys438, Cys441, Cys461 and Cys464) and zinc – binding site H2C2 (His452, His457, Cys475 and Cys478) are shown. Helices are depicted in blue and β-sheets in red, flexible loops and coils in grey, amino acid side chain structures in green and Zn^{2+} molecules in black.

MDM2 as an E3 Ubiquitin ligase

Regulation of protein levels within a cell can be achieved by either preventing translation, via gene transcription repression, or through proteolysis (protein degradation). Proteolysis involves the breakdown of peptide bonds catalysed by proteolytic enzymes. This process typically occurs within the proteasome.[38] Proteins are targeted for proteasomal degradation by ubiquitination, which is achieved through recruitment of ubiquitination enzymes in a three step process.[38] Ubiquitin is firstly activated via loading onto a ubiquitin-activating enzyme (E1) before being transferred to a ubiquitin-conjugating enzyme (E2).[38] Ubiquitin-ligase (E3) is then recruited to aid relocation of Ubiquitin from E2 to a lysine residue on the target substrate.[38] The catalytic activity of E3-ligase is mediated by a RING finger domain, which creates a favourable environment for transfer of ubiquitin directly to the target protein.[39] MDM2

exhibits E3-ligase activity, dependent on its C-terminal RING finger domain, thus targeting p53 for degradation via ubiquitination.[37, 40] MDM2-induced p53 ubiquitination is inhibited in stress conditions allowing for p53 driven cell degradation and apoptosis.[41]

MDM2-directed p53 ubiquitination

MDM2-induced ubiquitination of p53 is proposed to occur through a dual-site mechanism involving two separate interactions between MDM2 and p53.[25] p53 BOX-1 binding to the MDM2 hydrophobic pocket is essential for targeted ubiquitination, however this interaction alone is not sufficient to complete the process.[25] This initial p53-MDM2 interaction creates cross-talk between the hydrophobic pocket and CAD of MDM2, of which the latter subsequently binds to the BOX-V site within the p53 core domain.[25] This secondary binding event confirms the p53 ubiquitination signal.[25] Previous studies have shown the RING finger domain to be critical for MDM2-mediated ubiquitination.[40, 42-44] Evidence suggests that binding of certain ligands to the MDM2 RING finger domain stabilizes the CAD in a conformation favourable for the secondary binding event with substrates such as p53.[24] Mutation of cysteine residues within this domain have also been shown to enhance the binding affinity of the MDM2 hydrophobic cleft.[24]

Protein interactions are crucial to regulatory process such as MDM2-mediated ubiquitination and are therefore important to be able to monitor. A number of techniques exist for protein interaction studies, many of which are described in the next section.

1.1.3 – Coiled coil peptides

The coiled coil peptide conformation was initially identified in structural studies of tropomyosin and alpha-keratin.[45, 46] Various coiled coil based protein structures have since been elucidated and are predicted to make up to 10 % total translated protein.[47, 48] Coiled coils are often referred to as 'cellular velcro' owing to the high binding specificity and variety of functionalities in holding together subcellular components.[49] Their structures consist of repeating amino acid heptad units (section 1.2.1). Naturally occurring coiled coils are classified as either short (2 – 7 heptad units) or long (greater than 7 heptad units) coiled coils.[49-51]

The shortest coiled coils found in nature are in yeast transcription factors and comprise of 14 and 19 residue helices.[50] Short coiled coils, traditionally leucine zippers, act as specific binding domains in transcription factors.[52, 53] Functionality in macromolecular ion signalling complexes and other signal transduction components have also been reported.[49, 54-57] Specificity of coiled coil formation has been demonstrated through manipulation of amino acid composition and residue side chain modification.[58] The exclusivity of these specific binding events is however questionable with some coiled coil sequences accepting multiple coiled coil binding partners within signalling processes.[59]

Long coiled coils are associated with complex structural and regulatory cellular processes and are much more prevalent in eukaryotes than in prokaryotes owing to the complexity of cellular organization.[49, 60] Bacterial coiled coils are primarily involved in cytoskeletal structure and maintaining cell shape.[61, 62] Eukaryotic coiled coils have a diverse range of structural and dynamic functions within cellular infrastructure and membrane transport regulation.[60, 63-68] The longest coiled coil, comprising of 1485 residues, is found in the nuclear mitotic apparatus protein, NuMA, involved in dynamic and structural roles in mitosis.[64] Cytoskeletal motor proteins such as kinesin, dynein and myosin exploit the elastic properties in coiled coil domains for microtubule motor

processes and muscle contraction.[63, 65, 66] Coiled coils are also conserved in SNARE proteins, involved in regulation of vesicle transport and membrane fusion, and a coiled coil domain in Influenza Hemagglutinin has been shown to aid viral membrane fusion.[67, 68]

Coiled coils show huge potential in the development of novel biomaterials and drug delivery vectors owing to their biocompatibility, self-assembly, binding specificity and ease of manipulation. Chapter 4 investigates the use of coiled coil peptides for controlled nanoparticle assembly.

1.1.3.1 – Structure

Crick *et al* first described the α-helical coiled coil structure in 1953, however it was not until two decades later that experimental confirmation was published relating to rabbit skeletal tropomyosin.[46, 69] Despite identification of an amino acid heptad repeat in the coiled coil forming α-helices of tropomyosin in 1975, coiled coils didn't attract much attention until leucine zippers were identified as transcription factor dimerization domains in the late 1980s.[53, 70] Coiled coils are typically left handed helical oligomers of α-helices that pack together via hydrophobic 'knobs into holes' interactions along the dimer interface.[69, 71] Interacting helices contain heptad repeats, abcdefg, which make up approximately 1 nm in length. Right handed coiled coil structures have also been identified in which peptide helices follow undecad periodicities, however these are much rarer in nature and have not been studied extensively.[72] In left handed coiled coils hydrophobic residues at positions a and d are involved in interface packing while charged amino acids at e and g are for intermolecular electrostatic interactions (figure 1.7).[71, 73, 74] As coiled coil structure relies on both hydrophobic and electrostatic interactions, conformations are susceptible to manipulation through minor compositional changes and environmental factors such as temperature and pH.[75-77] In

the same instance orientation and stability of synthetic coiled coils can be controlled through amino acid sequence changes and modifications.[78-82]
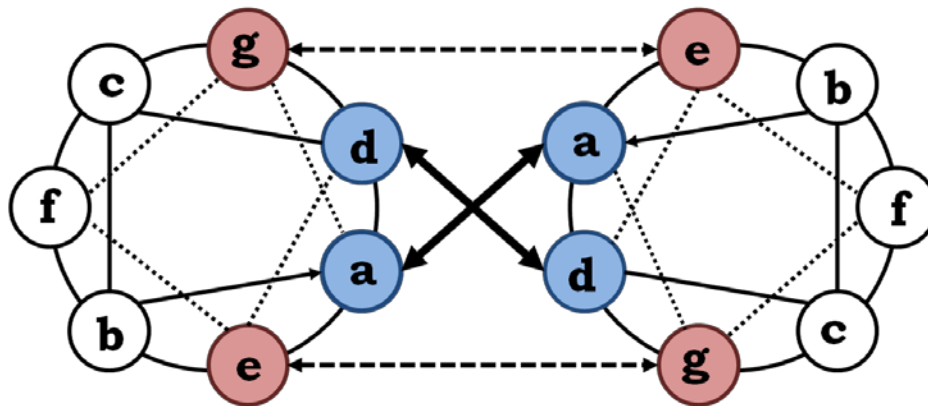
Figure 1.7 – Schematic of parallel coiled coil formation. Solid line and dashed line double headed arrows represent hydrophobic and electrostatic interactions respectively.

Structural stability of coiled coils has demonstrated some dependence on helix length.[83] Modifications such as fluorination of core residues to enhance hydrophobic packing and altering charged residues at e and g to achieve strong electrostatic ability have enabled synthesis of stable coiled coil structures as short as 2 nm.[78, 81] Parallel and antiparallel orientation has demonstrated dependence on both intermolecular interactions and the amino acid composition of the hydrophobic core.[75, 80] Leucine zippers typically occur as homodimers in nature with opposing charges situated at e and g. Heterodimeric structures have been demonstrated by mixing two differently charged peptides, incorporating either lysine or glutamic acid at both e and g positions.[74] Whilst electrostatic charges are crucial to heterodimer formation, specificity of the interaction remains partially dependent on hydrophobic packing.[84] Acidic and basic peptide mixtures showed heterodimer specificity depending on substitution of the residue at position a.[84]
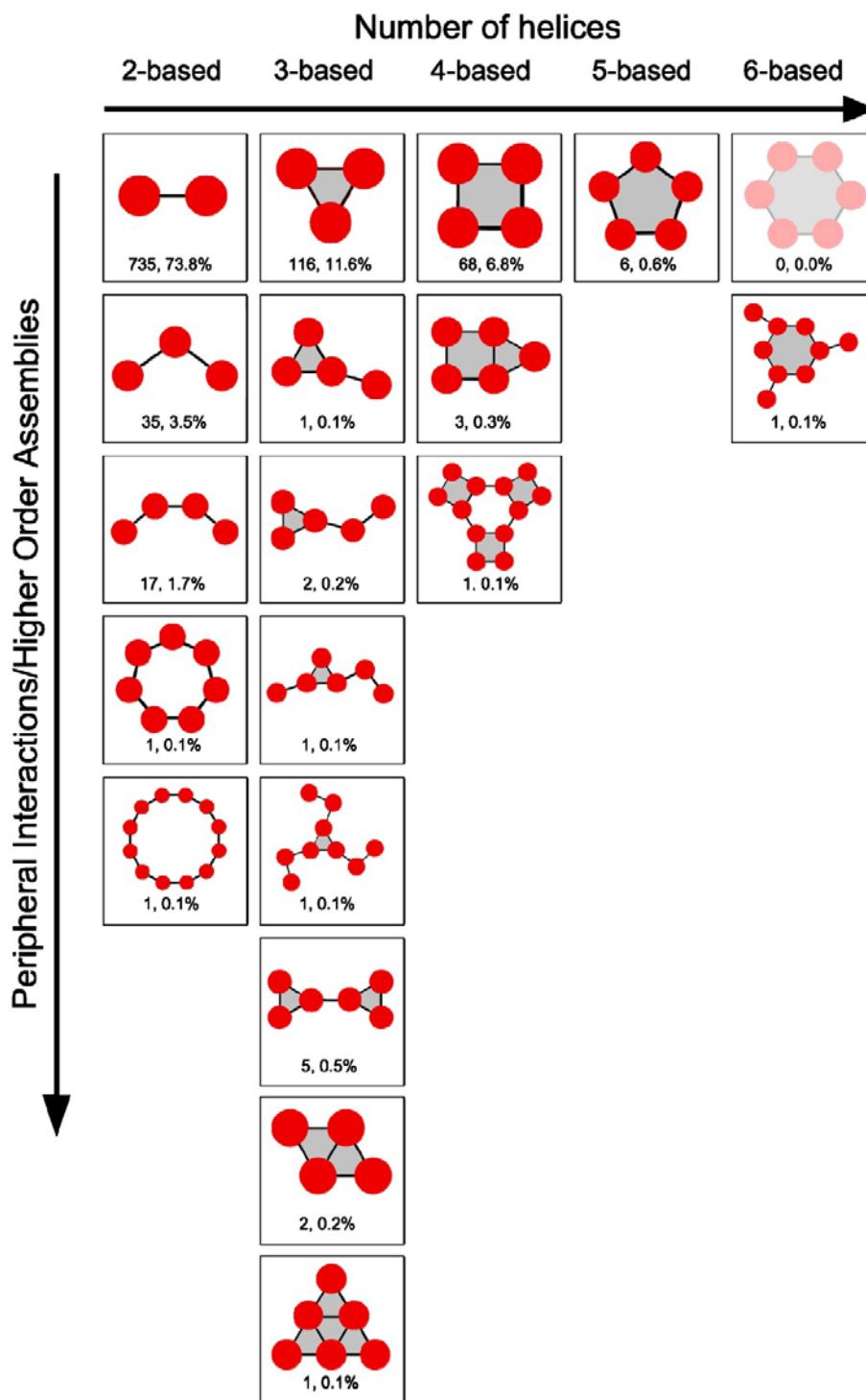
Figure 1.8 – Periodic table of coiled coil peptide structures showing helices (red circles), ionic interfaces (lines) and hydrophobic cores (grey areas). Reproduction of a figure by Moutevelis and Woolfson, J. Mol. Biol. (2009) 385, 726-732.[47]

Coiled coils are classically referred to in the dimeric state, however oligomers exist consisting of up to six helices adopting a number of structures outlined in the table reported by Moutevelis and Woolfson (figure 1.8).[47] The oligomerization state can be controlled by varying hydrophobic core residues such that designed computer algorithms can accurately predict coiled coil oligomerization states from the primary amino acid sequence.[77, 85] Peripheral residues in the b, c, e, f and g positions also contribute to the organization of higher oligomerization states.[86] One notable example of controlled oligomer formation is the favoured dimer formation when isoleucine and leucine are positioned at a and d respectively.[85, 87] The heterodimer formation described in chapter 4 is based on acidic and basic peptides with this Ile / Leu hydrophobic interface.

1.1.3.2 – Higher order coiled coil structures and applications

Coiled coils provide ideal substrates for synthetic biological systems and functional biomaterials. Higher order coiled coil assembly has become increasingly studied over the past 15 years. Long coiled coils found in nature predominantly adopt rod like fibrous structures therefore self assembly of synthetic peptides can provide insight into protein fibrillogenesis.[49, 60, 61, 64]

Fibrils

Coiled coil self assembly into fibrils was first described by Kojima *et al*. in 1997 and although it was known that hydrophobic and electrostatic interactions were involved the molecular assembly was not fully understood.[88] Three years later Pandya *et al.* employed a 'sticky-end' approach, analogous to DNA assembly in molecular biology, for fibril formation.[89] In this case fibril assembly was primarily directed by electrostatic

interactions between staggered peptides resulting in elongated coiled coils with 'sticky ends' (figure 1.9 a).[89] Mature fibres were also observed due to lateral associations between elongated coiled coil structures.[89] Subsequent studies highlighted the importance of peripheral residues at b, c and f positions for intermolecular interactions driving fibre thickening.[90, 91] Various methodologies have since been employed to generate fibres with coiled coils organized in parallel to the fibril axis.[1, 90-92] Axially staggered peptides designed to favour a pentamer structure, were self-assembled into a superhelix resembling pentameric coiled coil features.[92] Fibril formation was also demonstrated via concentration dependent 'blunt-end' dimer oligomerization (figure 1.9 b).[90] Incorporating alanine residues between heptad repeats resulted in coiled coil staggering in such a way that 'sticky-end' self assembly was driven by hydrophobic rather than electrostatic interactions.[1] Alternatively, fibrils have been described from self-assembly of helix-turn-helix coiled coil motifs orientated perpendicular to the fibril axis and supramolecular assembly of coiled coils on dendrimer scaffolds (figure 1.9 c and d).[93, 94] Protein scaffolding and silica templating applications of synthetically produced fibres have been reported with electrostatically directed staggered fibrillogenesis and modification of amino acid peripheral residues.[95, 96] Supramolecular structures have been prepared incorporating designed reaction sites thus providing a tuneable polynanoreactor capable of functions such as nanoparticle formation.[97] Nanoparticles have also been shown to regulate the secondary structure of model peptides and promote fibril formation.[98]
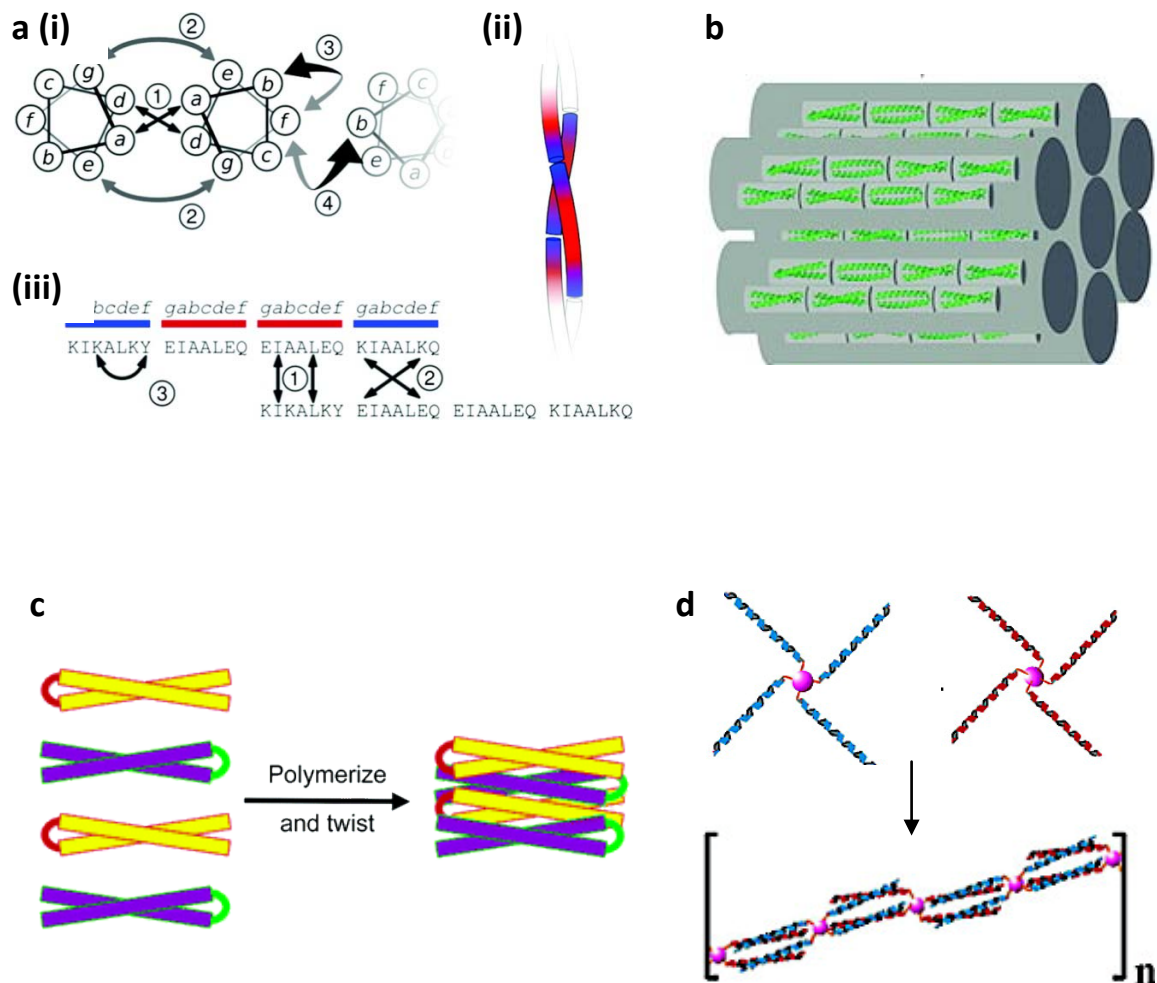
Figure 1.9 – Published examples of coiled coil fibril formation. a) schematic of 'stick end' coiled coil fibril formation: i) helical wheel representation, ii) peptide sequence illustrating acidic (red) and basic (blue) regions and iii) resultant fibril structure.[89, 91] b) Matured fibres produced through lateral association of dimeric coiled coils.[90] c-d) Fibril formation driven by c) lateral stacking of helix-turn-helix motifs[93] and d) acidic (red) and basic (blue) coiled coils on dendrimer scaffolds.[94] Reproduction of figures from a) Gribbon *et al*. Biochemistry (2008), 47, 10365-10371 b) Dong *et al.* J. Am. Chem. Soc. (2008) 130, 13691-13695 c) Lazar *et al*. Biochemistry (2005) 44, 12681-12689 and d) Zhou *et al.* J. Am. Chem. Soc. (2004) 126, 734-735.

Hydrogels

Self assembling coiled coils have been employed in the formation of hydrogels, many of which incorporate different synthetic or biological molecules.[99-103] In fibrillogenesis polar or charged amino acids are commonly situated at b, c and f positions, hence aiding solubility and promoting lateral intermolecular electrostatic interactions required for fibre thickening.[1, 99] In contrast, peptides utilized in hydrogel formation are designed with either alanine or glutamine at b, c, and f peripheral positions within the coiled coil.[99] Alanine and glutamine can form either weak intermolecular Van der Waals interactions or hydrogen bonding respectively and thus random hydrogel formation is favoured over lateral interactions.[99] Hydrogels prepared with alanine demonstrated increasing stability with temperature up to 95 $^{\circ}$C.[99] Glutamine hydrogels were seen to liquefy within the temperature range, 16-19 $^{\circ}$C, and return to gel state at temperatures above 19 $^{\circ}$C.[99] Hydrogelation of artificial proteins, incorporating leucine zipper domains, has been documented and shown to be controllable at ambient temperatures and pH.[102] Coiled coil fusion of hydrophobic and hydrophilic polymers has also resulted in an amphiphilic triblock copolymer.[100] These models present potential for biomaterials and controlled drug release (figure 1.10).

Hydrogels formed with metal complexing capabilities have been shown to function as recognition structures for His-tagged proteins.[103] Similarly, keratin hydrogels have shown recruitment and proliferation of neural stem / progenitor cells in the presence of growth factors.[101] Development of complex synthetic biological systems exploiting coiled coil properties is a continually developing field with the design of increasingly diverse and structurally robust building blocks.[104, 105]
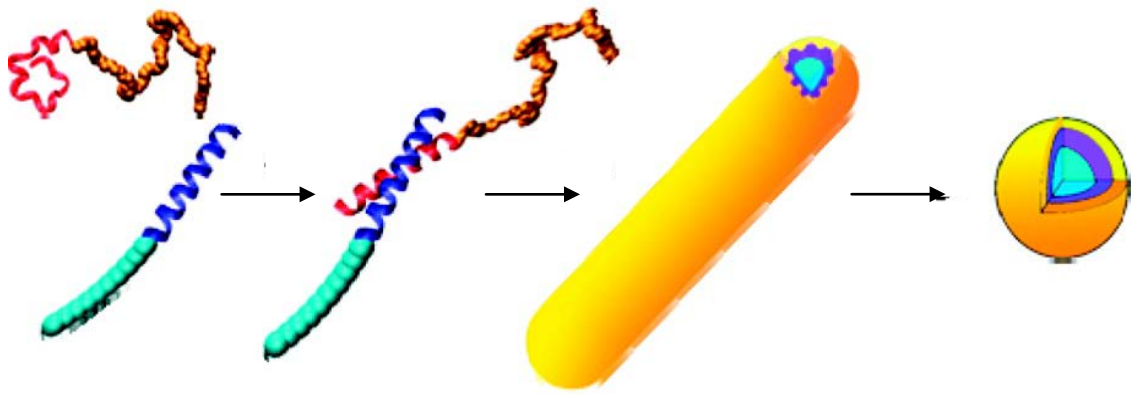
Figure 1.10 – Schematic representation of the triblock copolymer rods and micelles resulting from coiled coil assembly of polystyrene modified E-rich peptides, PS-E (aqua and blue) and poly(ethylene glycol) modified K-rich peptides, K-PEG (red and orange).[100] Coiled coil peptide dimers are represented by purple in rods and micelles. Reproduction of an figures by Robson Marsden *et al*. J. Am. Chem. Soc. (2008) 130, 9386-9393.

1.2 – Peptide functionalized nanoparticles (PNP)

In the late 1990's investigations demonstrated the potential for nanoparticle (NP) structures in cellular delivery of proteins and peptides.[106-109] These NPs were constructed from various polymers including polystyrene, gelatine, agarose and lipids.[106-109] Metallic NPs display unique optical properties, as a result of their localized surface plasmon resonance (LSPR), which is altered dependent on nanoparticle size, shape and aggregation state.[110, 111] Changes in the LSPR of such structures are susceptible to detection with various spectroscopic techniques.[110, 112] Peptide functionalized NPs (PNPs) have thus been increasingly explored for various biological applications including biosensing and bioimaging.

1.2.1 – PNP Design

The first report of a PNP involved the functionalization of cross-linked iron oxide (CLIO) particles with a peptide sequence derived from the HIV trans-acting transcriptional factor (TAT) protein, designed for intracellular magnetic imaging of different target cells.[113] PNP were prepared via disulphide linkages between the NP surface and a terminal cysteine residue on the TAT sequence.[113] More recent studies have focussed on the preparation of peptide gold NPs (PGNs) and peptide silver NPs (PSNs).[114-117] Thiolated ligands are able to covalently bond with the metallic NP surface and as such cysteine residues are commonly employed for peptide-NP attachment. Stable, water soluble PGNs were first reported through the formation of self-assembled monolayers (SAMs) of the pentapeptide sequence, CALNN.[118] This peptide sequence was rationally designed to incorporate a gold binding residue, Cys, a hydrophobic core for SAM formation, Ala-Leu, and a hydrophilic terminal for aqueous solubility of PGNs, Asn-Asn.[118] Multiple peptide sequences, with different biofunctionalities, have since been explored for PGN synthesis via thiol linkages.[114, 116, 119, 120] Investigations have illustrated the propensity of intra and intermolecular interactions of functional peptides in mixed-monolayers to be dependent on spacing on the NP surface.[116] Structural studies of helical peptides on gold NPs (AuNP) of varying sizes has also shown an effect of surface curvature on helical formation.[121] Peptides immobilised on NP with over 20 nm diameter or on flat surfaces demonstrated an α-helical content of 100 %.[121] The α-helical content of NP-bound peptides decreased in correlation with AuNP size below diameters of 20 nm.[121]

A novel methodology for PGN preparation was reported in 2009 in which peptide ligands were introduced into the NP synthesis protocol.[122] Rather than employing the commonly used citrate reduction method described by Turkevitch *et al.*,[123] AuNP were produced via HEPES-reduction of $AuCl_4^-$ in the presence of a cysteine-terminal peptide ligand.[122] In this protocol the thiol group present on the terminal cysteine residue

contributes to $AuCl_4^-$ reduction.[122] This reaction can be carried out at ambient temperature and neutral pH thus maintaining peptide functionality and PGN conjugates maintain solution stability for over six months.[122] Further to this study, reduction capabilities of the 20 commonly occurring amino acids were investigated.[115] Tryptophan demonstrated the fastest rate of $AuCl_4^-$ reduction and as such was chosen as the common constituent in multiple peptide sequences explored to control the size and shape of produced PGN.[115]

PSN are less well studied than PGN, however similar reaction chemistries could be employed for, silver NPs (AgNPs), prepared using a modified Lee and Meisel citrate-reduction method,[124] with respect to thiol linkages. Peptide capping of AgNP has been documented using the tripeptide, Lys-Lys-Cys.[117] In this study peptide surface orientation and PSN aggregation state was shown to vary dependent on the solution pH. PSN plasmonic properties were exploited using surface-enhanced Raman scattering (SERS) in order to characterise the peptide capping in different conditions.[117]

1.2.2 – Biological applications of PGN

The use of PGN for imaging and therapeutic purposes is still in its infancy, however significant developments have been made over the last decade.[119, 120, 125-131] The first cell penetrating peptide was identified from the HIV-TAT protein at the turn of the century.[113, 127] Cellular uptake of CLIO NPs was increased upon TAT conjugation[127] and this initiated a field of study into the use of nanoparticles as vectors to transport exogenous molecules across cell membranes.[128, 130] The peptide sequence, CALNN, has been shown to form SAMs on AuNP leading to stable, aqueous soluble PGNs.[118] PGN functionalised with a CALNN peptide derivative, $CALNNR_8$, demonstrated spontaneous cellular uptake.[130] Internalization of PGN into cells was not observed when Arginine residues were substituted with Lysine or Serine indicating that membrane shuttling is a

charge and residue specific function.[130] Control of subcellular localization was also demonstrated by altering proportions of CALNN and CALNNR$_8$ in mixed-monolayer PGNs.[130] Cellular uptake of PGNs has also been demonstrated with Proline-rich peptides exhibiting minimal cytotoxicity.[128] Once incorporated into a cell charged PGN structures are highly susceptible to non-specific interactions with endogenous molecules. Non-specific PGN interactions with biological media have been minimised by creating mixed-monolayers of functional peptide with thiol-polyethylene glycol (HS-PEG).[119]

Thus far PGN preparation has been described incorporating peptide sequences favourable for cell membrane penetration. Recent developments in the design of PGN have incorporated peptides targeting specific cell surface receptors on tumour cells.[126, 129] Further to this, multifunctional PGN have been reported that exhibit a mixed monolayer of two specific peptide sequences, a Bombesin peptide analogue and a RAF drug peptide ligand.[126] Bombesin (BN) peptide analogues recognise gastrin-releasing peptide receptors (GRPr), commonly over-expressed by tumour cell lines, and mediate cell uptake of PGNs.[126] The RAF protein is involved in signalling pathways associated with cellular growth, proliferation and differentiation. As such a RAF drug peptide ligand was designed to disrupt a specific protein interaction resulting in reduced tumour proliferation.[126] *In vitro* studies have also demonstrated initiation of macrophage responses following incubation with PGN incorporating amyloid growth inhibitor peptide (AGIP).[125]

Alternative investigations have elucidated biotin functionalised AuNP through an intermediate functionalisation with a multidentate peptide.[120] PGNs have also been described, using CALNN peptide derivatives, that bind lanthanide ions for use in bioimaging applications.[131]

1.2.3 – PNP self-assembly

Controlled nanoparticle assembly is of great interest for the development of novel nanomaterials. To that end, programmed self-assembly of PGNs has been investigated in recent years.[117, 132-134] Research has demonstrated pH triggered reversible assembly of both PGN and PSN.[117, 133] In the case of PGN assembly, AuNP were functionalised with a disulphide modified peptide, SSPLGA, with the propensity for helical formation at low pH.[133] By lowering the pH conditions, helix formation and consequential PGN assembly was observed.[133] PSN reversible aggregation was controlled by orientation of the capping tripeptide, Lys-Lys-Cys.[117] At pH 3, lysine residue positive charges create sufficient electrostatic repulsion for PSN monodispersion, whereby zwitterionic properties exhibited at pH 7 lead to unstable solutions with small PSN clusters.[117] Aggregation is observed at high pH where the terminal carboxylate group carries a negative charge creating insufficient electrostatic repulsion for monodispersion, hydrogen bonding can also occur between neutral lysine residues.[117] PGN assembly has also been illustrated through the addition of aggregating molecules.[132, 134] In such cases capping peptides were designed to interact with incorporated substrates such as metal ions or DNA.[132, 134] DNA-binding PGN assembly architecture can be manipulated through DNA template selection.[132] The work documented in chapter 4 investigates pH dependent coiled coil mediated PGN and PSN assembly. PSN were also developed with a specific p53 peptide mimic to investigate the p53-MDM2 interaction described in section 1.1.2. Chapter 3 investigates the assembly of these specifically designed PSN for the detection of protein – protein interactions in a novel assay format.

1.3 – Existing techniques for protein interaction studies

The first radioimmunoassays (RIA) for detection of biomolecule interactions were described in the late 1950s and used I^{131} labelled insulin.[135, 136] Since then numerous readout techniques have been developed, some of which are more established than others.[137-148] Physicalities of antigen – antibody interactions have been examined using atomic force microscopy (AFM),[149] however labelling strategies are more commonly used. Although radioactive and metal ion labels have been employed in immunoassays with a degree of success,[135, 136, 143] fluorescence has become widely favoured, owing to sensitivity, stability and ease of handling.[140, 141, 146, 148]

1.3.1 – Fluorescence

A number of fluorescence-based techniques have been developed over the last 50 years for the investigation of biological systems. The enzyme – linked immunosorbent assay (ELISA), also known as an enzyme immunoassay (EIA), is one of the oldest methodologies and was first described in 1971.[137, 145] In a typical ELISA, proteins interact with antibodies on a surface and are subsequently detected by monitoring the activity of conjugated enzymes.[137, 145] Modern ELISA technologies often incorporate fluorescent-labelled substrates for lower detection limits.[140, 144, 146]

Fluorescence resonance energy transfer (FRET)

Fluoroimmunoassays, developed in the early 1990s, investigate biological interactions via antibody – lanthanide complexes.[141, 148] Lanthanide ions form fluorescent chelates with comparatively narrow emission spectra and these can be measured in a time resolved format.[141] Lanthanides have also been employed in fluorescence resonance

energy transfer (FRET) immunoassays.[140] Hormone detection in serum has been demonstrated by exploitation of FRET between europium (III) (Eu^{3+}) and a Cy5 organic dye.[140] In this instance, Cy5-labelled antibody binding to europium labelled bovine serum albumin (BSA) was detected.[140] Upon biomolecule interaction energy is transferred from Eu^{3+} to Cy5 molecules which are in close proximity resulting in a long-lived emission from the Cy5.[140] The interaction can thus be monitored through measuring the long-lived Cy5 emission in a time-resolved format.[140] More recently, higher detection sensitivity was attained through the incorporation of AgNP into a similar assay system.[150] Donor Eu^{3+} polystyrene particles have also demonstrated detection of acceptor-labelled protein aggregation using time-resolved luminescence resonance energy transfer (TR-LRET).[151] FRET-based immunoassay methodologies require careful labelling of biomolecules and detection is limited to donor and acceptor separation distances of less than 10 nm.

Fluorescent nanoparticles

Fluorescent nanoparticles have shown enormous potential in bioanalytical applications.[142, 144, 152, 153] Quantum dots (semiconductor nanospheres, typically 2-8 nm in diameter) are comprised of a cadmium selenide core capped with zinc sulphide.[144] They exhibit luminescence and can be easily conjugated to biomolecules, allowing analysis of biomolecular interactions via photoluminescence.[142, 144, 152, 153] An advantage of using quantum dots over other fluorescent beacons is the comparatively narrow emission spectra, controlled by the crystal size and composition.[142] This enables simultaneous excitation of multiple quantum dots and reproducible deconvolution of emission spectra.[142] Multiplexing capabilities of quantum dots, along with resistance to photobleaching, make them a desirable tool for probing biological systems.[142, 146, 152] To this end quantum dots have been employed for multiplexed quantum dot staining in tissue samples and *in vivo* monitoring of enzyme activity.[142, 152] Large Stokes shifts and

high quantum yields associated with quantum dots also render them ideal acceptors in bioluminescent resonance energy transfer (BRET).[146] This allows for *in vivo* imaging in the absence of a light source as many bioluminescent proteins are able to act as BRET donors.[146]

ALPHAscreen^(TM)

The Amplified Luminescence Proximity Homogeneous binding assay (ALPHAscreen[TM]) is a protein – protein interaction screening platform available from Perkin Elmer. Protein binding partners are immobilized on donor and acceptor beads. Upon protein interaction the beads come into close proximity. Excitation of a photosensitizer in the donor bead results in the transfer of one oxygen molecule to the acceptor bead and subsequent fluorophore activation and emitted light. This immunoassay platform allows for high throughput sample analysis and as such has been employed in the screening of 1000s of interaction inhibitors.[154] ALPHAscreen technologies have been previously used to confirm MDM2-p53 interaction inhibitor molecules.[155]

1.3.2 – Surface plasmon resonance (SPR)

Surface plasmons can be described as electromagnetic waves close to a metal surface.[111, 156] Oscillations propagate in a direction parallel to the metal surface and are sensitive to surface structure alterations, for example surface roughening or molecule adsorption.[111] Surface plasmon resonance involves excitation of this surface polarization as a result of incoming light.[111, 156] As such, changes in SPR, due to mass changes at the metal boundary, can be utilized as a sensitive detection technique for proteins adsorbed onto surfaces.[138, 147] Real time analysis of enzyme activity has been achieved monitoring SPR changes induced by serum antibodies binding to immobilized

protein.[147] Interrogation of SPR has also been successfully applied to investigate the complex architecture of proteins.[138] Using this format, SPR changes were recorded following stepwise addition of each complex component of the p14 ARF – MDM2 – p53 system.[138] The SPR of roughened metal materials has also been shown to enhance Raman scattering allowing for the development of novel biomolecule interaction detection methodologies.[112, 157]

1.4 – Raman Theory

Raman is an optical detection technique which can be used as an alternative to fluorescence for investigating biomolecular interactions. Light interacting with matter can either be absorbed, scattered or pass through without interacting with the material.[156] Absorbance of photons occurs when they exhibit the same energy as that between the ground state and an excited state of the interacting molecule.[156] This causes promotion of the molecule to its excited state and the resulting depletion of radiation energy from light is measured in absorption spectroscopy.[156] If the energy of interacting photons fails to match that between molecular energy states, the photon is scattered.[156] Scattering of photons can be either elastic or inelastic and involves transition of the molecule into a virtual energy state.[156] Elastic scattering, often referred to as Raleigh scattering, is the dominant of the two processes and occurs through interaction of the photon with the electron clouds around nuclei.[156] As electrons are relatively light, photons are scattered with minimal change in frequency. Photons scattered in an inelastic manner are Raman scattered.[156]

1.4.1 – Raman scattering

Raman is an inherently weak process with an estimated 1 in 10^6 photons being scattered in this way.[156] Photons interacting with a molecule can induce nuclear motion, which results in energy transfer between the interacting photon and the molecule.[156] Energy transfer arises from the molecular transition between vibrational energy levels when photons are re-radiated, illustrated in figure 1.11.[156] Transition of a molecule from its ground state into an upper vibrational state involves transfer of energy from the photon to the material (Stokes scattering).[156] Transfer of energy from the material to the incident photon occurs when molecules already exist in higher vibrational states (anti-Stokes scattering).[156] Stokes and anti-Stokes are analogous to Compton and inverse-Compton effects in X-ray and gamma radiation. Stokes scattering is the dominating process at room temperature as the majority of molecules reside in the ground vibrational state.[156] Anti-Stokes scattering is increased at elevated temperatures as a higher proportion of molecules are present in excited vibrational states.[156] Raman spectroscopy is an attractive choice for detecting substances in aqueous solutions due to the low spectral interference from water molecules. Raman spectra are highly informative and display narrow peak widths, however low sensitivity limits the use of Raman spectroscopy as an analytical technique.
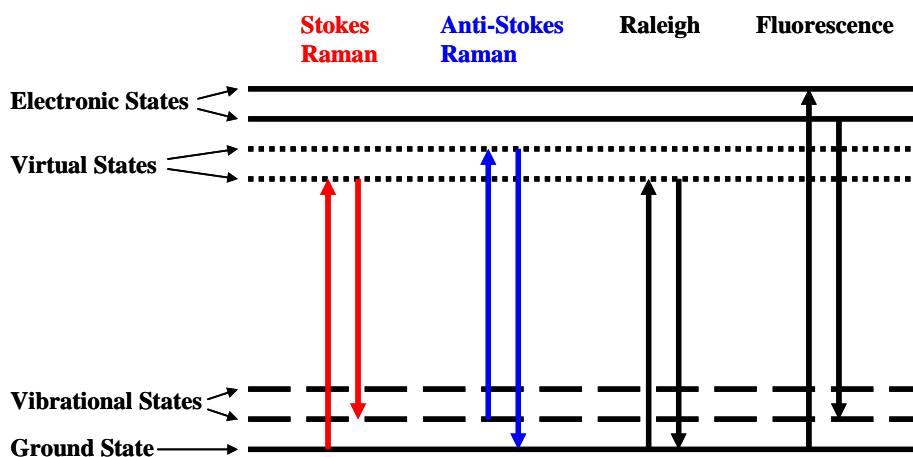
Figure 1.11 - Jablonski diagram illustrating transitions between energy levels involved in absorption and scattering.

1.4.2 – Surface-enhanced Raman scattering (SERS)

Raman scattering of an analyte can be greatly enhanced when adsorbed onto a roughened metal surface resulting in surface-enhanced Raman scattering (SERS).[112] This was first reported in 1977 from initial studies of chemisorbed molecules on roughened electrode surfaces.[158, 159] Surface-enhancement of Raman scattering has since been exploited in numerous methodologies involving the adsorption of molecules onto Au, Ag, and Cu nanoparticles in solution.[112] Surface plasmons of these metals lie in the visible region of the electromagnetic spectrum, thus making them ideal for SERS,[160] with enhancements of up to 10^6 possible.[112] Enhancement of Raman signals via adsorption on a metal surface is the product of two proposed mechanisms, electromagnetic and chemical.[112, 156] Conducting materials, such as metals, exhibit electromagnetic resonance owing to a surface plasmon of freely flowing electrons confined to the metal surface.[110-112, 156] Electromagnetic enhancement results from adsorbed molecules interacting with the surface plasmon, thus disrupting the electromagnetic field.[112, 156] The chemical component in SERS relies on formation of a

bond between the analyte and metal surface.[156] Complexes formed are often referred to as Raman intermediates, allowing charge transfer between the analyte and metal surface.[156] Polarization of the molecule is increased by surface plasmon electrons resulting in enhancement of Raman scattering.[156] Roughened metal surfaces provide crevices where plasmon electrons become trapped, giving rise to localised areas with larger electromagnetic fields.[110, 112] Such areas are known as 'hot spots' in which SERS is maximised.[110]

1.4.3 – Surface-enhanced resonance Raman scattering (SERRS)

Surface-enhanced resonance Raman scattering (SERRS) combines SERS with further enhancement from a resonant chromophore. Resonance Raman scattering involves transition of the molecule into an excited electronic state.[156] By employing an excitation wavelength with frequency corresponding to the energy difference between these two molecular states, Raman scattering can be further enhanced.[156] Detection limits as low as single molecule have been proposed using SERRS, showing the strength of the technique in sensitive detection of specific analytes.[161, 162] Narrow spectral peaks make SERS / SERRS ideal for multiplexing and molecular recognition has been achieved using SERRS with detection limits comparable to fluorescence.[163, 164] SERRS therefore provides an ideal analysis tool for ultrasensitive multianalyte detection.

1.4.4 – Raman reporters

The detection of biological interactions in SERS-based assays occurs via Raman active molecules either conjugated to analytes, or adsorbed onto nanoparticle surfaces (section 1.5). These molecules have become widely known as Raman reporters and often contain fluorescent chromophores. It is important to ensure that reproducible

SERS spectra can be obtained from these reporter molecules in order to obtain reliable results.

Benzotriazole Raman dyes

Raman spectral intensities from molecules adsorbed onto metal surfaces can be affected by their molecular orientation.[165] This renders SERS spectra subject to change depending on analyte concentration resulting in poor reproducibility. Benzotriazole forms a stable complex with metal surfaces via interactions of N_1 and N_3 lone electron pairs.[166, 167] These covalent interactions exhibit steric hindrance, which is advantageous in producing reproducible SERS.[166, 167]
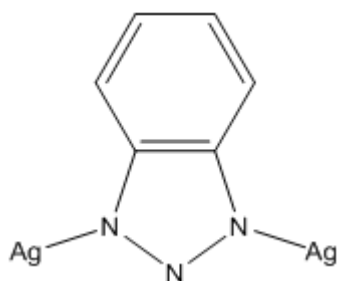
Figure 1.12 – Proposed structure of benzotriazole in complex with silver surface.[166, 167]

Reproducible Raman spectra from benzotriazole dyes adsorbed on silver colloid, irrespective of concentration, was first reported in 1998.[168] Quantitative nanoparticle-based studies of benzotriazole derivatives have since shown concentration dependent SERS intensities.[169, 170] Structural studies illustrate that the benzotriazole moieties in these dyes are unaffected by delocalized electrons in the azo bond, leaving it free to bind to metal surfaces.[171] More recently benzotriazole dyes have been synthesised

incorporating reactive functional groups for the application of SERS to biological interactions.[172-174] Bifunctional reactants have been described that incorporate ketone and maleimide moieties, whilst reacting various diazonium salts of aromatic amines with 5-aminobenzotriazole has yielded various trifunctional benzotriazole structures.[172-174]

Small molecules

Small molecules are readily available, inexpensive and some can give strong SERS signals.[175-179] SERS detection of 2-naphthalene thiol has been achieved at zeptomolar concentrations using AgNP.[175] Many small molecules exhibit Raman activity at wavelengths in the near-infra red region thus lending to *in vivo* imaging applications.[175, 178, 179] The molecular size and simplicity of structure allows for ease of functionalization with different biomolecules. Mixed monolayers can also be formed with peptides with minimal masking of amino acid sequences. The simplicity of the resultant spectra of small molecules permits facile deconvolution of multiplexed spectra.[176, 179, 180] Multiplexed imaging of small molecule capped AuNP has been observed *in vivo*[179] and SERS-based immunoassay detection limits of ~0.2 nM have been attained with three differently functionalized AuNPs.[181] Porter *et al*. also commonly exploit the bifunctionality of the small molecule Raman reporter, 5,5'-Dithiobis(succinimidyl-2-nitrobenzoate) (DSNB), in SERS-based immunoassays.[182-185]

1.4.5 – NP aggregation SERS enhancement

Colloidal metal NP solutions are commonly used in conjunction with SERS analysis. Metal NPs, produced using various reduction methodologies, exhibit a net negative surface charge.[124, 186] This overall negative surface charge produces stable solutions of

monodispersed NPs as a consequence of electrostatic repulsion.[157] Citrate-reduced AuNP were used for preliminary PNP studies in chapter 4, owing to their use in previous assembly methodologies.[132-134] Ethylenediamine tetraacetic acid (EDTA)-reduced AgNP were employed for SERS analysis owing to higher sensitivity, compared to AuNP, and the associated colloidal suspension stability over time.[157] Aggregation of NPs in solution has been shown to dramatically increase the SE(R)RS response due to formation of 'hot spots' at NP junctions.[110, 187] This enhancement in Raman scattering, resulting from NP assembly, is shown to be dependent on the analyte distance from the NP surface as well as the interparticle spacing.[188, 189] NP aggregation is commonly employed in SERS-based systems to 'turn on' the SERS response.[190] Aggregation of NPs can be monitored via a red shifting in the UV absorbance spectrum due to a change in the surface plasmon resonance, solution colour changes can also be observed by eye.[190]
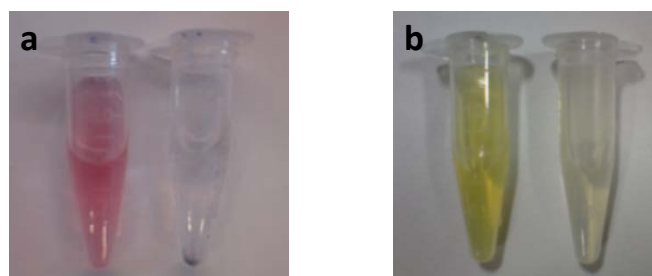
Figure 1.13 – a) Gold and b) silver NP suspensions before (left) and after (right) aggregation.

1.5 – SERS-based immunoassays

A number of SERS based immunoassays have been reported for detection of biological interactions.[180-185, 191-197] The first SERS-based method took the form of a sandwich assay for thyroid stimulating hormone (TSH).[195] In a protocol similar to ELISA, anti-TSH antibody was labelled with a resonant dye, *p*-dimethylaminoazobenzene (DAB), and used to detect antibody captured anti-TSH antigens on a smooth silver surface.[195] Enzyme-linked SERS immunoassays have been described, whereby antibody-enzyme binding events are represented through generation of a SERS active entity.[191, 192, 196] Many SERS-based assays also employ reporter molecules directly conjugated to different protein ligands, attached to a surface, in ELISA-derived methodologies.[194] In such cases colloidal silver staining was utilized to quantitatively detect surface-bound reporter molecules.[194] Porter *et al.* pioneered research into the application of functionalized Au nanoparticles as protein reporter molecules in sandwich immunoassays.[180-185] These protein reporters were first described in 1999 coining the term extrinsic Raman labels (ERLs).[181] Recent developments, demonstrating increased sensitivity of ERL-based SERRS assays, include the use of silver enhancement methods and cube-shaped Au ERL nanoparticles.[184, 198] Antibody-antigen sandwich formation on magnetic beads also allows for SERS detection in solution via secondary antibody conjugation to a Raman dye label.[193] In an alternative approach, assembly of ligand functionalized AuNP via protein interactions in solution has been illustrated by exploiting the Raman scattering of coomassie brilliant dyes.[199] Raman analysis of coomassie brilliant blue staining has also been employed in a novel SERS-based protein concentration assay which demonstrated a much wider linear concentration range and lower detection limit than is possible with Bradford analysis.[200]
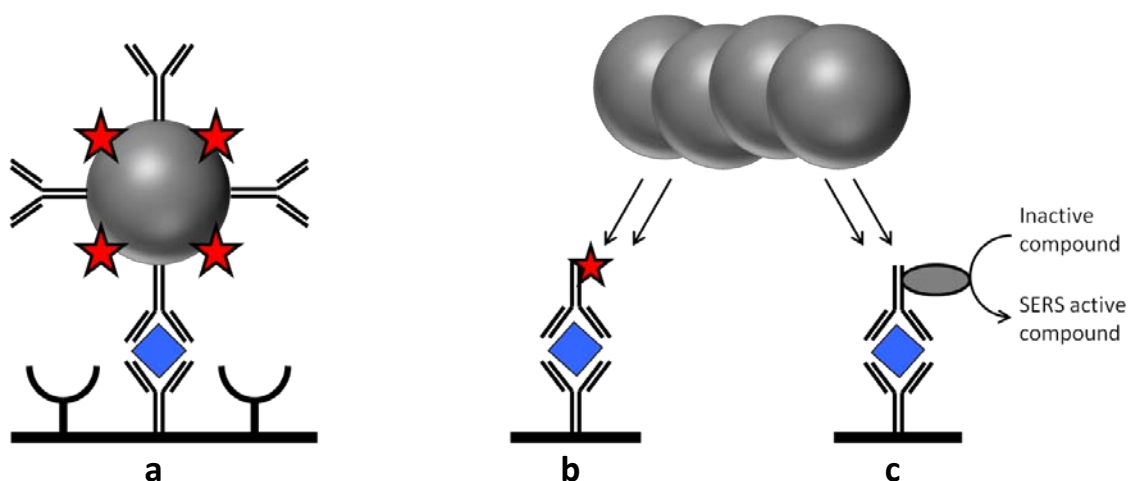
Figure 1.14 – Schematic representation (not to scale) of the three main SERS assay formats incorporating ELISA type antibody-antigen (blue diamond)-antibody binding on a gold surface. a) Secondary antibody and Raman tag (red star) mixed monolayer ERL binding to immobilized antigen.[180-185] b) The secondary antibody is functionalised with a Raman reporter for detection following colloidal staining.[194, 198] c) The secondary antibody is modified with an enzyme which converts a small molecule into a Raman sensitive compound that is detected following colloidal staining.[191, 192]

The first quantitative results for SERS-based protein detection, with sensitivity comparable to ELISA, were demonstrated by Porter *et al*. in 2003.[183] ERLs, prepared using a bifunctional reporter molecule and specific antibodies, were used to detect prostate-specific antigen (PSA) down to a concentration of 1 pg/mL. Although errors remain reasonably large, this proposed method shows great promise for antigen-antibody complex quantification through further optimisation and different Raman sensitive dyes.[201] A detection limit of 0.9 pg/mL was proposed for protein-ligand interactions on a surface using colloidal silver staining and SERS.[194] A recent immunoassay using silver deposition onto silica and polystyrene beads has also demonstrated streptavidin detection at concentrations of 10^{-13} Molar.[202] Most recently

the tumour necrosis factor alpha (TNFα) protein was observed with a detection limit of 0.049 - 0.195 pg/mL by employing a SERRS-based ELISA methodology.[196] ERL-based methods have also been used to detect potential disease markers in serum samples demonstrating the potential of SE(R)RS for use in diagnostics.[203] SERS-based methodologies have been used to achieve sensitive detection of various biomolecular interactions and SERS therefore shows great promise for future bioanalytical applications. The work presented in this thesis explores the use of SERS to investigate the allosteric interactions of MDM2 and to monitor nanoassembly driven by the formation of coiled coil peptide structures.

Chapter 2 – Aims

Chapter 3 aims to develop a novel methodology for investigating the p53-MDM2 interactions in solution using peptide functionalized nanoparticles (PNP) and surface-enhanced Raman spectroscopy (SERS). This will require the rational design of biologically specific and SERS-active PNP. Development of a solution based protein interaction assay will enable allosteric investigations of full-length wild-type MDM2 through the introduction of various binding ligands.

The aim of the work in chapter 4 is to investigate the controlled assembly of PNP through coiled coil heterodimerization. This will require rationally designed PNP which are SERS-active. This work aims to advance the development of biocompatible nanomaterials for use in a number of applications.

Chapter 5 investigates the potential for investigating protein interactions in microfluidic channels using PNP and SERS. This work aims to increase sensitivity of SERS detection of PNP assembly by scaling down solution volumes.

Chapter 3 – A novel assay for investigating MDM2 allostery

3.1 – Introduction

This chapter describes the development of a novel SERS-based immunoassay to investigate allosteric interactions of MDM2 full-length protein. Raman active PSN were designed, using a p53 peptide mimic, which have an affinity for the N-terminal domain of MDM2. It was hypothesised that MDM2 would bind the PSN and that MDM2 oligomerization would thus result in PSN clustering detectable using SERS.

MDM2 is a negative regulator of the tumour suppressor protein, p53. Regulation of p53 with MDM2 is a complex multi-subunit process, described in chapter one, which has been elucidated through investigating individual binding events using protein domain constructs. The multiple binding events of MDM2 are not mutually exclusive and intramolecular domain crosstalk has been observed to affect individual interactions.[24, 25, 43] The p53 BOX-1 domain interacts with the MDM2 N-terminal hydrophobic pocket and MDM2 dimerization, via the C-terminal, is theorised to be essential for MDM2 E3-ligase activity on numerous proteins, including p53. Both the p53-MDM2 interaction and MDM2 dimerization are essential for the assembly of peptide silver nanoparticles (PSN) illustrated in figure 3.1. Using a solution based SERS approach (figure 3.1) will potentially allow investigation of MDM2 allosteric interactions using full-length wild-type MDM2. From this, insight can be gained into MDM2 domain crosstalk and the allosteric effect of specific binding events on subsequent interactions.

Raman spectroscopy is an emerging technology for investigating protein interactions.[194, 195] SERS spectra are observed from NP-immobilized Raman labels, which can be further enhanced by aggregation.[161, 181, 190] SERS therefore presents a sensitive detection technique for MDM2 directed NP assembly illustrated in figure 3.1.

This NP assembly can also be monitored through changes in plasmon absorbance in extinction spectroscopy.
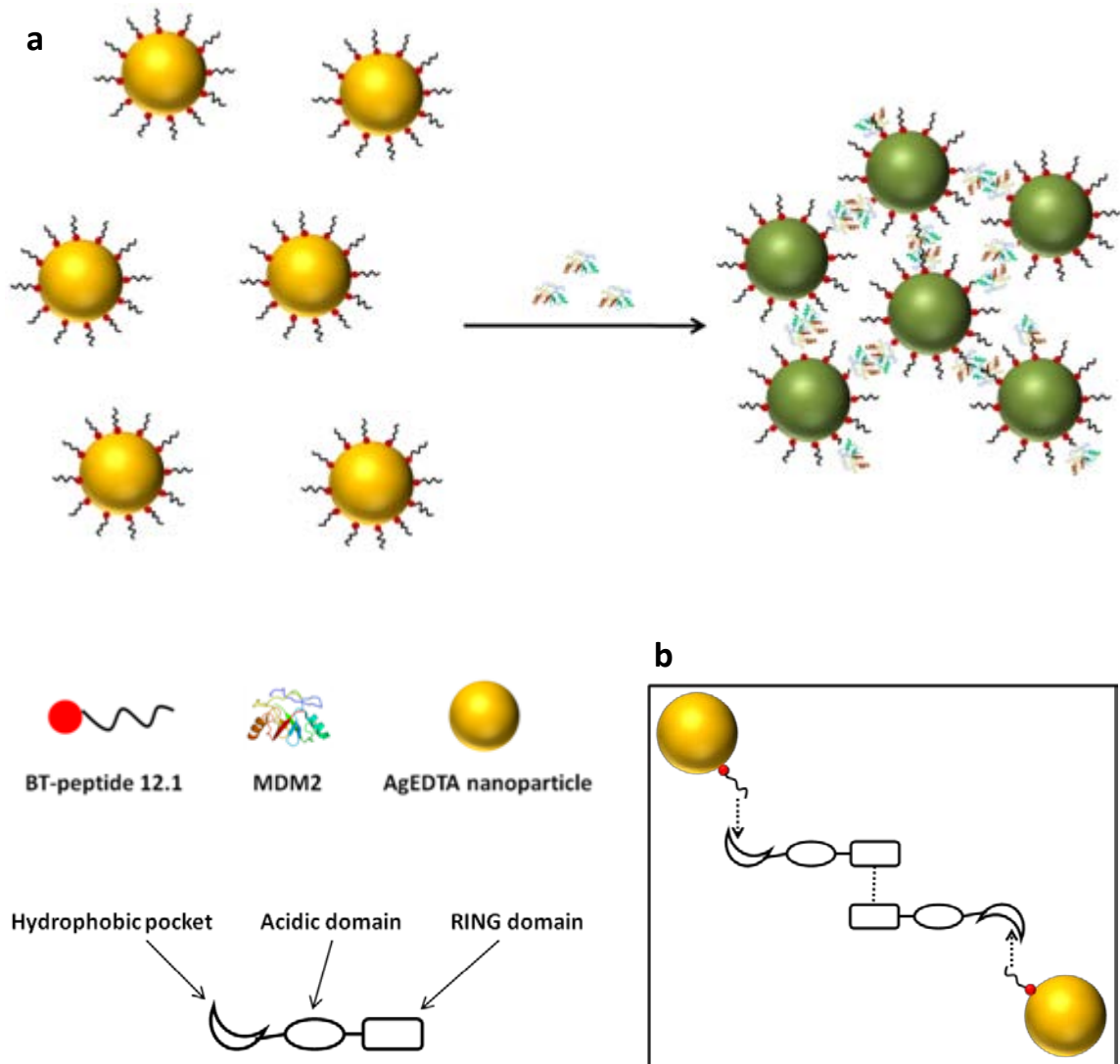
Figure 3.1 – Schematic of the proposed MDM2 assay. a) MDM2 induced aggregation of PSN-12.1 and b) MDM2 interactions (dotted lines) driving NP assembly.

3.2 – Peptide modification

The MDM2 assay illustrated in figure 3.1 requires the rational design of peptide PSN incorporating a Raman tag for detection by SERS. This section describes the modification of a p53 peptide mimic, peptide 12.1, with a benzotriazole Raman dye.

3.2.1 – Benzotriazole Raman dye

The in-house linker, benzotriazole-PEG$_3$ (BT), was employed as a Raman tag for SERS detection of MDM2-induced PSN assembly. BT functionalisation of NP occurs via the triazole moiety which forms a stable complex with the metal surface. Studies have shown that triazole dyes predominantly attach to metal surfaces in the same orientation.[166, 167] This prevents surface orientation induced variation of the relative peak intensities in Raman spectra, thus allowing for more reliable quantitative measurements.[168] BT has an absorbance maximum at 487 nm in extinction spectroscopy and is therefore close to resonance when employing an excitation at 514.5 nm (figure 3.3). Raman spectra can also be attained using a 632.8 nm excitation wavelength (figure 3.3). BT was covalently linked to peptides through the carboxylic acid group. Figure 3.2 illustrates the molecular structure of BT and notable functional groups for the MDM2 aggregation assay.
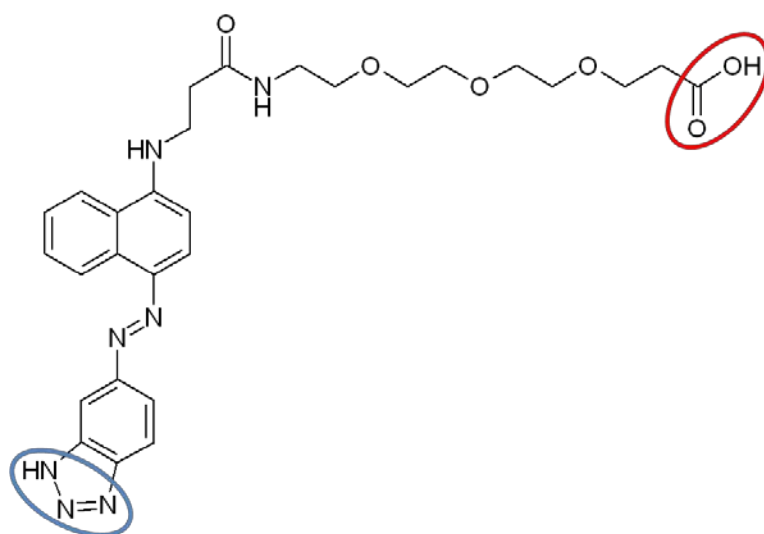
Figure 3.2 – Benzotriazole-PEG$_3$ (BT) dye structure with the triazole group and carboxylic acid group highlighted by blue and red rings respectively.
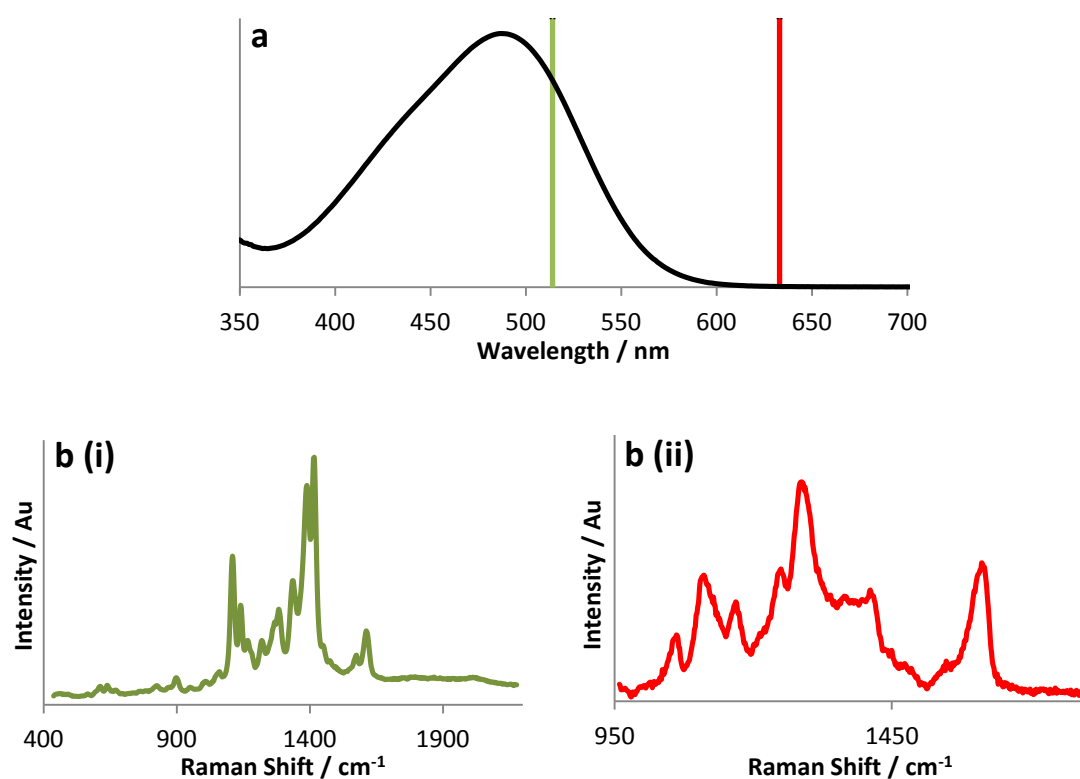
Figure 3.3 – a) extinction spectra of BT depicting laser excitation wavelengths of 514.5 nm (green) and 632.8 nm (red). b) Raman spectra from BT when employing an excitation wavelength of i) 514.5 nm and ii) 632.8 nm.

3.2.2 – Peptide-BT coupling

BT modification of the p53 peptide mimic was carried out prior to NP functionalisation. This yielded multifunctional peptide-BT conjugates which could be attached to NP in a simple one-step PSN preparation protocol.

Selection of the peptide sequence

The p53 BOX-1 domain binds the MDM2 hydrophobic pocket via the formation of an ampipathic α-helix containing a specific amino acid sequence motif, FxxxWxxL.[8] Residues F, W and L form aromatic-aromatic interactions with hydrophobic residues in the MDM2 cleft. Studies have also shown that within the sequence motif, Tryptophan is the most important residue involved in MDM2 binding.[204, 205] Peptide 12.1 originates from a library of peptides containing the FxxxWxxL motif and demonstrates high affinity to the N-terminal of MDM2.[206] Peptide 12.1 was modified with BT and subsequently attached to AgEDTA to create PSN-12.1. Peptide 12.1$_{W\Delta A}$ was also synthesised in which Tryptophan was replaced with Alanine to ensure biological specificity of the MDM2-PSN interaction. Peptide sequences were synthesised with a serine-glycine spacer region at the C-terminus, closest to the NP surface. The SGSG sequence enhances peptide flexibility on the NP and maintains distance between the peptide binding motif and the dye molecule. A 3-PEG spacer within the BT structure also lengthens the distance between the chromophore and the peptide sequence, thus ensuring that the binding affinity remained as unchanged as possible. The BT structure was directly immobilized onto the NP surface for maximum Raman activity.[188]

Peptide 12.1   -   SGSGMPR**F**MDY**W**EG**L**N

Peptide 12.1$_{W\Delta A}$ -   SGSGMPR**F**MDY**A**EG**L**N

Synthesis of BT modified peptides
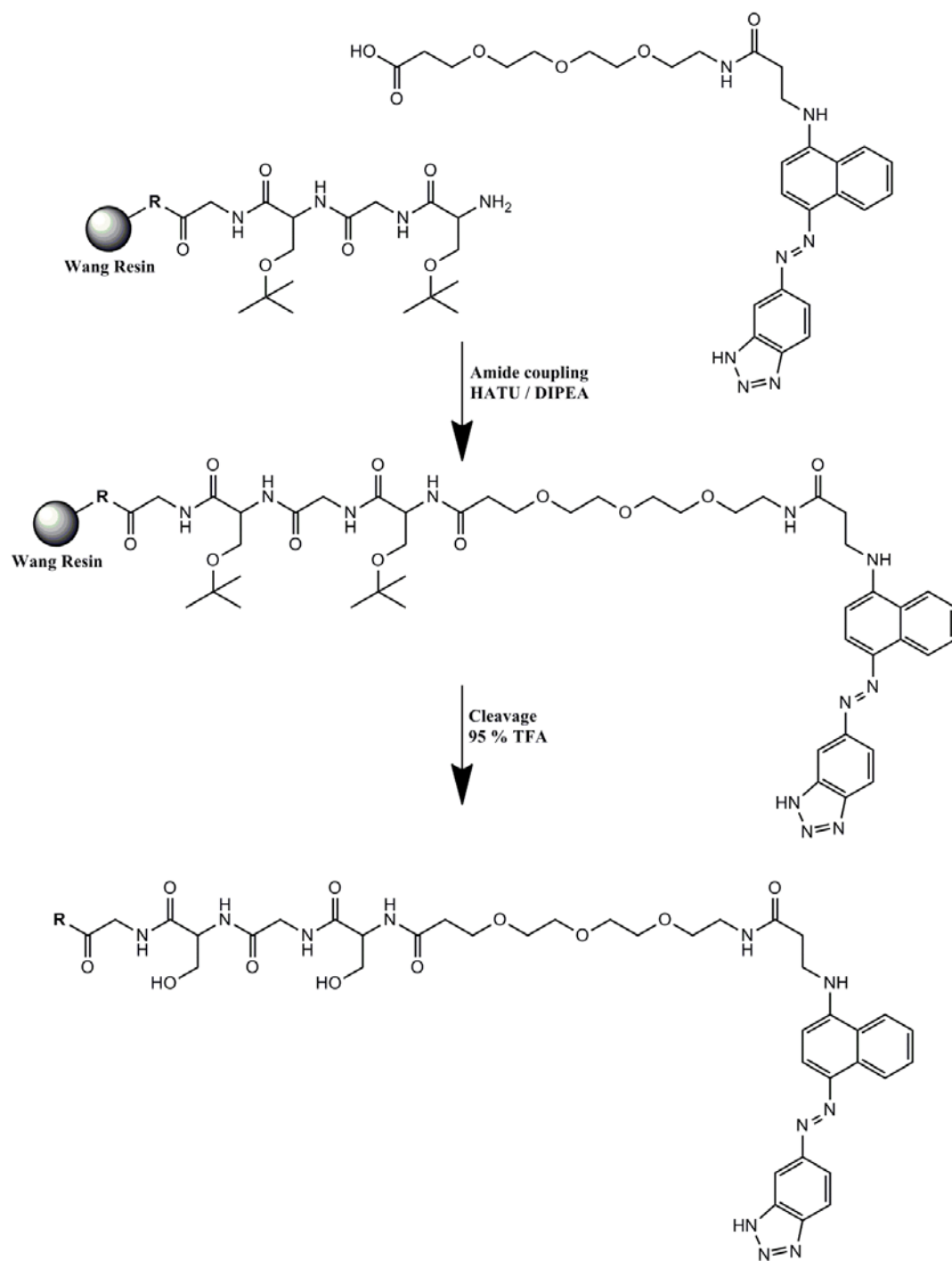
Figure 3.4 – Schematic illustrating solid phase peptide modification, deprotection and cleaving.
R can represent peptide 12.1 or peptide 12.1$_{W\Delta A}$.

Peptides 12.1 and 12.1$_{W\Delta A}$ were anchored onto Wang resin at the C-terminus with all residue side chains protected. The N-terminus was unprotected and available for amide bond formation with the BT carboxylic acid group. Peptide-BT coupling was found to proceed most efficiently when using *O*-(7-Azabenzotriazol-1-lyl)-*N,N,N,N*-tetramethyluronium hexafluorophosphate (HATU) as the coupling agent in the presence of a base, diisopropylethylamine (DIPEA) (figure 3.4). A reaction mixture containing 95 % Trifluoroacetic acid (TFA) was then used to cleave peptide-BT conjugates from the resin and remove all the side chain protecting groups (figure 3.4). The modified peptide products were dissolved in milliQ H$_2$O and added directly to AgEDTA to form PSN as described in chapter 8.

3.2.3 – Characterisation of peptide – BT conjugates

Successful modification of peptide 12.1 with BT was characterised using mass spectrometry. Circular dichroism was also performed to ensure that BT modification didn't prevent peptide 12.1 from developing the helical conformation necessary for MDM2 binding. Extinction spectroscopy was employed to determine peptide concentrations in solution.

3.2.3.1 – Matrix-assisted laser desorption ionisation mass spectrometry (MALDI-MS)

Matrix-assisted laser desorption ionisation – mass spectrometry (MALDI-MS) was used to characterise peptide 12.1 – BT conjugates. No sample preparation was required as the analysis was being conducted on pure peptide product dissolved in milliQ water. Singly charged masses of 563.9, 1845.9 and 2391.9 m/z were identified in MALDI-MS analysis of peptide 12.1 – BT samples, representing BT, peptide 12.1 and peptide 12.1 –

BT respectively (figure 3.5). Ions with 563.9 and 2276.3 m/z, corresponding to BT and peptide $12.1_{W\Delta A}$ – BT, were evident in the MALDI-MS spectrum obtained for peptide $12.1_{W\Delta A}$ – BT (figure 3.5). Additional peaks observed in MALDI spectra were confirmed to be associated with peptide fragmentation and side chain modifications. The most apparent modification methionine oxidation, resulting in the observation of ions with m/z of 16 and 32 higher than the associated peptide mass (figure 3.5).
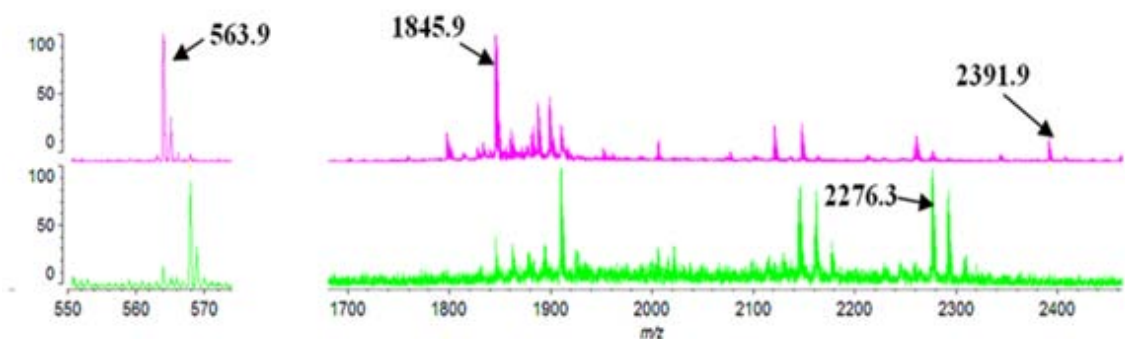
Figure 3.5 – MALDI-MS analysis of peptide 12.1 – BT (pink) and peptide $12.1_{W\Delta A}$ – BT (green).

3.2.3.2 – Circular Dichroism

Circular dichroism (CD) is a measurement of the difference in absorbance between left handed circularly polarised light (L-CPL) and right handed circularly polarised light (R-CPL) of chiral molecules. Spectral measurements are largely influenced by the three-dimensional macromolecular structures and consequently CD is widely used for the determination of protein secondary structure architecture.[207] Secondary structure conformations, including α-helices and β-sheets, demonstrate distinct spectral signatures in CD analysis.[207]

As aforementioned, peptides containing the FxxxWxxL motif are known to form ampipathic α-helices to interact with the MDM2 hydrophobic pocket via aromatic –

aromatic interactions.[8] It was therefore essential to ascertain that the BT modification didn't have a negative effect on helical secondary structure formation of peptide 12.1. Peptide 12.1 and peptide 12.1 – BT were analysed by CD in varying amounts of 2,2,2-trifluoroethanol (TFE). TFE has been shown to aggregate and displace water molecules around peptides, preventing intermolecular interactions and therefore promoting intramolecular interactions that lead to secondary structure formation.[208] Addition of TFE to peptide samples promotes secondary structure and demonstrates whether or not helical formation is possible.[209]
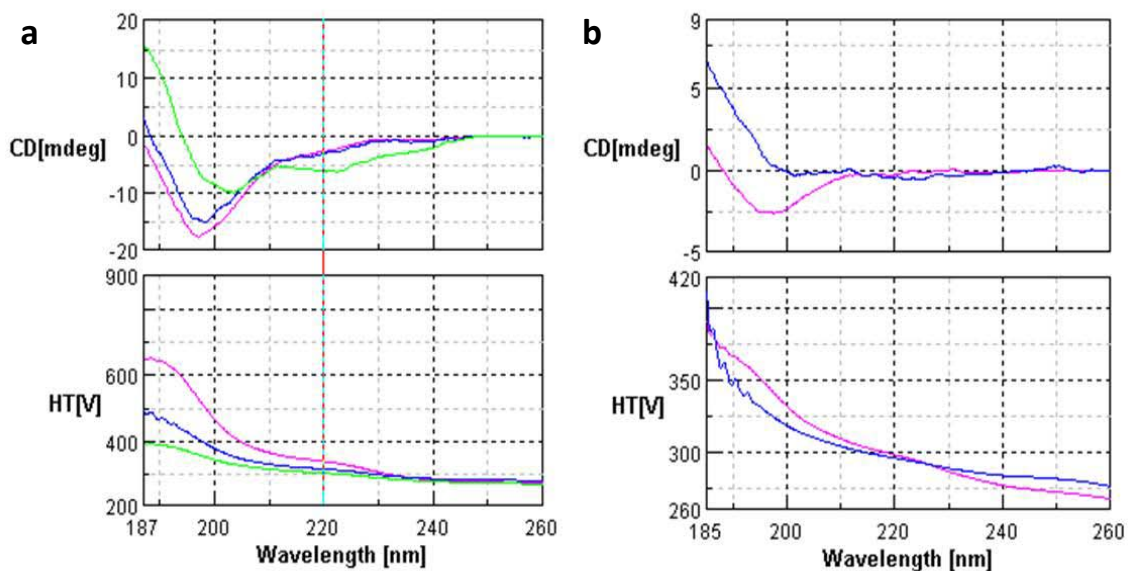
Figure 3.6 - a) Far UV CD spectra of unmodified peptide 12.1 in H_2O (pink) in 10 % TFE (blue) and 50 % TFE (green). b) Far UV CD spectra of peptide 12.1-BT in H_2O (pink) and 50 % TFE (blue).

In the absence of TFE, both peptide samples exhibited far-UV spectra characteristic of random coil formation. Analysis of samples in 50 % TFE yielded spectra consistent with α-helical conformation.[207] The data shows that modification of peptide 12.1 with BT

does not affect secondary structure formation and therefore should not reduce the MDM2 binding affinity.

3.2.3.3 – Quantification

Unmodified peptide solution concentrations were determined using extinction spectroscopy and the sum of the extinction co-efficients of tryptophan (ε = 5379 L M^{-1} cm^{-1}), tyrosine (ε = 1400 L M^{-1} cm^{-1}) and phenylalanine (ε = 4 L M^{-1} cm^{-1}) residues. These co-efficients correspond to absorbance at 275 nm in 0.1 M phosphate buffer, pH 7. The side chains of these amino acids have been shown to exhibit absorbance at 275 nm due to the side chain aromatic ring structures. Extinction co-efficients for peptides 12.1 and 12.1$_{W\Delta A}$ were therefore calculated from composite aromatic residues.

Peptide 12.1   -   SGSGMPR**F**MD**YW**EGLN ε = 6783 L M^{-1} cm^{-1}

Peptide 12.1$_{W\Delta A}$ -   SGSGMPR**F**MD**Y**AEGLN ε = 1404 L M^{-1} cm^{-1}

Peptide – BT solution concentrations were determined using extinction spectroscopy from the BT chromophore. In this case the extinction co-efficient for BT was calculated using solutions of known concentration in assay buffer (25 mM HEPES, 20 mM KCl, pH 7.5). A calibration was carried out for absorbance at λ-max (487 nm) versus BT concentration and the extinction co-efficient calculated to be 12017.

y = 12017x
R² = 0.9999
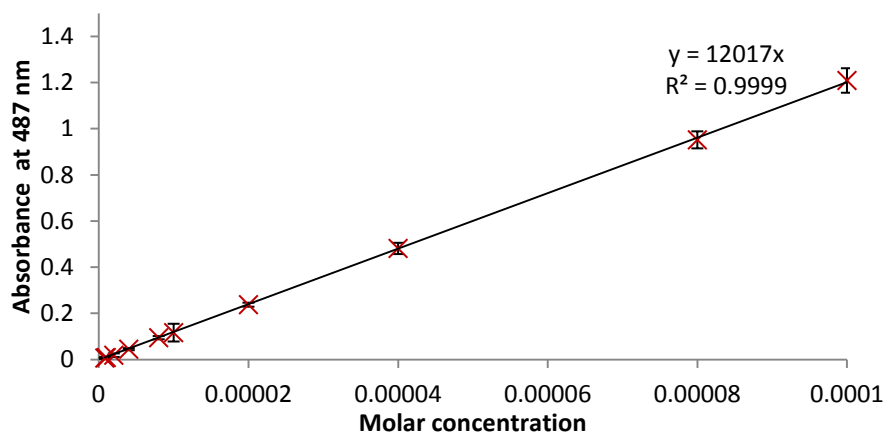
Figure 3.7 – BT concentration calibration. The graph illustrates absorbance at 487 nm against the molar concentration of BT.

3.3 – Peptide silver nanoparticles (PSN)
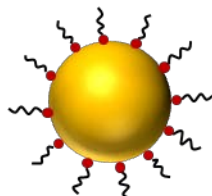
Figure 3.8 – Peptide silver nanoparticle

Proposed MDM2-induced PSN aggregation was described in section 3.1 and peptide – BT conjugation was achieved as illustrated in section 3.2. This section focuses on the functionalization of AgEDTA-reduced NP with peptide – BT conjugates (figure 3.8).

3.3.1 – Optimizing BT concentration

In order to produce stable PSN, it was necessary to calculate the optimum molar excess of ligand for stability and aggregation induced SERS enhancement. A 1000 fold serial dilution was carried out from a 2 x 10^{-2} M BT stock solution. 50 μL of each BT concentration was added to 1 mL colloidal AgEDTA, 133 pM in assay buffer, resulting in final BT concentrations from 1 x 10^{-3} M to 1 x 10^{-10} M. Samples were left overnight before centrifugation, 1900 g for 20 minutes, and resuspension in assay buffer to remove any unbound BT.

Solutions in which less than 1 x 10^{-7} M BT was present were seen to aggregate following centrifugation and hence were not analysed. Red shifting of the λ-max in extinction spectroscopy was observed for all solutions containing BT, except at a concentration of 1 x 10^{-7} M, inferring that the dye molecule was immobilized on the surface (figure 3.9 a). At 1 x 10^{-7} M the sample exhibits a relatively small full width to half max (FWHM) suggesting stability, however the higher absorbance at longer wavelengths compared with other solutions indicated instability. This concentration of BT yielded the highest SERS intensity without an aggregating agent, thus confirming NP instability.

Extinction spectroscopy analysis showed a BT concentration of 1 x 10^{-6} M to yield the most stable NP solutions with a FWHM of 92 and a 2 nm red shift in the λ-max. This sample also demonstrated the highest SERS intensity following the addition of spermine as an aggregating agent, 25 μL of 0.1 M added to 500 μL NP (figure 3.9 b). It was therefore concluded that the optimal ligand concentration was 1 x 10^{-6} M and this was carried forward into all subsequent experimentation.
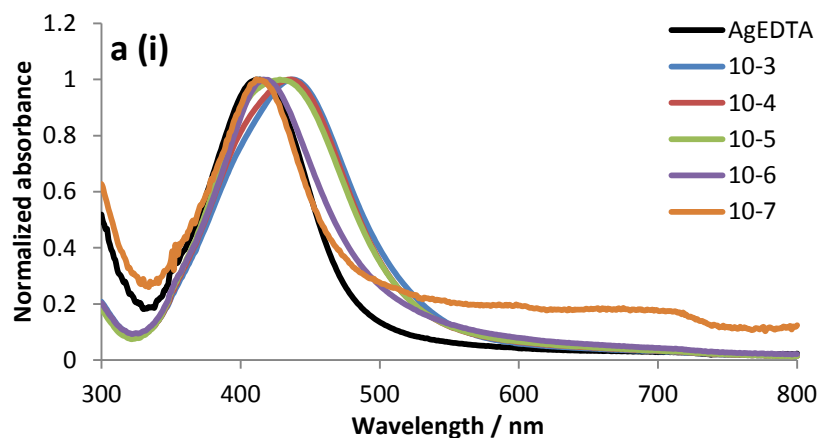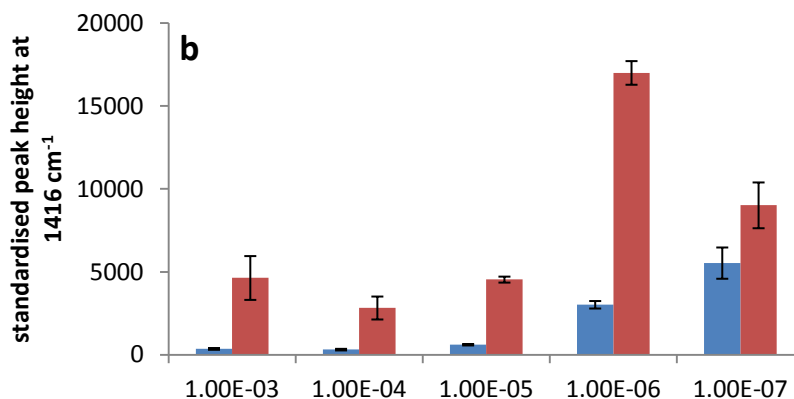
Figure 3.9 – a i) normalized extinction spectra for AgEDTA solutions without BT (black) and with 1×10^{-3} (blue), 1×10^{-4} (red), 1×10^{-5} (green), 1×10^{-6} (purple) and 1×10^{-7} (orange) M BT concentrations. a ii) Table indicating λ-max and FWHM values for samples in extinction spectroscopy. b) Average SERS intensity of AgEDTA-BT samples before (blue) and after (red) aggregation with Spermine. Error bars indicate the standard deviations in peak height.

3.3.2 – PSN characterisation

PSN and AgEDTA-BT were prepared by adding appropriate volumes of peptide – BT and free dye respectively in d_2H_2O to AgEDTA, 133 pM in assay buffer, to achieve a final concentration of 1×10^{-6} M. Samples were shaken overnight before centrifugation, 1900 g for 20 minutes, and resuspension in assay buffer. PSN-12.1 and PSN-12.1$_{W\Delta A}$ solutions were then analysed using extinction spectroscopy and MALDI-MS, to confirm successful immobilization of peptide – BT conjugates on the NP surface.
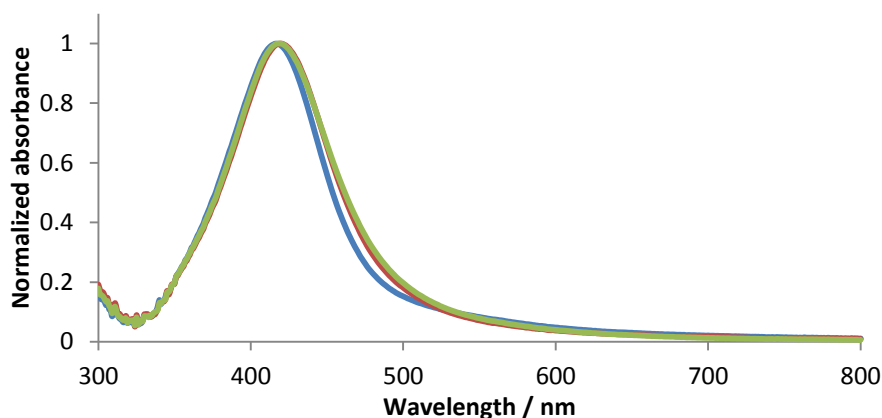
Figure 3.10 – Nomalized extinction spectra for AgEDTA (blue), PSN-12.1 (red) and PSN-12.1$_{W\Delta A}$ (green).

Stable solutions of PSN-12.1 and PSN-12.1$_{W\Delta A}$ were achieved, as demonstrated by extinction spectroscopy (figure 3.10). A red shift of 3-5 nm in the absorbance λ-max and slight peak broadening was observed with addition of peptide – BT to AgEDTA. The λ-max red shift appeared more pronounced for peptide 12.1 (5 nm) than for peptide 12.1$_{W\Delta A}$ (3 nm), possibly a result of replacing the bulky, hydrophobic tryptophan residue with alanine which may have affected peptide conformation on the NP surface.

Extinction spectroscopy results suggested that PSN had been created by observing the changes in plasmon absorbance, however this analysis gives no identification of the number of molecules adsorbed onto the NP surface.

In order to determine the functionality of PSN, adsorbed molecules were removed from the NP surface, desalted and analysed using MALDI-MS. Analytes were removed from NPs by treatment with dithiothrietol, DTT (10 mM final concentration), for a minimum of 30 minutes. Solutions were then centrifuged, 1900 g for 20 minutes, allowing separation of the bare NP from the unbound molecules. The supernatant was subsequently desalted, using PepClean spin columns, in preparation for MALDI-MS analysis.

Figure 3.11 illustrates MALDI-MS analysis, confirming successful modification of AgEDTA with peptides 12.1 – BT and peptide $12.1_{W\Delta A}$ – BT. Ions with m/z 563.9, 1845.9 and 2391.9 represent BT, peptide 12.1 and Peptide 12.1 – BT respectively whilst values of 1730.7 and 2276.3 m/z correspond to peptide $12.1_{W\Delta A}$ and peptide $12.1_{W\Delta A}$ - BT. MALDI spectra for PSN supernatant samples appeared cleaner than those obtained for peptide – BT solutions. This could be partly due to the desalting step, however it is possible that NP immobilization acts as a crude affinity purification step. It is also important to note that MALDI-MS is not a quantitative methodology and peak intensity is largely a result of the ease of ionization of different molecular structures. MALDI-MS analysis of AgEDTA-BT, DTT treated, supernatant samples identified only one ion (m/z = 563.9) corresponding to the BT linker. Hence, it can be suggested that all other ions observed relate to various peptide fragments.
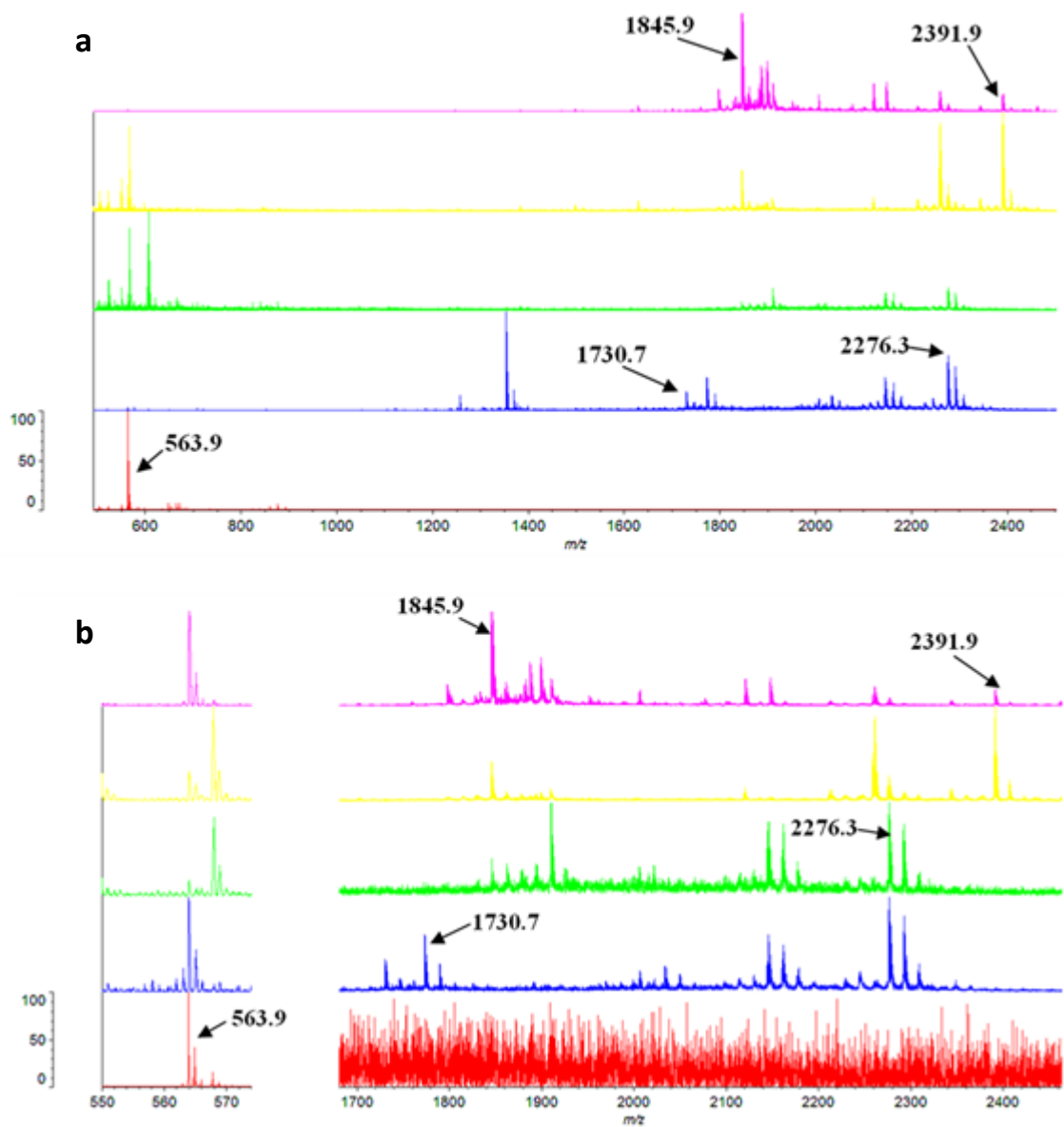
Figure 3.11 - MALDI-MS analysis of peptide 12.1 – BT (purple), peptide 12.1 – BT removed from nanoparticles (yellow), peptide 12.1$_{W\Delta A}$ – BT (green), peptide 12.1$_{W\Delta A}$ – BT removed from nanoparticles (blue) and BT removed from nanoparticles (red). Notable m/z values are highlighted.

3.4 – MDM2-induced PSN assembly

Thus far this chapter has described the production of stable PSN solutions for use in the proposed MDM2 assay (figure 3.12). Peptide 12.1 has a high affinity for the hydrophobic pocket of MDM2, therefore assembly of PSN-12.1 will theoretically occur in the presence of MDM2 dimers. Peptide $12.1_{W\Delta A}$ was synthesised which has a lower affinity for the MDM2 N-terminal domain than peptide 12.1. Consequently, PSN-$12.1_{W\Delta A}$ will have a lower propensity to assemble in the presence of MDM2 dimers than PSN 12.1.
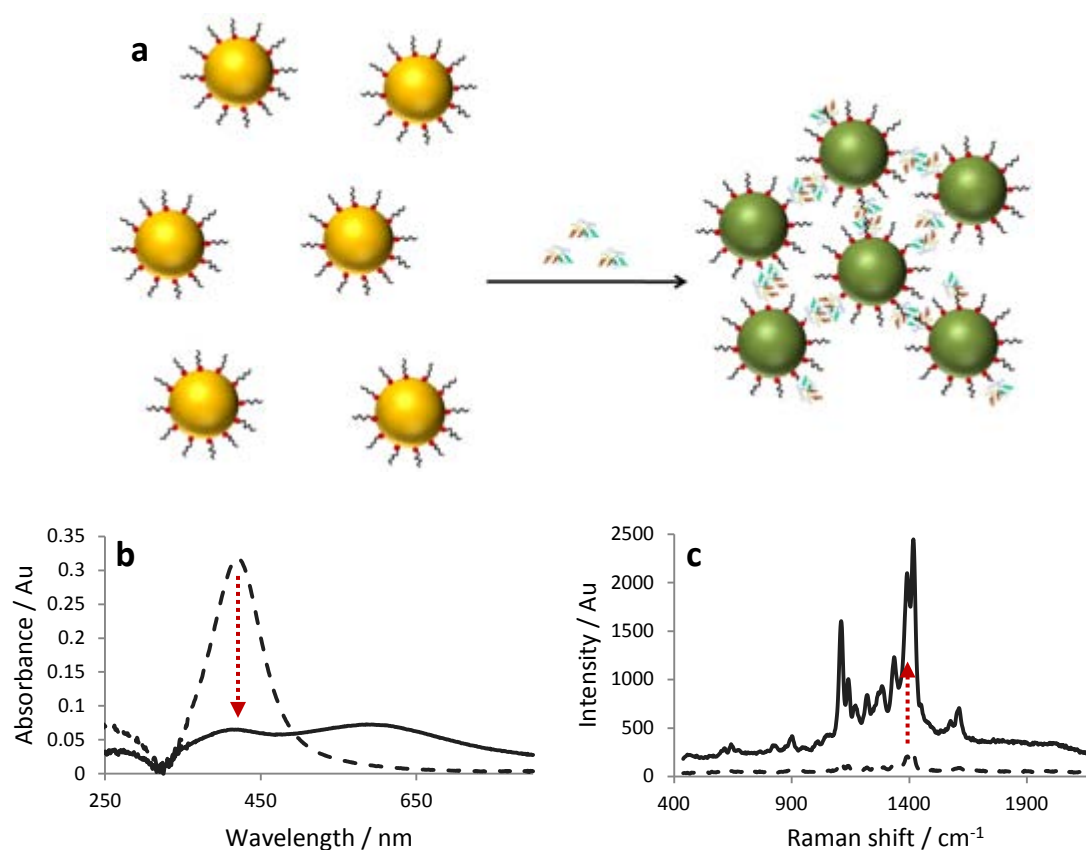
Figure 3.12 – a) Schematic illustrating MDM2-induced assembly of PSN. b) Extinction spectroscopy and c) SERRS analysis before (dashed) and after (solid line) addition of MDM2 to PSN-12.1.

3.4.1 – Buffer optimization

Appropriate buffer conditions are essential in order to achieve accurate results in protein binding investigations. It was essential to find buffer conditions in which MDM2 was active and PSN solutions were not susceptible to non-specific aggregation. MDM2 was stored in 25 mM HEPES pH 7.5, therefore this was chosen as the primary buffer component for this assay. A number of other constituents of the MDM2 storage buffer (25 mM HEPES pH 7.5, 10 % glycerol, 1 mM benzamidine, 5 mM DTT, 290 mM potassium chloride) were seen to cause non-specific NP aggregation. Each of the buffer components were introduced into PSN solutions and all except 25 mM HEPES resulted in aggregation. Glycerol and benzamidine function as a cryoprotectant and protease inhibitor, respectively, in storage and are therefore not essential buffer components for the MDM2 assay. DTT is a reducing agent used for reducing disulphide interactions within proteins and is also known to remove BT from NP surfaces. Subsequent investigations into KCl showed 20 mM to be the highest concentration at which PSN maintained stability in solution (figure 3.13 a ii). Initial assay studies were carried out in 25 mM HEPES pH 7.5 with and without 20 mM KCl. MDM2 addition resulted in PSN assembly in both buffer conditions, however the extent of aggregation was much greater in the presence of KCl indicating a requirement for salt in MDM2-p53 binding (figure 3.13 b). From these investigations it was concluded that HEPES-KCl (25 mM HEPES, 20 mM KCl, pH 7.5) provided optimum buffer conditions for the MDM2 assay.
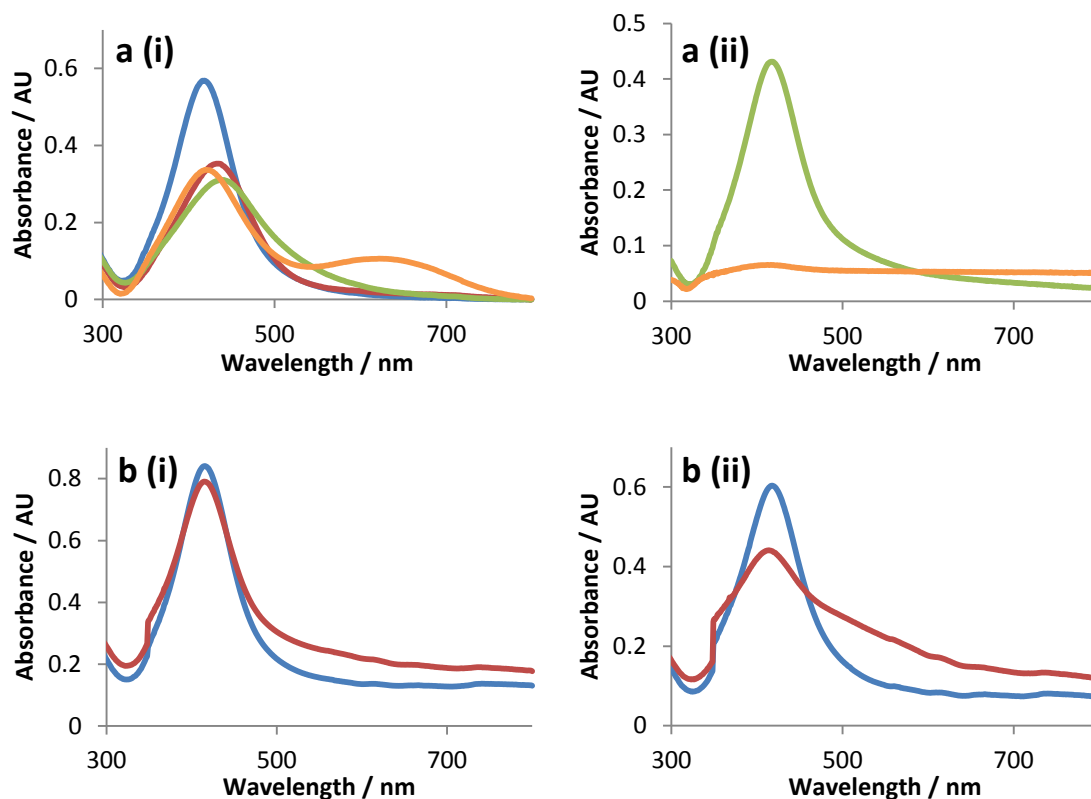
Figure 3.13 – Extinction spectroscopy. ai) 100 pM PSN-12.1 (blue) with 5 mM DTT (red), 10 % Glycerol (green) and 290 mM KCl (orange) in 25 mM HEPES pH 7.5. aii) 90 pM PSN-12.1 in 25 mM HEPES pH 7.5 with 20 mM (green) and 30 mM (orange) KCl. B) 121 pM PSN-12.1 with (red) and without (blue) 100 x molar excess MDM2 in i) 25 mM HEPES pH 7.5 and ii) 25 mM HEPES pH 7.5, 20 mM KCl.

3.4.2 – Optimizing PSN concentration

MDM2 induced PSN assembly was observed to vary dependent on PSN concentration and the molar excess of MDM2 to PSN. MDM2-induced PSN assembly was investigated using 5 – 20 pM PSN and up to 100 fold molar excess of MDM2. Samples were treated with MDM2 for 1 hour before analysis using extinction spectroscopy. The absorbance at λ-max in the extinction spectrum was used as the value for assessing the extent of

PSN aggregation. PSN-12.1 assembly was observed to the greatest extent at a PSN concentration of 15 pM, at which no aggregation of PSN-12.1$_{W\Delta A}$ was seen (figure 3.14). 5 – 15 pM PSN concentrations were analysed in a separate experiment to samples with 15 – 20 pM PSN. 15 pM PSN samples were analysed in both experiments and the results pooled for comparison purposes. Pooling the results from two experiments resulted in large errors for 15 pM PSN samples. Despite the errors observed, 15 pM PSN samples gave the best discrimination between PSN-12.1 and PSN-12.1$_{W\Delta A}$ and was therefore used in subsequent experimentation.
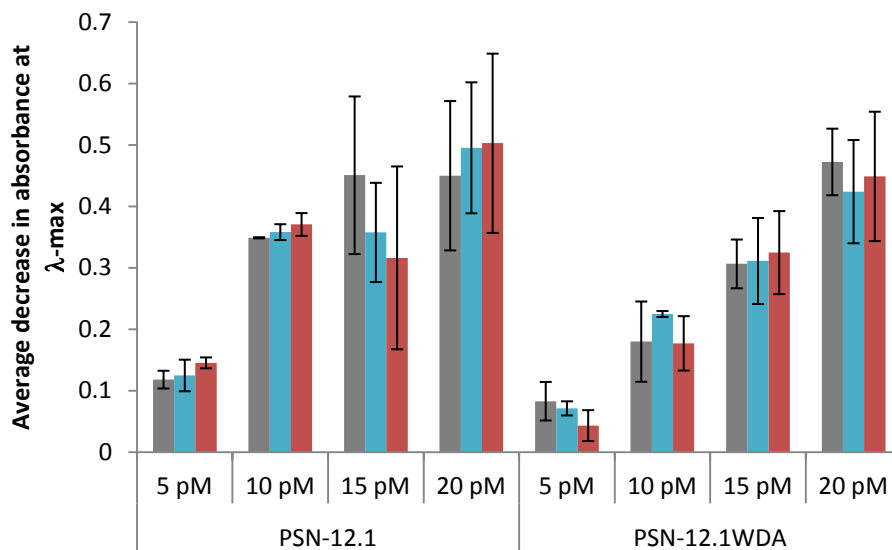
Figure 3.14 – Average absorbance at λ-max in extinction spectroscopy analysis of different PSN concentrations without protein (grey), and with a 50-fold (blue) and 100-fold (red) molar excess of MDM2. Error bars indicate the λ-max absorbance standard deviations.

3.4.3 – Monitoring MDM2-induced PSN assembly

Section 3.1 describes the proposed MDM2-directed assembly of specific PSN. The two primary technologies employed in the detection of PSN assembly, extinction spectroscopy and SERS, are highlighted in figure 3.12. Thus far, stable PSN have been achieved, incorporating a Raman tag for SERS analysis. Assay conditions have also been investigated and 15 pM PSN in assay buffer (25 mM HEPES, 20 mM KCl, pH 7.5) found to be optimum for this experimental design. Subsequent to the results illustrated in figure 3.14, section 3.4.2, MDM2-induced PSN assembly has proved to be concentration dependent and a much larger excess than 100 fold MDM2 to PSN required for substantial aggregation (figure 3.14). The large excess of protein required could be speculated to result from variable oligomerization states of MDM2. However, this is more likely due to PSN surface area coverage as calculations predict that an excess of approximately 1000 MDM2 monomers to PSN are required to achieve monolayer formation. In this section different methodologies are explored to monitor MDM2-directed PSN assembly.

3.4.3.1 – Extinction spectroscopy

Plasmon absorbance changes in extinction spectroscopy can be used as a measurement of NP distribution in solution. A reduction in absorbance at λ-max and an increase in absorbance at longer wavelengths is seen as a result of NP clustering. PSN-12.1 and PSN-12.1$_{W\Delta A}$ suspensions were treated with MDM2 and subsequently analysed using extinction spectroscopy to monitor any plasmon absorbance changes. MDM2 was added to 15 pM PSN solutions at various concentrations based on a PSN:MDM2 molar ratio (1:300, 1:500, 1:1000 and 1:2000) and samples left for a minimum of 24 hours before analysis (figure 3.15).
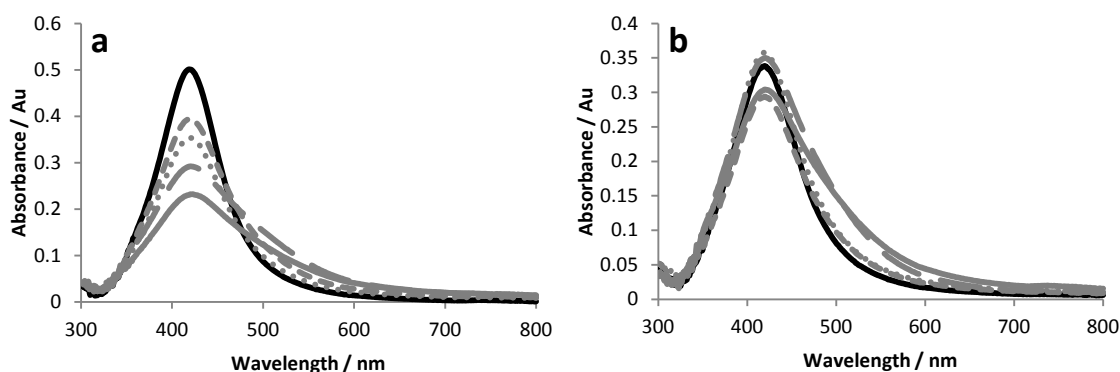
Figure 3.15 - Extinction spectroscopy analysis of a) PSN-12.1 and b) PSN-12.1$_{W\Delta A}$ solutions without MDM2 (black) and 96 hours after addition of 300 (dotted grey), 500 (short dashed grey), 1000 (long dashed grey) and 2000 (solid grey) MDM2 monomers per PSN.

Extinction spectroscopy analysis demonstrated a broadening in the plasmon absorbance and a decrease in λ-max for PSN-12.1 samples in the presence of MDM2 (figure 3.15). This was not observed to the same extent for PSN-12.1$_{W\Delta A}$ samples. It can therefore be inferred that MDM2 was present in dimer (or oligomer) formation and was able to bind peptide 12.1 on the NP surface resulting in PSN assembly as proposed in figure 3.12. Reduction in the absorbance at λ-max was larger with higher MDM2 concentrations, thus indicating PSN assembly to be a concentration dependent process. Plasmon absorbance broadening in PSN-12.1$_{W\Delta A}$ samples was only observed at higher MDM2 concentrations (figure 3.15). This demonstrated biological specificity of the MDM2-induced PSN assembly.

The data illustrated in figure 3.15 were obtained 96 hours following the addition of MDM2 to PSN solutions. In a typical ELISA protocol, binding interactions occur within a one hour time duration. Temporal extinction spectroscopy analysis of MDM2-induced PSN assembly was therefore carried out to investigate the time duration required for aggregation to reach completion. PSN samples were monitored using extinction spectroscopy for 30 minutes immediately following the addition of MDM2 (figure 3.16).

MDM2 was introduced to 15 pM PSN samples at the same molar ratios as used for previous extinction spectroscopy analysis and the absorbance at λ-max, 419 nm, was recorded every 60 seconds as a measurement of NP assembly. Full analysis of all samples was carried out following temporal study completion.

Figure 3.16 illustrates temporal extinction spectroscopy analysis of PSN with various concentrations of MDM2. For clarity, temporal monitoring of the absorbance at 419 nm is only displayed for PSN samples with a 1000 fold excess of MDM2 to PSN (figure 3.16 a). Longer time durations were initially investigated, however PSN assembly was observed to reach completion within 30 minutes.

Increasing PSN assembly was observed for PSN-12.1 and PSN-12.1$_{W\Delta A}$ in correlation with MDM2 concentration, however assembly of the latter occured to a lesser extent. Discrimination between PSN-12.1 and PSN-12.1$_{W\Delta A}$ samples was reduced at low and high ends of the MDM2 concentration range. At a PSN:MDM2 molar ratio of 1:100, MDM2 was not present in enough excess for PSN aggregation and as such a negligible decrease in the absorbance at λ-max was observed for both PSN solutions. When MDM2 was present in a 2000-fold molar excess to PSN, assembly was observed in PSN-12.1 and PSN-12.1$_{W\Delta A}$ to a similar extent indicating saturation of the system. MDM2 binds to peptide 12.1$_{W\Delta A}$ with a lower affinity than to peptide 12.1, however at the highest concentration MDM2 is present in such an excess that binding to PSN-12.1$_{W\Delta A}$ will occur more easily due to the thermodynamics of the solution. These data illustrates a dynamic range for specific PSN assembly, with MDM2 present in molar excess between 300 and 1000 fold. Analysis showed the extent of PSN assembly to increase linearly with MDM2 concentration within this dynamic range (figure 3.16 b).
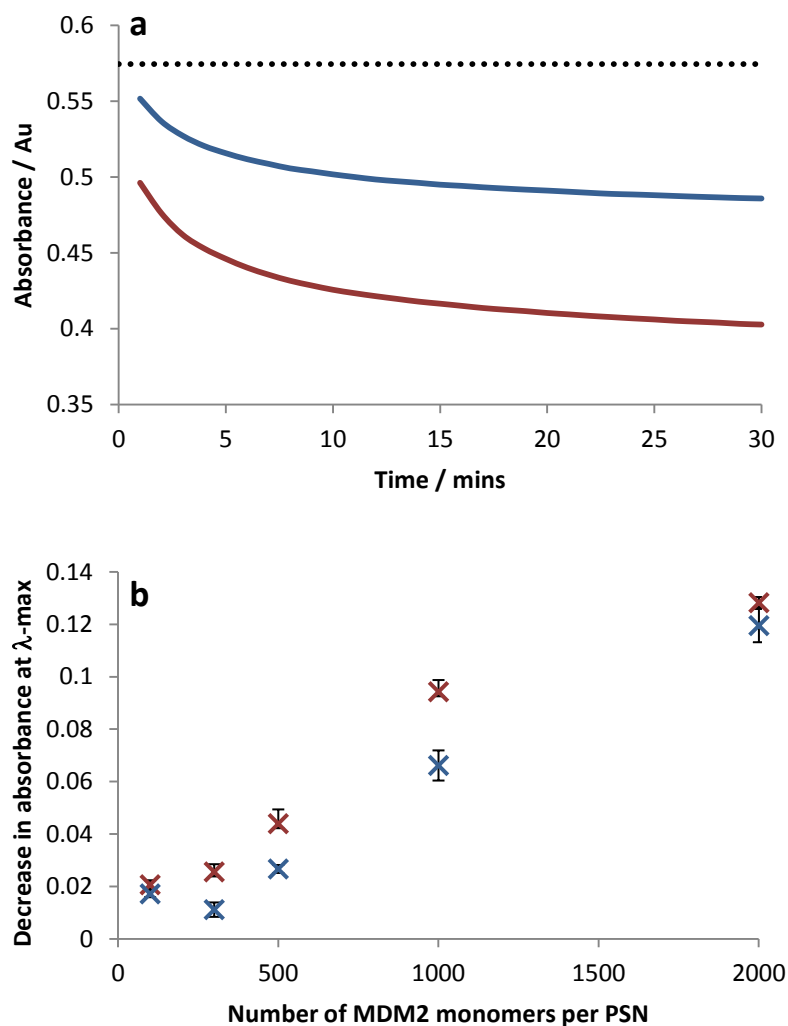
Figure 3.16 - Temporal extinction spectroscopy analysis of PSN aggregation. a) Absorbance at 419 nm in extinction spectroscopy monitored for a 30 minute duration following MDM2 addition to PSN-12.1 (red) and PSN-12.1$_{W\Delta A}$ (blue) at a PSN:MDM2 molar ratio of 1:1000. Dotted line indicates the absorbance at 419 nm for PSN before MDM2 addition. b) Change in the plasmon absorbance of PSN-12.1 (red) and PSN-12.1$_{W\Delta A}$ (blue) with a 100-2000 fold MDM2 excess after the 30 minute temporal analysis. Error bars illustrate the standard deviation in absorbance changes.

3.4.3.2 – Dynamic Light Scattering (DLS)

Extinction spectroscopy analysis has demonstrated specific assembly of PSN-12.1 in a concentration dependent manner between 1:300 and 1:1000 molar ratios of PSN:MDM2. Dynamic light scattering (DLS) presents an alternative analysis to investigate the PSN solution distribution. PSN samples were thus analysed using DLS to verify the changing PSN distributions observed in extinction spectroscopy (figure 3.16).
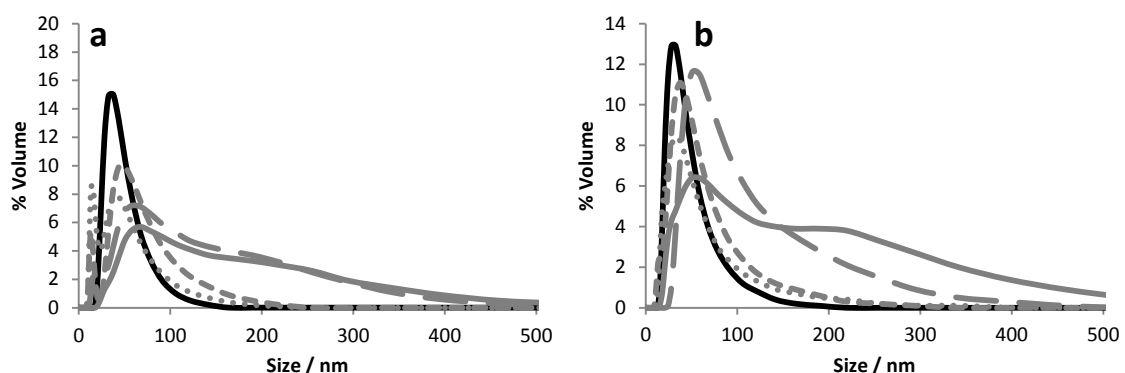
Figure 3.17 – DLS measurements of a) PSN-12.1 and b) PSN-12.1WDA solutions without MDM2 (black) and 96 hours after addition of 300 (dotted grey), 500 (short dashed grey), 1000 (long dashed grey) and 2000 (solid grey) MDM2 monomers per PSN.

Figure 3.17 shows DLS measurements acquired from samples containing PSN:MDM2 molar ratios of 1:300, 1:500, 1:1000 and 1:2000 following the extinction spectroscopy analysis illustrated in figure 3.16. At the highest MDM2 concentration, 2000 fold molar excess, an increase in PSN clusters of larger sizes was evident for both PSN-12.1 and PSN-12.1$_{W\Delta A}$ samples. This correlates with the previous analysis and gives further evidence for MDM2 saturation at molar excesses over 1000-fold. At MDM2 concentrations within the dynamic range (section 3.4.3.1) PSN-12.1$_{W\Delta A}$ solutions remained predominantly monodispersed whilst PSN-12.1 solutions demonstrated a

more diverse particle distribution with larger clusters. The proportion of single PSN-12.1 in solution decreased with increasing MDM2 concentration, again showing PSN assembly to be a concentration dependent process (figure 3.17).

3.4.3.3 – Surface-Enhanced Raman Scattering

Assembly of PSN has been achieved via specific biological interactions as proposed in figure 3.1 and detected using extinction spectroscopy and DLS. Surface-enhancement of Raman scattering is described in chapter one. Raman analysis delivers a unique vibrational fingerprint of analytes adsorbed onto metal surfaces and narrow spectral peaks enable potential multiplex detection.[163] Further enhancement of SERS is observed when SERS-active NP aggregate in solution, owing to the increased magnetic field at NP junctions.[110, 190] As such, SERS has proved to be a valuable technique for detecting NP assembly directed by DNA hybridization.[210] A BT Raman tag was incorporated into the design of PSN subjected to MDM2-induced assembly. SERS was therefore investigated as a potential detection technique for MDM2-directed PSN aggregation. Previous studies have been published on protein directed AuNP assembly,[211-213] however this is the first use of AgEDTA NP for SERS detection of protein-peptide interactions.

Figure 3.18 illustrates the BT dye structure and corresponding Raman spectrum achieved when employing an excitation wavelength of 514.5 nm. SERS analysis of PSN samples was carried out before and after the addition of MDM2 and Raman spectral intensity was used to monitor the assembly process. Quantification of PSN assembly was achieved by measuring the peak height at 1416 cm^{-1} relating to the azo stretch in the BT structure (figure 3.18).
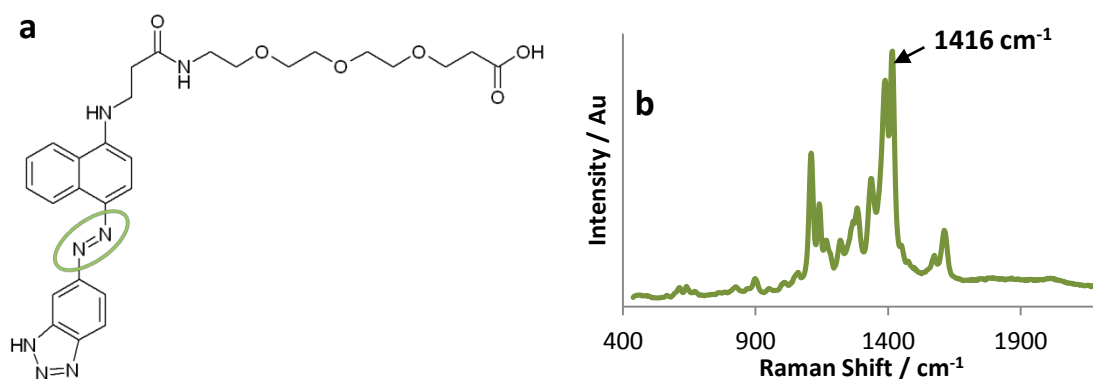
Figure 3.18 – a) Molecular structure of the BT Raman tag with the azo stretch highlighted by a green ring. b) Raman spectrum of BT using an excitation wavelength of 514.5 nm. The peak at 1416 cm^{-1} corresponds to the BT azo stretch.

MDM2 was added to 15 pM PSN solutions at PSN:MDM2 molar ratios ranging from 1:100 to 1:2000. PSN samples with various MDM2 concentrations were then subjected to temporal extinction spectroscopy analysis before SERS interrogation. An excitation wavelength of 514.5 nm was employed and five scans, of one second duration, acquired per PSN sample replicate. Figure 3.19 shows the results of SERS analysis carried out on PSN samples within eight hours following the addition of MDM2. Peak heights at 1416 cm^{-1} were observed to increase with MDM2 concentration for both PSN-12.1 and PSN-12.1$_{W\Delta A}$ samples as seen in previous analysis (figures 3.16 and 3.17). Initial examination of the recorded peak heights at 1416 cm^{-1} didn't show any obvious discrimination between assembly of PSN-12.1 and PSN-12.1$_{W\Delta A}$. This was due to PSN-12.1 and PSN-12.1$_{W\Delta A}$ samples without MDM2 exhibiting differential SERS intensities (figure 3.19 a). X-fold increases in SERS signals were therefore investigated and larger discrimination between PSN-12.1 and PSN-12.1$_{W\Delta A}$ samples observed (figure 3.19 b).
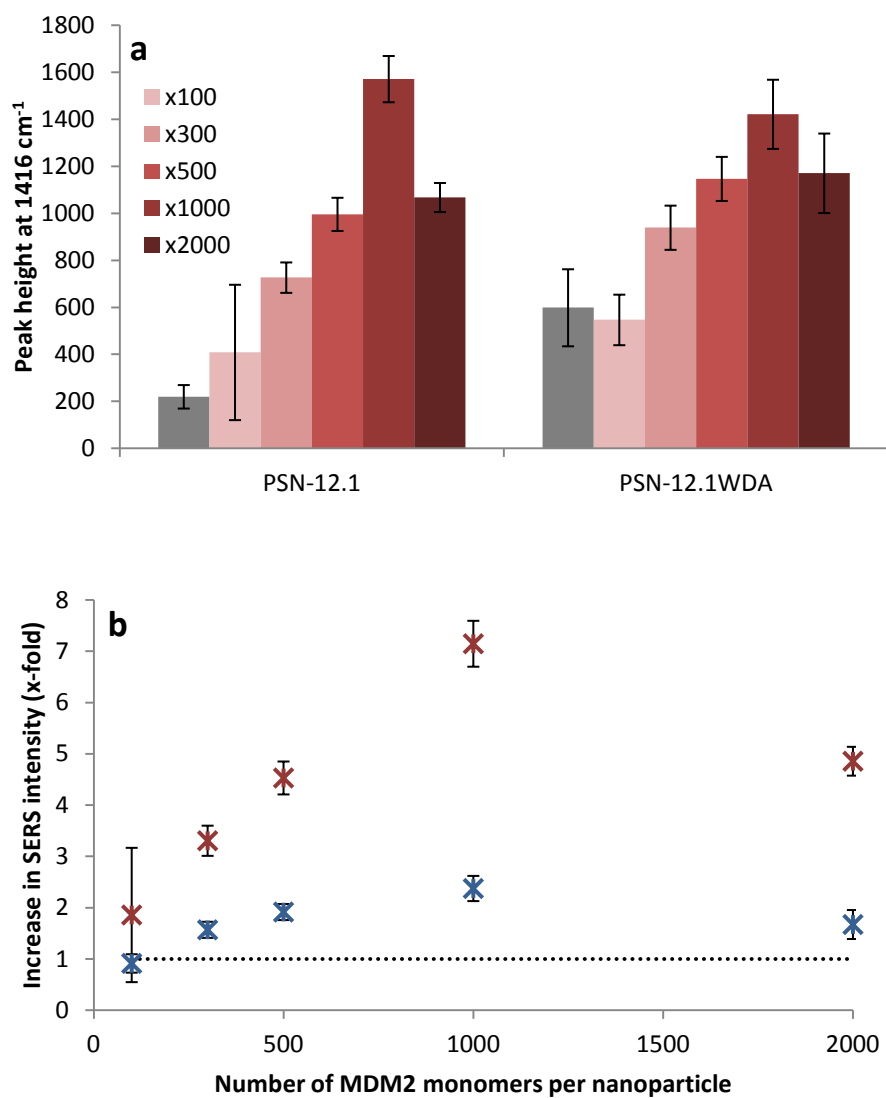
Figure 3.19 – SERS analysis of MDM2-induced PSN assembly recorded after temporal extinction spectroscopy analysis. a) Standardised peak heights at 1416 cm^{-1} for PSN without (grey) and with increasing MDM2 concentrations (red). b) x-fold increase in SERS for PSN samples following MDM2 addition. Dotted line indicates SERS intensity for PSN without MDM2. Error bars indicate the standard deviation of a) peak height and b) x-fold increase. Five one second scans were acquired for each sample replicate using 100 % laser power and an excitation wavelength of 514.5 nm.

At the optimum MDM2 concentration for PSN assembly, a PSN:MDM2 molar ration of 1:1000, an eight-fold increase in SERS is seen for PSN-12.1 compared to just over a two-fold increase for PSN-12.1$_{W\Delta A}$ samples. When employing a 2000-fold excess of MDM2 to PSN, SERS signal intensity was reduced compared to solutions with 1000 fold excess. Extinction spectroscopy and DLS analysis of samples indicated MDM2 saturation of the assay system at concentrations over a PSN:MDM2 molar ratio of 1:1000 (figures 3.16 and 3.17). Although aggregation was observed in samples oversaturated with MDM2, SERS intensity was decreased (figure 3.19) owing to possible monolayer coverage of PSN with MDM2 oligomers. If MDM2 is present on the PSN surface in dimer (or oligomer) formation, there are no free dimer interfaces available to bind other PSN bound monomers. Raman intensity was increased in samples with 2000-fold excess MDM2, compared to unaggregated samples, however the signal from BT dye molecules on PSN was dampened due to masking by MDM2 bound in such excess. These data affirm that MDM2-induced PSN assembly can be monitored at molar excess of MDM2 of 1000 fold and under, representing MDM2 concentrations of less than monomer monolayer coverage. SERS analysis showed greater sensitivity in monitoring PSN assembly than extinction spectroscopy, displaying a larger discrimination between PSN-12.1 and PSN-12.1$_{W\Delta A}$ samples. Signal amplification of up to eight-fold was observed in SERS compared to absorbance measurement reduction of less than 0.1 in extinction spectroscopy within an eight hour time frame.

Section 3.4.3.1 investigated the possibility of temporal extinction spectroscopy analysis of the PSN assembly process. NP assembly reached completion within 30 minutes, however the rate of assembly was difficult to extract from the data owing to the non-linear reduction in absorbance at λ-max. It was also evident that a significant amount of PSN assembly occurred in the first 60 seconds, before it was practically possible to record any measurements. Subsequent to SERS studies illustrated in figure 3.19, PSN assembly was explored using temporal Raman interrogation (figure 3.20).
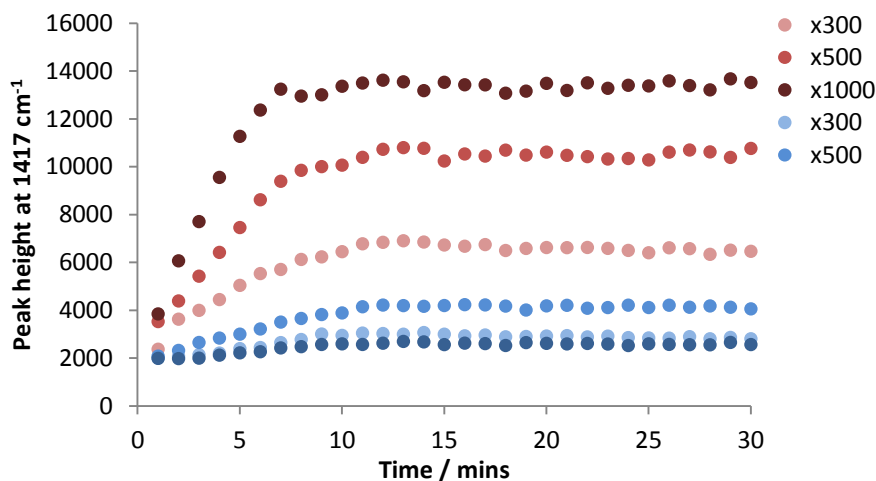
Figure 3.20 – Temporal SERS analysis of PSN assembly. Peak height at 1416 cm^{-1} monitored for 30 minutes following addition of varying amounts of MDM2 to PSN-12.1 (red) and PSN-12.1$_{W\Delta A}$ (blue). A one second scan was acquired every 60 seconds using 100 % laser power and an excitation wavelength of 514 nm.

SERS temporal analysis was carried out by focussing the laser through PSN solutions under continuous rotation. PSN solution rotation served two purposes in this analysis. Primarily, constant mixing was introduced to maintain uniform distribution of PSN and prevent precipitation of large clusters out of solution. This was essential to reduce variations in SERS signal intensities associated with different solution components in the interrogation volume of the laser beam. Secondly, solution mixing ensured maximum propensity for NP assembly through enhancement of molecular collisions. Figure 3.20 demonstrates the results obtained for SERS analysis of MDM2-induced PSN assembly, over 30 minutes, for samples with PSN:MDM2 molar ratios within the dynamic range identified in section 3.4.3.1 (1:300, 1:500 and 1:1000). Peak height measurements at 1416 cm^{-1} increased over time for PSN-12.1 samples with MDM2 in a concentration dependent manner. The same amplification in SERS signals was not observed for PSN-12.1$_{W\Delta A}$ solutions, indicating that MDM2 had induced PSN assembly

through a biologically specific interaction. Peak height measurements at 1416 cm^{-1} initially increased in a linear fashion before reaching a plateau indicating assembly completion (figure 3.20). Both the rate and extent of PSN assembly observed was dependent on MDM2 concentration. PSN assembly reached completion after seven, nine and eleven minutes in solutions with 300, 500 and 1000 fold molar excess MDM2. The linear increase in SERS intensity, relating to the PSN assembly process, gives rise to possible rate determination studies.

3.4.3.4 – Scanning Electron Microscopy

Thus far section 3.4.3 has described the use of extinction spectroscopy, DLS and SERS to detect MDM2-directed PSN assembly. The change in PSN-12.1 solution distribution occurred as a result of the biological interactions illustrated in figure 3.1. Specificity of these interactions and consequential PSN assembly was demonstrated using negative control samples, PSN-12.1$_{W\Delta A}$ (figures 3.16 – 3.20). Scanning electron microscopy (SEM) analysis was also investigated for further confirmation of the MDM2-induced PSN assembly.
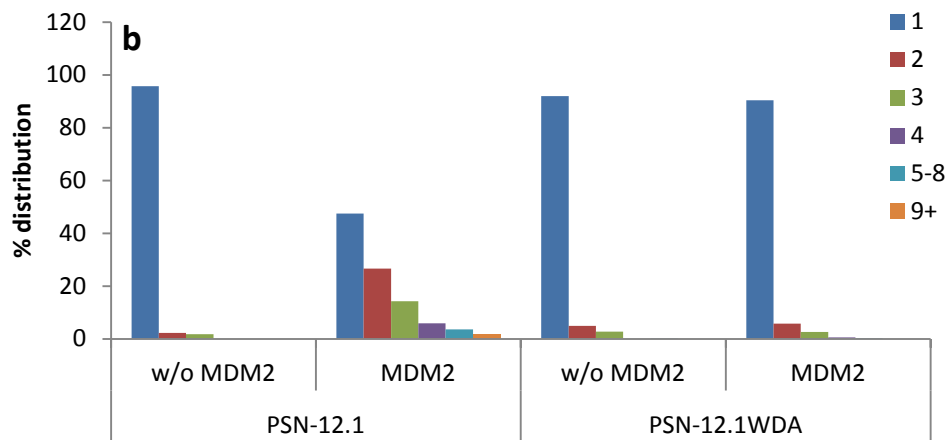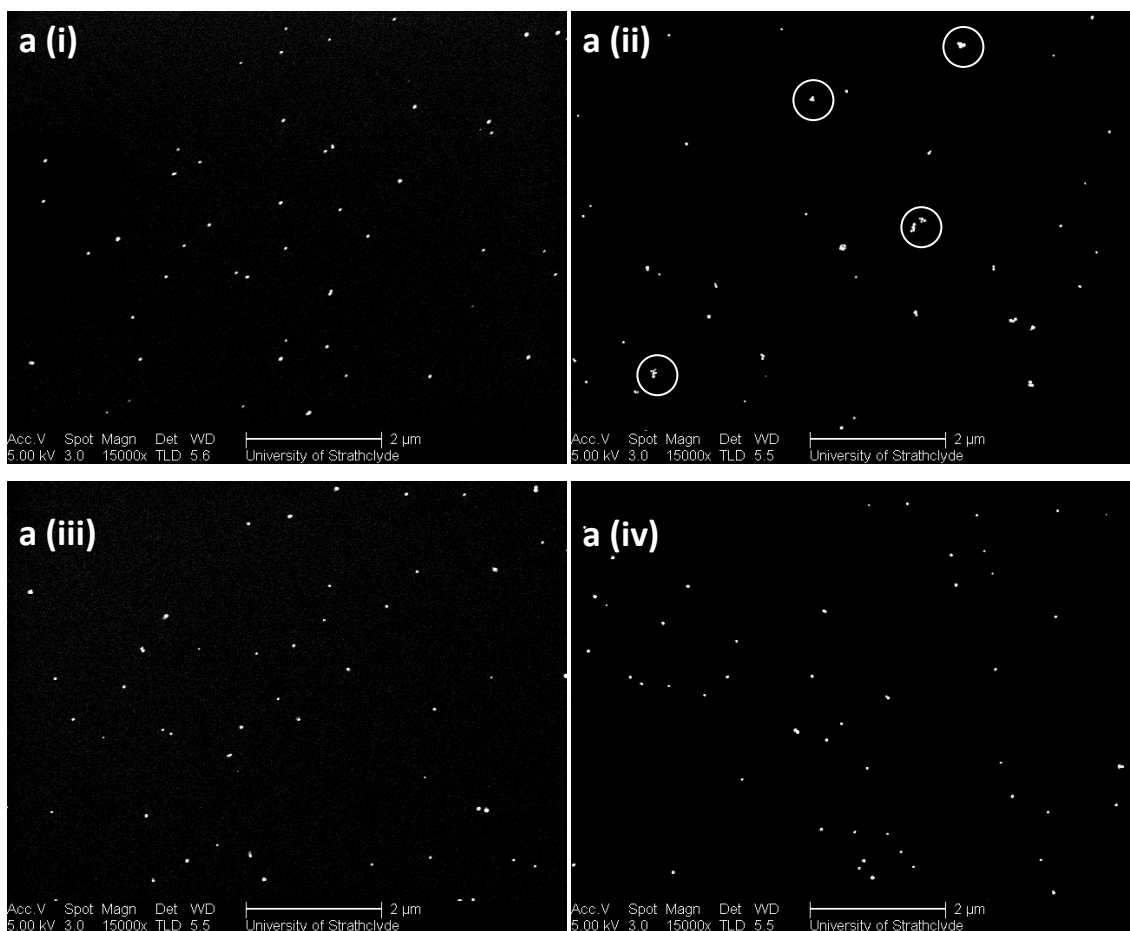
Figure 3.21 - a) SEM images of i) PSN-12.1, ii) PSN-12.1 with MDM2, iii) PSN-12.1$_{W\Delta A}$ and iv) PSN-12.1$_{W\Delta A}$ with MDM2 at 15000x magnification. Scale bars represent 2 microns. b) Statistics from SEM analysis showing the percentage of differently sized clusters present. Legend illustrates the number of NP present in differently sized clusters.

SEM analysis was carried out using silicon wafers coated in poly(diallyldimethylammonium), PDDA. This created a hydrophobic polymer coating on the silicon to prevent surface-induced aggregation of PSN. PSN solutions were deposited on PDDA coated silicon wafers and left for 25 minutes before washing steps were carried out in preparation for analysis using a Field-emission electron microscope. A PSN:MDM2 molar ratio of 1:1000 was shown to be optimal for PSN assembly in earlier analysis (figures 3.16 – 3.20), hence 15 pM PSN samples were prepared with this ratio for SEM analysis. Figure 3.21 demonstrates SEM images of PSN-12.1 and PSN-12.1$_{W\Delta A}$ samples with and without MDM2. The images in figure 3.21 show representative distributions for all PSN samples and exhibit the same size scale for comparison purposes. All other images recorded are illustrated in appendix B(i). All solutions, except PSN-12.1 with MDM2, exhibited a monodispersed distribution of PSN (figure 3.21 a). Analysis of PSN-12.1 with MDM2 showed a varied distribution containing some PSN monomers alongside PSN clusters of different sizes. Some of these PSN trimers and larger clusters have been highlighted in figure 3.21. SEM analysis of PSN-12.1 with MDM2 demonstrated only partial aggregation and sample distributions are therefore hard to discern optically. Statistical analysis was carried out on PSN samples during SEM to quantify the proportion of PSN present in larger clusters. To that end, the number of monomers, dimers, trimers, clusters of four, clusters of five to nine PSNs and larger cluster structures were counted for each sample. PSN-12.1 samples with MDM2 showed a 47 % distribution of PSN monomers with various proportions of larger cluster structures. All other samples consisted of over 90 % PSN monomers in solution. The partial aggregation reported here correlates with minimal changes in extinction spectroscopy illustrated in figure 3.16 and demonstrates the sensitivity of SERS detecting in small changes in PSN distribution (figures 3.17 and 3.20).

3.5 – Investigating MDM2 allostery

MDM2-induced PSN assembly has been demonstrated in section 3.4 and monitored using a variety of analytical techniques. This section focuses on using the MDM2 assay to explore the allosteric activity of MDM2.
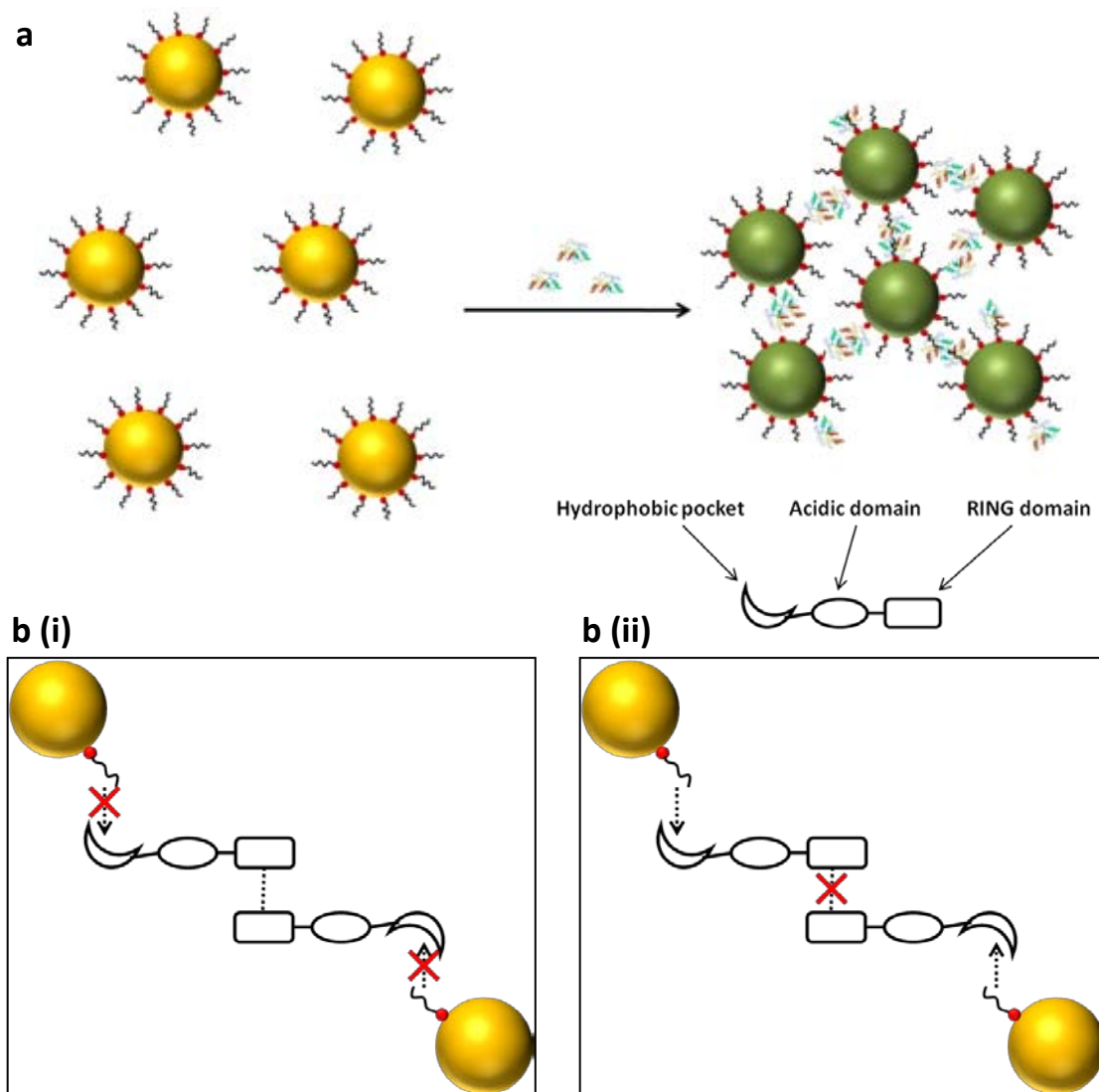
Figure 3.22 – Schematic of the proposed MDM2 assay. a) MDM2 induced aggregation of PSN-12.1 and b) inhibition of PSN assembly by blocking i) protein-peptide interactions and ii) MDM2 dimer formation. Dotted lines represent the interactions driving PSN assembly and red crosses indicate binding events targeted in PSN assembly inhibition.

The proposed PSN assembly is dependent on two simultaneous binding events of MDM2. MDM2 is a conformationally flexible protein with numerous binding partners and as such protein allostery plays an important role in MDM2 interactions. Various ligands, known to bind different MDM2 domains, were introduced into the PSN assembly assay to investigate MDM2 allostery (figure 3.22). The allosteric effects of N-terminal binding ligands (peptide 12.1 and Nutlin-3), RING domain ligands (self-peptides and zinc) and the acidic domain binding ligand (peptide Rb1) were investigated for disruption or enhancement of the PSN assembly process.

3.5.1 – Peptide 12.1

Peptide 12.1 forms an ampipathic helix containing the sequence motif, FxxxWxxL, which binds the MDM2 hydrophobic pocket with high affinity.[8, 206] Biological specificity of this interaction is demonstrated through MDM2-induced assembly of PSN-12.1 compared with PSN-12.1$_{W\Delta A}$ (figures 3.16 – 3.21).

Peptide 12.1   -   SGSGMPR**F**MDY**W**EG**L**N

Peptide 12.1$_{W\Delta A}$ -   SGSGMPR**F**MDY**A**EG**L**N

Solution kinetics suggest that MDM2 would have a higher binding affinity for free peptide 12.1 than NP-bound peptide 12.1. PSN assembly could therefore be disrupted by the addition of free peptide 12.1 (inhibitor peptide 12.1). To that end, MDM2 was pre-incubated with different concentrations of inhibitor peptide 12.1 for 30 minutes before addition into PSN solutions. Pre-mixing the MDM2 with inhibitor peptide allows for peptide-protein binding, thus blocking the active sites on MDM2. This would have a negative effect on PSN assembly as MDM2, bound to inhibitor peptide 12.1, can undergo dimer formation but is unable to interact with PSN-12.1 (figures 3.22 bi and 3.23).
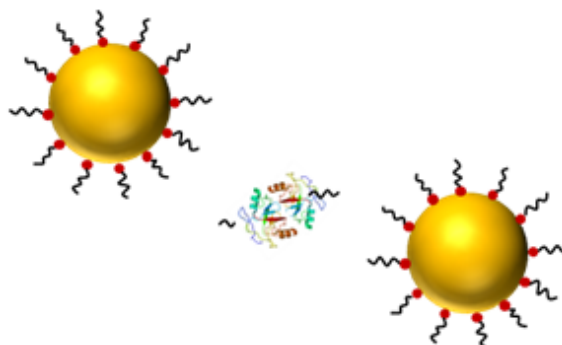
Figure 3.23 – Schematic illustrating PSN assembly inhibition with an MDM2 N-terminal binding ligand.

All PSN assembly inhibition experimentation was carried out using previously optimized conditions, 15 pM PSN with a PSN:MDM2 molar ratio of 1:1000. MDM2 was pre-treated with inhibitor peptide 12.1 at molar excesses of 1, 10, 25 and 50 prior to mixing with PSN-12.1. Changes in the absorbance at λ-max in extinction spectroscopy and peak height measurements at 1416 cm^{-1} in SERS analysis were used to analyse PSN assembly.

Addition of inhibitor peptide 12.1 caused a reduction in signal changes in extinction spectroscopy and SERS indicative of PSN assembly (figure 3.24). It can therefore be inferred that PSN assembly has indeed been disrupted. Increased dampening of signal changes was observed in correlation with inhibitor peptide 12.1 concentration (figure 3.24). This demonstrates that PSN disruption is dependent on inhibitor molecule concentration, just as PSN assembly is dependent on MDM2 concentration. Examination of the x-fold signal changes gives a direct comparison between extinction spectroscopy and SERS measurements and highlights SERS as a more sensitive technique. Extinction spectroscopy showed complete PSN assembly inhibition when inhibitor peptide 12.1 was present at a 50-fold molar excess to MDM2 (figure 3.24 a). SERS analysis of the same samples demonstrated the occurrence of partial aggregation

undetected in extinction spectroscopy (figure 3.24 b). The preventative action of inhibitor peptide 12.1 on PSN assembly reported here presents a potential application for MDM2-induced PSN assembly as a ligand screening assay.
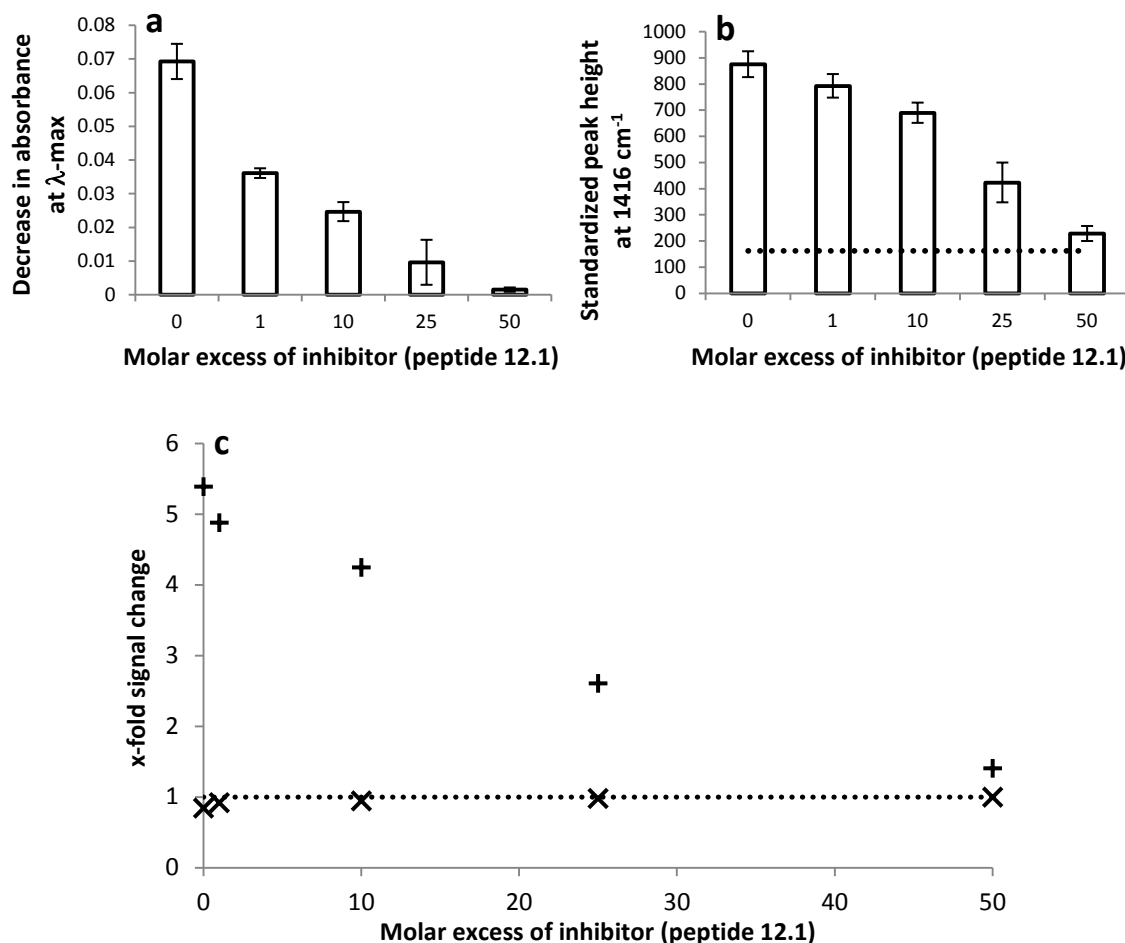
Figure 3.24 - Competitive inhibition of MDM2-induced PSN aggregation. a) Decrease in the plasmon band absorbance monitored by extinction spectroscopy and b) peak height measurements at 1416 cm^{-1} in SERS analysis following a 30 minute incubation of MDM2 with varying concentrations of inhibitor peptide 12.1. c) x-fold change in the plasmon band in extinction spectroscopy (X) and the x-fold increase in SERS intensity (+) derived from data in a and b. Dotted lines indicate PSN-12.1 measurements when MDM2 is absent.

3.5.2 – Nutlin-3
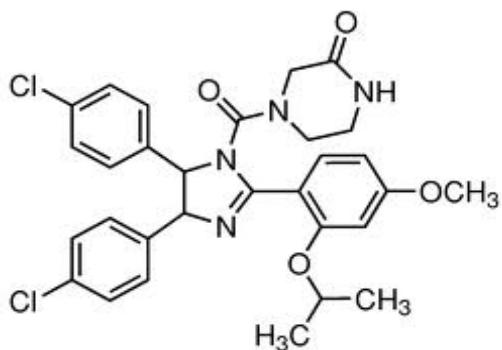
Figure 3.25 – Molecular structure of Nutlin-3

Inhibition of PSN assembly has been demonstrated through pre-incubation of MDM2 with an excess of inhibitor peptide 12.1 to block the N-terminal domain active sites that interact with PSN-12.1. This shows potential for the MDM2 assay for screening ligands that disrupt the p53-MDM2 interaction. To test this further, a known MDM2 N-terminal binding ligand, Nutlin-3, was introduced to inhibit MDM2-induced PSN aggregation. Nutlins are a series of cis-imidazolines identified from a library of synthetic compounds screened against MDM2.[214] The active enantiomer of Nutlin-3 demonstrated the most potent binding activity to MDM2, disrupting the p53-MDM2 interaction with an IC_{50} of 0.09 µM, and has since been developed into an FDA approved drug.[214]

MDM2 was pre-treated with Nutlin-3 and subsequent PSN-12.1 assembly investigated. Nutlin-3 molecules also occupy the N-terminal binding site on MDM2. Inhibition of PSN assembly will therefore occur as depicted with inhibitor peptide 12.1 (figures 3.23 and 3.26). MDM2 was pre-incubated with a 50-fold excess of Nutlin-3. This concentration was based on earlier results that showed almost complete PSN assembly inhibition through the addition of this molar excess of inhibitor peptide 12.1. Analogous to

inhibitor peptide 12.1 studies, MDM2 and Nutlin-3 were incubated for 30 minutes prior to introduction into PSN-12.1 solutions. Treated and non-treated MDM2 were added to 15 pM PSN-12.1 at a 1000-fold molar excess and assembly was analysed after a minimum of 30 minutes.
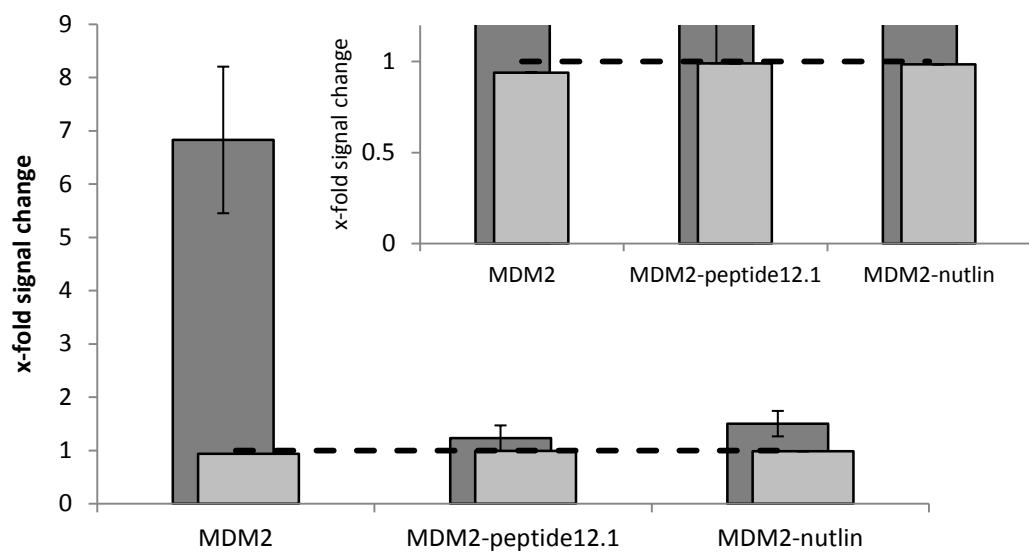
Figure 3.26 - Competitive inhibition of MDM2-induced PSN aggregation with inhibitor peptide 12.1 and Nutlin-3. x-fold decrease in the plasmon band monitored by extinction spectroscopy (light grey) and x-fold SERS intensity increase (dark grey) following a 30 minute incubation of MDM2 with 50-fold excess of inhibitor. Inset illustrates the graph on a smaller scale to show the change in extinction spectroscopy signal.

Addition of MDM2 to PSN-12.1 resulted in a 6.83-fold amplification in SERS signal intensity and a 6 % decrease in the plasmon band absorbance in extinction spectroscopy. Such signal changes were not evident when MDM2 was pre-incubated with Nutlin-3. The presence of Nutlin-3 reduced signal changes to a 1.5-fold increase in SERS and a 2 % decrease in extinction spectroscopy measurements. Hence, it can be

deduced that Nutlin-3 has an inhibitory effect on PSN-12.1 assembly that is not dissimilar to the effect seen with inhibitor peptide 12.1.

3.5.3 – RING domain peptides

Sections 3.5.1 and 3.5.2 have illustrated inhibition of MDM2-induced PSN assembly through disruption of the interaction between PSN-12.1 and the hydrophobic pocket of MDM2. PSN aggregation in this system is also dependent on MDM2 RING domain dimerization (figure 3.22). If PSN-12.1 aggregation proceeds via the molecular interactions proposed, disrupting MDM2 dimer formation should have a negative effect on the assembly process. To that end, a number of self-peptides from the MDM2 dimerization domain were introduced. These peptides were synthesised to represent portions of the MDM2 RING domain and will therefore bind full-length MDM2 in solution mimicking dimerization. As with N-terminal binding ligands, these peptides will block MDM2 C-terminal active sites and prevent dimer formation between two full-length proteins. MDM2 maintains the ability to form hydrophobic pocket interactions with PSN-12.1 but dimer prevention will prohibit PSN-12.1-MDM2 cluster formation (figure 3.22 bii and 3.27).
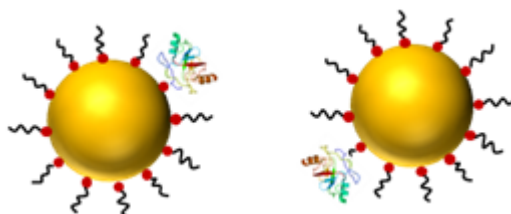
Figure 3.27 – Schematic illustrating the effect of MDM2 dimer inhibition on PSN assembly.

Six RING domain peptides were investigated to inhibit MDM2 dimer formation, with overlapping sequences spanning the MDM2 dimerization active site. Table 3.1 illustrates some properties of MDM2 RING domain peptides used.

RING peptide	Primary sequence	Isoelectric point (pI)	Number of Cysteine residues
Peptide 43	DKEESVESSLPLNAI	3.7	0
Peptide 44	PLNAIEPCVI**C**QGRP	6.1	1
Peptide 45	**C**QGRPKNG**C**IVHGKT	9.9	2
Peptide 46	VHGKTGHLMA**C**FT**C**A	8.3	2
Peptide 47	**C**FT**C**AKKLKKRNKPC	10.4	2
Peptide 48	RNKP**C**PV**C**RQPIQMI	10.1	2

Table 3.1 – Table illustrating primary amino acid sequences and pI values of MDM2 RING domain peptides. Constituent cysteine residues are quantified and highlighted in bold red.

MDM2 RING peptides were introduced into PSN-12.1 samples and analysed using SERS and extinction spectroscopy to screen for PSN assembly inhibition. All MDM2 assay SERS analysis up to this point has been conducted by focussing the laser beam through the bulk solution either in NMR tubes or cuvettes. This served the purpose of reducing inherent variations associated with Raman analysis of solutions with polydispersed distributions. Using this methodology reduces the amount of samples that can be successfully analysed in one experiment. For example, conducting 30 minute temporal SERS analysis on six samples in triplicate requires nine hours instrument time and manual sample changeover means that this cannot be run overnight. In order to successfully adapt the MDM2 assay for screening purposes, other analysis methodologies are necessary that allow higher sample throughput. To achieve this, end-point measurements were acquired of samples in 96-well microtitre plates. SERS measurements obtained by focussing on the surface and through the bulk of solutions

were compared to ascertain which method gave the most reliable results. A cyclohexane standard was employed to focus the laser through the bulk of the solution.

MDM2 samples were pre-treated with a 50-fold molar excess of each RING peptide, for a minimum of two hours, before mixing with PSN-12.1 at a PSN:MDM2 molar ratio of 1:1000. RING peptides were also added to PSN-12.1 solutions without MDM2 at the same final molar excess, 50000-fold (50-fold excess of inhibitor to protein, 1000-fold excess of protein to PSN-12.1), to ensure that any PSN assembly changes resulted from MDM2 interactions. Samples were prepared in triplicate in a 96-well plate and surface and solution SERS analysis carried out for comparative purposes (figure 3.28). SERS signal intensities were calculated by monitoring the peak height at 1417 cm^{-1} and results obtained using surface and solution laser focussing elicited similar results (figure 3.28). Peak height measurements acquired when the laser was focussed through the bulk solution yielded smaller errors and therefore bulk solution analysis was used in further studies.

MDM2-induced PSN assembly occurred to a much lesser extent than previously observed with 1.7 and 1.6-fold increases in peak height at 1417 cm^{-1} evident in surface and solution SERS analysis respectively. This reduction in PSN assembly was proposed to result from variation between MDM2 fractions eluted in purification. The MDM2 fraction used here, and for remaining experimentation in this chapter, was eluted after that used in previous studies and may have a different purity. This elution fraction contained a lower concentration of active MDM2, calculated using ELISA, and a higher concentration of impurities which could potentially interfere with PSN assembly. Temporal SERS studies (figure 3.30) using this protein elution fraction also demonstrated a lower extent of PSN assembly.
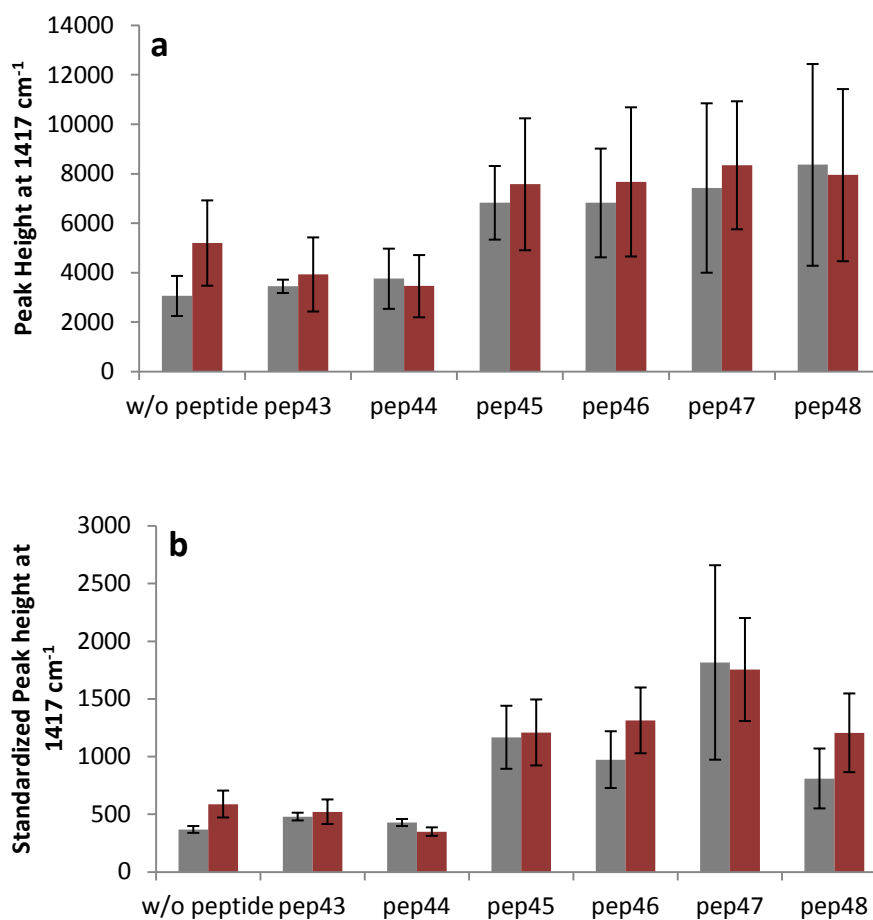
Figure 3.28 – SERS analysis of PSN-12.1 in the absence (grey) and presence (red) of MDM2 with different RING peptides. Error bars indicate the standard deviations associated with peak height measurements at 1417 cm^{-1}. Five SERS spectra, with a time duration of one second, were acquired for each sample focussing a) on the surface and b) through the solution bulk. A laser excitation of 514.5 nm was employed.

Negligible changes in SERS intensities were observed for PSN-12.1 samples in the presence of peptides 43 and 44. This data suggested a possible inhibitory effect of peptides 43 and 44 on MDM2-induced PSN assembly, however further experimentation was required to verify the results. In contrast, incorporation of peptides 45-48 to PSN-12.1 samples resulted in a two-four times amplification in SERS

signals. Raman signal intensification was observed in solutions with and without MDM2, thus showing non-specific PSN aggregation (figure 3.28). Following SERS interrogation, triplicate samples were pooled and subjected to extinction spectroscopy analysis, which confirmed PSN aggregation in all samples containing peptides 45-48.

Two potential explanations were formulated for PSN aggregation with peptides 45-48 and not peptides 43 and 44. Firstly, peptides 43 and 44 have pI values of 3.7 and 6.1 respectively whilst the pI values of peptides 45-48 range from 8.3 – 10.4 (table 3.1). Peptides 43-44 and 45-48 therefore exhibit net negative and positive charges respectively in the assay buffer, pH 7.5. Any exposed NP surface is negatively charged and electrostatic interactions with positively charged species, such as peptides 43 and 44, could result in aggregation. Secondly, peptides 45-48 all contain two cysteine residues not present in peptides 43 and 44. Cysteine residues are known to form disulphide linkages with other cysteine residues and with NP surfaces. The presence of two cysteine residues allows for NP bridging through NP attachment and inter-peptide linkages. Peptide 44 contains one cysteine residue, however cannot cause NP bridging as only one linkage can be formed, either with a NP surface or another peptide molecule. In order to test whether or not non-specific aggregation of PSN-12.1 was dependent on net peptide charge, negatively and positively charged peptides containing only one cysteine residue were added to PSN-12.1 solutions. Negative (Em) and positive (Km) peptides (chapter 4) exhibit pI values of 2.9 and 10.7 respectively. PSN-12.1 solutions, 15 pM, were prepared and mixed with Km and Em peptides for two hours at a molar ratio of 1:50000. SERS analysis of the bulk solution was carried out in a 96-well plate, recording the peak height at 1417 cm^{-1}, before triplicate samples were pooled and analysed using extinction spectroscopy (figure 3.29).
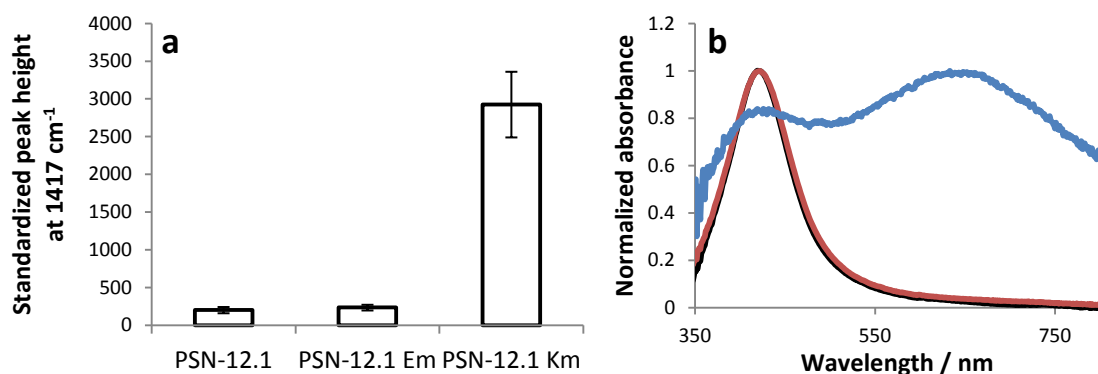
Figure 3.29 – SERS and extinction spectroscopy analysis of 15 pM PSN-12.1 with a 50000-fold excess of peptides Em and Km. a) Sample peak heights at 1417 cm^{-1} in SERS analysis standardized against cyclohexane. Five one second scans were acquired per samples using 100 % laser power and an excitation wavelength of 514.5 nm. b) Normalized extinction spectra of PSN-12.1 samples without (black) and with peptides E (red) and K (blue).

SERS and extinction spectroscopy analysis demonstrated aggregation of PSN-12.1 following the addition of peptide Km. This was shown by an increase in SERS intensity and a reduction in the plasmon absorbance band in extinction spectroscopy (figure 3.29). It can therefore be deduced that the net positive charge of peptides 45-48 was responsible for non-specific aggregation of PSN-12.1 illustrated in figure 3.28. NP bridging through sulphur linkages may contribute, however peptides are unlikely to immobilize on NP surfaces functionalized with peptide – BT.

PSN assembly appeared to be reduced following MDM2 pre-treatment with RING peptides 43 and 44. These peptides were investigated using temporal SERS analysis to test for PSN assembly inhibition. MDM2 was pre-incubated for 30 minutes with a 50-fold molar excess of peptides 43 and 44. SERS analysis of PSN-12.1 solutions was conducted for 30 minutes immediately following the addition of treated and untreated MDM2 at a PSN:MDM2 molar ratio of 1:1000 (figure 3.30).
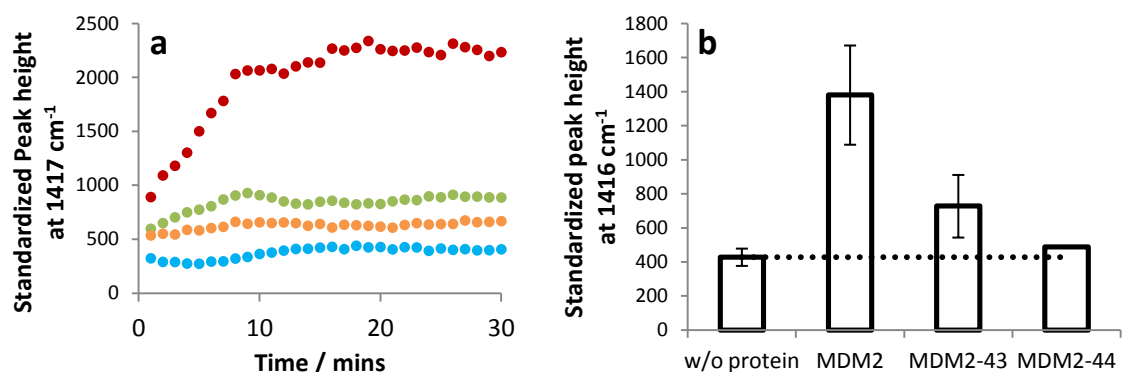
Figure 3.30 – a) Temporal SERS analysis of PSN assembly. Peak height at 1416 cm^{-1} monitored for 30 minutes following addition of MDM2 (red), MDM2-peptide 43 (green) and MDM2-peptide 44 (orange) to PSN-12.1 and MDM2 to PSN-12.1$_{W\Delta A}$ (blue). A one second scan was acquired every 60 seconds using 100 % laser power and an excitation wavelength of 514.5 nm. b) Peak height measurements recorded for PSN-12.1 samples after completion of temporal analysis. All peak heights are standardized against cyclohexane.

Samples of PSN-12.1 with MDM2 demonstrated increased signal intensities in SERS analysis indicative of PSN assembly (figure 3.30). Pre-incubation of MDM2 with peptides 43 and 44 resulted in a comparative reduction in SERS thus demonstrating an inhibitory effect on PSN assembly. PSN assembly inhibition by peptides 43 and 44 was verified by extinction spectroscopy (figure 3.31). A marginal increase in SERS was observed when MDM2 was treated with peptide 43 inferring that this peptide has a lower potency for disruption of MDM2 dimerization. RING peptides are short, overlapping primary sequences from the MDM2 RING domain which contain a linear motif (aa 430-LPLNAI-435) known to stabilise MDM2/MDMX heterodimer.[44] The difference in dimer inhibition potency between peptides 43 and 44 suggests specific areas of the RING domain are more important for dimer formation. The binding orientation of other RING domain ligands may therefore have an effect on inhibition potency.
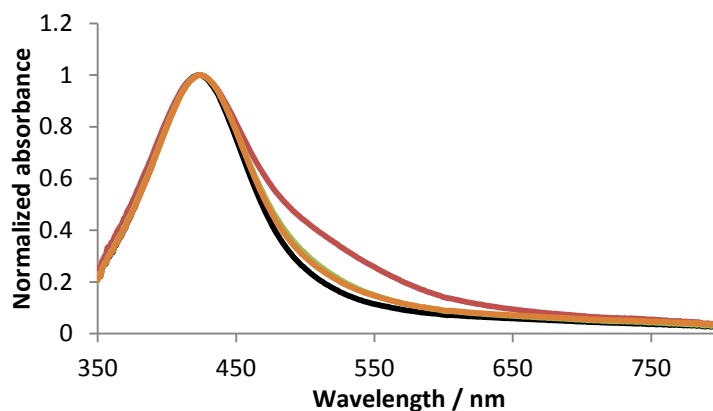
Figure 3.31 – Normalized extinction spectra of PSN-12.1 (black) without MDM2 and following addition of MDM2 (red), MDM2-peptide 43 (green) and MDM2-peptide 44 (orange).

3.5.4 – Acidic domain binding ligand (peptide Rb1)

PSN assembly has been demonstrated, driven by two simultaneous biological interactions (figure 3.22). Inhibition of the MDM2-induced PSN assembly has also been achieved through selective disruption of either MDM2 hydrophobic pocket binding to PSN-12.1 or RING domain dimerization. In order to investigate the allosteric nature of MDM2 in more detail, other MDM2 binding ligands were studied. Interactions of such ligands with MDM2 do not directly disrupt the binding events driving PSN aggregation but may cause an allosteric effect that either promotes or hinders the assembly process. Retinoblastoma protein (pRb) is a tumour suppressor that plays a critical role in cell cycle progression. The C-terminal domain of pRb is known to interact with the central acidic domain of MDM2 causing an inhibitory effect on MDM2 – mediated p53 degradation.[215] MDM2 – mediated ubiquitination of p53 is a multi-subunit process involving two separate MDM2-p53 binding events (section 1.1.2.2). pRb interacts with MDM2 at the same position as the BOX-V domain on p53 and consequently it is hypothesised that pRb prevents this secondary binding event.[215] Introducing a pRb peptide mimic into the MDM2 assay described here may give some insight into the

effect of pRb-MDM2 interactions on p53 BOX-1 binding to the MDM2 hydrophobic pocket (figure 3.32). Peptide Rb1 (SGSGDQIMMCSMYGICKVKNIDLK) represents a portion of the C-terminal domain of pRb that binds to the MDM2 central acidic domain.[25]
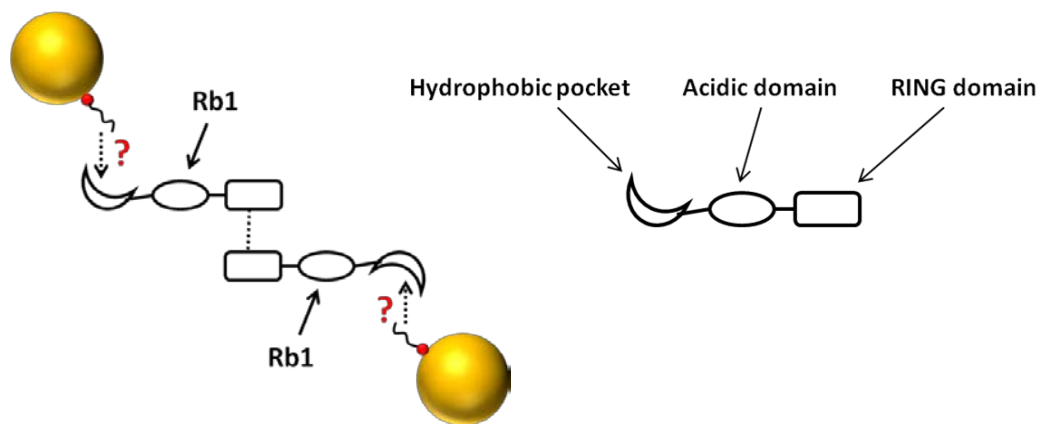
Figure 3.32 – Schematic illustrating Rb1 binding to MDM2 and the biological interactions upon which this could cause an allosteric effect (red question marks).

MDM2 was incubated for 30 minutes with peptide Rb1, 50-fold molar excess, and added to PSN-12.1 immediately before the start of temporal SERS analysis. The same experimental parameters were used as for the studies involving RING peptides 43 and 44. An increase in SERS from PSN-12.1 was observed following addition of MDM2 in the presence of peptide Rb1. This signal amplification was however reduced, comparable to MDM2 without Rb1, indicating that PSN assembly had occurred to a lesser extent (figure 3.33). Peak height measurements at 1416 cm^{-1} recorded after completion of temporal analysis demonstrated a 3.2-fold signal increase with MDM2 compared to a 2.3-fold increase with MDM2 which had been pre-treated with peptide Rb1. Extinction spectroscopy analysis showed partial aggregation of PSN-12.1 after addition of MDM2 with and without peptide Rb1, however earlier studies have shown SERS to be a more

sensitive analytical technique (figures 3.26 and 3.20). Data shown here demonstrate a mild inhibitory effect of peptide Rb1 on PSN assembly suggesting an allosteric effect of Rb1 binding on the p53-MDM2 interaction. These data correlate with previously published studies that demonstrate an affect of MDM2 acidic domain binding ligands on the binding activity of the hydrophobic pocket.[25]
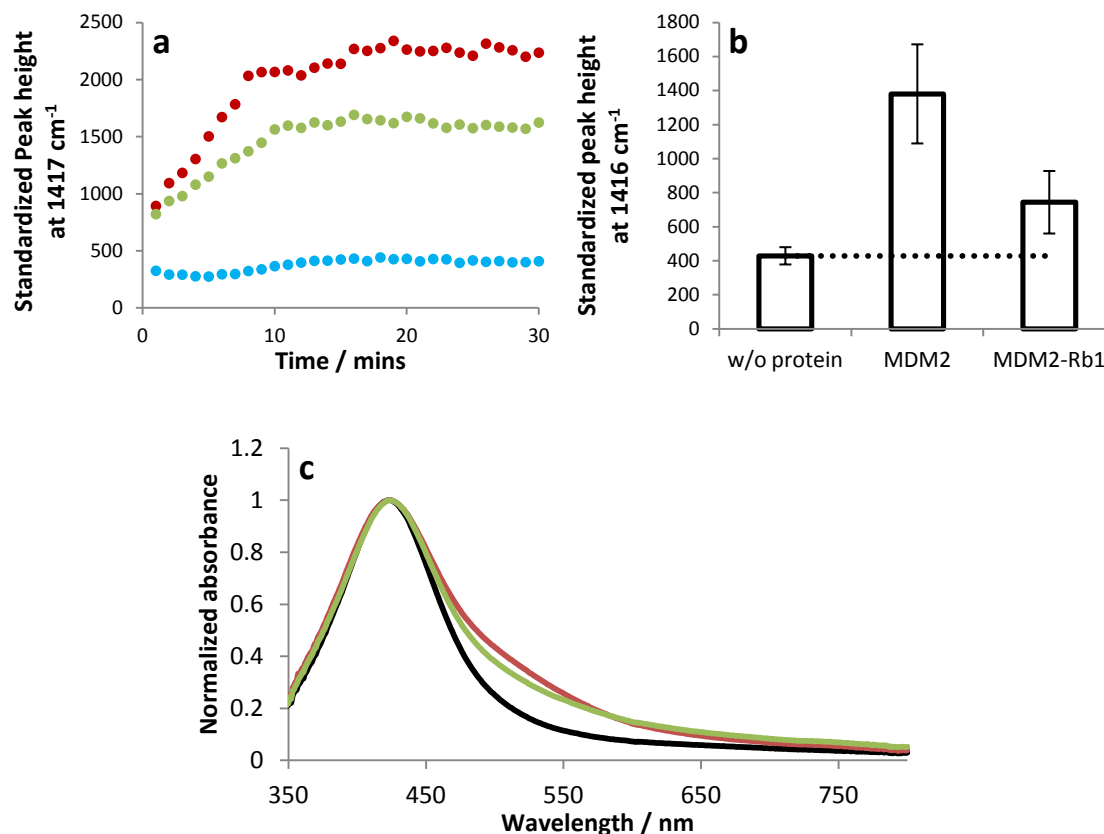
Figure 3.33 – a) Temporal SERS analysis of PSN assembly. Peak height at 1416 cm^{-1} monitored for 30 minutes following addition of MDM2 (red) and MDM2-Rb1 (green) to PSN-12.1 and MDM2 to PSN-12.1$_{W\Delta A}$ (blue). A one second scan was acquired every 60 seconds using 100 % laser power and an excitation wavelength of 514.5 nm. b) Peak height measurements recorded for PSN-12.1 samples after completion of temporal analysis. All peak heights are standardized against cyclohexane. c) Normalized extinction spectra of PSN-12.1 without MDM2 (black) and following the addition of MDM2 (red) and MDM2-Rb1 (green).

3.5.5 – Zinc

Experimentation outlined in section 3.5.4 illustrated a use of the MDM2 assay in detecting allosteric protein interactions. Peptide Rb1 interactions with one MDM2 domain effected the binding activity of a different domain with PSN-12.1. Further to these investigations, zinc was added into the reaction mix and PSN assembly examined.
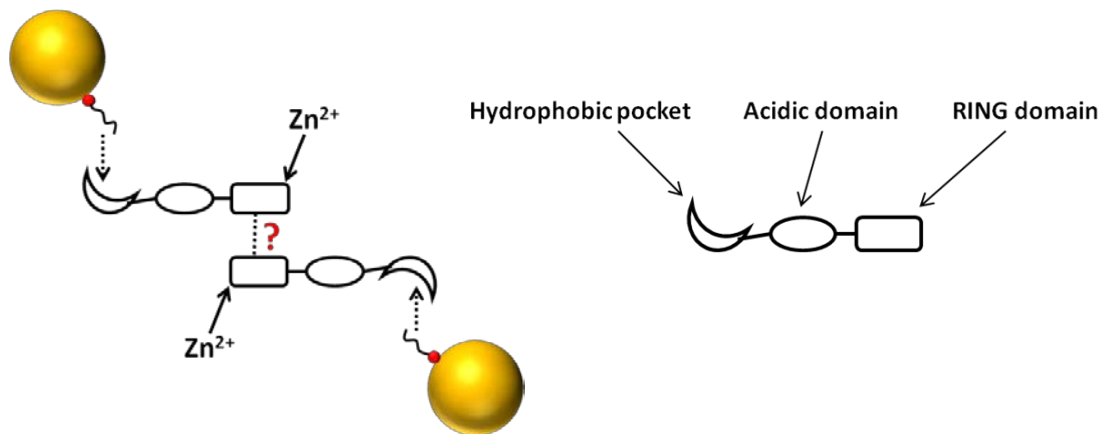
Figure 3.34 – Schematic illustrating MDM2 Zn^{2+} coordination and the biological interaction upon which this could cause an allosteric effect (red question mark).

The MDM2 RING finger domain contains two coordination sites for Zn^{2+}.[37] Incorporation of Zn^{2+} into the RING domain has demonstrated an essential role in the E3-ligase and autoubiquitination activity of MDM2.[37] Studies also show RING finger domain homodimerization to be necessary for MDM2 autoubiquitination.[43] It was therefore proposed that addition of Zn^{2+} to MDM2 would enhance dimerization and therefore promote the assembly of PSN-12.1.

Zn^{2+} was incorporated into the MDM2-mediated PSN-12.1 assembly assay using the same experimental conditions as applied to peptides 43, 44 and Rb1. A 50-fold molar

excess of Zn^{2+} was mixed with MDM2 for 30 minutes prior to addition into PSN-12.1 solutions. Temporal SERS analyses showed SERS enhancements for PSN-12.1 samples incorporating MDM2 with and without Zn^{2+}. A lesser increase in SERS was observed when MDM2 was pre-treated with Zn^{2+}, however a larger signal amplification was evident than with peptide Rb1. Peak height measurements at 1416 cm^{-1} recorded after PSN-assembly completion demonstrated signal increase of 1.7-fold, compared to 2.3-fold and 3.2-fold seen in the presence of peptide Rb1 and with MDM2 only respectively (figure 3.33 and 3.35). Extinction spectroscopy results demonstrated partial assembly of PSN 12.1 with and without Zn^{2+} (figure 3.35 c).

Figure 3.35 shows a mild inhibitory effect of Zn^{2+} on PSN assembly. Theory suggests that Zn^{2+} is essential for correct RING finger domain folding and hence dimerization. An increase in PSN assembly was therefore expected following Zn^{2+} addition. Zn^{2+} coordination and MDM2 dimerization are required for autoubiquitination so it could be theorised that enhanced dimerization resulted in allosteric changes in MDM2 conformation to favour intramolecular interactions. This would result in disruption of the MDM2-p53 interaction, however it would also contradict all previous work in this chapter. It is possible that MDM2 was already present in dimer formation at a sufficient concentration for maximum PSN assembly, or Zn^{2+} was already present in the reaction mix, therefore addition of excess Zn^{2+} would not have any effect on PSN-assembly. More experimentation is required before any conclusions can be drawn regarding the effect of Zn^{2+} on PSN assembly.
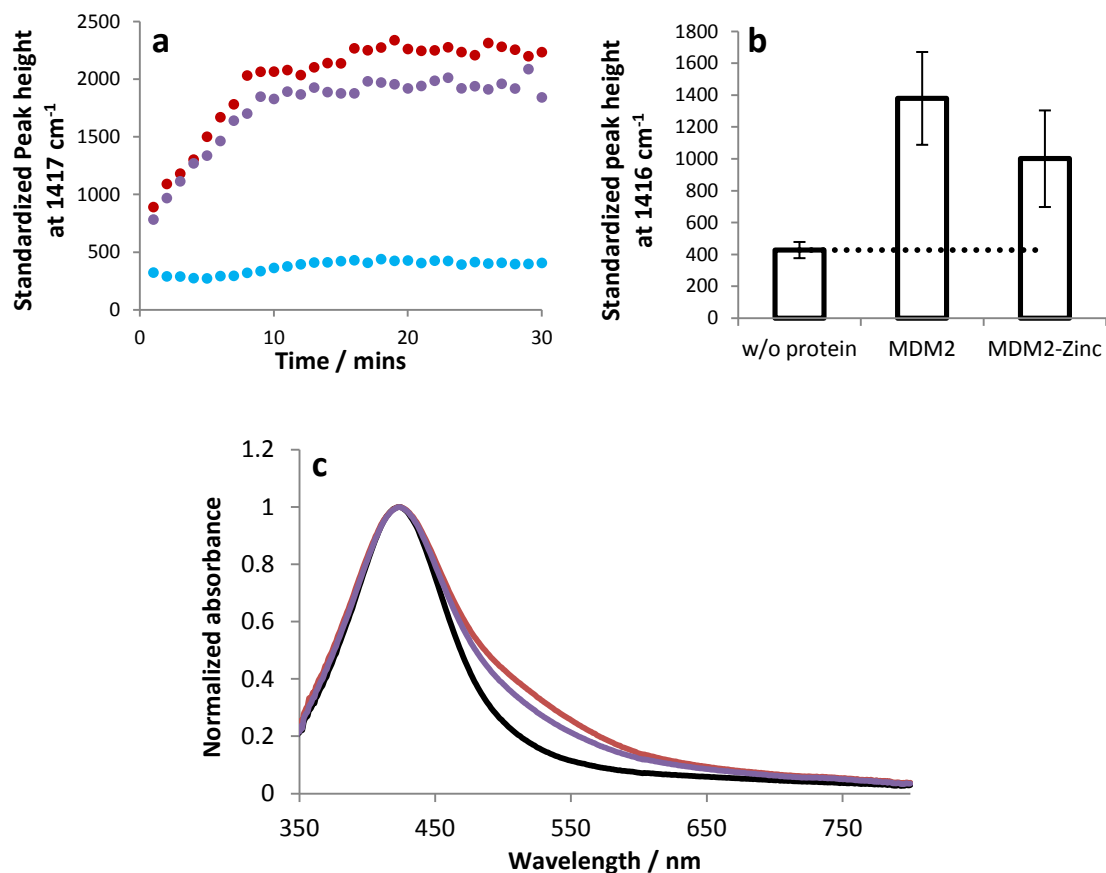
Figure 3.35 – a) Temporal SERS analysis of PSN assembly. Peak height at 1416 cm^{-1} monitored for 30 minutes following addition of MDM2 (red) and MDM2-Zinc (purple) to PSN-12.1 and MDM2 to PSN-12.1$_{W\Delta A}$ (light blue). A one second scan was acquired every 60 seconds using 100 % laser power and an excitation wavelength of 514.5 nm. b) Peak height measurements recorded for PSN-12.1 samples after completion of temporal analysis. All peak heights are standardized against cyclohexane. c) Normalized extinction spectra of PSN-12.1 without MDM2 (black) and following the addition of MDM2 (red) and MDM2-Zinc (purple).

3.6 – Pilot screen of potential chemotherapeutic compounds

This chapter has so far demonstrated MDM2-directed PSN assembly dependent on two simultaneous biological interactions. Inhibition of PSN assembly was also achieved through selective disruption of these specific biological interactions. The incorporation of alternate MDM2 binding ligands also illustrated the assay potential for investigating MDM2 allosteric activity. In section 3.5.3 the use of 96-well microtitre plates were introduced for higher throughput analysis of samples and a screening application for the MDM2 assay suggested. Owing to the successful detection of changes to PSN assembly with different binding ligands, a pilot screen of natural compounds was proposed.

3.6.1 – Initial screen of natural products

A total of unknown natural product mixtures, derived from plants, were acquired from the Strathclyde Institute of Pharmacy and Biomedical Sciences (SIPBS) to conduct a pilot screen to identify novel MDM2 binding partners. Experimental parameters used for the pilot screen were analogous to those used in inhibition experiments described earlier. A 15 pM concentration of PSN was employed with a 1000-fold excess of MDM2 as these conditions provided optimum MDM2-induced PSN aggregation (figures 3.15 - 3.20). Accurate molar concentrations for the natural products could not be ascertained due to the unknown molecular structure and mixture composition. MDM2 was therefore pre-incubated with a 50-fold molar excess of natural product based on a molecular weight estimate of 1000 g. This equated to a final concentration, in PSN solutions, of 7.5×10^{-4} mg / mL. MDM2 was incubated with natural products for 30 minutes prior to mixing with PSN-12.1. PSN-12.1 solutions were also analysed with natural products in the absence of MDM2 to check for non-specific aggregation akin to that observed in section 3.5.3. Samples were analysed in triplicate with standards of

PSN-12.1 and PSN-12.1$_{W\Delta A}$ with and without MDM2 on each 96-well plate. This allowed for a maximum of 14 natural products to be screened per experiment and a total of six 96-well plates were used to complete the screen. Each experiment was run over two days with SERS analysis through the bulk solution acquired on day 1. Triplicate samples were pooled following SERS interrogation and further SERS and extinction spectroscopy analysis of the pooled solutions were conducted on day 2. Once all 80 natural product mixtures had been screened, the results were examined and 14 mixtures were highlighted from which analysis yielded interesting results. The 14 selected natural product mixtures were re-analysed in an additional 96-well plate investigation. Figures 3.36 – 3.40 illustrate the results from analysis of the 14 selected natural product mixtures. Appendix C illustrates results obtained from the complete natural product screen.
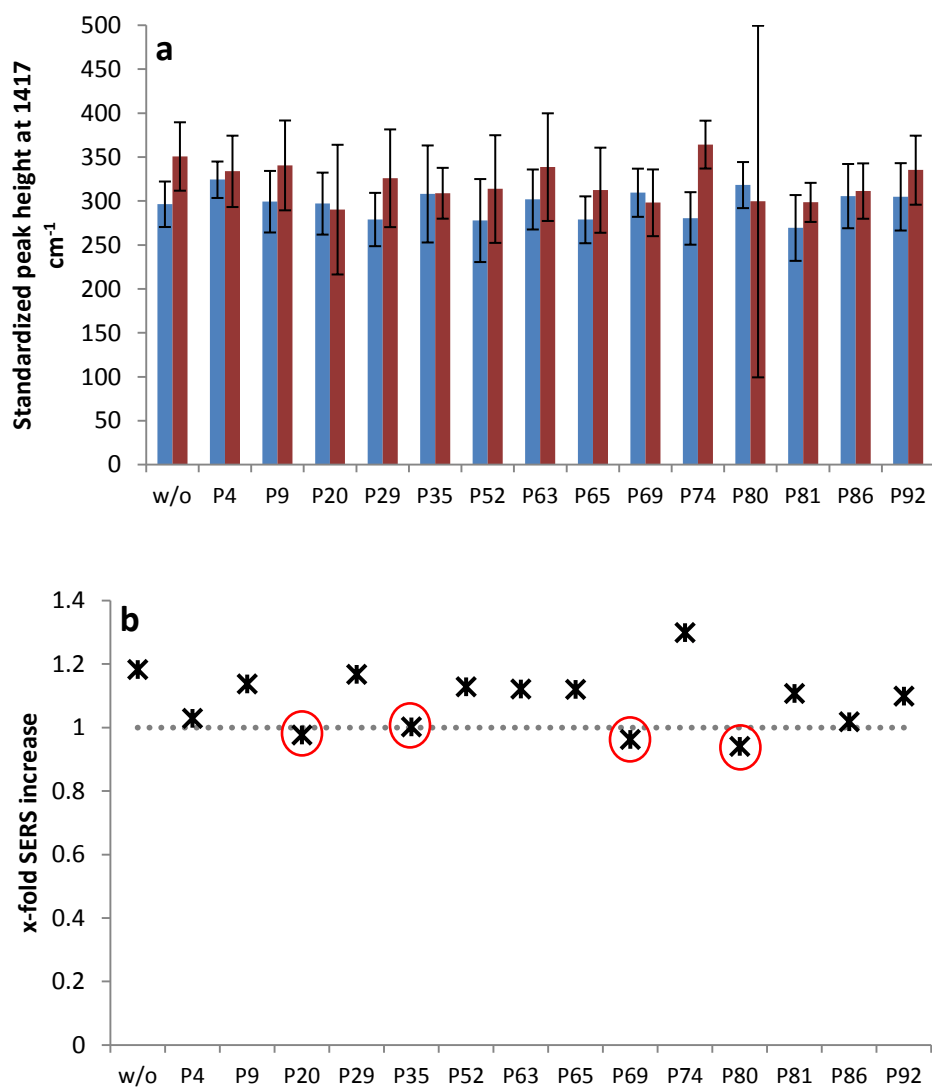
Figure 3.36 – Day 1 SERS analysis. a) Peak height measurements at 1417 cm^{-1} recorded in SERS analysis of PSN-12.1 samples with natural products in the absence (blue) and presence (red) of MDM2. Five replicate scans with, one second time duration, acquired for each sample replicate using 100 % laser power and an excitation wavelength of 514.5 nm. Error bars indicate the standard deviation in peak heights standardized against cyclohexane. b) Calculated x-fold increase in SERS for PSN-12.1 with natural product and MDM2 compared to samples with natural product only. Grey dotted line represents the SERS response for PSN-12.1 without MDM2 or natural product. Red circles indicate natural products taken forward for further analysis.

Figure 3.37 – Day 2 SERS analysis. a) Peak height measurements at 1416 cm^{-1} recorded in SERS analysis of PSN-12.1 samples with natural products in the absence (blue) and presence (red) of MDM2. Five replicate scans with, one second time duration, acquired for each sample using 100 % laser power and an excitation wavelength of 514.5 nm. Error bars indicate the standard deviation in peak heights standardized against cyclohexane. b) Calculated x-fold increase in SERS for PSN-12.1 with natural product and MDM2 compared to samples with natural product only. Grey dotted line represents the SERS response for PSN-12.1 without MDM2 or natural product. Red circles indicate natural products taken forward for further analysis.

Figure 3.38 – Normalized extinction spectra of PSN-12.1 with a) natural product and b) MDM2 and natural product. PSN-12.1 samples before (black solid line) and after (black dashed) addition of MDM2 are added for reference purposes.
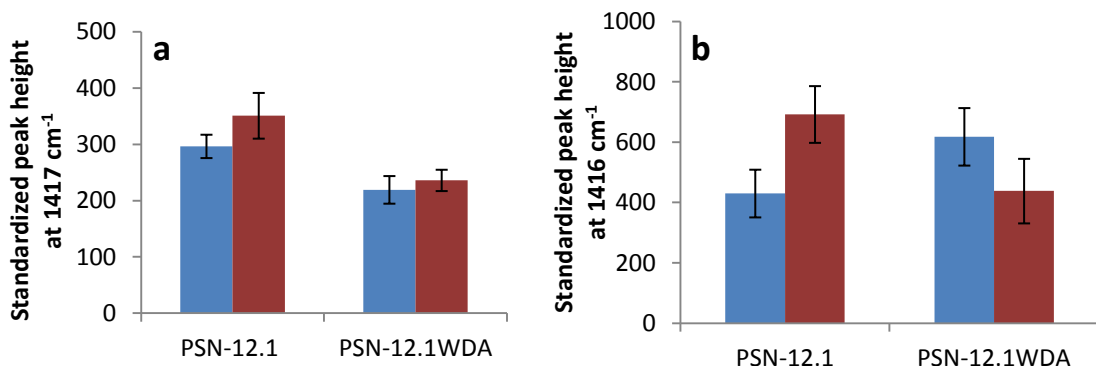
	Day 1	Day 2
PSN-12.1	1.183304	1.609172
PSN-12.1$_{W\Delta A}$	1.076637	0.708923

Figure 3.39 – a) Peak height measurements at 1416 cm^{-1} recorded in SERS analysis of PSN-12.1 and PSN-12.1$_{W\Delta A}$ in the absence (blue) and presence (red) of MDM2 on a) day one and b) day two. Five replicate scans with, one second time duration, acquired for each sample using 100 % laser power and an excitation wavelength of 514.5 nm. Error bars indicate the standard deviation in peak heights standardized against cyclohexane. Table shows the calculated x-fold increase in SERS for PSN samples with MDM2 on both days.
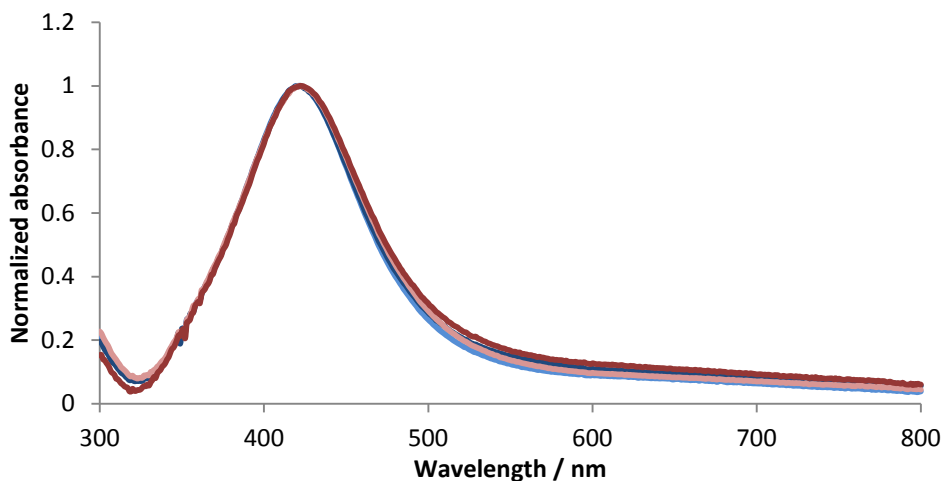
Figure 3.40 – Normalised extinction spectra of PSN-12.1 (red) and PSN-12.1$_{W\Delta A}$ (blue) with (dark shade) and without (light shade) MDM2.

Figures 3.36 and 3.37 illustrate peak height data obtained in SERS analysis on day one and day two respectively. Extinction spectroscopy measurements recorded on day two are shown in figure 3.38. Spectra have been normalized for ease of comparison. Standard samples, PSN-12.1 and PSN-12.1$_{W\Delta A}$ with and without MDM2 were also analysed and figures 3.39 and 3.40 demonstrate the SERS and extinction spectroscopy results attained.

SERS interrogation conducted on day one highlighted four samples in which a negative change in intensity was observed (figure 3.36). These four samples, P20, P35, P69 and P80, were selected from the initial screen of 80 natural product mixtures owing to a reduced amplification in SERS response compared with other solutions. Results from both sets of analysis therefore show consistency indicating that these four natural products may have an inhibitory effect on PSN assembly. Samples containing natural products P20, P35, P69 and P80 do not exhibit the lowest SERS intensity increase in day two analysis, however the intensification in SERS was lesser than that observed in standard samples of PSN-12.1 with MDM2 (figure 3.37). The SERS response for standard samples, PSN-12.1 with MDM2, was relatively low compared to previous experimentation with an 1.18-fold and 1.61-fold increases seen on day one and day two respectively. These small changes in SERS intensity indicate a minimal extent of PSN assembly which is confirmed by extinction spectroscopy analysis. PSN samples with P20, P35, P69 and P80 demonstrate less assembly than PSN-12.1 with MDM2 in extinction spectroscopy (figures 3.41), however this conclusion is speculative as sample discrimination is negligible.
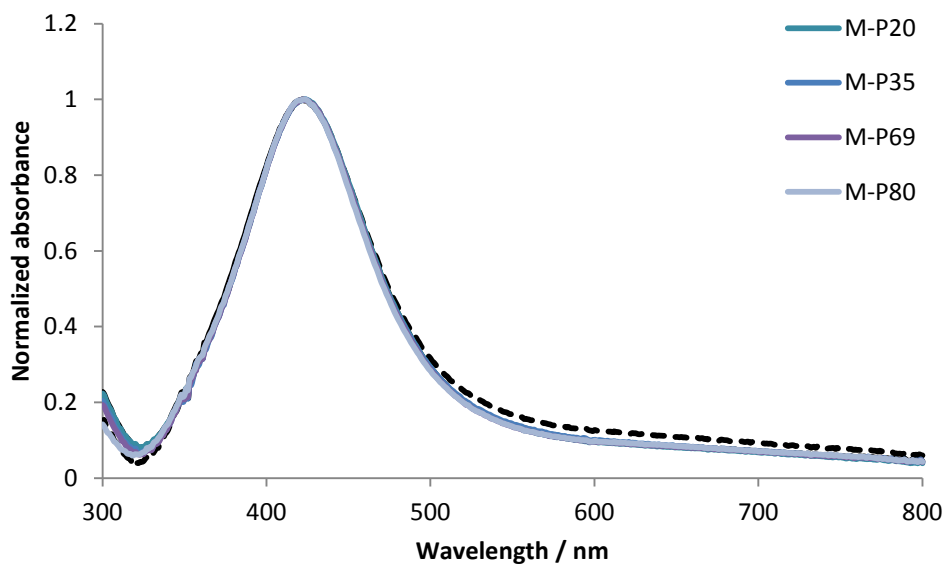
Figure 3.41 – Normalized extinction spectra of PSN-12.1 with MDM2 and natural products. PSN-12.1 samples before (black solid line) and after (black dashed) addition of MDM2 are added for reference purposes.

3.6.2 – Temporal analysis of selected natural products

A pilot screen of natural products has been completed, using the MDM2 assay described in figure 3.22, to identify novel MDM2 binding ligands that elicit either positive or negative effects on PSN assembly. Four natural product mixtures were selected from the initial 80 that demonstrated possible inhibitory effects on PSN assembly (figures 3.36 and 3.37). Temporal SERS analysis was carried out on these natural product samples, P20, P35, P69 and P80, to ascertain whether or not prevention of PSN assembly was caused (figure 3.42). Table 3.2 shows the origin of these natural product mixtures.

	Species	Family	Plant part	Origin
20	Cosmibuena valerii	Rubiaceae	leaf	Costa Rica
35	Opilia amentacea	Opiliaceae	leaf	Papua New Guinea
69	Tibouchina inopinata	Melastomaceae	wood / bark	Costa Rica
80	Povedaphne quadriporata	Lauraceae	leaf	Costa Rica

Table 3.2 – Table illustrating the plant origins of the four selected natural product mixtures.

MDM2 was pre-incubated with a 50-fold excess of natural products, calculated based on a natural product molecular weight estimation of 1000 g, for 30 minutes. MDM2 and natural product mixtures were mixed with PSN-12.1 immediately before analysis. Temporal SERS interrogation was carried out over a 30 minute time duration and further SERS examination of PSN solutions was conducted following PSN-assembly completion. PSN-12.1 samples demonstrated an increased SERS response following the addition of MDM2 which was evident to a much lesser extent for PSN-12.1$_{W\Delta A}$ control solutions with MDM2. The discrimination between SERS measurements of PSN-12.1 and PSN-12.1$_{W\Delta A}$ with MDM2 demonstrates the biological specificity of PSN assembly as earlier ascertained in section 3.4.3. Addition of natural products, P20, P35, P69 and P80, to PSN-12.1 resulted in a reduction in SERS intensity inferring the PSN assembly was prohibited (figure 3.42). The inhibitory effect of these natural products on PSN assembly was confirmed by extinction spectroscopy (figures 3.41 and 3.42). A broadening in the plasmon absorbance band for PSN-12.1 samples with MDM2 is indicative of partial aggregation. Exclusive of PSN-12.1 with MDM2, no PSN samples demonstrated any assembly with MDM2 in extinction spectroscopy (figures 3.41 and 3.42). These data demonstrate PSN assembly inhibition with four 'hits' of natural product mixtures identified through the MDM2 assay pilot screen. Further

experimentation and concentration studies are required to characterise MDM2 binding with the natural products and PSN assembly inhibition.
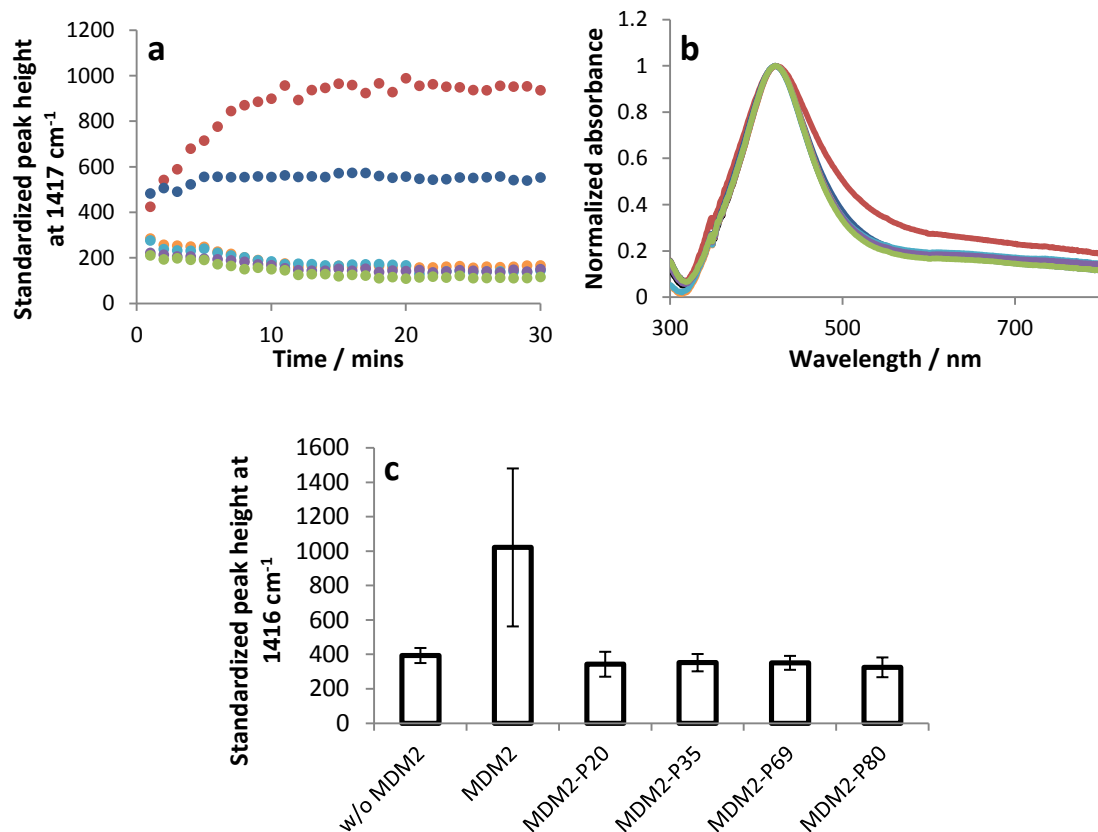
Figure 3.42 – a) Temporal SERS analysis of PSN assembly. Peak height at 1416 cm^{-1} monitored for 30 minutes following addition of MDM2 (red), MDM2-P20 (orange), MDM2-P35 (light blue), MDM2-P69 (purple) and MDM2-P80 (green) to PSN-12.1 and MDM2 to PSN-12.1$_{W\Delta A}$ (dark blue). A one second scan was acquired every 60 seconds using 100 % laser power and an excitation wavelength of 514.5 nm. b) Normalized extinction spectra of PSN samples including PSN-12.1 without MDM2 (black). c) Peak height measurements recorded for PSN-12.1 samples after completion of temporal analysis. All peak heights are standardized against cyclohexane.

3.6.3 – Characterising natural product inhibition of PSN assembly

Four natural product 'hits' have been identified (table 3.2), from an MDM2 assay pilot screen, that were seen to inhibit PSN assembly. Section 3.4.3 describes the selective inhibition of PSN assembly through disrupting specific biological interactions with known binding ligands. In such cases the molecular basis for prevention of PSN assembly is understood. The natural products identified through MDM2 assay screening represent novel MDM2 binding partners. The MDM2 sites with which these natural products interact is unknown. Consequently the binding events disrupted by these natural products PSN assembly inhibition cannot be deduced. Figure 3.43 illustrates the potential solution constituents following inhibition of PSN assembly with MDM2 hydrophobic pocket binding ligands and RING domain peptides. The development of further characterisation experimentation is required to distinguish which binding event, MDM2 dimerization or MDM2-p53, is disrupted by analysing the resultant solution constituents.

SEM analysis was employed as a technique for identifying which interactions were inhibited in PSN assembly inhibition by natural product mixtures P20, P35, P69 and P80. If SEM, as an analytical technique, can detect the presence of protein on NP surfaces this presents a valid methodology for distinguishing the solution constituents illustrated in figure 3.43. To test this theory, PSN-12.1 samples from experimentation described in section 3.6.2 were analysed using SEM. SEM analysis of PSN suspensions was carried out on PDDA coated silicon wafers as detailed in section 3.4.3.4 to prevent surface associated aggregation and results are illustrated in figures 3.44 - 3.45 and appendix B(ii).

a

Hydrophobic pocket   Acidic domain   RING domain

b

MDM2-p53 inhibition (i)	MDM2 dimer disruption (ii)
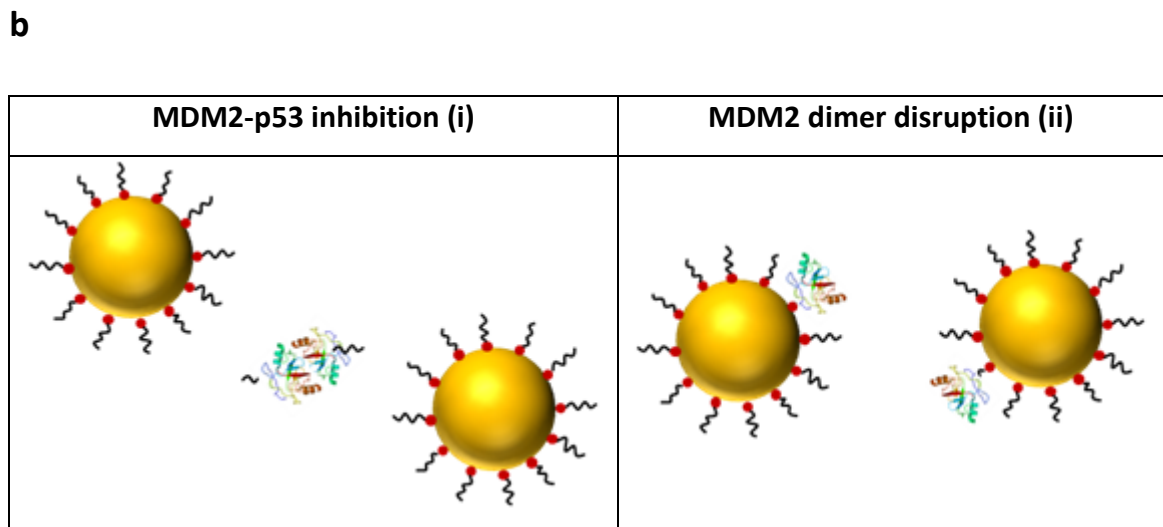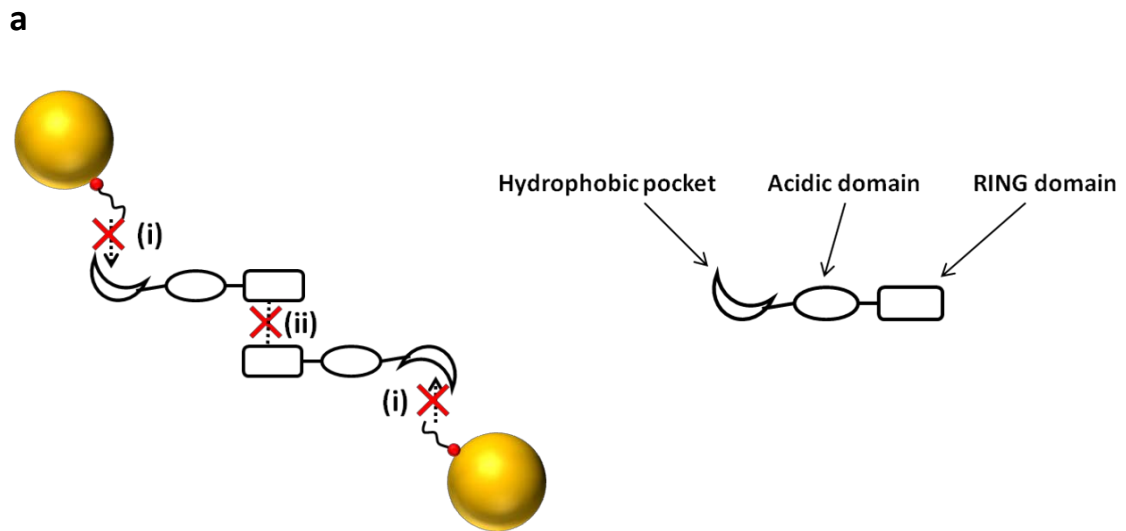
Figure 3.43 – a) Schematic illustrating the MDM2 interactions disrupted in PSN assembly inhibition. B) PSN and MDM2 solution constituents following inhibition of PSN assembly through inhibition of MDM2 binding to PSN-12.1 (i) and disruption of MDM2 dimer formation (ii).
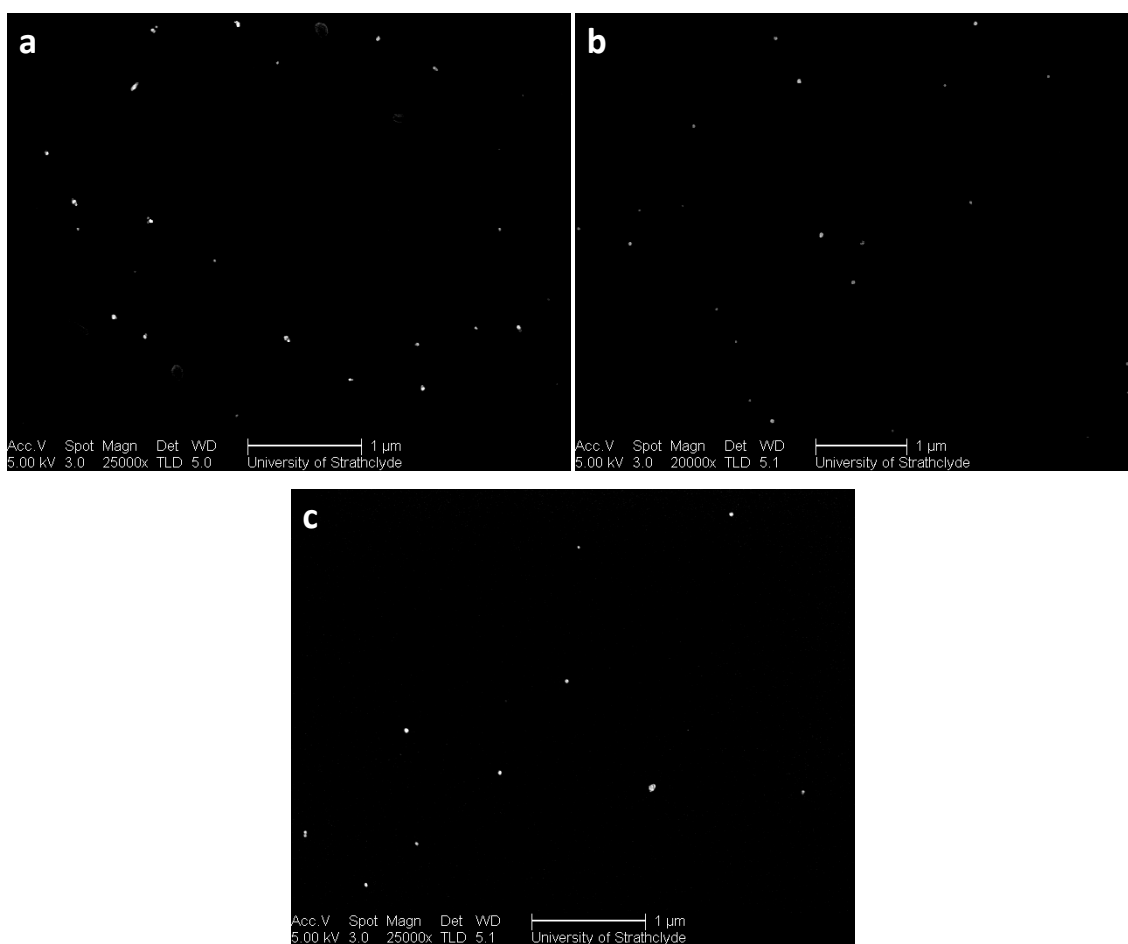
Figure 3.44 - SEM images of a) PSN-12.1, b) PSN-12.1 with MDM2-P35 and c) PSN-12.1 with MDM2-P80 at 20000-25000x magnification. Scale bars represent 1 micron.

SEM imaging of PSN-12.1 samples in the absence of MDM2 and with MDM2 and natural products, P35 and P80, demonstrated monodispersed distributions of PSN (figure 3.44). This correlates with previously illustrated SERS and extinction spectroscopy data. Figure 3.44 shows a representative of PSN solutions relative to a one micron scale. Partial aggregation of samples containing PSN-12.1 with MDM2 was obtained in previous analysis, however few PSN were evident in SEM analysis, hence no corresponding image is included (figure 3.44). PSN-12.1 solutions with MDM2 exhibited sparse PSN clusters that could be observed when employing a higher magnification in SEM analysis (figure 3.45).
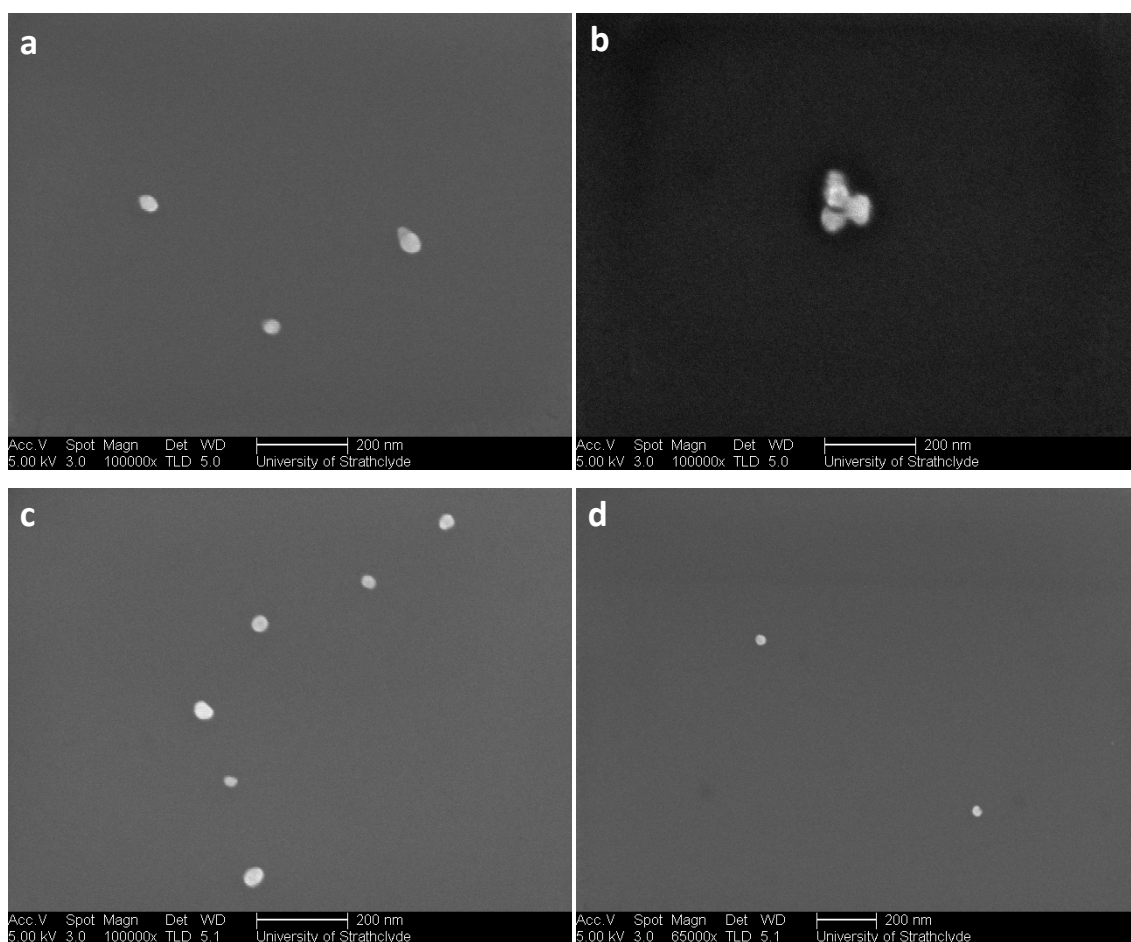
Figure 3.45 - SEM images of a) PSN-12.1, b) PSN-12.1 with MDM2, c) PSN-12.1 with MDM2-P35 and d) PSN-12.1 with MDM2-P80 at 100000x magnification. Scale bars represent 200 nm.

Monodispersed PSN observed in PSN-12.1 samples without MDM2 and with MDM2 and natural products are indistinguishable from one another at both high and low magnification in SEM imaging (figures 3.44 and 3.45). These data suggest a similar composition for these three samples. A sample representative PSN cluster observed in SEM analysis of PSN-12.1 samples with MDM2 is shown in figure 3.45 b. Difficulty was encountered in focussing on PSN clusters in these samples indicating a coating on PSN which may have shielded charge from the NP surface. An explanation for this could the presence of MDM2 on PSN-12.1, however PSN-12.1 aggregation with MDM2 has been

previously detected using SEM imaging in section 3.4.3.4. It is possible that an MDM2 elution fraction of different purity was used for this experimentation thus resulting in higher biomolecule concentration than was previously observed. Variation in PSN-12.1 assembly resulting from different elution fractions was previously mentioned in section 3.5.3.

Coating of PSN-12.1 with MDM2, shown in figure 3.45 b, lends to the speculation that other samples did not exhibit any bound protein. This would suggest that PSN assembly inhibition by natural products in mixtures P35 and P80 occurred through the disruption of MDM2 hydrophobic pocket interactions with PSN-12.1. Extinction spectroscopy analysis of the same samples shows no red-shift in the plasmon absorbance band at λ-max and therefore complements this speculation (figure 3.42). These data give an indication of the molecular basis for natural product PSN assembly inhibition but no conclusions can be made with any confidence without further investigation.

3.7 – Conclusions

A NP-based assay has been developed to investigate the allostery of full-length MDM2 in solution, detectable using SERS. PSN, prepared with a BT Raman tag and a p53 peptide mimic, were aggregated following addition of MDM2. MDM2-mediated PSN assembly proceeded in a concentration dependent manner and biological specificity of the PSN assembly was demonstrated using PSN-12.1$_{W\Delta A}$ as a negative control. MDM2-directed PSN assembly was illustrated using extinction spectroscopy, SERS, DLS and SEM, of which SERS was found to be the most sensitive analytical technique. Temporal analysis of PSN assembly, in samples under continuous rotation, demonstrated a linear increase in SERS response. This shows the potential of SERS analysis for determination experiments. The SERS signal was seen to plateau within ten minutes of MDM2 addition indicating completion of PSN assembly. The described PSN assembly occurred as a result of MDM2 RING finger domain dimerization and hydrophobic pocket binding to PSN-12.1. Selective disruption of each of these binding interactions through the introduction of MDM2 binding ligands resulted in inhibition of MDM2-induced PSN assembly. This was shown to be a concentration dependent response with almost complete PSN assembly inhibition achieved via pre-incubation of MDM2 with a 50-fold excess of inhibitor peptide 12.1. Reduced PSN assembly was also observed as a result of allosteric interactions induced through addition of peptide Rb1, which interacts with the central acidic domain on MDM2. Addition of Zn^{2+} also caused a marginal reduction in PSN assembly, contradictory to the theory that zinc coordination would enhance MDM2 dimerization and consequently PSN assembly. Further studies are necessary to fully understand the effects of peptide Rb1 and Zn^{2+} on MDM2 allostery.

Owing to the ability of MDM2 N-terminal and C-terminal domain binding ligands to disrupt PSN assembly, a small pilot screen of 80 natural product mixtures was conducted to test for novel MDM2 binding partners. In order to increase sample throughput for screening purposes, assay samples were transferred to 96-well

microtitre plates and end-point analysis conducted. Extinction spectroscopy and SERS analysis were used to analyse PSN pilot screen samples. Out of the 80 natural product mixures, four 'hits' were identified that demonstrated inhibition of PSN assembly. Extinction spectroscopy and SEM imaging analysis of PSN samples suggests the cause of inhibition to be disruption of the MDM2-p53, however this can only be speculated.

3.8 – Future work

The MDM2 assay described in this chapter has identified four 'hits', from a screen of 80 natural products, that may be novel MDM2 binding ligands. Further experimentation is required to characterise MDM2 interactions with these natural products and test their potential as chemotherapeutic compounds.

MDM2-mediated PSN assembly was observed dependent on MDM2 concentration and inhibition of this assembly was also shown to be dependent on inhibitor concentration. The effect of concentration on PSN assembly inhibition shows potential for binding affinity studies using the MDM2 assay. Nutlin-3 disrupts the MDM2-p53 interaction with a known IC_{50} of 0.09 μM and has been shown in this chapter to inhibit PSN assembly. PSN inhibition concentration studies with Nutlin-3 and other binding ligands with known IC_{50} values could produce reference calibrations. This would allow for binding affinity studies of novel MDM2 ligands using this approach.

Thus far, peptide Rb1 and Zn^{2+} have been incorporated to investigate the allosteric activity of MDM2. Rb1 interacts with the central acidic domain and Zn^{2+} is coordinated into the RING finger domain of MDM2. Peptide Rb1 caused a reduction in PSN assembly, presumably through an allosteric effect on peptide 12.1 binding to the MDM2 hydrophobic pocket. This requires more investigation but the results obtained give insight into pRb tumour suppressor activity. Future investigations with alternative acidic domain binding ligands could provide interesting information about MDM2 allostery. Zn^{2+} demonstrated a marginal reduction in PSN assembly, contradictory to theory. To investigate this further, pre-incubation of MDM2 with a metal chelator would remove any Zn^{2+} coordinated into the RING finger domain. A comparison of PSN assembly with MDM2 in combination with zinc and a metal chelator would provide a more in depth study of the effect of Zn^{2+} coordination on MDM2 dimerization and subsequent PSN assembly.

Finally, the developed PSN assembly assay has been developed to investigate full-length MDM2, however the methodology could be transferred to alternative protein systems. PSN design is such that the functionality can be changed by conjugating a different peptide to the BT Raman tag prior to NP immobilization. BT-peptide conjugation was achieved using a standard amide coupling procedure. This assay system also has scope for multiplexing different binding ligands for one protein by varying the Raman tag employed.

Chapter 4 – Controlled NP assembly via coiled-coil peptide interactions

4.1 – Introduction

As described in chapter 3 MDM2-induced PSN assembly, has been achieved through specific protein-peptide interactions. This methodology has shown huge potential for interrogating the activity of proteins in their native forms. This chapter focuses on the controlled assembly of PGN and PSN via specific peptide-peptide interactions.

PNP have become increasingly used for numerous applications, as outlined in section 1.2. The biocompatability, structural diversity and specificity of peptides renders them ideal vectors in drug delivery and cellular imaging, while their self assembly properties are harnessed in the understanding of complex biological systems and development of advanced functional materials.

Coiled coil peptide conformations account for up to 10 % of translated protein and are involved in a diverse range of complex cellular functions (section 1.1.3). Towards the development of bionanomaterials, the work in this chapter describes PNP assembly directed by the formation of a heterodimeric coiled coil peptide. This is a relatively novel field of study with the first study published as recently as 2003.[216] Here, extinction spectroscopy and SERS are employed to monitor coiled coil mediated PNP assembly over a pH range (pH 3 – pH 11). Competitive inhibition of the assembly process with inhibitor peptides is also investigated.

4.1.1 – Coiled coil induced PGN assembly

The first assembly study of NP conjugated to coiled coil forming peptides illustrated a 'belt and braces' system.[216] An anionic 'belt' peptide formed heterodimeric coiled coils with two cationic 'brace' peptides immobilized on AuNPs, hence resulting in NP aggregation detectable by optical spectroscopy (figure 4.1 a).[216] Assembly of peptide functionalised AuNP has since been demonstrated through metal induced homodimer coiled coil stabilization and helix-turn-helix heterodimerization resulting in peptide bridging.[217, 218] In the former NP immobilized metal binding helical peptides formed coiled coils in the presence of zinc.[217] In the latter, helix-turn-helix peptides, dimerized through disulphide linkages between the turns, were shown to heteroassociate with NP-bound peptides.[218] In both cases the assembly process was reversible either by EDTA zinc chelation or disulphide reduction.[217, 218] Coiled coil heterodimer formation has also been used to assemble AuNPs modified with different coiled coil forming peptides without induction by additional molecules or peptides.[219, 220] AuNPs were modified with coiled coil peptides containing either lysine or glutamic acid at positions e and g in the α-helix.[219, 220] Association of differentially functionalized AuNPs was demonstrated in mixed solutions via heterodimer coiled coil formation (figure 4.1 b).[219, 220]

Recent reports have illustrated pH controlled assembly of anionic and cationic AuNP through the formation of homodimeric coiled coils displaying positively and negatively charged peripheral residues respectively (figure 4.1 c).[221, 222] In such cases the coiled coil presents as a molecule of opposing charge to the NP surface and therefore electrostatic charge mediated assembly proceeds.[221, 222] A number of studies also demonstrate coiled coil interactions of peptides conjugated directly onto metallic nanomaterials. This approach is being investigated for biosensor development, of which an example is the detection of redox proteins linked to carbon nanotubes via metal binding coiled coils.[223]
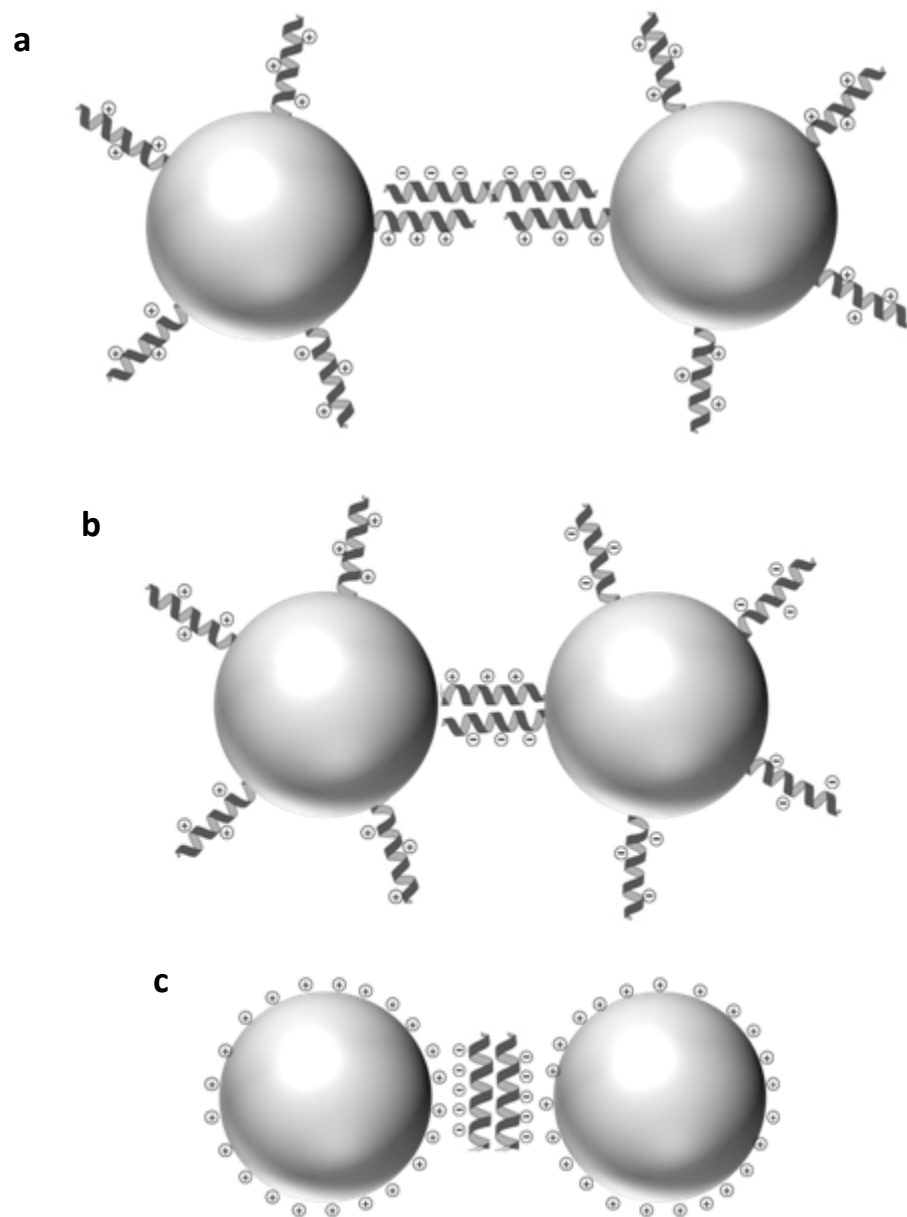
Figure 4.1 – Schematic illustrations of NP assembly based on heterodimerization via a) a 'belt and braces' approach[216] and b) differently modified NPs.[219, 220] c) electrostatic NP association with coiled coil peptides.[221]

4.1.2 – Proposed PNP assembly directed by coiled coil heterodimerization

As described in section 4.1.1, PGN assembly has been achieved via heterodimer coiled coil associations.[219, 220] Changing NP distributions, controlled by pH and near infra-red irradiation, were monitored primarily by extinction spectroscopy and transmission electron microscopy.[219, 220] In this work heterodimerization-induced PNP assembly, analogous to previous studies, on both gold and silver NPs was interrogated using SERS.
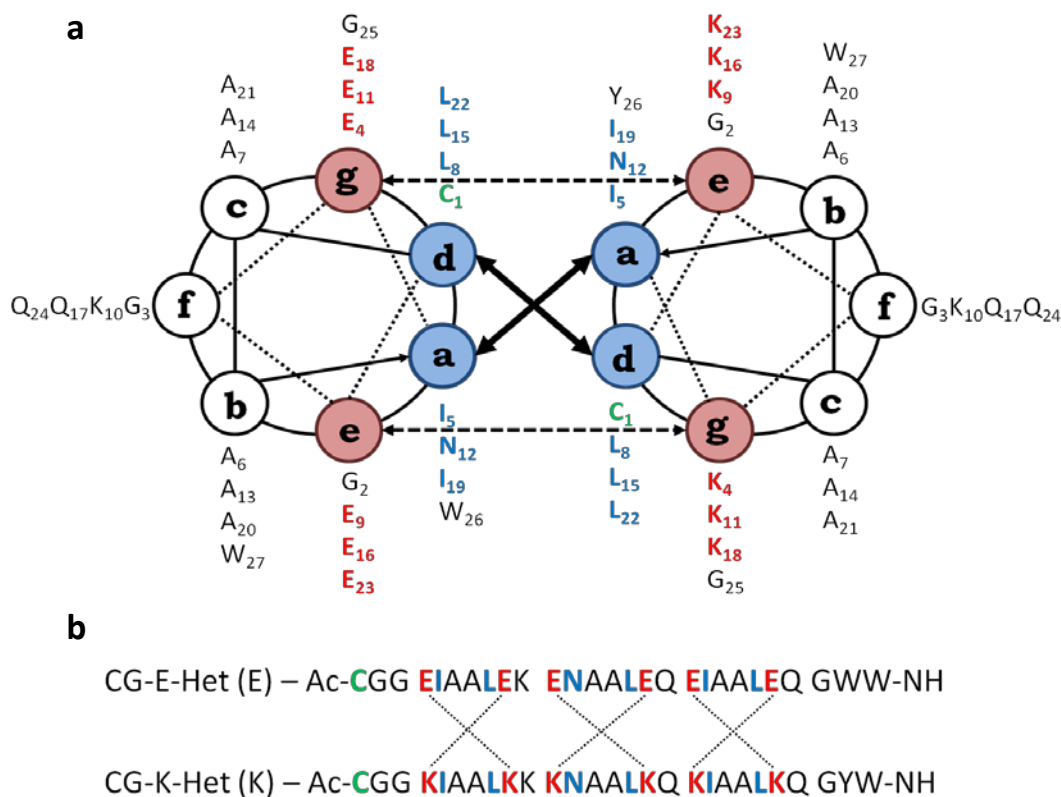
Figure 4.2 – a) Designed peptides GC-E-Het and GC-K-Het shown on a 3.5 residue-per-turn helical wheel. b) Electrostatic interactions are indicated (dotted lines) between the peptides within a parallel dimeric coiled coil. Residues involved in NP binding (green), hydrophobic packing (blue) and electrostatic interactions (red) are highlighted.

Two peptides, CG-E-Het (E) and CG-K-Het (K), were designed based on the same principles used to create the anionic and cationic peptides employed in the 'belt and braces' linker system described by Rydanov *et al.* (figure 4.2).[216] The proposed heterodimer coiled coil comprises of three heptad repeats, shown to be the minimum length required for stable coiled coil formation from autonomous peptide folding.[224] Hydrophobic residues isoleucine and leucine were placed at positions a and d to favour a dimer coiled coil conformation.[85] Asparagine was included in place of isoleucine at a in the middle heptad to add specificity, via hydrogen bonding, and further promote parallel peptide orientation.[73] In the antiparallel orientation asparagine residues will pack against non-polar sidechains causing helix destabilization.[73] Heterodimerization is directed by the positioning of glutamic acid and lysine at e and g in peptides E and K respectively and peptides are prepared with an N-terminal cysteine for nanoparticle immobilization. Owing to high helical propensity, alanine is situated at b and c within heptad repeats and two of the three f positions are filled with glutamine to disfavour potential lateral interactions between coiled coils.[99] Finally, aromatic residues are included at the peptide C-termini to provide an inbuilt chromophore.[216]

Figure 4.3 illustrates the proposed assembly of either PGN or PSN. Conjugates prepared with peptides E and K are given the denomination PGN/PSN-E and PGN/PSN-K respectively. Schematics are shown for NP assembly via parallel and antiparallel coiled coil formation in more detail (figure 4.3 a). Peptide design favours the parallel orientation, however there is more steric hindrance for this conformation with NP immobilized peptides compared to the antiparallel orientation. Coiled coil helix orientation in NP assembly will thus depend on whether peptide design or steric hindrance is the dominating force.
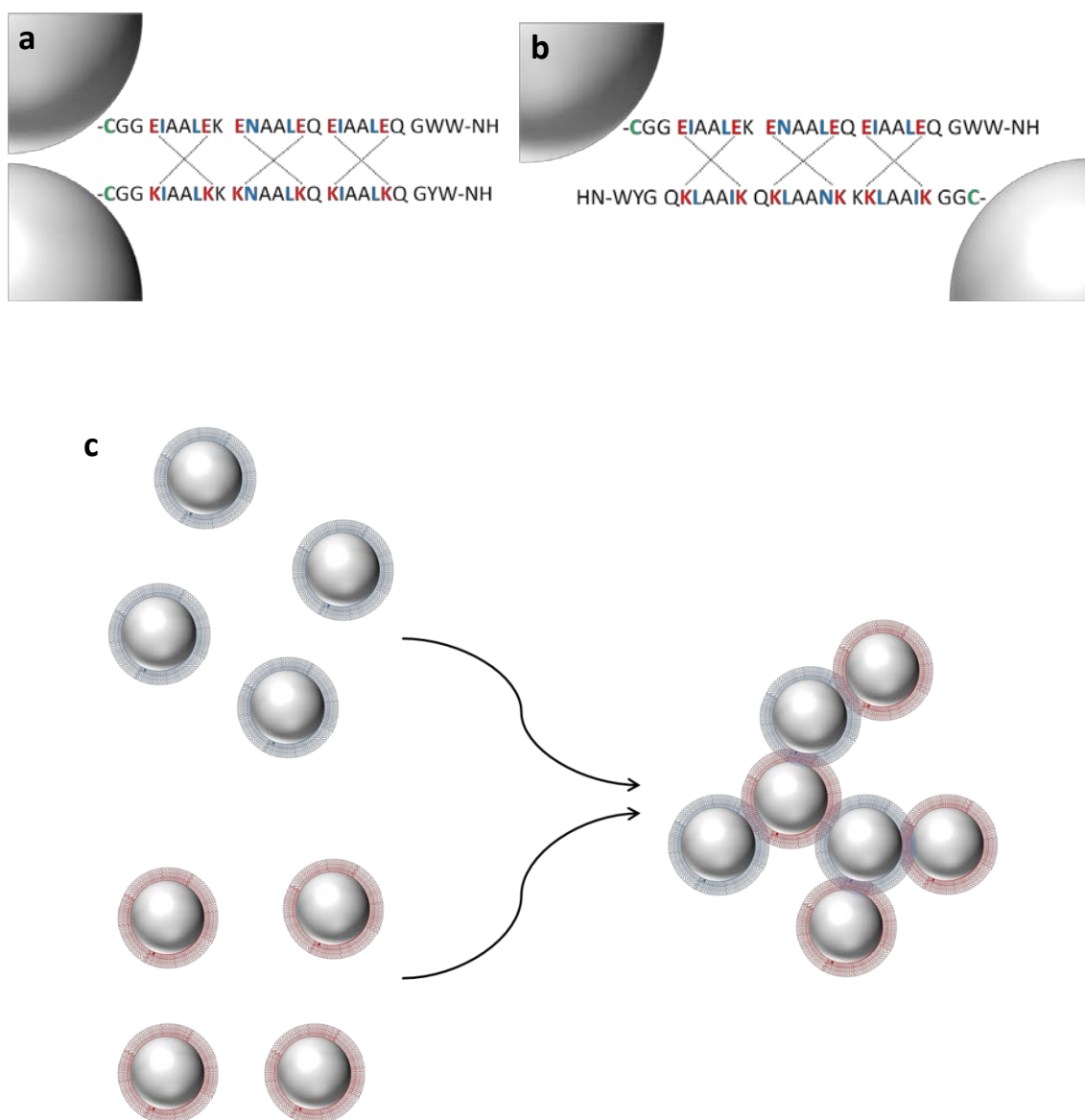
Figure 4.3 – a) parallel and b) antiparallel coiled coil orientations of peptides immobilized on NPs. Dotted lines indicate electrostatic interactions and residues involved in hydrophobic packing (blue), electrostatic interactions (red) and NP binding (green) are highlighted. c) Proposed NP assembly based on coiled coil formation between anionic (blue) and cationic (red) peptides.

4.2 – PGN preparation

In order to investigate controlled NP assembly, described in section 4.1.2, stable PNPs must first be achieved with both E and K peptides. Peptide conjugation was initially investigated to yield PGN in line with previous coiled coil peptide studies.[216-222]

PGN-E were achieved by adding the anionic coiled coil forming peptide to NP solutions via thiol attachment. The overall negative charge on the peptide meant that electrostatic repulsion of negatively charged NPs was maintained and thus PGN-E were stably dispersed in solution. PGN-K were more problematic than PGN-E to prepare as negatively charged NPs had the tendency to aggregate in the presence of the cationic coiled coil forming peptide, K. Various NPs conjugation protocols were tested before stable PGN-K were achieved, some of which are described here.

4.2.1 – 'Belt and Braces' procedure for AuNP-peptide conjugation

As previously mentioned, the peptides used in this study are derivatives of those used in the 'belt and braces' system for AuNP assembly.[216] In this paper an anionic 'belt' peptide was used to assemble AuNPs functionalized with positively charged 'brace' peptides.[216] The conjugation protocol outlined in this paper, adding a 73000 x molar excess of peptide directly to AuNP in H_2O, was therefore investigated for PGN-E and PGN-K preparation.

AuNP conjugation was unsuccessful with both E and K peptides, shown by the depletion in plasmon absorbance in extinction spectroscopy indicative of nanoparticle aggregation (figure 4.4). PGN-E were achieved subsequently by increasing AuNP concentration and decreasing the peptide molar excess, however PGN-K could not be prepared successfully in this way.
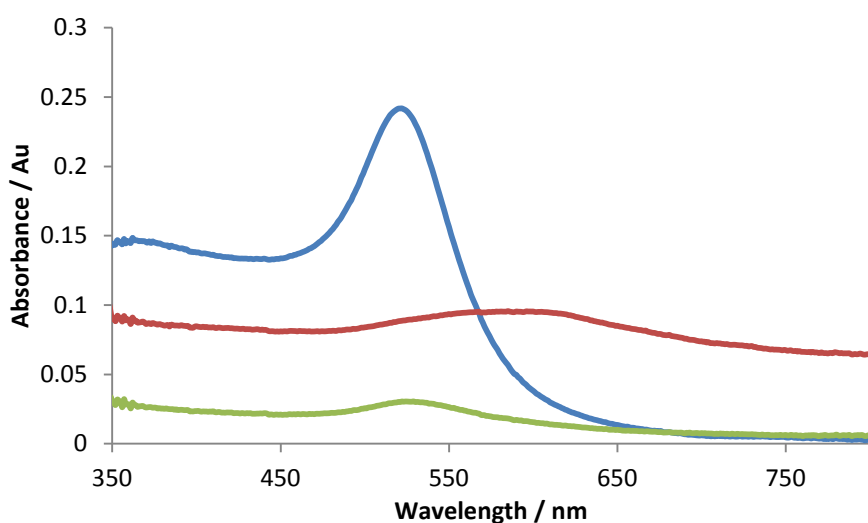
Figure 4.4 – Absorbance profile of AuNP (blue), PGN-E (red) and PGN-K (green) in H_2O.

4.2.2 – Tween stabilization

Tween20 is a surfactant, composed of branched polyethylene glycol units, commonly applied in biology. It has also been employed in nanotechnology to enhance nanoparticle solution stability during the modification process.[225] Tween20 attaches to the NP surface via physisorption and is subsequently displaced when molecules are immobilized through chemisorption.[225] Pre-functionalization of AuNP prior to the addition of peptide molecules (1000 fold excess of peptide to NP) was therefore investigated to acquire stable PGN. Using this methodology PGN-E were created, as illustrated by a red shift of 7 nm in the plasmon absorbance λ-max in extinction spectroscopy (figure 4.5). A broadening in the plasmon absorbance for PGN-E also indicated a loss in conjugate stability and increased variation in particle size distribution. PGN-K samples aggregated, as was seen for the previous methodology, therefore Tween20 was unable to maintain nanoparticle stability in this instance.
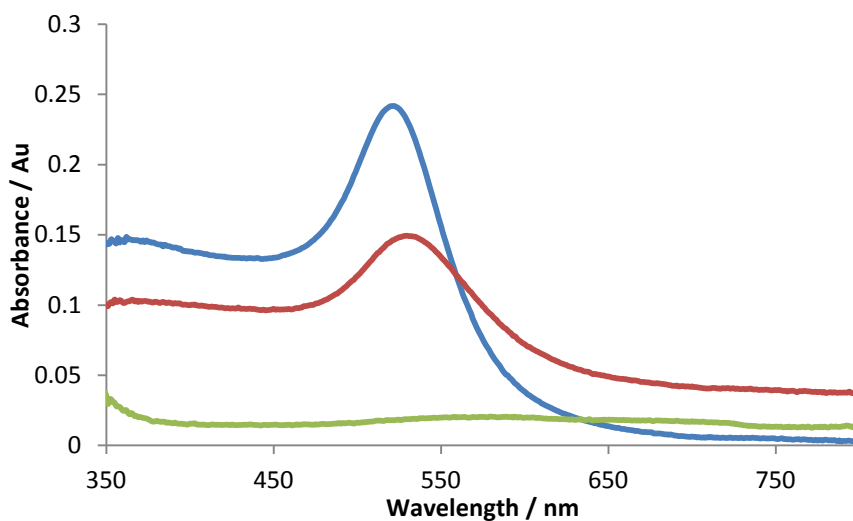
Figure 4.5 – Absorbance profile of AuNP (blue), PGN-E (red) and PGN-K (green) in H_2O.

4.2.3 – PEG-OH

Stable PGN were not achieved through pre-functionalization of AuNP with Tween20, however in-house experimentation has highlighted the potential of smaller PEG-based molecules in mixed monolayer formation to enhance stability. For this purpose PEG-OH (figure 4.6) was employed to pack between peptide molecules on the NP surface.
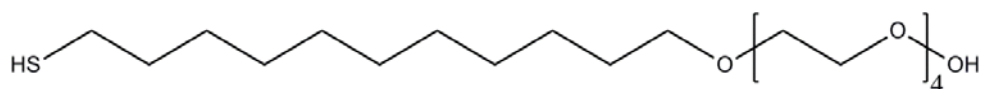
Figure 4.6 – Molecular structure of PEG-OH

Peptides were pre-mixed with PEG-OH at a various concentrations ranging from 1-20 % of the total molecular composition. Molecular mixtures of peptide and PEH-OH were then added to AuNP at a 20000 fold molar excess. Stable PGN-E and PGN-K were achieved with molecular mixtures of 1-5 % peptide, with a red shift in λ-max of 5 nm demonstrating molecule conjugation to the NP surface. No further red shift or broadening in the plasmon absorbance peak was observed in heterogeneous solutions of PGN-E / PGN-K (figure 4.7 a-b) indicating monodispersed solutions rather than the NP assembly proposed in section 4.1.2. These results signify that there is either insufficient peptide present on the NP surface or that PEG-OH interferes with coiled coil formation. The PEG-OH molecule will potentially extend out from the NP surface further than the first three peptide residues (figure 4.6). It is documented that three heptad repeats are required for stable coiled coil formation,[224] hence masking of all or part of the first heptad repeat by PEG-OH could affect the heteroassociation. Presence of a molecule, such as PEG-OH, between peptide sequences may also sterically interfere with interactions between the two peptides. Increasing the proportion of peptide relative to PEG-OH resulted in unstable PGN-K suspensions (figure 4.7 c-d).
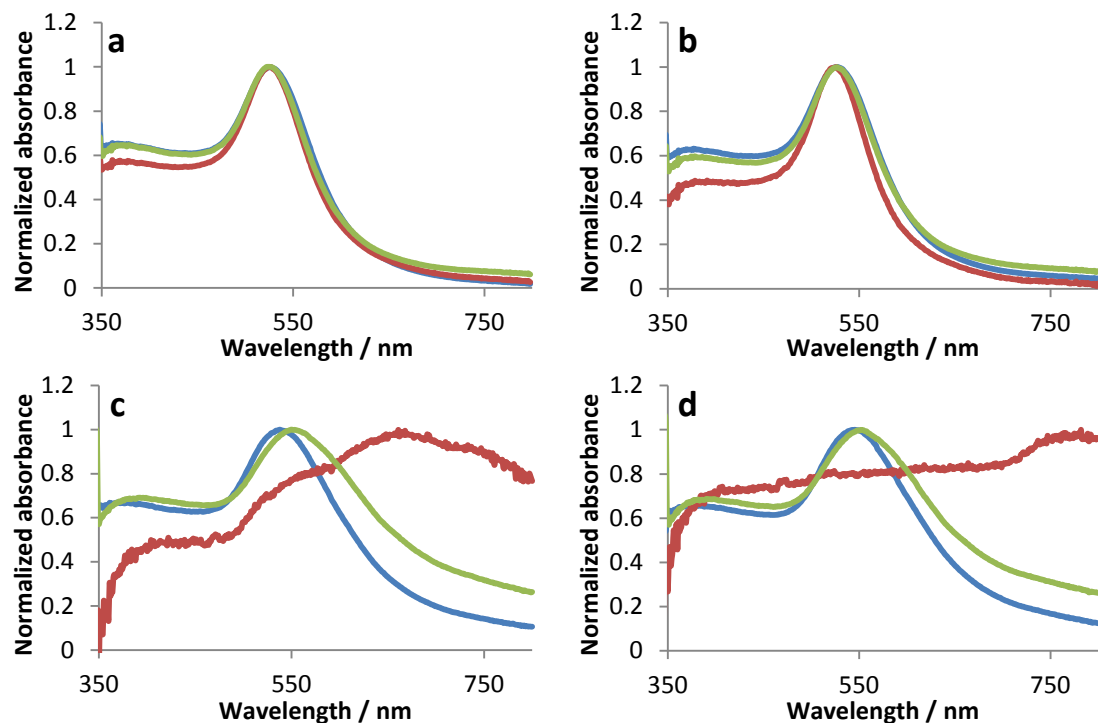
Figure 4.7 – Absorbance profiles of PGN-E (blue), PGN-K (red) and PGN-E / PGN-K heterogeneous mixtures (green) with a) 1 %, b) 5 %, c) 10 % and d) 20 % peptide in mixture with PEG-OH, pH 7.

4.2.4 – Three step protocol for PGN preparation

In 2004 Chen *et al.* published a functionalization method for neutral and positively charged ligands onto negatively charged AuNP.[226] They described a method in which AuNP, at pH 11, were pre-functionalized with thioctic acid (TA) which displaces the citrate and forms a thiol attachment to the NP surface.[226] Various positively charged and neutral thiol containing ligands were then added to thioctic acid modified AuNP (Au-TA), at pH 11, resulting in ligand exchange and the formation of positive and neutral NP conjugates.[226] The method outlined in this paper was investigated for PGN-K preparation and yielded stable conjugates. PGN-E were achieved by adding E directly to AuNP at neutral pH.

Two step method for PGN-K

Following the method described by Chen *et al.*, 15 nM AuNP solutions, in H_2O, were adjusted to pH 11 using sodium hydroxide (NaOH) and TA added at a 1000 fold molar excess. After centrifugation and resuspension in H_2O, on day two, 10 nM Au-TA solutions were adjusted to pH 11 with NaOH and a 1000 fold molar excess of peptide K added. Peptide E was added directly to AuNP at neutral pH using the same molar excess. On day three PGN-E and PGN-K were centrifuged and resuspended in H_2O at neutral pH. PGN-E samples appeared stable and exhibited the characteristic pink colouring of monodispersed AuNP, however the same was not observed for PGN-K (figure 4.8). Au-TA solutions displayed an immediate change in colour from pink to purple with the addition of peptide K. Centrifugation and resuspension in H_2O on day three resulted in aggregation of the NP which precipitated out of solution (figure 4.8). At pH 11, TA is deprotonated and as such Au-TA exhibit a negative surface charge, whereas peptide K has an isoelectric point of 10.7 and will therefore be deprotonated but may carry some positive charge. The aggregation of Au-TA, observed upon addition of peptide K at pH 11, may thus be attributed to electrostatic interactions between these two species.
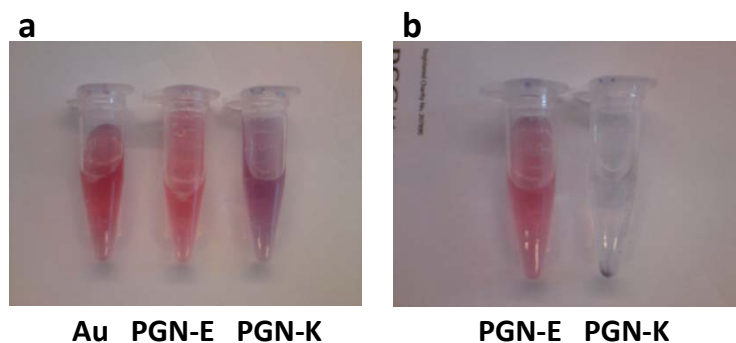
Figure 4.8 – Nanoparticle suspensions a) immediately following peptide addition on day two and b) after centrifugation and resuspension in H_2O on day three.

Three-step method for PGN-K

The aggregation of Au-TA observed following addition of peptide K at pH 11 was also described by Chen *et al.* when using the ligand 11-mercaptoundecylamine (11-MUAM). They managed to produce stable conjugates by adding in an additional step and further manipulating the solution pH.[226] Following 11-MUAM addition to Au-TA on day two a solution colour change from pink to purple was observed during ligand exchange.[226] This was reversed by introducing hydrochloric acid (HCl) an hour after 11-MUAM addition, resulting in an acidic solution and a colour change back to pink.[226] Analysis of the resultant solution demonstrated stable 11-MUAM modified AuNP.[226]

PGN-K were prepared as described in the two step method, adding in HCl an hour after peptide addition to Au-TA. As described in the publication, upon addition of HCl the PGN-K solution turned from purple back to pink.[226] The addition of HCl dramatically reduced the solution pH resulting in protonation of TA and peptide K. This reduced charge-dependent interactions between Au-TA and peptide K, allowing ligand exchange to occur creating stable PGN-K. Functionalized nanoparticles were monodispersed in solution on day three after centrifugation and resuspension in H_2O at neutral pH (figure 4.9).

Figure 4.9 – PGN-E (left) and PGN-K (right) solutions, pH 7. PGN-K were prepared using the three-step protocol

NP conjugation was verified by a red-shift of 2 – 3 nm in the plasmon λ-max. This is a smaller red-shift than was observed for any other conjugation method insinuating that PEG molecules were dominant over peptides in the mixed monolayers, thus explaining the stability of solutions incorporating higher proportions of PEG (figure 4.7). Homogeneous and heterogeneous solutions of PGN-E and PGN-K were prepared with total NP concentrations of 0.5 – 2 nM and analysed using extinction spectroscopy every day for five days. PGN-E solutions maintained a monodispersed distribution at all concentrations, however the stability of the PGN-K suspension increased with concentration. PGN-K retained solution stability for 1, 2 and 3 days at 0.5, 1 and 2 nM concentrations respectively (figure 4.10).

Heterogeneous PGN solutions were prepared by mixing PGN-E with PGN-K at a 1:1 molar ratio. It was expected that heterogeneous coiled coils would form between PGN-E and PGN- K, as indicated in figure 4.3, thus resulting in NP assembly and a change in the plasmon band observed in extinction spectroscopy. As predicted, extinction spectroscopy of heterogeneous PGN-E / PGN-K solutions demonstrated a decrease in plasmon absorbance at 522 nm and an increase at longer wavelengths indicating nanoparticle clustering (figure 4.11). NP aggregation became more pronounced over the duration of a week and proceeded at a slower rate with increasing concentrations (figure 4.11). To enhance data clarity, extinction spectra for PGN suspensions were excluded after aggregation had been observed for the first time. Figure 4.11b shows PGN solutions (2 nM) on day one. Homogeneous and heterogenous solutions appear pink and purple respectively, typical of the nanoparticle distributions displayed in extinction spectroscopy. The methodologies used here produced stable PGN-E and PGN-K conjugates, of which NP assembly was observed in heterogeneous solutions and monitored using extinction spectroscopy.
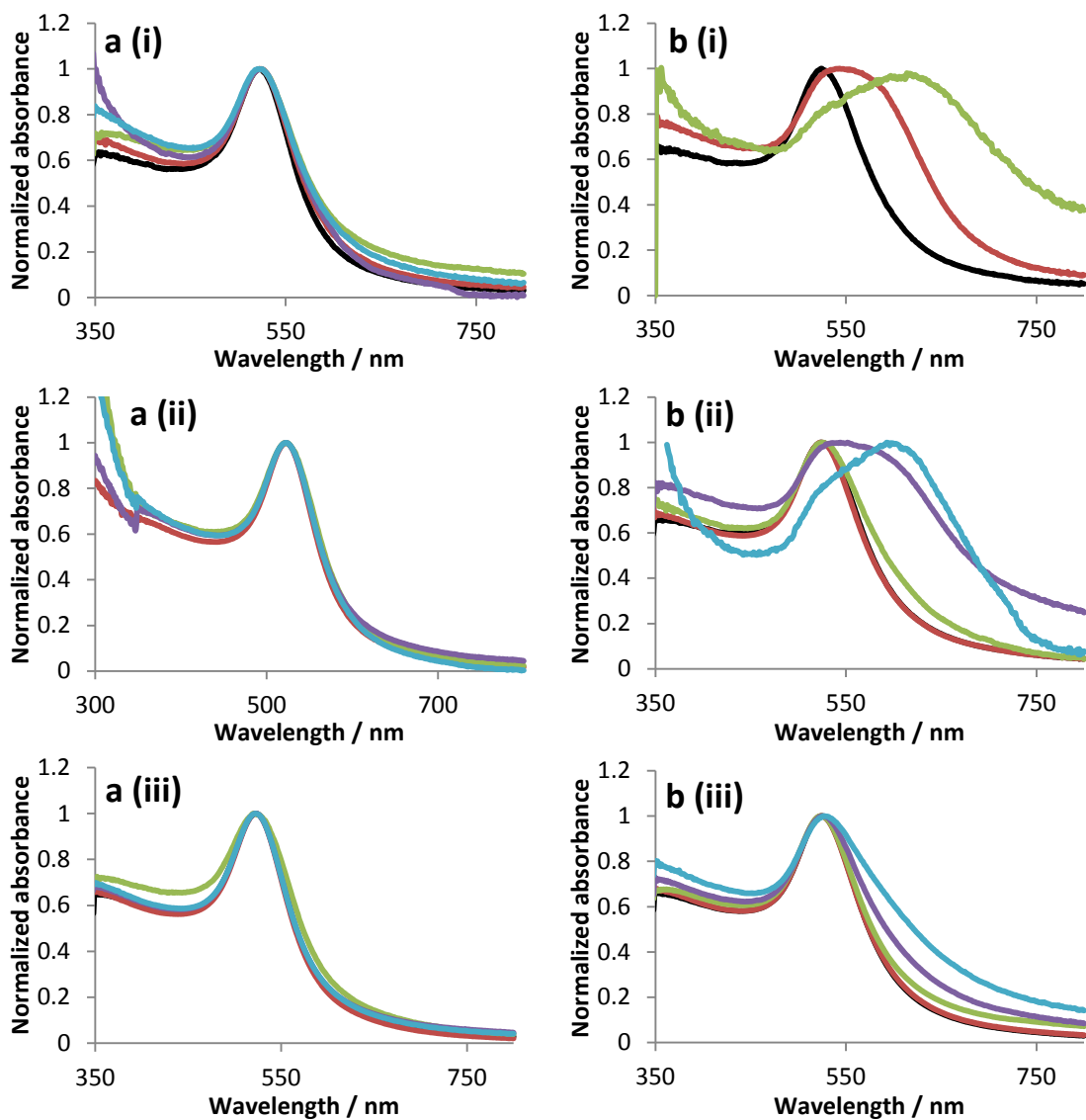
Figure 4.10 – Normalized extinction spectra of a) PGN-E and b) PGN-K solutions at concentrations i) 0.5 nM, ii) 1 nM and iii) 2 nM, pH 7. PGN suspensions were monitored for five days and spectra represent analysis conducted on day 1 (black), day 2 (red), day 3 (green), day 4 (purple) and day 5 (blue).
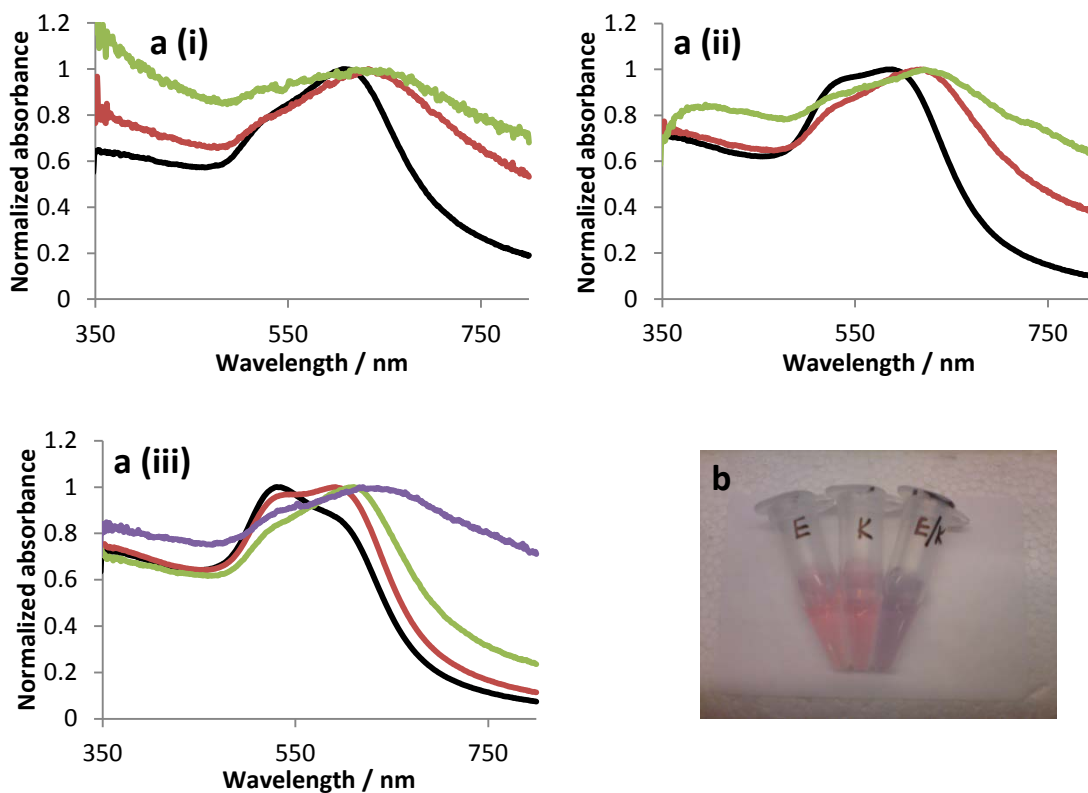
Figure 4.11 – a) Normalized extinction spectra of PGN-E / PGN-K heterogeneous solutions at concentrations i) 0.5 nM, ii) 1 nM and iii) 2 nM at pH 7. PGN suspensions were monitored for five days and spectra represent analysis conducted on day 1 (black), day 2 (red), day 3 (green), day 4 (purple) and day 5 (blue). b) PGN-E, PGN-K and PGN-E/PGN-K (from left to right) solutions photographed on day one.

4.3 – SERS-active PGN using small molecules

Assembly of PGN-E / PGN-K in heterogeneous solutions was described in section 4.2.5 and analysed using extinction spectroscopy. Aggregation of SERS active NPs in this manner has been previously detected through increased signal intensities in Raman spectroscopy, as demonstrated in chapter three. Raman spectroscopy showed higher sensitivity than extinction spectroscopy for analysis of MDM2-induced aggregation of AgEDTA. To investigate Raman spectroscopy as an analysis tool for coiled coil heterodimerization induced AuNP assembly, a Raman tag must be incorporated into PGN conjugates.

The advantages of using small molecules as Raman reporters in bioanalytical applications are outlined in chapter 1 (section 1.5.2). The simple molecular structures of small molecules exclude the requirement for expensive synthesis and once attached to NP surfaces they are small enough not to interfere with coiled coil heteroassociation between NP-bound peptides. Low detection limits have also been demonstrated when employing these analytes as Raman tags in SERS-based immunoassays.[175, 181] Hence, small molecules are ideal candidates to act as Raman tags. Figure 4.12 illustrates the proposed PGN assembly and associated SERS analysis resulting from heterogeneous coiled coil associations.
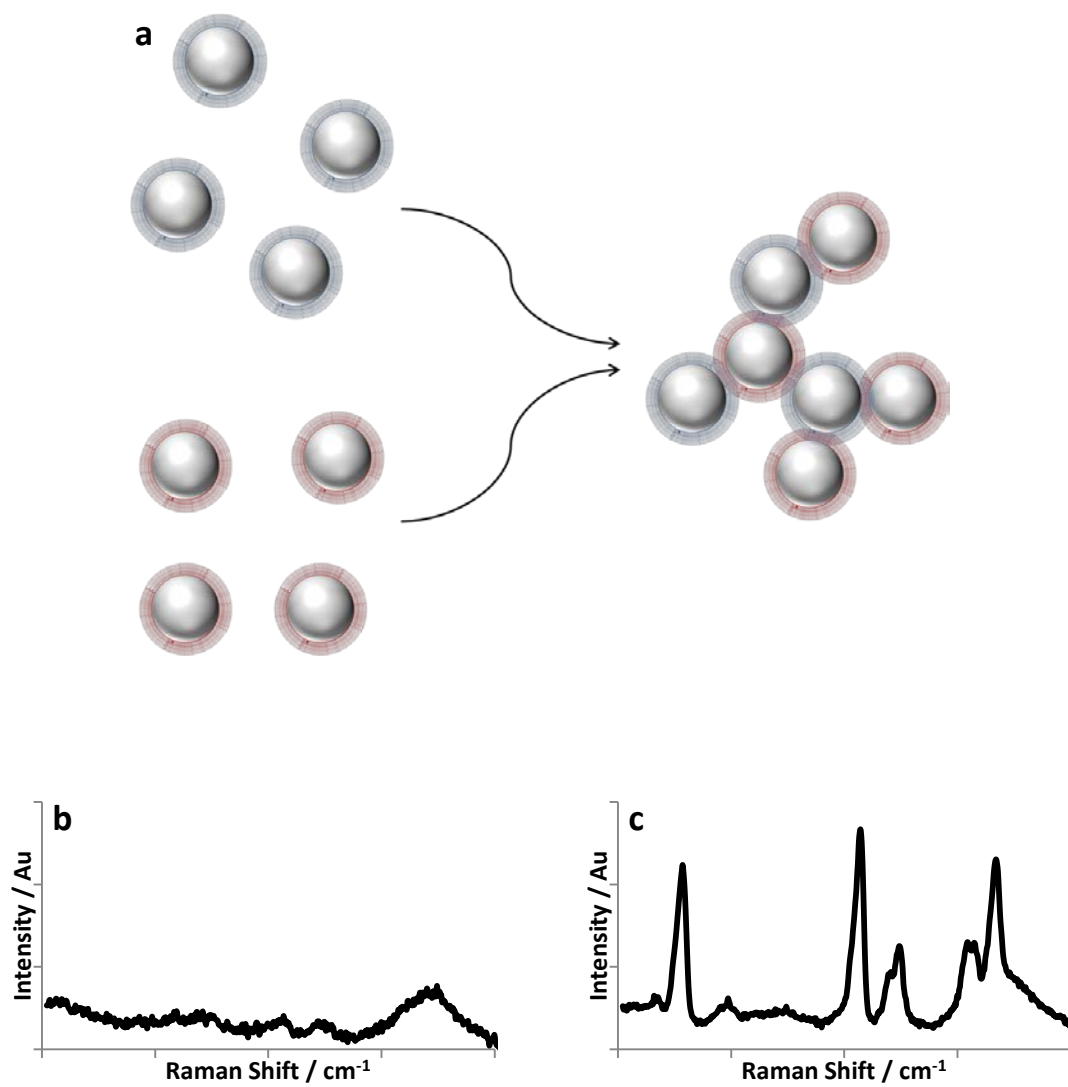
Figure 4.12 – a) schematic of the proposed heterogeneous PGN assembly and associated SERS spectra for b) monodispersed and c) aggregated PGN with 2-naphthalene thiol.

4.3.1 – SERS-403

SERS-403 (figure 4.13) has been previously used, with some success, as a Raman reporter for *in vivo* imaging studies.[179] In such investigations, SERS-403 was one of many small molecules incorporated into silica coated nanotags.[179] NP immobilization of SERS-403 was achieved via a single thiol linkage and, following silica encapsulation, the resultant nanotag was shown to exhibit strong SERS signals in multiplexed *in vivo* imaging.[179] A characteristic Raman spectral peak is observed at ~1550 cm^{-1} when employing an excitation wavelength of 632.8 nm.
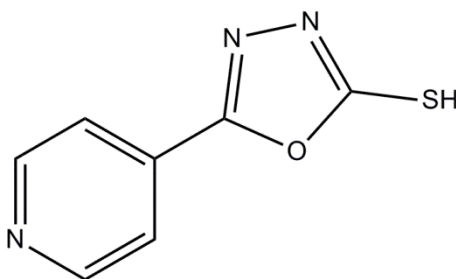
Figure 4.13 – Structure of SERS-403[179]

PGN-K were prepared using the three-step protocol described in section 4.2.5.2 and PGN-E via direct addition of peptide E to AuNP. In order to incorporate the Raman tag, peptides were pre-mixed with Raman tag at different peptide:SERS-403 ratios (1:1, 1:4 and 1:9) and added to either AuNP or Au-TA as previously described. SERS-403 was also added to NP solutions to ensure conjugate stability and that PGN assembly resulted only from peptide-peptide interactions.
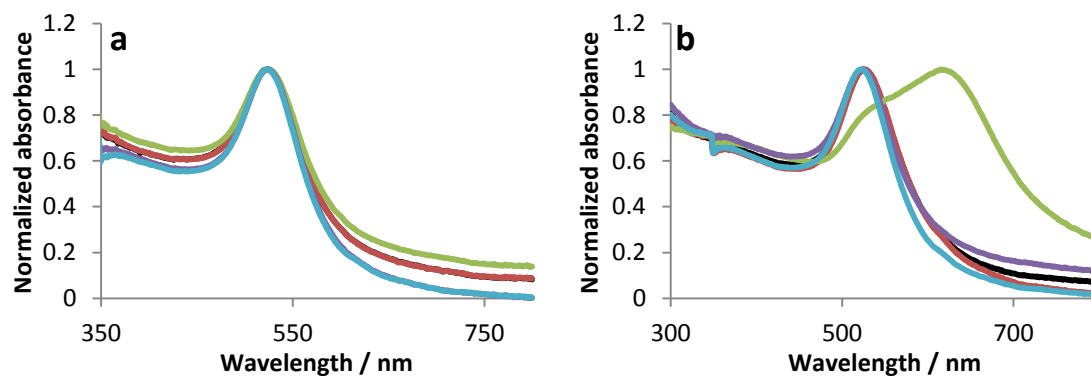
Figure 4.14 – Extinction spectra of a) PGN-E and b) PGN-K conjugate variations, pH 7. PGN were prepared with peptide only (black), 1:1 peptide:SERS-403 (red), 1:4 peptide:SERS-403 (green), 1:9 peptide:SERS-403 (purple) and a) AuNP and b) Au-TA with SERS-403 only (blue).

All PGN conjugates incorporating SERS-403, with one exception, demonstrated a plasmon absorbance λ-max at around 525 nm in extinction spectroscopy, typical of monodispersed solutions. (figure 4.14). PGN made with a 1:4 ratio of peptide:SERS-403 were discarded due to instability. Assembly of PGN-E / PGN-K heterogeneous solutions was investigated for conjugates with peptide:SERS-403 ratios of 1:1 and 1:9 via extinction spectroscopy and SERS (figure 4.15). All sample analysis was carried out using a 2 nM NP concentration.
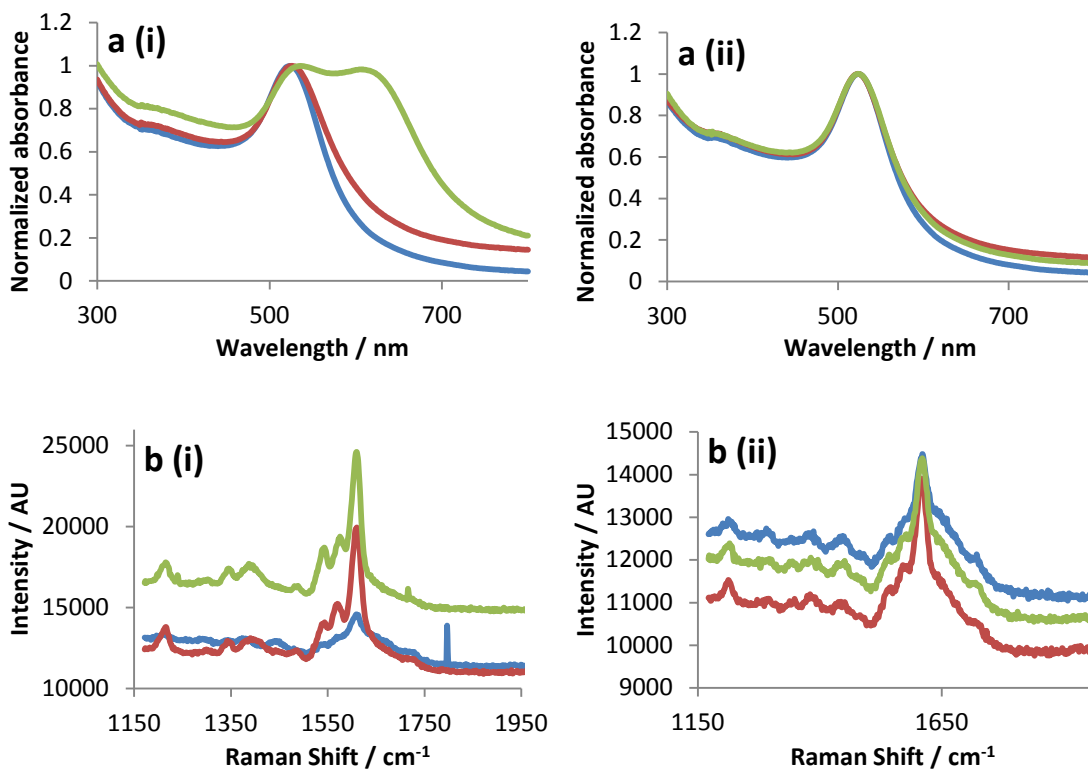
Figure 4.15 – b) Normalized extinction spectra and b) SERS analysis of i) 1:1 peptide:SERS-403 and ii) 1:9 peptide:SERS-403 PGN solutions, pH 7. PGN-E (blue), PGN-K (red) and PGN-E / PGN-K (green).

Extinction spectroscopy analysis of 1:1 peptide:SERS-403 PGN-E / PGN-K heterogeneous solutions showed an increase in absorbance at longer wavelengths indicating PGN assembly (figure 4.15 a i). SERS interrogation contradicted these findings with no notable difference in signal intensity between PGN-K homogeneous solutions and mixed PGN samples (figure 4,15 b i). No evidence for PGN assembly was observed in extinction spectroscopy or SERS analysis for 1:9 peptide:SERS-403 conjugates (figure 4.15 a ii and b ii). As PGN assembly was observed with a peptide:SERS-403 ratio of 1:1 it can be deduced that when a ratio of 1:9 is employed there is insufficient peptide present on the NP surface to facilitate heteroassociation. SERS intensities elicited from samples with 1:1 peptide:SERS-403 are more difficult to

interpret. One significant observation was the difference in SERS signal intensities between PGN-E and PGN-K samples with 1:1 peptide:SERS-403. SERS signals obtained for PGN-E were of similar intensity to that of PGN samples incorporating 1:9 peptide:SERS-403. It could therefore be suggested that the 1:1 peptide:SERS-403 sample was partially aggregated, resulting in a high SERS intensity and slight broadening in the plasmon absorbance band in extinction spectroscopy (figure 4.15 ai and bi). Although PGN assembly is observed for the heterogeneous solutions, no further increase in SERS intensity was observed, only an increase in background signals. Extinction spectroscopy and SERS analysis demonstrated partial NP assembly in heterogeneous solutions of PSN-K, without Raman tag, and SERS-403 functionalised AuNP (figure 4.16). These data indicate that partial aggregation of SERS-403 modified PSN-K is due to interactions between peptide K and ring nitrogens in the SERS-403 structure. Further assembly of Raman active PSN-K, following addition of PSN-E, didn't cause any further increase in SERS, thus in this instance partial aggregation gave an optimal SERS response. Owing to interactions with peptide K, SERS-403 was deemed unsuitable for use as a Raman tag for coiled coil induced PSN assembly.
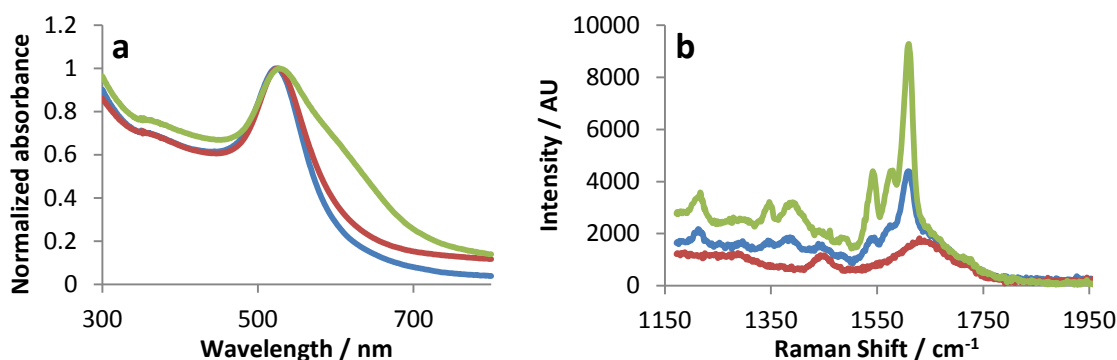
Figure 4.16 – a) Normalized extinction spectroscopy and b) baselined SERS analysis of AuNP-SERS-403 (blue), PGN-K without Raman tag (red) and a mixed solution of AuNP-SERS-403 and PGN-K (green) at pH 7. Five 30 second scans were recorded for each sample replicate using an excitation wavelength of 632.8 nm in SERS analysis.

4.3.2 – 2-Naphthalene thiol (2-NPT)
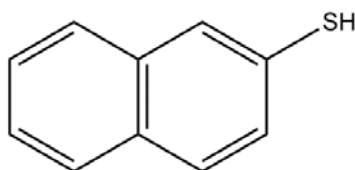
Figure 4.17 – Structure of 2-NPT

2-Naphthalene thiol (2-NPT) has a similar structure to SERS-403 but without the ring nitrogens, hence employing this small molecule was proposed to eradicate non-specific interactions between the Raman reporter molecules and NP-bound peptides. PGN conjugates were prepared in the same way as described for SERS-403 (section 4.3.1) with premixed solutions of peptide and NPT at ratios of 1:1, 1:4 and 1:9. PGN-K were functionalized using the three step protocol and PGN-E by adding the peptide:NPT mixtures directly to AuNP. In line with previous studies, all samples were prepared with a total NP concentration of 2 nM.

PGN-K prepared using a peptide:NPT ratio of 1:1 displayed an increase in absorbance at longer wavelengths in extinction spectroscopy indicating instability and NP clustering (figure 4.18). Conjugates incorporating a 1:1 peptide:NPT ratio were therefore discarded and assembly studies were carried out on PGN-E / PGN-K solutions made with 1:4 and 1:9 ratios of peptide:NPT via extinction spectroscopy and SERS.
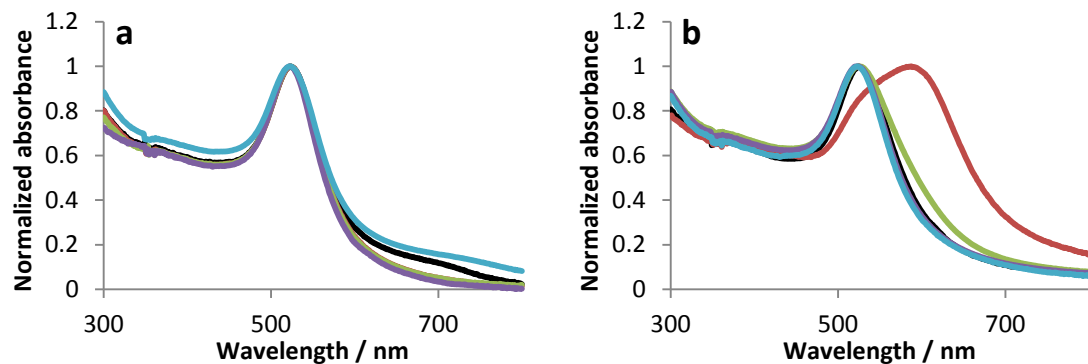
Figure 4.18 – Extinction spectra of a) PGN-E and b) PGN-K conjugate variations with 2-NPT. NP conjugates were prepared with peptide only (black), 1:1 peptide:NPT (red), 1:4 peptide:NPT (green), 1:9 peptide:NPT (purple) and a) AuNP and b) AuNP-TA with NPT only (blue). Recordings represent PGN solutions at pH 7.
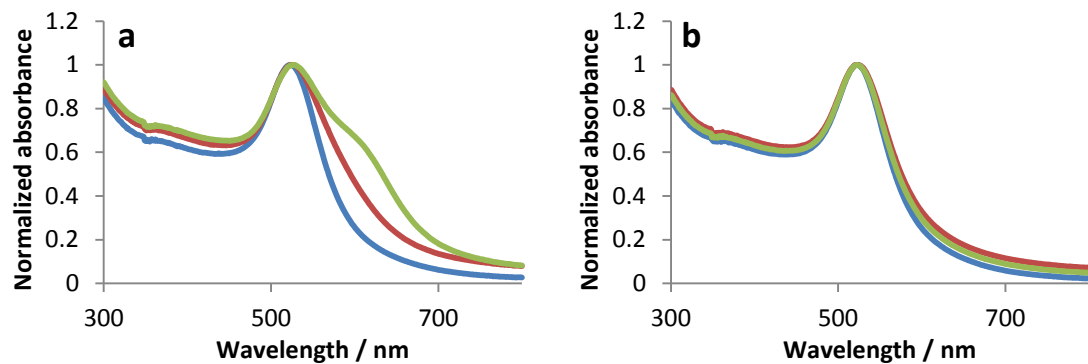
Figure 4.19 – PGN prepared with a) 1:4 and b) 1:9 peptide:NPT ratio. Normalized extinction spectra of PGN-E (blue), PGN-K (red) and PGN-E / PGN-K suspensions (green). Recordings represent PGN solutions at pH 7.

Extinction spectroscopy analysis showed partial aggregation of PGN-E / PGN-K mixtures prepared using a 1:4 ratio of peptide:NPT by the emergence of a shoulder at higher wavelengths within the plasmon peak (figure 4.19 a). NP assembly was not as pronounced as observed for PGN with SERS-403 (1:1 peptide:SERS-403), suggesting the formation of small clusters rather than large assemblies. Peptide surface concentration could account for the variation in cluster sizes as PGN made with 1:4 peptide:NPT will present fewer surface peptides than PGN incorporating 1:1 peptide:SERS-403. Observed assembly differences could also relate to the Raman tags as peptide K was shown to interact with SERS-403. PGN assembly displayed with 1:4 peptide:NPT PGN-E / PGN-K heterogeneous mixtures is more likely to be the result of specific coiled coil heterodimerization. Mixed suspensions of PGN-E / PGN-K prepared with a ratio of 1:9 peptide:NPT showed no indication of NP association, therefore it was inferred that insufficient peptide was present on the NP surface for heterodimerization to occur (figure 4.19).

SERS analysis of 2-NPT incorporating PGN solutions yielded characteristic peaks for Au-NPT only when no other ligands were present on the NP surface (figure 4.20 a).[175] Solutions of AuTA-NPT also displayed an increased SERS response following aggregation with spermine (figure 4.20 b). SERS signals were negligible in all other samples even after spermine-induced aggregation. Some evidence of a SERS signal could be seen in aggregated solutions of PGN-K (1:9 peptide:NPT), however this is negligible and wasn't observed for equivalent PGN-E samples. These data indicate that 2-NPT failed to immobilize onto NP surfaces in the presence of other ligands, possibly due to the hydrophobic nature of the ring structure.
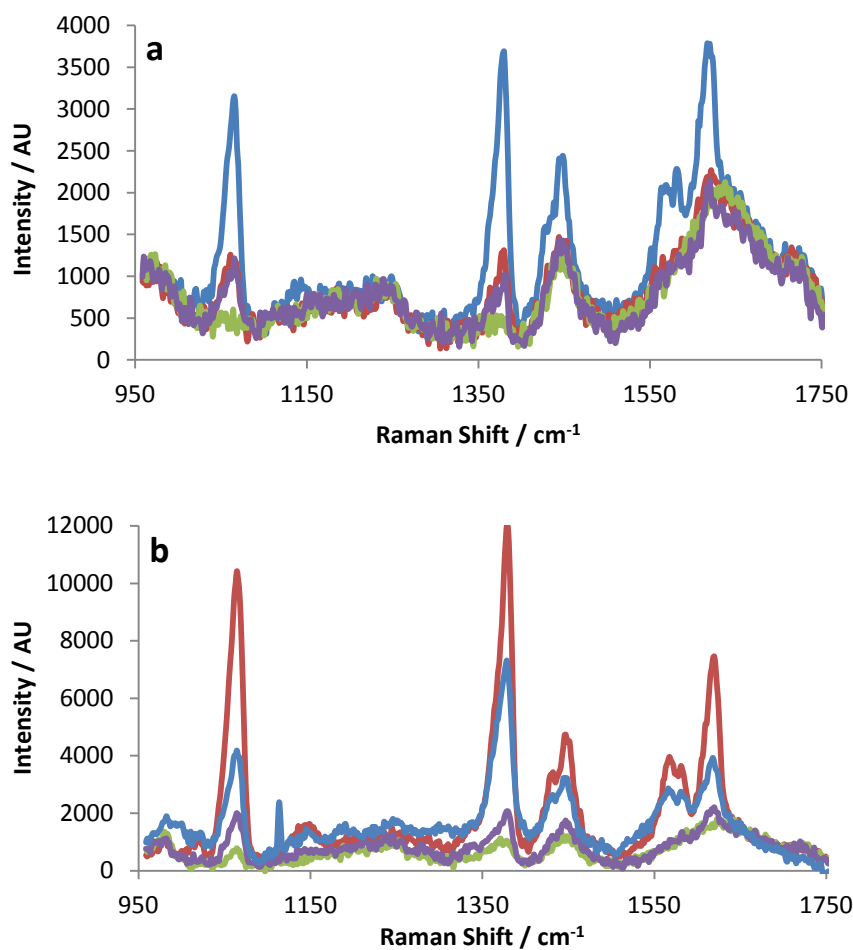
Figure 4.20 – Baselined SERS analysis of NP solutions prepared with 1:9 peptide:NPT a) before and b) after aggregation with spermine. Au-NPT (blue), AuTA-NPT (red), PGN-E (green) and PGN-K (purple). Five 30 second scans were recorded for each sample replicate using an excitation wavelength of 632.8 nm in SERS analysis. Recordings show PGN solutions at pH 7.

To overcome the difficulty of 2-NPT immobilization, NPs were pre-functionalized with the small molecule, added at 1000-fold excess. Following centrifugation and resuspension in H_2O peptides E and K were added to Au-NPT at 1000-fold excess. Au-NPT suspensions were adjusted to pH 11 before addition of peptide K, analogous to the three-step protocol with Au-TA, whilst peptide E was added at neutral pH. Resultant

PGN-K solutions demonstrated cluster formation in extinction spectroscopy (figure 4.21). It can therefore be deduced that step one in the three-step functionalisation protocol requires a negatively charged ligand. Heterogeneous PGN-E / PGN-K solutions exhibited an extinction spectrum illustrating a mixture of the two homogeneous spectra. Interpretation of the extinction spectroscopy results suggested that no specific peptide-peptide interactions had occurred. The structure of 2-NPT comprises solely of a hydrophobic imidazole ring (figure 4.17), thus peptides would struggle to penetrate a monolayer and bind the metal surface. The NP clustering observed in PGN-K samples indicates possible sub-monolayer 2-NPT coverage. In this case surface hydrophobicity may have prevented peptides attaching to the NP surface but simultaneously, some surface charge remained exposed. Electrostatic interactions between the cationic peptide and exposed negative charges on the NP surface may have caused the clustering shown in figure 4.21. All these results taken together show 2-NPT and peptide NP immobilization to be mutually exclusive and hence 2-NPT is not a suitable Raman tag for investigating coiled coil NP assembly.
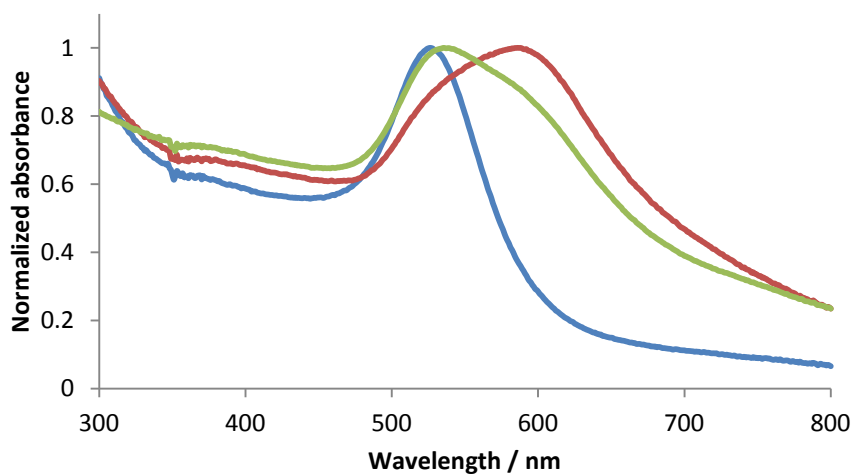
Figure 4.21 – Normalized extinction spectra of PGN-E (blue), PGN-K (red) and a PGN-E / PGN-K mixture (green) following pre-functionalization with 2-NPT.   Recordings represent PGN solutions at pH 7.

4.3.3 – Mercaptobenzoic acid (MBA)

Small molecule Raman reporters chosen thus far have proved to be unsuitable, therefore a different approach was adopted to create SERS active PGN with peptides E and K. The three-step functionalization protocol for PGN-K, describes NP pre-functionalization with TA which is then displaced by peptide K. Ligand exchange was performed by adding up to 1000 fold excess of peptide K to Au-TA and lowering the solution pH. A much larger excess of peptide would be required to achieve monolayer coverage, therefore it is highly probable that PGN-K prepared in this way retain some surface attached TA molecules. If this prediction is correct, replacing TA with a Raman active alternative could lead to SERS active PGN-K conjugates. Mercaptobenzoic acid (MBA) is a small molecule, with similar charge and size to TA, which exhibits a Raman response when using an excitation wavelength of 632.8 nm (figures 4.22 and 4.24).[176] PGN-MBA-K conjugates were prepared using the three-step protocol (section 4.2.5), substituting MBA in the place of TA, and peptide E was added directly to AuNP to yield PGN-E without any Raman reporter.
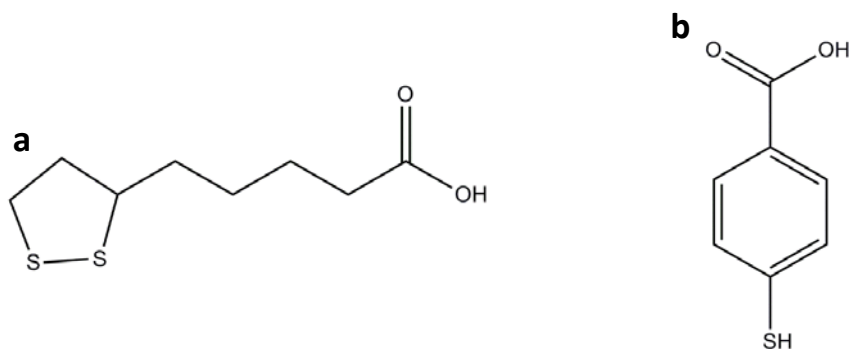
Figure 4.22 – Structures of a) thioctic acid and b) MBA

PGN preparation was carried out as previously described except for the excess of peptide E and K added to AuNP and Au-MBA respectively. Conjugation was performed

with the addition of 500-fold and 1000-fold peptide excess to investigate the stability of PGN prepared with different peptide concentrations. Extinction spectroscopy analysis of PGN solutions, pH 7, showed broadening in the plasmon absorbance band of PGN-MBA-K compared with PGN-E indicating partial aggregation in solutions of the former (figure 4.23). Differences in the stability of PGN suspensions prepared using different peptide concentrations were minimal, however addition of 1000-fold excess peptide K, rather than 500-fold, to Au-MBA was seen to yield NP solutions of slightly higher stability (figure 4.23). MBA is deprotonated at neutral pH and carries a negative charge, whilst peptide K is positively charged. Hence, a mixture of different charges is present on NP surfaces exhibiting a mixed monolayer of these two species. Using a higher excess of peptide K resulted in PGN-MBA-K with a larger proportion of positively charged species on the surface, thus enhancing interparticle electrostatic forces. This theory provides an explanation for the differences in solution stability observed for PGN-MBA-K prepared using 500-fold and 1000-fold peptide K excesses (figure 4.23).
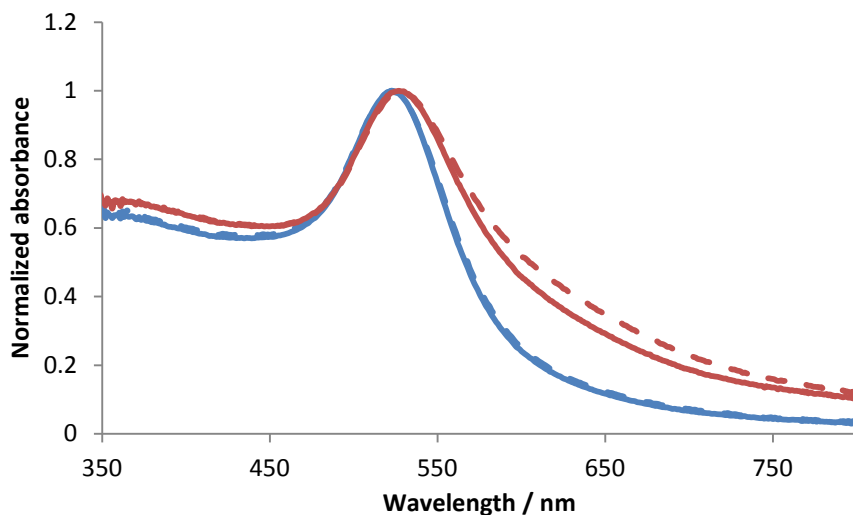
Figure 4.23 – Normalized extinction spectra of PGN-E (blue) and PGN-MBA-K (red) prepared with 500x (dashed line) and 1000x (solid line) peptide excess, pH 7.

NP assembly was investigated with 2 nM homogeneous and heterogeneous solutions of PGN-E / PGN-MBA-K, prepared with both 500-fold and 1000-fold peptide excess, via extinction spectroscopy and SERS (figure 4.24). Heterogeneous solutions demonstrated absorbance profiles in extinction spectroscopy indicative of PGN assembly, however SERS analysis was inconclusive. Aggregation appeared more pronounced with 500x peptide excess compared to 1000x peptide excess. MBA was only present on one conjugate and solution preparation was based on total NP concentration, therefore the SERS intensity observed for PGN-MBA-K was not directly comparable to that from PGN-E / PGN-MBA-K. To compensate for this, 1 nM PGN-MBA-K solutions were included in SERS analysis as a more direct comparison to 2 nM heterogeneous solutions. Figure 4.24 b illustrates the raw SERS data obtained, from which sample SERS intensities were quantified by monitoring peak heights at 1071 cm^{-1} and 1585 cm^{-1} (figure 4.24 c). A negligible increase in SERS was observed in mixed PGN-E / PGN-MBA-K suspensions prepared with 500x peptide excess. This increase was not observed with conjugates made using 1000x excess, correlating to the variation in aggregation illustrated by extinction spectroscopy. Although SERS intensity changes were minimal, MBA showed potential as a Raman tag for detection of peptide-peptide interactions. MBA was consequentially used in all further coiled coil NP investigations. Higher signals could potentially be achieved by employing silver rather than gold NPs.[157]
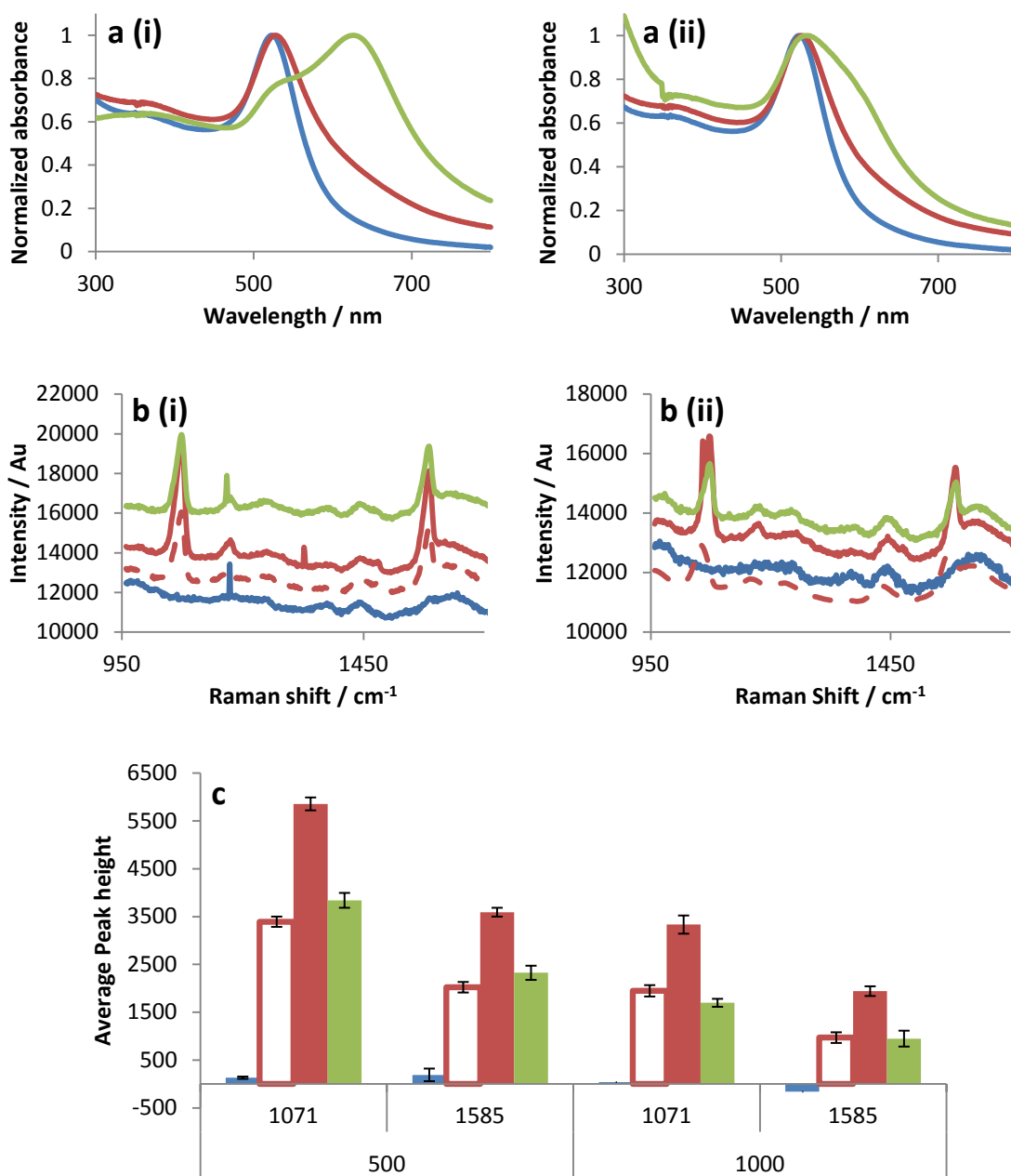
Figure 4.24 – a) Normalized extinction spectra, b) raw SERS spectra and c) SERS peak height measurements at 1071 cm^{-1} and 1585 cm^{-1} for PGN prepared with i) 500x and ii) 1000x peptide excess. 2nM PGN-E (blue), PGN-K (red solid line / filled bar) and PGN-E / PGN-K (green) and 1 nM PGN-K (red dashed line / empty bar). Five 1-2 second scans were recorded for each sample replicate using an excitation wavelength of 632.8 nm in SERS analysis. Recordings represent PGN solutions at pH 7.

4.4 – Investigating different coiled coil NP assemblies

Section 4.3 described the functionalization of AuNP and coiled coil forming peptides E and K to create monodispersed solutions of PGN. Assembly of PGN in heterogeneous solutions was demonstrated by extinction spectroscopy and incorporation of a Raman tag in PGN-MBA-K has shown potential for monitoring the NP assembly process via SERS. Despite peptide design of E and K favouring heterodimerization in a parallel orientation, anti-parallel heterodimer is promoted by structural NP arrangements (figure 4.3). The orientation of E / K coiled coils inducing PGN assembly cannot be distinguished using the analytical tools in this study. Peptide variations of E and K, NP-bound via a cysteine on the middle heptad repeat, were employed to investigate the effect of NP surface peptide surface orientation on PGN assembly.

4.4.1 – Peptide orientation

The helical peptide structures of E and K (figure 4.2) and proposed PGN assemblies through parallel and anti-parallel coiled coil formation (figure 4.3) are illustrated in section 4.1.2. These peptides were designed with a terminal cysteine residue allowing helices to extend from the NP surface. Peptides E-Het-Cys (Em) and K-Het-Cys (Km) exhibit the same helical structure as E and K, however the sequence has been modified to allow NP immobilization through a cysteine residue situated at position f in the central heptad repeat (figure 4.25).

E-Het-Cys (Em) – Ac-G **E**I**AA**L**E**K **E**N**AA**L**E**C **E**I**AA**L**E**Q GWW-NH

K-Het -Cys (Km) – Ac-G **K**I**AA**L**K**K **K**N**AA**L**K**C **K**I**AA**L**K**Q GYW-NH
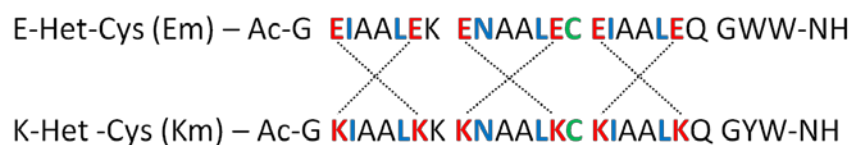
Figure 4.25 – Primary sequences of designed peptides E-Het-Cys and K-Het-Gys. Electrostatic interactions between the peptides within a parallel dimeric coiled coil are indicated (dotted lines). Residues involved in nanoparticle binding (green), hydrophobic packing (blue) and electrostatic interactions (red) are highlighted.

Residues situated at f are not involved in coiled coil helix formation but are known to impact on lateral interactions in higher order structures.[91] Helices which are surface attached via a mid sequence f positioned cysteine should therefore maintain the ability to form dimeric coiled coils. Interparticle spacing in assembled PGN-E / PGN-K and PGN-Em / PGN-Km is likely to vary due to the resultant coiled coil structural orientation relative to the NP surface (figures 4.3 and 4.26). For instance, Em / Km coiled coils will most likely form in a parallel orientation to the NP surface, whilst E / K coiled coils would extend out perpendicularly between NPs. This will result in much smaller interparticle spacing within PGN-Em / PGN-Km clusters compared to assemblies of PGN-E / PGN-K.

In order to investigate the assembly kinetics resulting from different peptide assemblies, stable PGN conjugates with the newly introduced peptides were required. SERS-active PGN-MBA-Km were prepared using the three-step functionalization process, incorporating MBA, as described for PGN-MBA-K in section 4.3.3. Em peptides were added directly to AuNP at neutral pH to create PGN-Em.
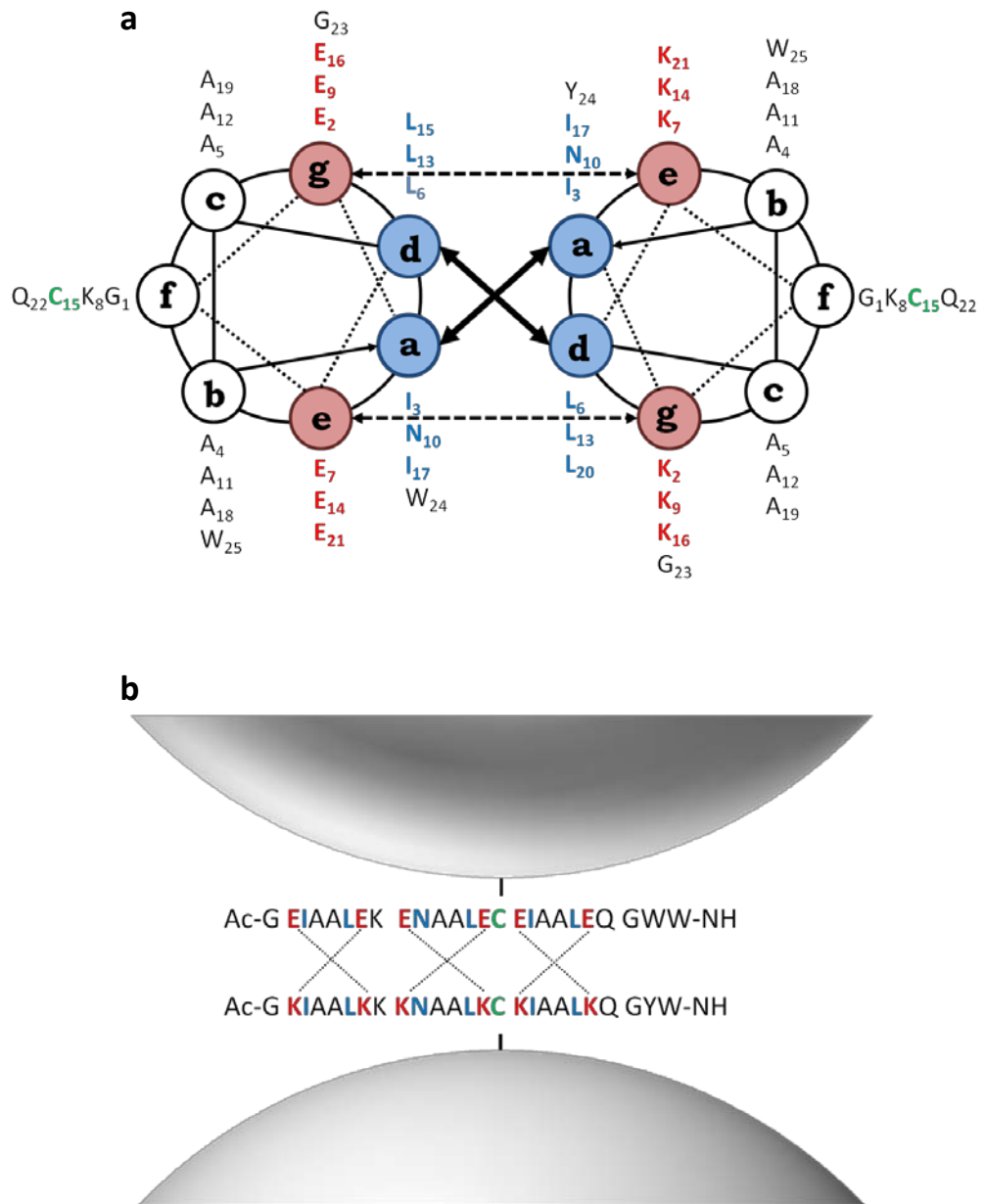
Figure 4.26 – a) Designed structures of E-Het-Cys (left) and K-Het-Cys (right), Em and Km, shown on a 3.5 residue-per-turn helical wheel and b) a schematic of PGN assembly based on parallel Em / Km coiled coil formation. Electrostatic interactions are indicated by a) dashed line arrows and b) dotted lines. Residues involved in nanoparticle binding (green), hydrophobic packing (blue) and electrostatic interactions (red) are highlighted.

Extinction spectroscopy analysis of PGN preparations made up using a 1000-fold excess of Em and Km peptides showed NP dispersions not dissimilar to PGN-E and PGN-MBA-K samples prepared with the same peptide excess (figures 4.24 and 4.27). Broadening in the plasmon absorbance band for PGN-MBA-Km indicated partial aggregation, whilst corresponding PGN-E samples appeared monodispersed in solution (figure 4.27). A further increase in absorbance at longer wavelengths was demonstrated for PGN-MBA-K prepared with 500-fold peptide excess (figure 4.27). Complete aggregation and precipitation of NP was observed in these solutions within a 24 hour time period. Nanoparticle assembly of 2 nM heterogeneous PGN-Em / PGN-MBA-Km solutions was investigated using extinction spectroscopy and SERS 1-2 hours following PGN mixing.
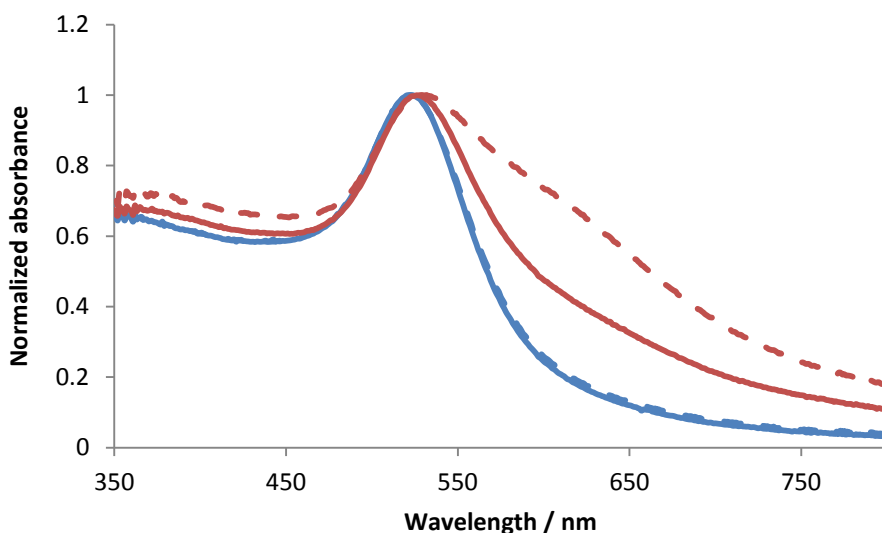
Figure 4.27 – Normalized extinction spectra of PGN-Em (blue) and PGN-Km (red) prepared with 500x (dashed line) and 1000x (solid line) peptide excess. Recordings represent PGN solutions at pH 7.

Figure 4.28 illustrates extinction spectroscopy and SERS analysis of homogeneous and heterogeneous PGN-Em / PGN-MBA-Km suspensions. A decrease in the plasmon absorbance at 520 nm and increased absorbance at longer wavelengths, indicative of NP clustering, was evident in heterogeneous PGN-Em / PGN-MBA-Km solutions prepared using both 500x and 1000x peptide excesses (the decrease in absorbance demonstrated for heterogeneous PGN solutions prepared using 1000x peptide excess is not illustrated in figure 4.28 aii due to normalization of the spectra). NP assembly appeared more pronounced for samples with 500-fold peptide excess, however this could be a result of pre-aggregated PGN-MBA-Km (figure 4.28 a). As aforementioned, PGN-E / PGN-MBA-K and PGN-Em / PGN-MBA-Km homogeneous samples, made with 1000-fold peptide excess, exhibit similar profiles in extinction spectroscopy. Heterogeneous solutions of the same conjugates demonstrated NP clustering to a larger extent in samples made with Em / Km than with E / K peptides (figures 4.24 and 4.28). These results suggest that coiled coil formation parallel to the NP surface was more favourable than perpendicular structures for PGN assembly. Helix orientation within the coiled coil may also contribute to this effect as the peptide designs favour a parallel orientation, of which the formation is sterically hindered in the PGN-E / PGN-MBA-K assembly (figure 4.3).
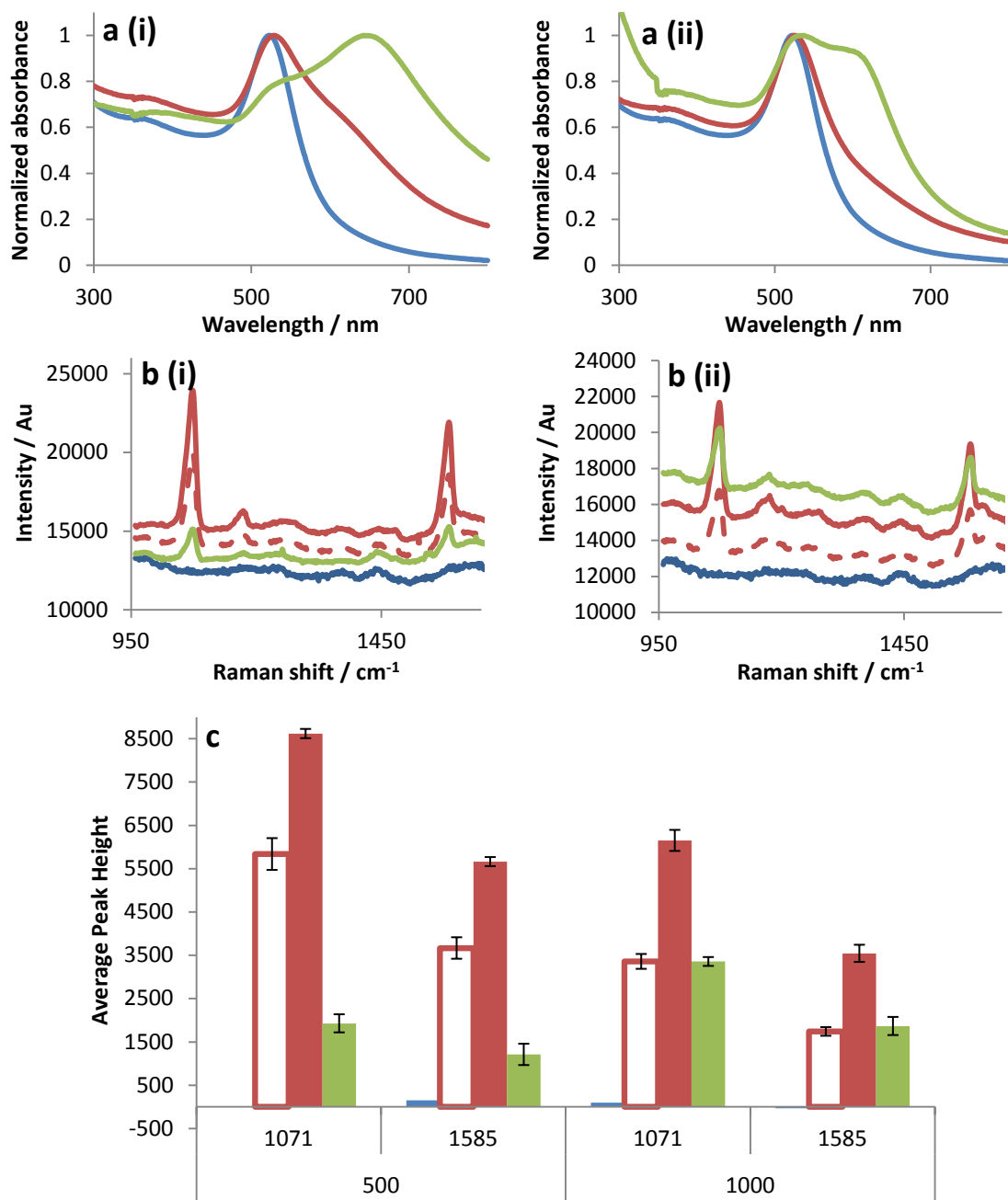
Figure 4.28 - a) Normalized extinction spectra, b) raw SERS spectra and c) SERS peak height measurements at 1071 cm^{-1} and 1585 cm^{-1} for PGN prepared with i) 500x and ii) 1000x peptide excess. 2nM PGN-Em (blue), PGN-Km (red solid line / filled bar) and PGN-Em / PGN-Km (green) and 1 nM PGN-Km (red dashed line / empty bar). Recordings represent PGN solutions at pH 7.

SERS analysis was carried out of all the PGN solutions and as previously described for E / K peptides, a 1 nM PGN-MBA-K solution was also interrogated for signal intensity comparisons between homogeneous and mixed solutions. A decrease in SERS intensity was observed for heterogeneous PGN solutions prepared using a 500x peptide excess (Em / Km) compared to homogeneous solutions. Negligible variation in SERS signals of PGN conjugates with 1000x excess Em / Km was seen (figure 4.28). The low SERS signal intensities observed in heterogeneous solutions, compared with homogeneous counterparts, was possibly a result of large aggregates precipitating out of solutions and thus out of the interrogation volume. This explanation was contested by the indication of cluster formation rather than complete aggregation in extinction spectroscopy, corresponding with optical observations of NP solutions (figures 4.28 and 4.29). Heterogeneous PGN suspensions demonstrated a colour change, indicative of a change in NP dispersion, however there was little evidence for precipitated aggregates. An alternative explanation is the masking of SERS signals from NP immobilized small molecules by coiled coils forming parallel to the NP surface.
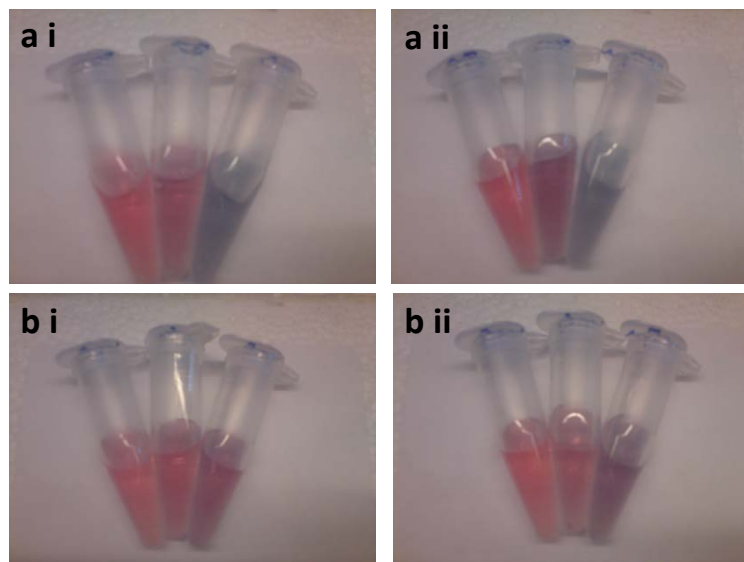
Figure 4.29 – PGN solutions prepared with a) 500x and b) 1000x peptide excess. Solutions of i) PGN-E, PGN-K and PGN-E / PGN-K and ii) PGN-Em, PGN-Km and PGN-Em / PGN-Km from left to right in each image. Images represent PGN solutions at pH 7.

Analysis of various PGN solution mixtures thus far has inferred an effect of peptide surface orientation on NP assembly. To this end, heterogeneous PGN suspensions were monitored over a period of 16 hours following mixture of anionic and cationic PGN using extinction spectroscopy (figure 4.30). Owing to homogeneous PGN solution stabilities, kinetic experimentation was carried out on PGN conjugates prepared with a 1000-fold peptide excess only. Four PGN mixtures were analysed (PGN-E / PGN-MBA-K, PGN-Em / PGN-MBA-Km, PGN-E / PGN-MBA-Km and PGN-Em / PGN-MBA-K) and due to restricted sample availability, solutions were diluted to 1 nM total NP concentrations. The extent of NP assembly was monitored by calculating the change in absorbance ratio between 535 and 625 nm.

The majority of NP assembly in all four heterogeneous PGN solutions was observed within five minutes of PGN mixing. The absorbance ratio was then seen to plateau indicating completion of assembly. All PGN mixtures, except PGN-E / PGN-MBA-Km, showed similar changes in absorbance ratio over time (figure 4.30). PGN-E / PGN-MBA-Km solution demonstrated a much larger increase in absorbance ratio which reached a plateau much earlier than was observed for any other sample. A red shift in the plasmon absorbance of PGN clusters was also observed in extinction spectroscopy analysis recorded at the end of the 16 hour period. These data indicate that a mixture of E and Km functionalized PGN is favourable for NP assembly and larger clusters were formed than with any other PGN heterogeneous mixture. Differences between PGN-E / PGN-MBA-K and PGN-Em / PGN-MBA-Km solutions were not as obvious, however a higher absorbance ratio and a small red shift in cluster plasmon absorbance was observed for Em / Km compared with E / K functionalized PGN.
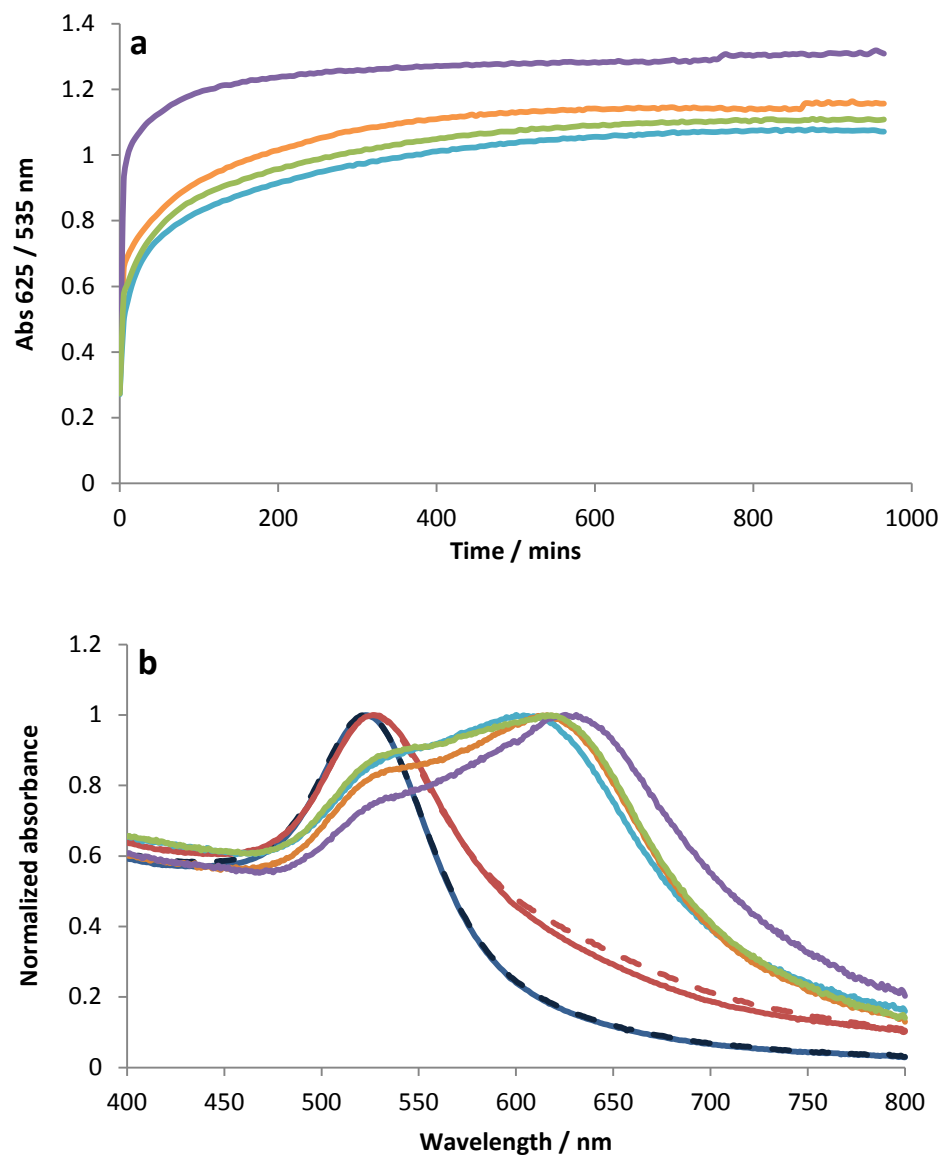
Figure 4.30 – Extinction spectroscopy analysis of PGN assembly. a) 625:535 nm absorbance ratio of PGN solutions monitored every 5 minutes for 16 hours. b) Normalized extinction spectra of homogeneous PGN solutions before analysis and of heterogeneous solutions following kinetic analysis. PGN-E (dark blue solid line), PGN-Em (dark blue dashed), PGN-MBA-K (red solid line), PGN-MBA-Km (red dashed), PGN-E / PGN-MBA-K (light blue), PGN-Em / PGN-MBA-Km (orange), PGN-E / PGN-MBA-Km (purple) and PGN-Em / PGN-MBA-K (green). Recordings represent PGN solutions at pH 7.

4.5 – SERS-active PSN preparation

NP assembly has thus far been demonstrated with heterogeneous solutions of PGN, detectable by extinction spectroscopy. SERS analysis provided more sensitive detection than extinction spectroscopy of MDM2-induced NP aggregation in chapter 3, however SERS analysis of coiled coil induced PGN assembly was inconclusive with MBA on AuNP. EDTA-reduced AgNP (AgEDTA) exhibit colloidal stability with higher SERS sensitivity than AuNP, thus they are an ideal tool for these studies.[157] BT functionalized AgEDTA conjugates have already proved successful in chapter 3. To this end AgEDTA was investigated to form stable PSN with the four previously described coiled coil forming peptides, using MBA as a Raman reporter.

AuNP and AgEDTA exhibit different surface chemistries due to the reduction methodologies employed in colloidal synthesis. Despite this many functional groups, including thiols, have shown affinity for both surfaces and both citrate reduced and EDTA reduced colloids have a net negative surface charge.[124, 186] The three-step functionalisation protocol was investigated to yield stable PSN-MBA-K and PSN-MBA-Km suspensions, however further adaptations were required to create AgEDTA conjugates.

4.5.1 – Optimizing AgEDTA and MBA concentrations

Colloidal AgEDTA was synthesised at lower concentrations than colloidal AuNP, therefore MBA and peptide concentrations required optimization before PSN conjugation could be addressed. AgEDTA sample concentrations of 15 pM were found to be optimal for MDM2-induced aggregation studies (chapter 3). With this in mind, AgEDTA solution concentrations were investigated for PSN conjugate solutions that could be diluted to 15 pM for NP assembly analysis. Various colloid (0.1 nM – 0.2 nM)

and MBA (0.1 μM – 2 μM) concentrations were mixed overnight to form AgEDTA-MBA conjugates (Ag-MBA). On day two samples were centrifuged, to remove any unbound ligand, and resuspended in H$_2$O. Following the determination of conjugate concentration, samples were diluted to 15 pM for analysis using extinction spectroscopy and SERS (figure 4.31).

Partial aggregation of some Ag-MBA samples was evident in extinction spectroscopy, characterised by a broadening and tailing, at longer wavelengths, of the plasmon absorbance peak (figure 4.31 a). SERS analysis of Ag-MBA samples was conducted before and after aggregation with spermine in order to highlight AgEDTA and MBA concentrations that gave rise to the largest SERS enhancement with aggregation. Signal intensities were quantified by monitoring the peak heights at 1071 cm^{-1} and 1585 cm^{-1} (figure 4.31 b). Ag-MBA conjugates prepared using 0.2 nM AgEDTA and 2 μM MBA showed the most stability in extinction spectroscopy and the largest increase in SERS when aggregated with spermine. PSN preparation via the three-step functionalization protocol was therefore adapted for these concentrations.
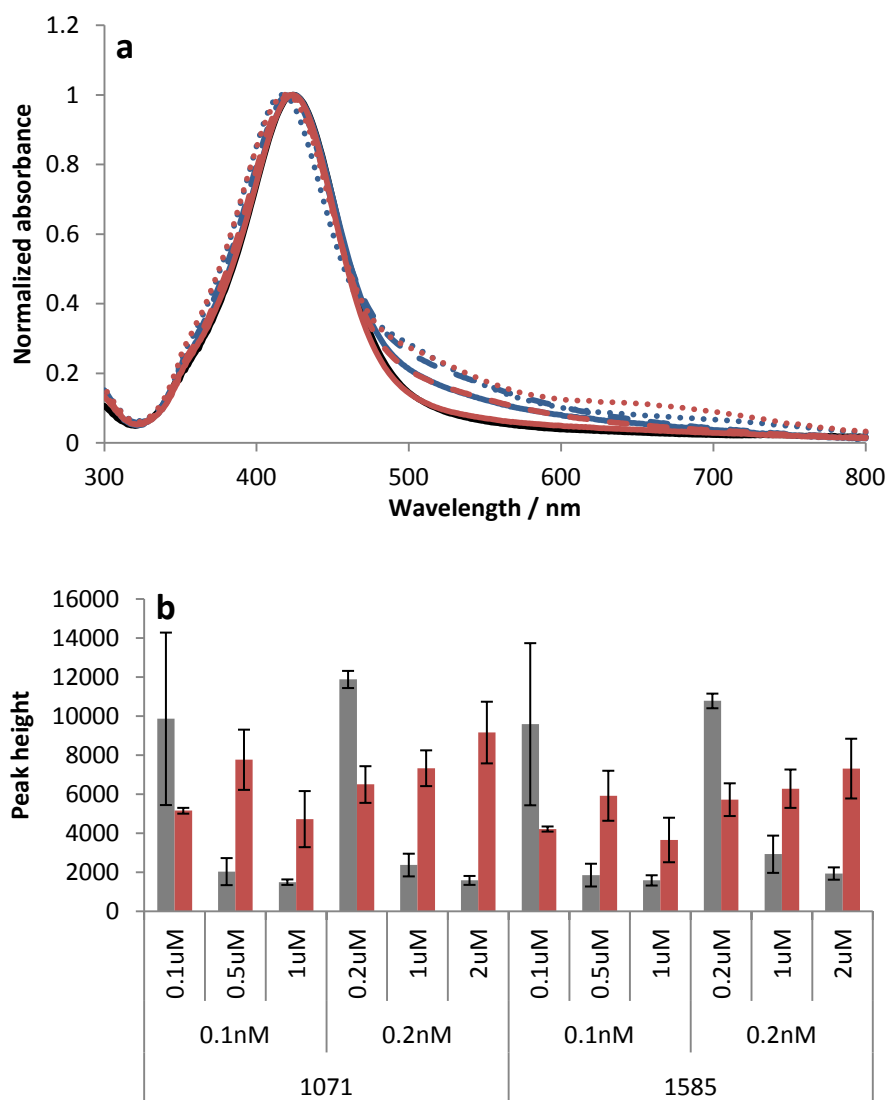
Figure 4.31 – a) Normalized extinction spectra of 15 pM AgEDTA (black) and Ag-MBA functionalized at various AgEDTA and MBA concentrations. 0.1 nM AgEDTA (blue) with 0.1 mM (dotted line), 0.5 mM (dashed line) and 1 mM (solid line) MBA. 0.2 nM AgEDTA (red) with 0.2 mM (dotted line), 1 mM (dashed line) and 2 mM (solid line) MBA. b) Average peak heights at 1071 cm^{-1} and 1585 cm^{-1} recorded in SERS analysis of Ag-MBA samples before (grey) and after (red) aggregation with Spermine. Five 1-2 second scans were recorded for each sample replicate using an excitation wavelength of 632.8 nm in SERS analysis. Recordings represent NP solutions at pH 7.

4.5.2 – AgEDTA and Ag-MBA stability over a pH range

Heterodimer coiled coil formation is susceptible to changes in pH owing to the electrostatic interactions between charged residues at positions e and g in the helical structure.[73, 74] Control of PGN assembly in heterogeneous solutions by pH manipulation has been detected using extinction spectroscopy.[220] One aim of this work was to investigate the effect of pH on PSN assembly and detect changes in the aggregation state using SERS. As a first step the Ag-MBA conjugates were analysed by extinction spectroscopy and SERS in a range of pH conditions.

Figure 4.32 illustrates extinction spectroscopy analysis of 15 pM Ag-MBA, which showed most stability in the pH range of 4-7. Partial aggregation was observed at higher pH values and conjugates were unstable at pH 3. AgEDTA alone also demonstrated instability in pH 3 solutions (data not shown). Surprisingly, SERS signal intensity of Ag-MBA samples is lowest at pH 3 where the suspension is least stable and highest at pH 5, shown to be one of the most stable by extinction spectroscopy (figure 4.32). These findings were taken into consideration when interrogating PSN assembly under different pH conditions.
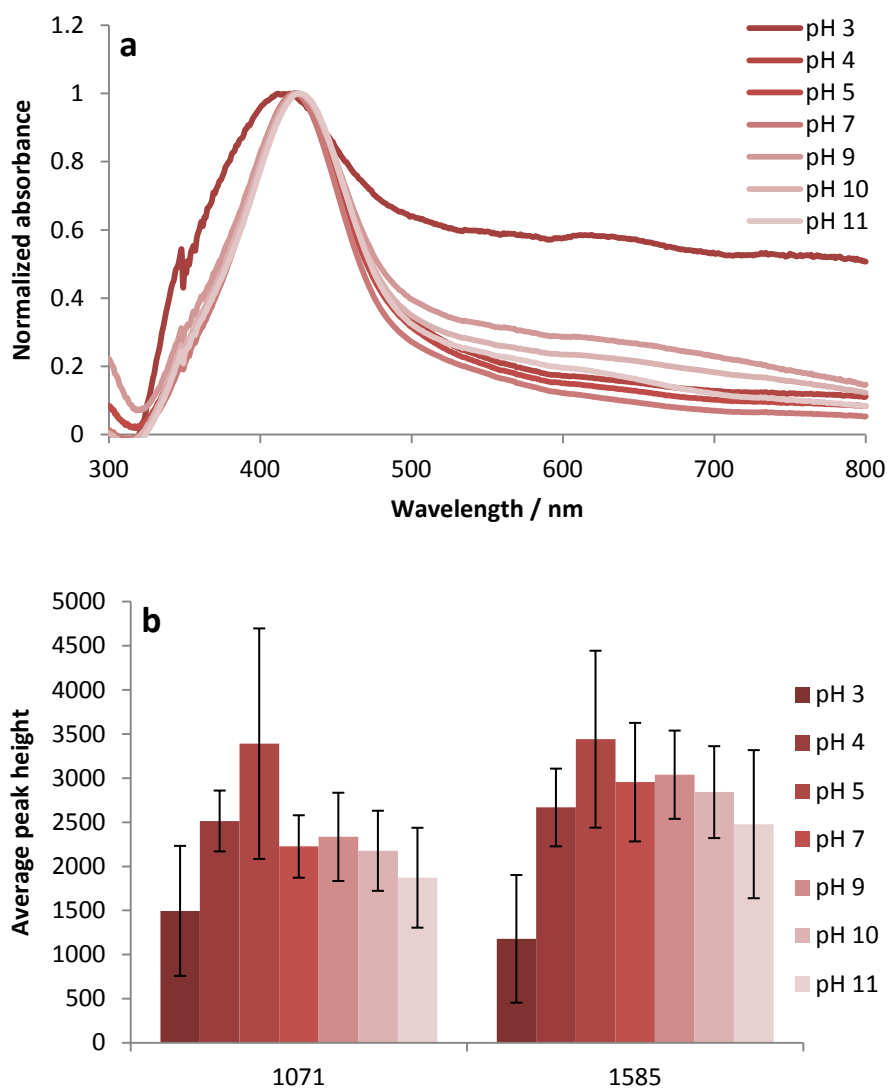
Figure 4.32 – a) Normalized extinction spectroscopy and b) Average peak height at 1071 cm^{-1} and 1585 cm^{-1} in SERS analysis of 15 pM Ag-MBA solutions. Five 1-2 second scans were recorded for each sample replicate using an excitation wavelength of 632.8 nm.

4.5.3 – SERS-active PSN

PSN-MBA-K preparation was achieved using an adaptation of the three-step functionalization protocol described for AuNP in section 4.2.5. Initially, concentrations were modified such that 2 μM MBA was added to 0.2 nM AgEDTA at pH 11 overnight. Following centrifugation and resuspension in H_2O, 0.2 nM solutions of Ag-MBA were adjusted to pH 11 and 2 μM peptide K added. The amount of HCl added in step three, one hour following peptide addition, was optimized and 1 μL 1 M HCl found to be sufficient to stabilize a 1 mL PSN solution. Resultant PSN-MBA-K displayed partial aggregation in extinction spectroscopy (figure 4.33), however solutions were used for further investigations as this effect was also seen in solutions of PGN-MBA-K. PSN-E were prepared by adding 2 μM peptide E directly to 0.2 nM AgEDTA at neutral pH, the resultant conjugates appeared monodispersed in extinction spectroscopy (figure 4.33).
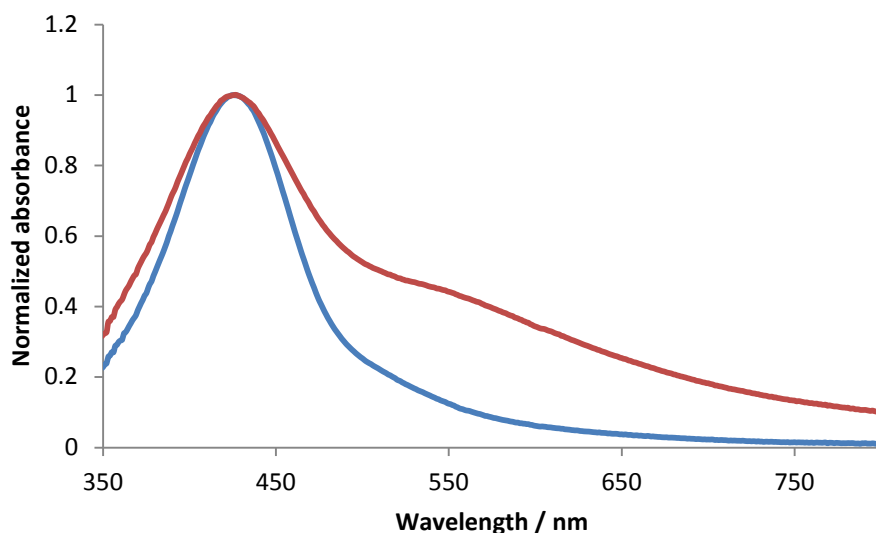
Figure 4.33 – Normalized extinction spectroscopy of 15 pM PSN-E (blue) and PSN-K (red), pH 7.

4.6 – PSN assembly induced by coiled coil heterodimerization

Extinction spectroscopy analysis of various heterogeneous PGN solutions in section 4.4 demonstrated an effect of immobilized peptide orientation on NP assembly. In order to monitor the different NP assembly processes by SERS, PSN conjugates were prepared with each of the four peptides (E, K, Em and Km). NP assembly in heterogeneous solutions was investigated via extinction spectroscopy and SERS.

4.6.1 – Peptide orientation

Heterodimeric coiled coil formation is driven by electrostatic interactions[73, 74] and consequently neutral pH provides the optimal conditions for heteroassociation. To that end, PSN assembly through interactions of differently orientated peptides was investigated using extinction spectroscopy and SERS at neutral pH (figure 4.34).

Heterogeneous solutions of PSN-E / PSN-MBA-K and PSN-Em / PSN-MBA-Km both demonstrated NP assembly at neutral pH, illustrated by increased absorbance at longer wavelengths in extinction spectroscopy and increased SERS intensity (figure 4.34). Heterogeneous and homogeneous PSN samples were subjected to SERS analysis at the same concentration, therefore PSN-MBA-K and PSN-MBA-Km SERS intensities do not reflect a direct comparison for mixed solutions where only 50 % of PSN contained a Raman tag, thus SERS enhancements would be larger than shown in this analysis. Solution dispersion changes were more pronounced for E / K functionalized PSN in extinction spectroscopy as these homogeneous PSN samples were more stable, however a low SERS increase was observed compared with Em / Km functionalized PSN. Despite the partial aggregation observed in the PSN-Em and PSN-MBA-Km homogeneous solutions, further assembly was observed in the heterogeneous solutions. A larger increase in SERS was obtained from Em / Km than for E / K

heterogeneous solutions even though extinction spectroscopy illustrated a similar extent of NP clustering. This could be an effect of the larger interparticle distances in clusters with coiled coil peptides perpendicular to rather than parallel to the NP surface.
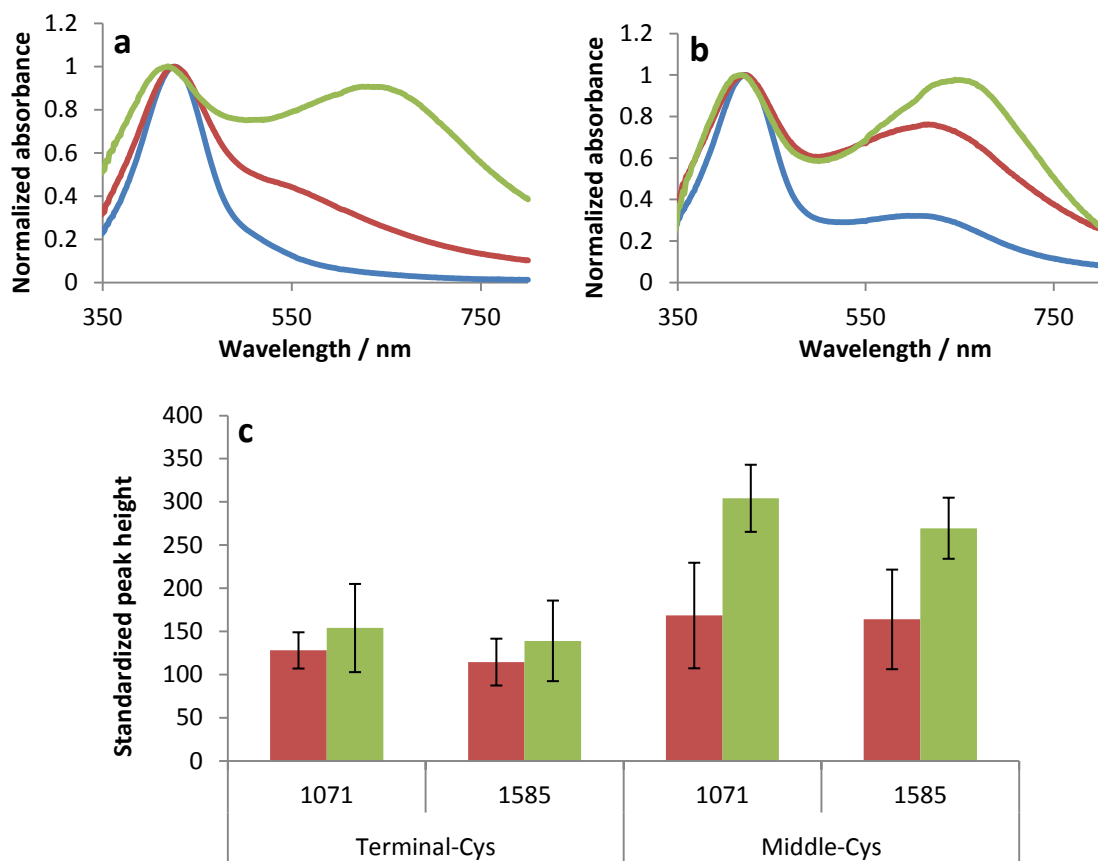
Figure 4.34 – Normalized extinction spectroscopy of a) PSN-E / PSN-MBA-K and b) PSN-Em / PSN-MBA-Km conjugate mixtures. PSN-E and PSN-Em homogeneous solutions (blue), PSN-MBA-K and PSN-MBA-Km homogeneous solutions (red) and heterogeneous mixtures of PSN-E / PSN-K and PSN-Em / PSN-Km (green). c) SERS standardized peak heights at 1071 cm^{-1} and 1585 cm^{-1} for 15 pM homogeneous solutions of PSN-MBA-K and PSN-MBA-Km (red) compared to heterogeneous solutions of PSN-E / PSN-MBA-K and PSN-Em / PSN-MBA-Km (green). PSN-E and PSN-Em homogeneous suspension SERS is not shown as no Raman tag is present. Five 1-2 second scans were recorded for each sample replicate using an excitation wavelength of 632.8 nm in SERS analysis. Recordings represent PSN solutions at pH 7.

4.6.2 – pH and PSN assembly

Section 4.6.1 describes PSN assembly in solution achieved through peptide-peptide interactions at neutral pH that was detected using extinction spectroscopy and SERS. SERS analysis of PSN assembly showed some discrimination between NP assemblies formed with differently orientated peptides. Owing to the electrostatic basis of the coiled coil peptide interactions, PSN assembly will potentially proceed differently depending on the solution pH.

PSN-E / PSN-MBA-K and PSN-Em / PSN-MBA-Km heterogeneous solutions were analysed using extinction spectroscopy and SERS over a pH range of 3 – 11. PSN assembly was observed in extinction spectroscopy for all pH values under pH 7. At pH 9 and pH 10 K / Km functionalized PSN were seen to assemble in homogeneous solutions. PSN clusters evident in mixed suspensions at these pH values can therefore not be attributed to heteroassociation. The stability of PSN-MBA-K and PSN-MBA-Km solutions appeared to be regained at pH 11 and PSN assembly in heterogeneous solutions was evident, albeit to a lesser extent than at neutral pH.

Peptides K and Km have an isoelectric point of 10.7 and as such some lysine residues will become deprotonated at pH 9 – 10. As the solution pH nears the pI of K / Km the positive charge will lessen, thus weakening the electrostatic repulsion of PSN resulting in clustering. At pH 11 lysine side chains on K / Km peptides will be deprotonated and therefore carry no charge, hence electrostatic repulsion is restored due to MBA molecules in the mixed monolayer. Heteroassociation with E / Em peptides in heterogeneous solutions is still possible through hydrophobic interactions alone but coiled coils will be less stable than at neutral pH. A similar effect was observed with PSN-E and PSN-Em (peptide pI of 2.9) solutions becoming unstable at pH 3 (figure 4.35), however this NP assembly can be partially attributed to the instability of AgEDTA and Ag-MBA at the same pH.
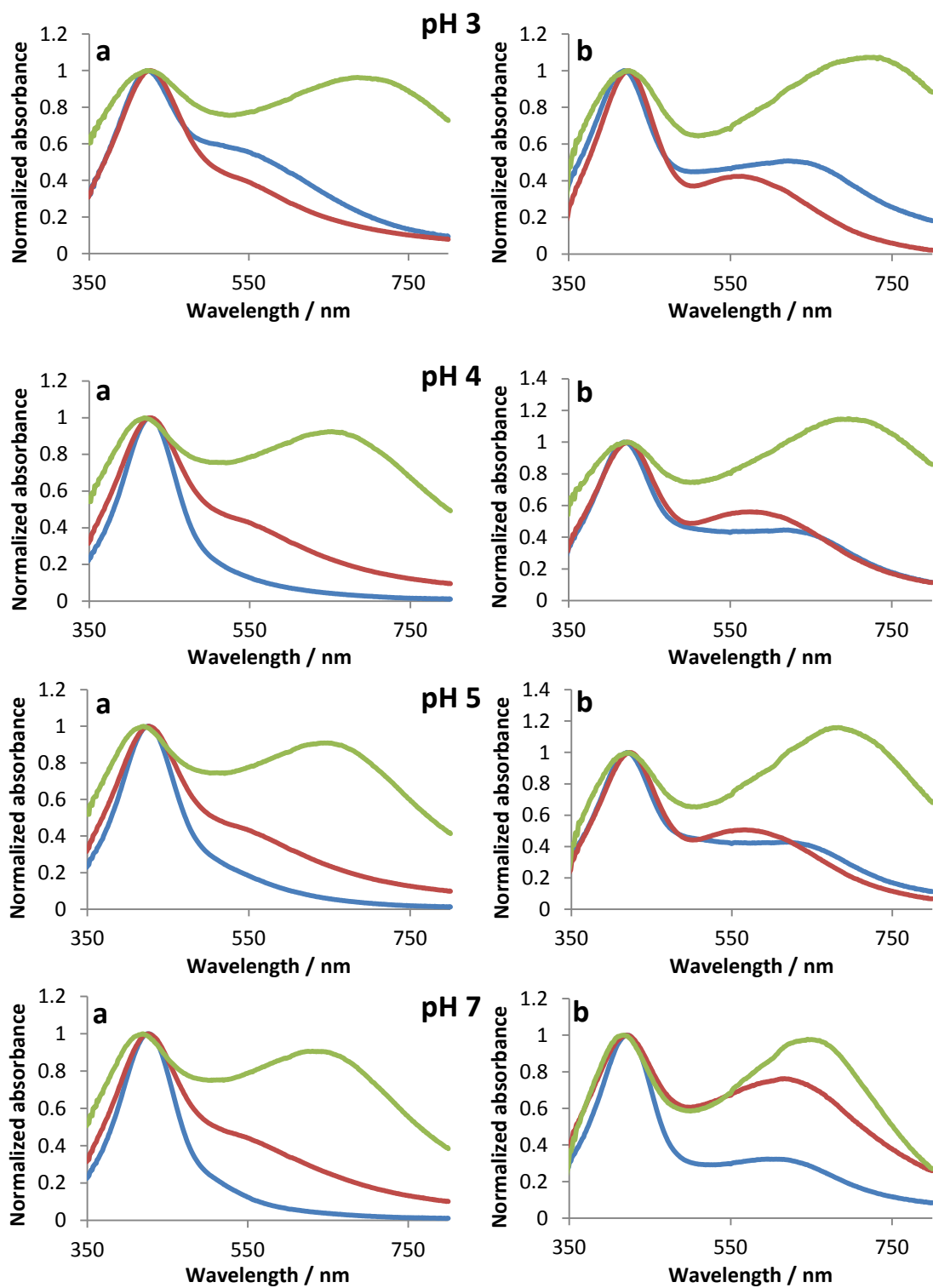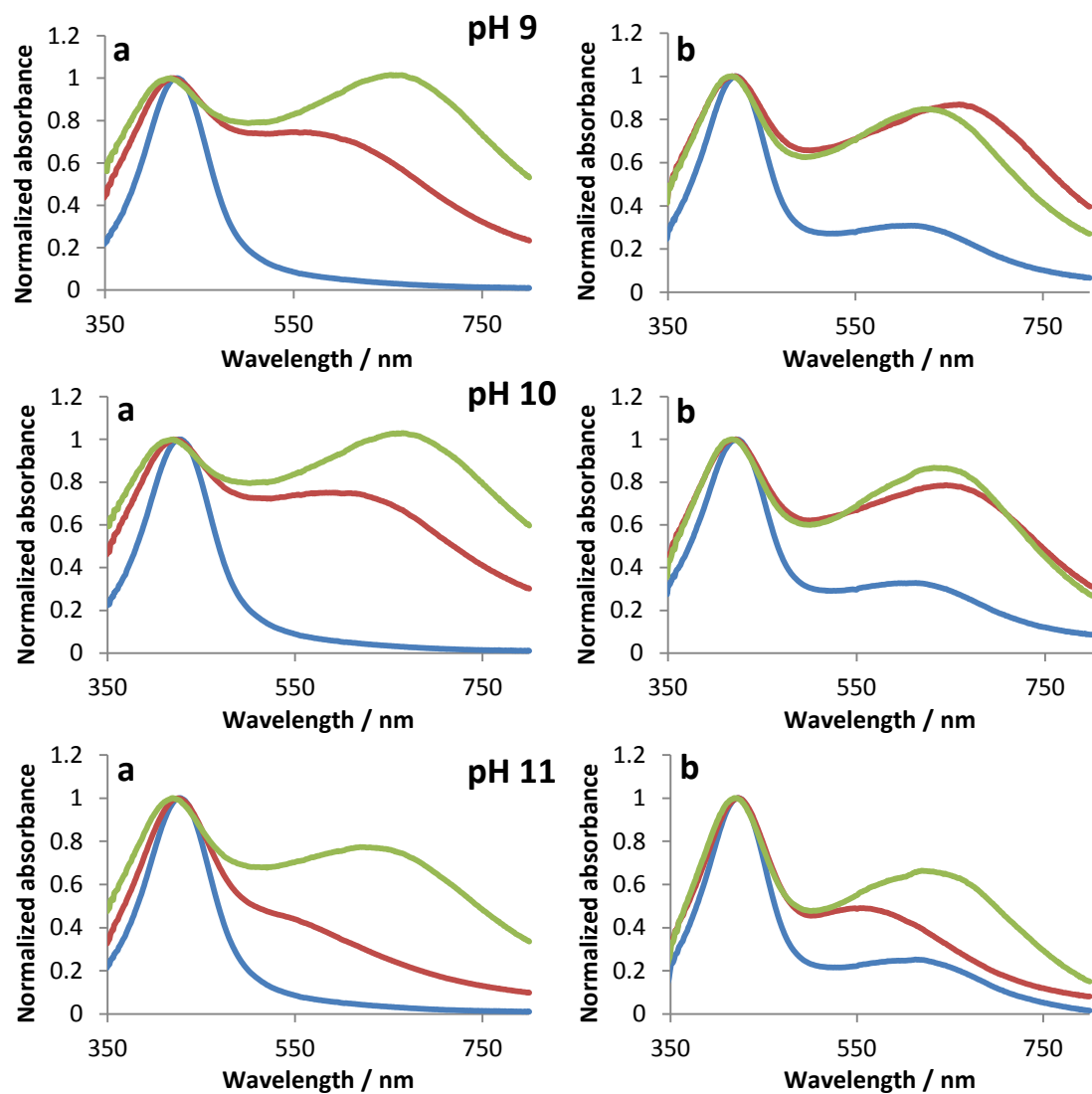
Figure 4.35 – Normalized extinction spectra of PSN conjugate solutions prepared with a) E / K and b) Em / Km. PSN-E and PSN-Em (blue), PSN-K and PSN-Km (red) and heterogeneous solutions of PSN-E / PSN-K and PSN-Em / PSN-Km (green) were analysed at pH values 3, 4, 5, 7, 9, 10 and 11.

The extent of aggregation seen in extinction spectroscopy was quantified using the absorbance ratio of 650:422 nm (figure 4.36). This quantification indicated that the largest extent of PSN assembly occurred at pH values 4 - 7 and 11. At pH 3, 9 and 10 the intrinsic instability of homogeneous solutions interfered with heterogeneous coiled-coil assembly.
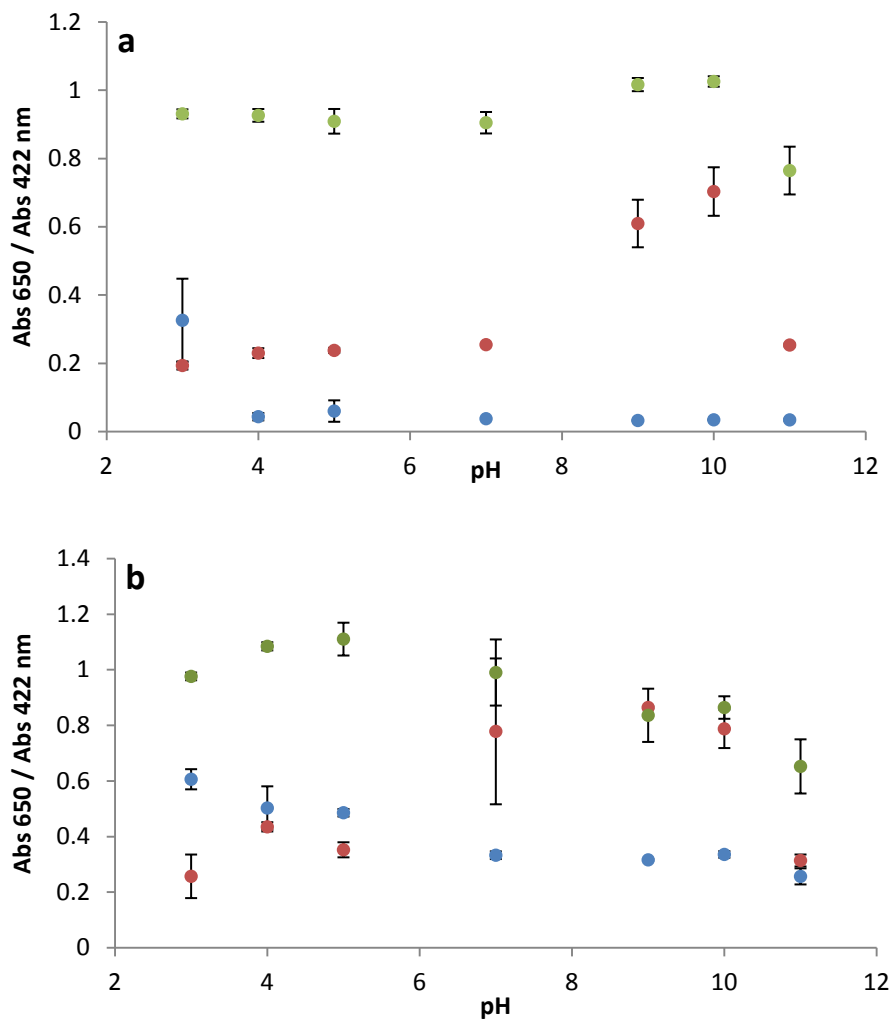
Figure 4.36 – Extinction spectroscopy analysis of a) E / K functionalized and b) Em / Km functionalized PSN over a pH range. Absorbance ratio of 650:422 nm for PSN-E / PSN-Em (blue), PSN-K / PSN-Km (red) and PSN-E / PSN-K and PSN-Em / PSN-Km mixtures (green). Error bars indicate the standard deviation of three replicate samples.

SERS analysis of PSN solutions showed an increase in signal intensity of heterogeneous solutions compared to homogeneous solutions (figure 4.37). As observed in extinction spectroscopy, the increase in SERS enhancement varied with pH and was largest at pH 5 and 7 for PSN-E / PSN-MBA-K and PSN-Em / PSN-MBA-Km solutions respectively. Despite the assembly of PSN-Em / PSN-MBA-Km observed at pH values 4 – 7 (figure 4.36 a), an enhancement in SERS was observed at only pH 7 in subsequent analysis (figure 4.37). Contrary to this, increases in SERS signal intensity were seen for heterogeneous PSN-E / PSN-MBA-K suspensions across the full pH range (figure 4.37). The SERS data for these samples correlate with the results from extinction spectroscopy analysis (figures 4.36 b and 4.37) The partial aggregation state of PSN-MBA-Km (figure 4.36 b) may provide an optimal SERS response and therefore no further signal enhancement is observed following the addition of PSN-Em.
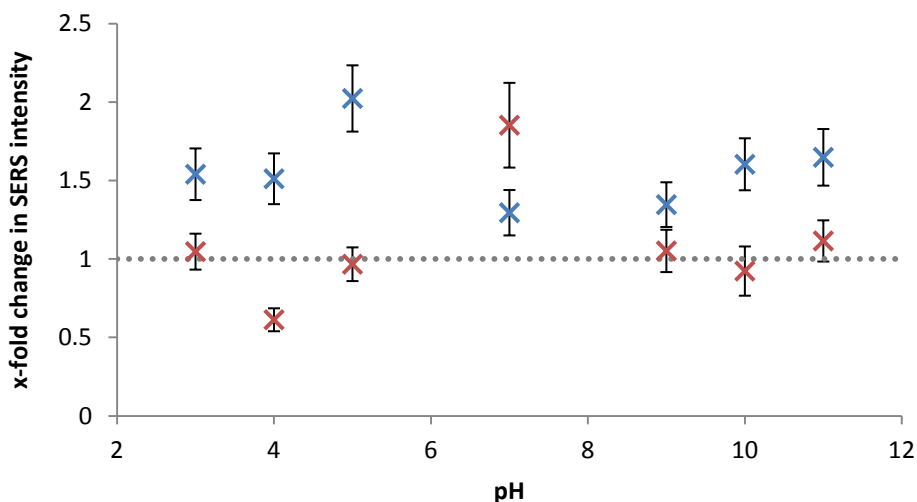
Figure 4.37 – x-fold change in SERS intensity monitored for 15 pM heterogeneous solutions of PSN-E / PSN-MBA-K (blue) and PSN-Em / PSN-MBA-Km (red) compared to homogeneous suspensions of PSN-MBA-K and PSN-MBA-Km respectively. Dotted line represents the SERS intensity of PSN-K and PSN-Km solutions before mixing with corresponding E and Em PSN. Error bars indicate the standard deviation in x-fold SERS change calculated using peak height measurements at 1074 cm^{-1} and 1585 cm^{-1}. Five 1-2 second scans were recorded for each sample replicate using an excitation wavelength of 632.8 nm in SERS analysis.

The extinction spectroscopy and SERS results acquired for Em / Km PSN solutions can possibly be explained, in theory, based on the protonation of MBA. MBA (pKa = 4.7) carries a negative charge at pH values 7 – 11 and will become protonated at pH values of 5 and below. At pH 7 – 11, Peptide Km interacts electrostatically with MBA on the NP surface thus causing the solution instability observed in extinction spectroscopy (figures 4.35 and 4.36). Although coiled coil formation occurs in heterogeneous solutions at neutral pH, the increase in SERS intensity is low due to high SERS obtained from unstable PSN-MBA-Km solutions. At pH 5 PSN-MBA-Km are monodispersed in solution due to the neutral charge on MBA ligands but peptide E (pI = 2.9) remains negatively charged, thus allowing for coiled coil induced PSN assembly and an associated SERS enhancement. The same theory applies for PSN-E / PSN-MBA-K solutions, however peptide orientation on the NP surface would disfavour electrostatic interactions with MBA. Peptide K is attached to the NP surface via a terminal cysteine, which is separated from the heptad repeat sequence by a two glycine residues. This provides a spacer region between the positively charged lysine residues and surface-bound MBA. The theory described here gives an explanation for the PSN assembly observed for PSN-E / PSN-MBA-K at pH values 4 – 7, however this doesn't provide any reasoning for the SERS data obtained at pH values 4 – 5. It could be speculated that electrostatic interactions occur between peptide K and MBA, at pH 7, causing the peptide to lie parallel to the NP surface. This would enable coiled coil heterodimer formation between PSN-E and PSN-MBA-K in the favoured parallel orientation, subject to steric hindrance when peptides extend perpendicularly from the surface (figure 4.3). Coiled coil formation in this manner would result in PSN clusters with smaller interparticle distances, similar to PSN-Em / PSN-MBA-Km aggregates, that are more optimal for SERS.

4.6.3 – PSN assembly kinetics

In order to assess the affect of pH on the rate of PSN aggregation, PSN assembly kinetics was investigated across the pH range (3 – 11). The aggregation state of heterogeneous PSN samples were monitored for 120 minutes immediately following mixing using the 650:422 nm absorbance ratio in extinction spectroscopy (figure 4.38).
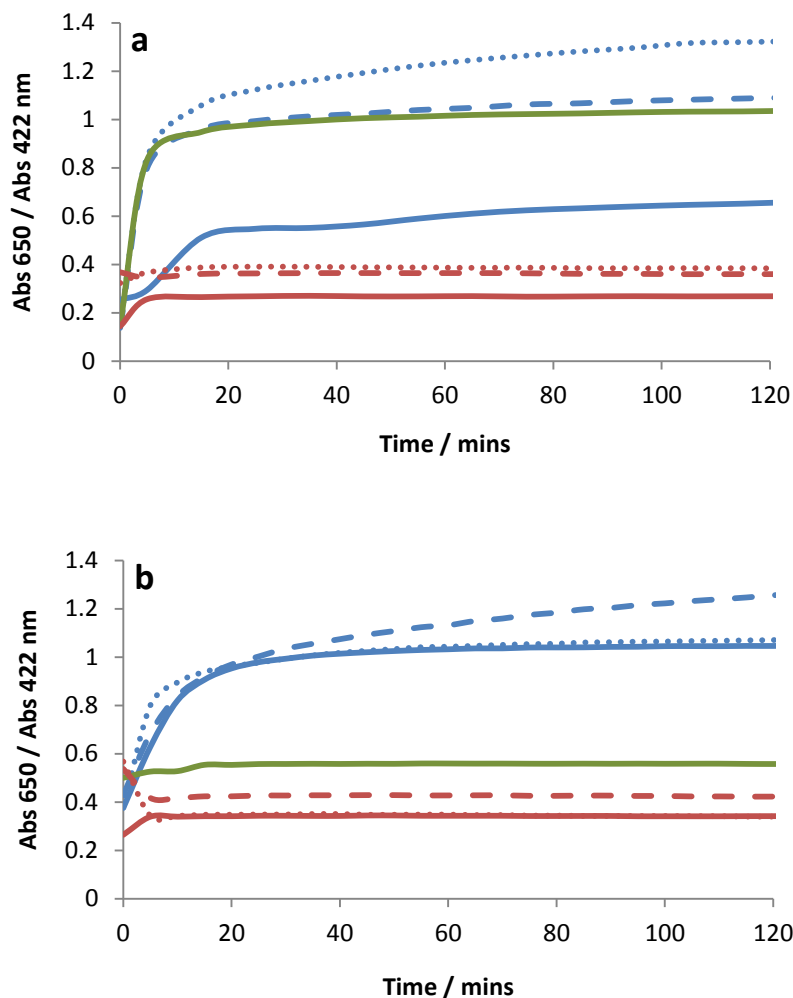
Figure 4.38 – Absorbance ratio of 650:422 nm measured every 5 minutes for two hours after mixing a) PSN-E / PSN-K and b) PSN-Em / PSN-Km at pH 3 (blue solid line), pH 4 (blue dashed line), pH 5 (blue dotted line), pH 7 (green), pH 9 (red dotted line), pH 10 (red dashed line) and pH 11 (red solid line).

Figure 4.38 demonstrates an increase in absorbance ratio of 650:422 nm recorded in extinction spectroscopy for all acidic and neutral solutions of PSN-E / PSN-MBA-K. This is representative of a decrease in absorbance at 422 nm and an increase in absorbance at longer wavelengths which is indicative of PSN assembly. Data obtained here are in accordance with extinction spectroscopy measurements (figure 4.36) which showed the greatest extent of PSN assembly at pH 4 – 7 for heterogeneous PSN solutions prepared with peptides E and K. An increase in the absorbance ratio (650:422 nm) was also evident for PSN-Em / PSN-MBA-Km samples under acidic conditions, in line with previous findings (figures 4.36 and 4.38). Contradictory to earlier findings, negligible changes in the absorbance ratio were observed for such heterogeneous solutions at pH 7. This can be attributed to the inherent instability of PSN-MBA-Km under neutral conditions (figures 4.35, 4.36 and 4.40). Minimal changes in the absorbance ratio of 650:422 nm were recorded for PSN-E / PSN-MBA-K and PSN-Em / PSN-MBA-Km suspensions at pH 9 – 10 (figure 4.38). As with PSN-Em / PSN-MBA-Km solutions at pH 7, homogeneous suspensions of PSN-MBA-K and PSN-MBA-Km displayed partial aggregation at basic pH values, therefore any additional aggregation would be difficult to observe (figure 4.35). Measurements recorded for all heterogeneous PSN samples demonstrated a small increase in the absorbance ratio (650:422 nm) indicating the occurrence of PSN assembly and again correlating with previous data (figure 4.36). This would suggest the formation of coiled coil heterodimers between negatively charged peptide E and deprotonated peptide K.

Aggregating heterogeneous PSN solutions showed an initial increase in the absorbance ratio of 650:422 nm in extinction spectroscopy. A plateau in the absorbance ratio (650:422 nm) was then observed to occur within 20 minutes. This indicates PSN assembly, resulting from coiled coil heterodimerization, reaches completion in 20 minutes.

4.7 – Inhibition of PSN assembly

PSN assembly reported so far in this chapter is thought to be the result of specific coiled coil heterodimerization. Assembly of PSN in heterogeneous solutions has demonstrated dependence on peptide surface orientation and pH and has been detected by extinction spectroscopy and SERS. In chapter 3 the inhibition of specific biological interactions prevented directed NP assembly. Analogous to the work carried out in chapter 3, inhibitor peptides E-Het (Ei) and K-Het (Ki) were introduced to PSN conjugate solutions to prevent the coiled coil directed assembly. Peptides Ei and Ki have the same design as E / Em and K / Km, respectively differing only in the absence of a cysteine residue for NP immobilization. These peptides are able to form coiled coils with NP-bound peptides, thus preventing interactions with other PSN conjugates. Figure 4.39 illustrates the molecular basis for the proposed PSN assembly inhibition.

Inhibitor peptides, Ei and Ki, were added to homogeneous solutions of PSN-MBA-K / PSN-MBA-Km and PSN-E / PSN-Em respectively 30 minutes prior to addition of differently functionalised PSN. This allows the free peptides to interact with NP-bound peptides rendering the PSN solution 'inert' to PSN assembly in a heterogeneous mixture. In initial studies inhibitor peptides were added at 100, 300 and 500 fold molar excesses to total NP concentration and samples analysed two hours following heterogeneous PSN mixing. Figure 4.40 illustrates the results obtained through extinction spectroscopy analysis.
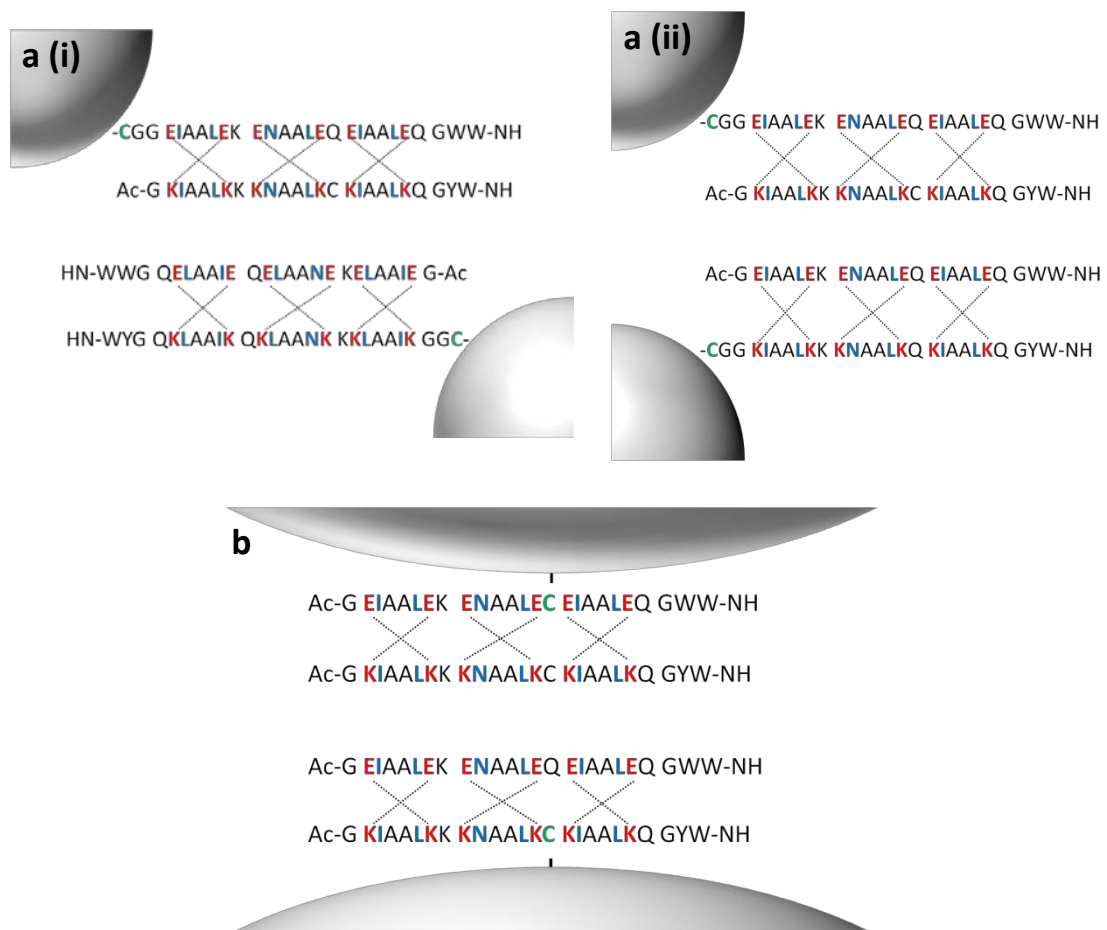
Figure 4.39 – Proposed inhibition of PSN assembly resulting from a) E and K peptides in i) parallel and ii) antiparallel coiled coil orientations and b) Em and Km peptides. Lines between peptide sequences indicate electrostatic interactions and residues involved in hydrophobic packing (blue), electrostatic interactions (red) and nanoparticle binding (green) are highlighted.
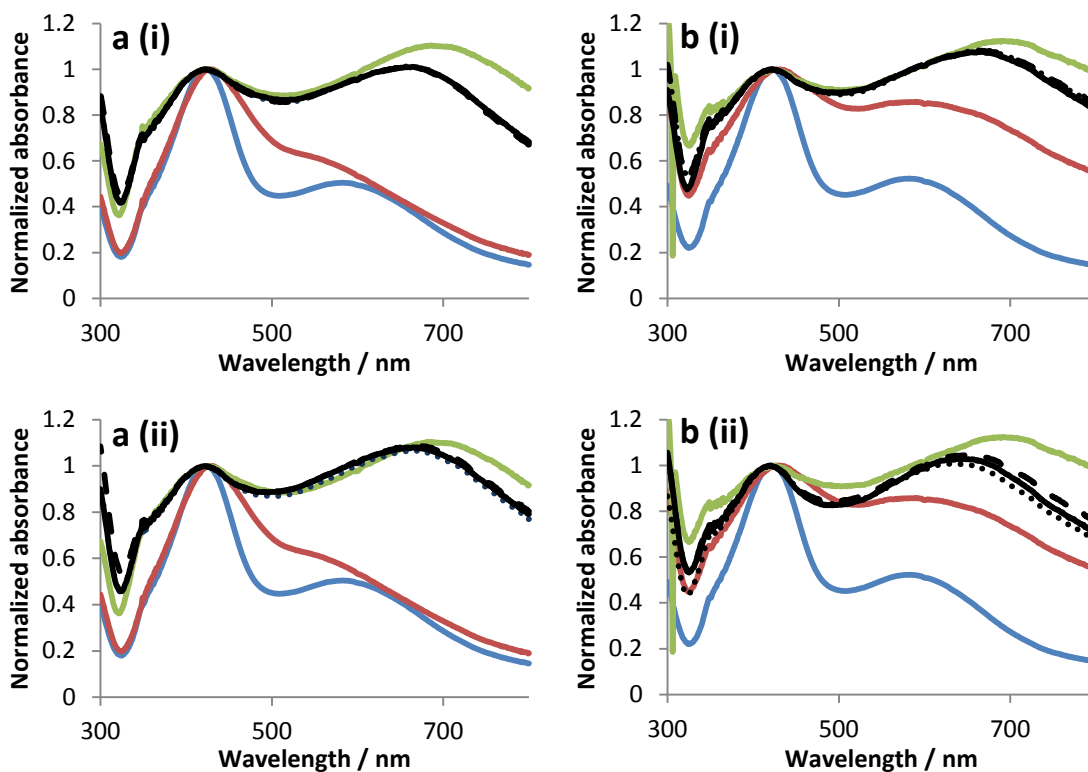
Figure 4.40 – Normalized extinction spectra of a) PSN-E / PSN-MBA-K and b) PSN-Em / PSN-MBA-Km with i) Ki and ii) Ei inhibitor peptides. PSN-E / PSN-Em (blue), PSN-K / PSN-Km (red), PSN-E / PSN-K and PSN-Em / PSN-Km without inhibitor (green) and with x100 (black dotted line), x300 (black dashed line) and x500 (black solid line) excess of inhibitor peptide:PSN. Data represent solutions at pH 7.

Prevention of PSN assembly was not evident in any of the samples, however a decrease in cluster size could be inferred, shown by a blue shift in the plasmon absorbance peak from ~700 to 650 nm (figure 4.40). This blue shift was most evident in PSN-E / PSN-MBA-K solutions in the presence of peptide Ki and PSN-Em / PSN-MBA-Km with peptide Ei. Further experimentation is however required before the blue shift, observed in figure 4.40, can be attributed to smaller aggregate formation as such extinction profiles may arise due to precipitation of larger clusters. Partial NP aggregation was seen in homogeneous PSN solutions containing oppositely charged inhibitor peptides (figure

4.41). This is likely due to mixed charges on PSN through interactions of Ei / Ki peptides with some of the NP bound peptide, lending to decreased electrostatic repulsion forces.
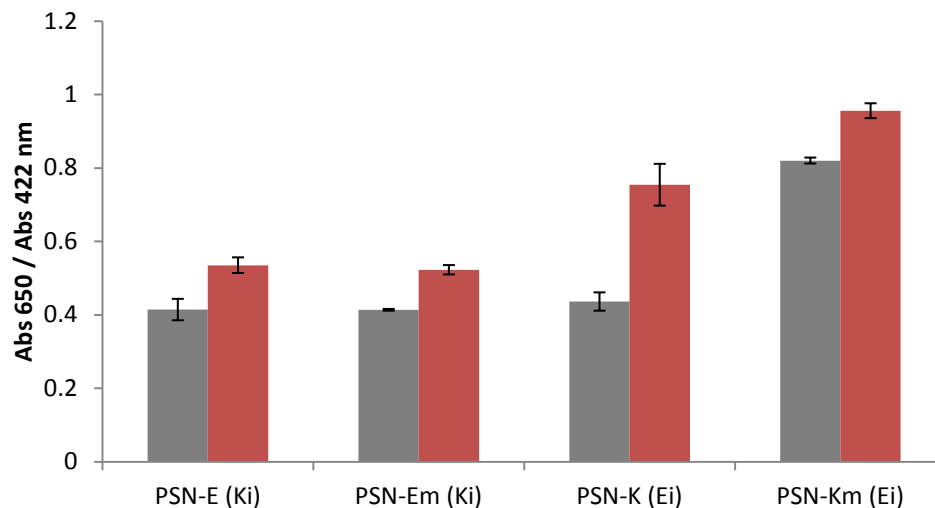
Figure 4.41 – Absorbance ratio of 650:422 nm recorded for PSN samples (pH 7) without inhibitor peptide (grey) and with inhibitor peptide specified in brackets (red) in extinction spectroscopy.

PSN assembly was observed in heterogeneous PSN samples containing up to 500-fold excess of inhibitor peptides (Figure 4.40). In order to completely eradicate PSN assembly enough inhibitor peptide is required to interact with all NP-bound peptides, for which 500 fold excess was insufficient. PSN samples were thus prepared with higher inhibitor peptide concentrations, 1000 and 2000 fold excess, and samples analysed using extinction spectroscopy and SERS. PSN-MBA-Km solution demonstrated a large extent of aggregation prior to addition of inhibitor peptides rendering the data obtained from PSN-MBA-Km / PSN-Em suspensions inconclusive. However, addition of peptide Ki to these samples appeared to stabilize the PSN clusters with an absorbance

maximum of ~600 nm. Extinction spectroscopy analysis of PSN-E / PSN-MBA-K illustrated an increase in PSN assembly following peptide Ki addition at both 1000x and 2000x excess. This provides evidence for PSN-E clustering resulting from sub-monolayer coverage of inhibitor peptide and non-specific electrostatic bridging which could result in further PSN assembly. A reduction in PSN assembly was observed for PSN-E / PSN-MBA-K heterogeneous solutions incorporating inhibitor peptide Ei (figure 4.42). This result signifies partial inhibition of PSN assembly through addition of Ei as proposed in figure 4.39. The extent of NP assembly illustrated in extinction spectroscopy was quantified using the ratio between 650 nm and 422 nm (figure 4.43a).
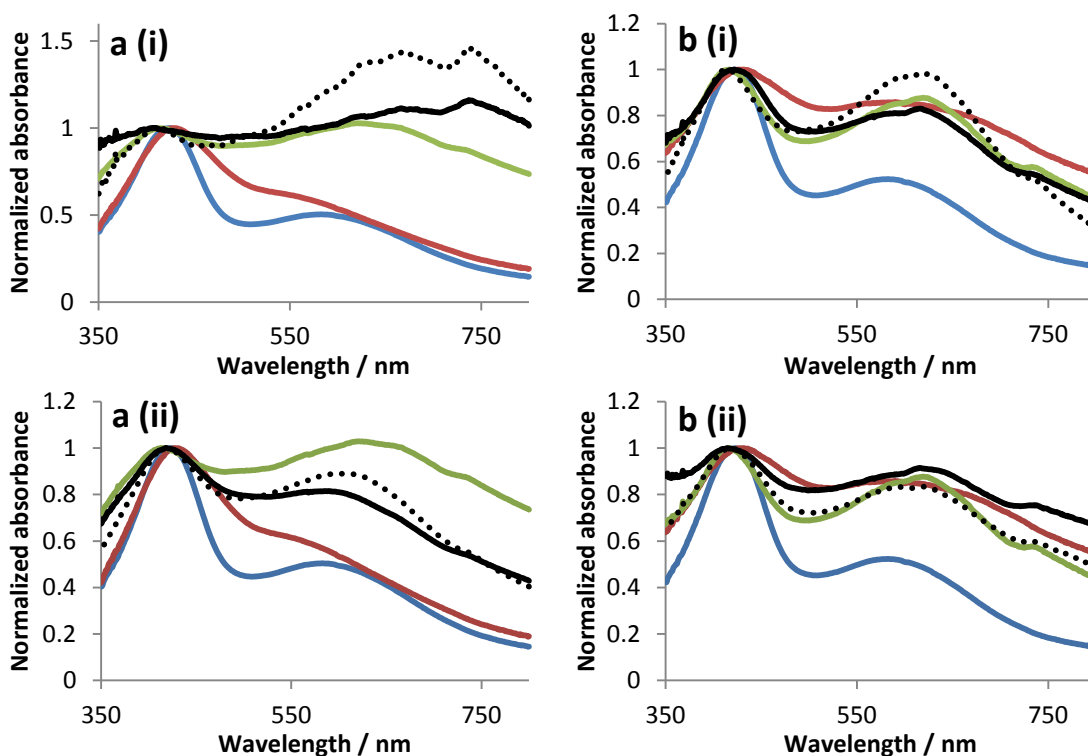

Figure 4.42 – Normalized extinction spectra of a) E / K PSN and b) Em / Km PSN mixtures with i) Ki and ii) Ei inhibitor peptides. PSN-E / PAN-Em (blue), PSN-K / PSN-Km (red), PSN-E / PSN-K and PSN-Em / PSN-Km mixtures without inhibitor (green) and with x1000 (black dotted line) and x2000 (black solid line) excess of inhibitor peptide:PSN. Data represent solutions at pH 7.

Heterogeneous PSN-E / PSN-MBA-K solutions exhibited a decrease in absorbance ratio which correlated with Ei inhibitor peptide concentration (figure 4.43a). This indicated that even greater excess of inhibitor peptide:NP, than 2000-fold, would be required for complete assembly inhibition. In this system inter-nanoparticle interactions occur both via coiled-coil formation and through non-specific electrostatic forces. To achieve complete inhibition of PSN assembly all NP-immobilized peptide molecules must be pre-bound to free peptides and electrostatic attractions between NP must be neutralized, requiring a large excess of inhibitor peptides. Absorbance measurements from PSN-Em / PSN-MBA-Km solutions indicated a reduction in PSN assembly with both Ei and Ki inhibitor peptides that is not observed for PSN-E / PSN-MBA-K suspensions (figures 4.42 and 4.43a).

PSN-Em / PSN-MBA-Km samples showed a decrease in SERS response with increasing inhibitor concentration in line with absorbance ratio measurements in extinction spectroscopy (figure 4.43). This effect was not immediatley evident in the full spectra from extinction spectroscopy, however Em / Km peptide orientations were found to be favourable for SERS analysis. In this instance, as with MDM2-directed PSN assembly (chapter 3), SERS may prove to be a more sensitive tool for monitoring small changes in PSN assembly. SERS data obtained for PSN-E / PSN-MBA-K suspensions contradicted the extinction spectroscopy measurements. PSN-E / PSN-MBA-K signal intensities were highest in the presence of inhibitor peptide Ei and lowest with Ki where extinction spectroscopy results indicated reduced and enhanced PSN assembly respectively (figures 4.42 and 4.43). The decrease in SERS signals with Ki could be explained by PSN aggregate precipitation. The orientation of E and K peptides on PSN was observed to be less favourable for SERS analysis of resultant assemblies compared to Em and Km.
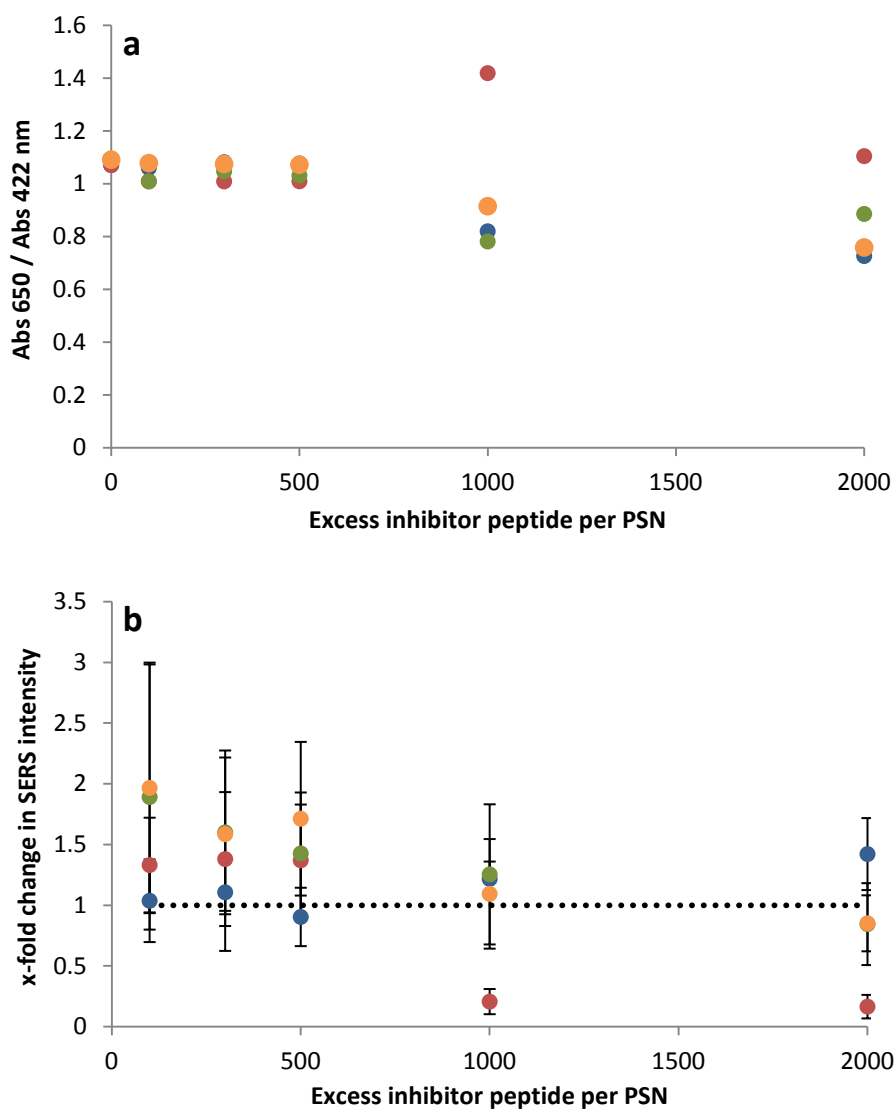
Figure 4.43 – a) Absorbance ratio of 650:422 nm recorded in extinction spectroscopy and b) x-fold change in SERS intensity of heterogeneous samples with varying concentrations of inhibitor peptides Ei and Ki. Heterogeneous solutions of PSN-E / PSN-K with Ei (blue) and Ki (red) and PSN-Em / PSN-Km with Ei (green) and Ki (orange) were analysed and recordings at time 0 in extinction spectroscopy and the dotted line in b) represent the mixed samples without inhibitor peptide. Five 1-2 second scans were recorded for each sample replicate using an excitation wavelength of 632.8 nm in SERS analysis. Data represent solutions at pH 7.

4.8 – Conclusions

The work in this chapter describes coiled coil directed assembly of peptide functionalized gold and silver nanoparticles. PGN and PSN were prepared with various coiled coil forming helical peptides exhibiting different charges and orientation on the NP surface. The small molecule, MBA, was incorporated into cationic NP conjugates to investigate the NP assembly process using SERS.

PGN assembly in heterogeneous solutions was observed using extinction spectroscopy, however SERS analysis was inconclusive. In order to obtain SERS detection of the NP assembly process, peptide conjugates were prepared employing AgEDTA in place of AuNP. Increased SERS intensities were observed with the PSN assembly in heterogeneous mixtures, correlating with extinction spectroscopy results. SERS analysis of PSN assembly demonstrated higher sensitivity in heterogeneous solutions of PSN-Em / PSN-MBA-Km compared with corresponding E / K suspensions, except at neutral pH. This was proposed to be a consequence of interparticle distances between assembled PSN resulting from coiled coil orientation. Each coiled coil heptad repeat is known to be approximately 1 nm in length, hence spaces between PSN in assemblies formed using terminally attached peptides will be between 3 and 4 nm. E / K peptides are designed with a terminal cysteine for NP immobilization and as such heterodimerized coiled coil peptides are likely to extend in a perpendicular orientation to the NP surface when MBA carries negligible charge. It was speculated that deprotonated MBA, exhibiting a negative charge, interacts with peptide K altering the surface orientation of the latter allowing heterodimer coiled coil formation parallel to the NP surface. Peptides Em and Km are designed to immobilize onto NP surfaces via a cysteine residue in the central heptad repeat. PSN assembly in these solutions is driven by coiled coil peptides forming parallel to the NP surface. Coiled coils formed parallel to the NP surface result in PSN clusters with much smaller NP spacings of approximately 1 nm. If this theory holds true, it can be proposed that the unfavoured anti-parallel coiled

coil orientation is adopted by peptides E and K in PSN assembly at pH 4 − 5, whilst parallel orientation is favoured under neutral conditions.

pH was investigated as an effecting factor of heterodimer coiled coil formation and PSN assembly. Homogeneous PSN solutions exhibited partial aggregation in pH conditions corresponding to the pI value of the immobilized peptides. This effect, detected using both extinction spectroscopy and SERS, is suggested to result from a weakening in NP electrostatic repulsion due to changes in the charged state of the immobilized peptides. PSN conjugates were observed to be most stable at pH 4 − 7. At these pH values peptides E / Em and K / Km are negatively and positively charged, respectively and PSN assembly was consequentially observed to be most pronounced within this range.

Finally, inhibition of PSN assembly was investigated through the incorporation of free coiled coil forming peptides. These peptides were designed to form coiled coils with NP-bound peptides, thus preventing interactions with other PSN in the solution. A reduction in PSN assembly based on coiled coil formation between peptides E and K was observed with the addition of >1000 x excess of inhibitor peptide Ei. Inhibitor peptide Ki was shown to increase PSN assembly in the same samples indicating a possible effect of non-specific peptide interactions. SERS data obtained for solutions of PSN-E / PSN-MBA-K solutions showed little correlation to extinction spectroscopy analysis. Inhibition of PSN assembly directed by Em / Km peptides was not observed in the spectra obtained in extinction spectroscopy, however absorbance ratio measurements and SERS data indicated marginal changes in the PSN assembly state. These results provide further evidence for a critical internanoparticle distance, between 1 and 3 nm, for effective PSN assembly monitoring.

4.9 - Future work

Coiled coil PSN assembly, directed by coiled coil formation, has been achieved which can be monitored using extinction spectroscopy and SERS, however the area of research is relatively new and as such potential further work is extensive. In order to increase reproducibility and reliability of the system experimentation is required to optimize PSN conjugate stability.

Time course investigations of PSN aggregation with and without inhibitor peptides could potentially elucidate a more detailed analysis of the assembly process. These experiments would then need to be run in parallel with SERS time course studies such that direct comparisons between extinction spectroscopy and SERS are available for all stages of PSN assembly. PSN assembly monitoring in this was could also provide evidence for optimal NP spacing required for sensitive SERS detection. Employment of electron microscopy techniques may provide an insight into NP spacing in this system, which could be further studied by repeating experimentation with coiled coil peptides comprising one or two heptad repeats. Three heptad repeats are known to be required for stable coiled coil formation, however NP-bound peptides of a shorter length may form more stable dimers resulting from additional thermodynamic forces present in NP solutions.

Thus far, inhibition of PSN assembly has been investigated by adding inhibitor peptides to pre-formed PSN conjugates. Using this methodology, occupation of peptide binding sites on the NP surface may be problematic. Further studies should investigate pre-mixing of NP binding peptides with free peptides before NP functionalisation. This would ensure all NP-bound peptides are in coiled coil dimer formation before PSN heterogeneous solutions were mixed minimizing the propensity for PSN assembly.

Chapter 5 – Microfluidic SERS mapping of NP aggregation

5.1 – Introduction

This chapter documents preliminary investigations, carried out to ascertain the potential for real-time monitoring of biologically driven NP assembly in microfluidic channels using SERS. The experimentation was conducted in order to develop technology allowing for more in-depth analysis of the MDM2-mediated PSN assembly described in chapter 3.

Owing to small dimensions and consequentially high surface-volume ratio, microfluidics has proved advantageous for molecular analysis and reaction monitoring. Reaction volumes associated with microfluidic devices allow for highly sensitive detection of solution components and quantitative interrogation of diffusion coefficients from molecular redistribution between two streams of solution in laminar flow. Analysing reactions in continuous homogeneous flow has also been shown to greatly improve the reproducibility of SERS measurements allowing highly sensitive and information rich data from this readout technique on a quantitative basis.

5.1.1 – Flow-injection reaction monitoring using SERS

Combining SERS analysis with microfluidic reaction volumes gives the potential for highly sensitive detection of NP assembly, however it can be difficult to attain reproducible results. This variability can be addressed by reducing the reaction volume and introducing flow to the system. Flow-injection sampling was first investigated in the late 1990's and has been coupled with detection techniques such as fluorescence flow cytometry and quench-flow analysis, to observe rate kinetics for sub-millisecond reactions.[227, 228] *Dou et al*. introduced Raman detection for quantitative rate

measurements of glucose oxidase catalysed reactions in a quartz sampling system.[229] *Freeman et al.* yielded reproducible analysis of complex solutions by integration of SERS with a flow-injection liquid chromatograpy separation system.[230] Following on from this *Taylor et al.* compared the reproducibility of droplet, cuvette and flow-injection sampling modes for SERS investigations of dilute aqueous solutions, of which the latter proved paramount.[231] In this study a limit of detection for crystal violet of 1×10^{-12} M was shown with a variation coefficient of 2.37 % of the mean for replicate samples.[231] Over the past 15 years Raman probing of microfluidic platforms has become increasingly studied owing to the high sensitivity and reproducibility illustrated in these initial investigations.[231]

5.1.2 – Effective mixing in microfluidics

As aforementioned in chapter 3 (section 3.4.3.3) effective mixing of solutions is required to obtain reliable SERS analysis of NP assembly. The small dimensions and low flow-rates associated with microfluidic platforms typically mean that fluids within the system exhibit a low Reynold's number and as such laminar flow is induced when two solutions are mixed at a t-junction.[232] Laminar flow can be described as the phenomenon whereby two streams of solution merge and flow adjacently with no convective mixing between solutions.[232] The only molecular transport between two streams in laminar flow occurs via diffusion and as such the region between these streams is termed the 'interdiffusion region'.[232] Investigative studies of molecular interactions in laminar flow has enabled the determination of rate kinetics and diffusion characteristics of interacting molecules,[232] however in most cases mixing of the two solutions is induced to drive the reaction forward. Numerous microchannel designs have been investigated to induce turbulent flow and promote fluid mixing in laminar flow.[233-237] Chaotic advection has been induced by the introduction of multiple bends in the channel in 3D designs[233-235] whilst other designs used transverse

components on the channel floor.[237] Zigzag microchannels induce passive mixing via the recirculation phenomenon[236] and this design bears the most resemblance to the serpentine channel design, used in this investigation, that incorporates multiple 180° channel bends. Mixing characteristics in a microchannel can be monitored by confocal fluorescence microscopy (CFM), however confocal Raman microscopy (CRM) has also emerged as a powerful tool for this purpose.[238, 239] By mapping the area across a microfluidic channel CRM can extract structural changes occurring in chemical reactions that cannot be mapped using CFM.[238] CRM has also been effectively utilized to quantitatively monitor the interdiffusion process of two pure solutions.[239]

## 5.1.3 – Raman and Surface-enhanced Raman reaction monitoring on a chip

To date, a number of studies have been published demonstrating the potential of SERS for the monitoring of biological molecules on a chip. Raman spectroscopy has been used as a detection technique for enzyme reaction monitoring in a flow-injection sampling system.[229] Continuous-flow reaction monitoring using Raman in microfluidics is becoming more widely used in a number of biological and chemical applications.[240-243] Chemical applications include both single and multi-stage organic synthesis reaction monitoring[241, 242] whilst biological applications point towards diagnostic assays and drug quantitation.[240, 243] Initial investigations into the use of SERS substrates for detection in microfluidics included *in situ* formation of silver nanoparticles utilizing the interdiffusion region in laminar flow.[244] Introduction of a dye downstream of colloid formation yielded reproducible detection with a femtomolar limit of detection across the interdiffusion region.[244] This set-up is however not suitable for reactions requiring complete mixing of substrate solutions. The first instance of SERS multiplexing in a microfluidic device was published by Docherty *et al*. in 2004 who demonstrated

simultaneous detection of three labelled oligonucleotides.[245] Subsequent to this *Park et al*. employed confocal SERS for the quantitative detection of two labelled oligonucleotides demonstrating a 10^{-11} M detection limit.[246] Diagnostic assays for infectious diseases have also been developed in which labelled detection probe concentration is monitored after heat induced release from bead-immobilised target DNA.[243] In a different approach Popp *et al*. have developed a microfluidic system whereby analyte flow has is segmented using oil droplets.[247] A highly desirable property of this system is that the oil droplets prevent NP residue collecting on the microchannel walls therefore omitting the need for nitric acid cleaning of chips between measurements.[247] The droplet microfluidics design has been used with SERS for the quantification of low-concentrated drugs as well as Raman analysis to successful discriminate between nine *E.coli* strains.[240, 248]

5.1.4 – Microfluidic immunoassays

A number of microfluidic immunoassays have been developed for microfluidics for the detection proteins and bacteria.[249-253] These assays incorporate colorimetric, fluorescence, impedance and electrophoretic measurement technologies and all take advantage of a surface immobilisation step.[249-253] Raman has been employed for bacterial strain discrimination and SERS has been employed in DNA-based diagnostic assays as described in 3.1.3.[243, 248] To date there have been no publications whereby protein interactions have been studied via SERS detection in microfluidic technologies.

5.1.5 – Proposed microfluidic platform for monitoring NP assembly
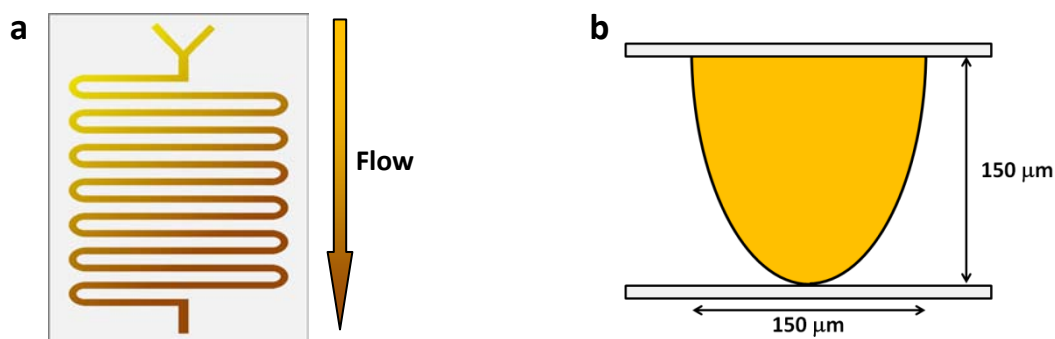
Figure 5.1 – a) Schematic of the microreactor chip and b) a channel cross-section. Proposed mixing-induced aggregation of NP is shown by a colour change in solution (yellow - brown).

Controlled nanoparticle aggregation has been achieved in solution via specific protein-peptide interaction (chapter 3). This has proven to yield reproducible results, however respective to other similar assays a relatively large volume and excess of protein is required, per nanoparticle conjugate, for a significant amount of aggregation to occur. Highly sensitive and reproducible analysis of chemical reactions has been achieved by CRM of continuous flow in microchannels.[238, 239] As such it was proposed that CRM mapping of nanoparticle assembly in a microfluidic platform would reduce sample volume and enable MDM2 detection at lower concentrations. A simple 2D serpentine channel design was investigated with two inlets and one outlet (figure 5.1). The microchannel, described in chapter 8, had a total internal volume of 13 μl and was set up in a microscope slide chip such that it was adaptable to various analytical instruments. Nanoparticle conjugate and aggregate solutions were introduced through the two inlet ports and CRM analysis of the mixing solutions is carried out following merging of the two channels. It was hypothesised that nanoparticle assembly,

controlled by passive mixing in the microreactor, could be interrogated by Raman mapping of flow through the microfluidic device.

5.2 – Point Raman mapping across a microchannel

Preliminary studies were conducted prior to mapping analysis in order to decipher optimal conditions for the aggregation study. Firstly, a suitable reporter molecule needs to be used that is Raman active at the excitation wavelength of the mapping instrument. It is then crucial to ensure that successful Raman mapping of nanoparticle conjugates can be achieved in a microchannel format.

5.2.1 – Near-IR Raman linker for mapping at 784.6 nm

Using the experimental set-up available in-house, Raman mapping was conducted using an excitation wavelength of 784.6 nm. Thus far, SERS analysis in chapters 3 and 4 has been carried out using shorter excitation wavelengths (514.5 nm / 632.8 nm) and the reporter molecules used do not exhibit resonance when employing an excitation wavelength of 784.6 nm. Hence, an in-house near-IR linker was conjugated to NP for microfluidic SERS interrogation. Owing to the success of PSN assembly detection in chapters 3 and 4, AgEDTA NP were also used. Figure 5.2 shows the structure of the near-IR linker which attaches to metal surfaces via the thioctic acid moiety.
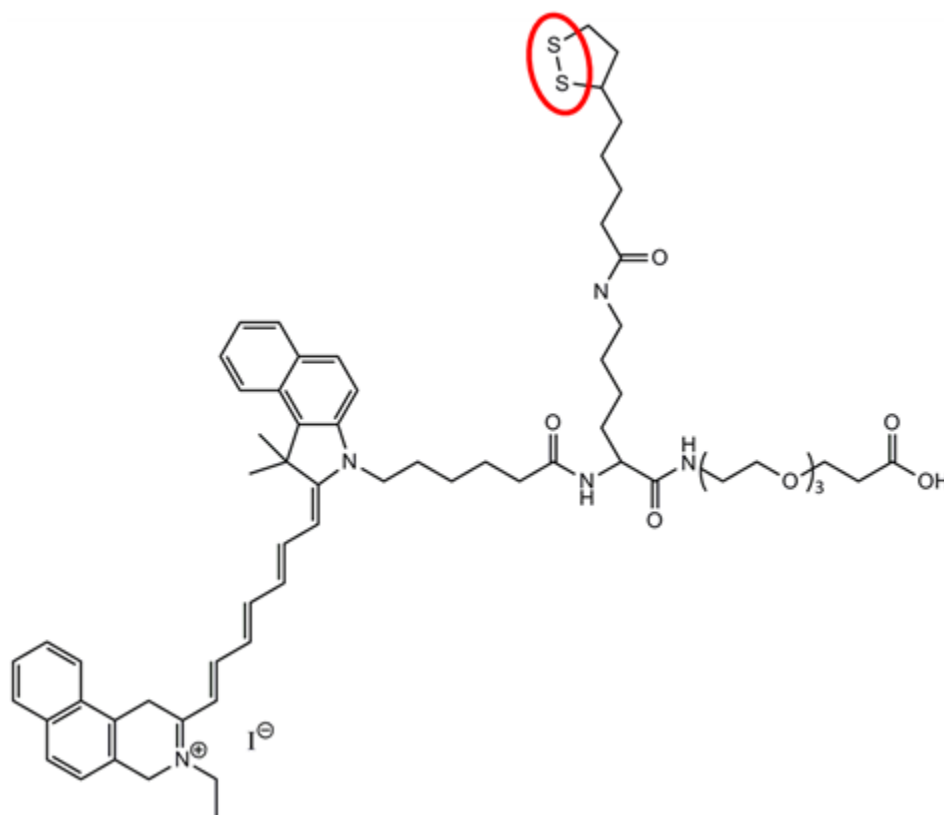
Figure 5.2 – Molecular structure of the near-IR Raman linker. Red circle indicates the thioctic acid group.

In order to identify spectral peaks for Raman mapping, extended scans of aggregated AgEDTA-IR (Ag-IR) acquired using the Raman mapping instrumentation focussing on the bulk of the solution. Aggregation was induced by adding 10 μL aggregating agent (1 M MgSO$_4$) to 500 μL Ag-IR (~0.2 nM). Raman analysis of Ag-IR showed numerous spectral peaks, of which the two sharpest and most intense were highlighted, occurring at Raman shifts of 296 cm^{-1} and 586 cm^{-1} (figure 5.3). Observation of these spectral peaks showed Ag-IR to be a suitable NP conjugate for use in the preliminary studies of microfluidic NP assembly analysis. Ag-IR suspensions were suspended in buffer (10 mM phosphate buffer, pH 7.5) for all microfluidic analysis.
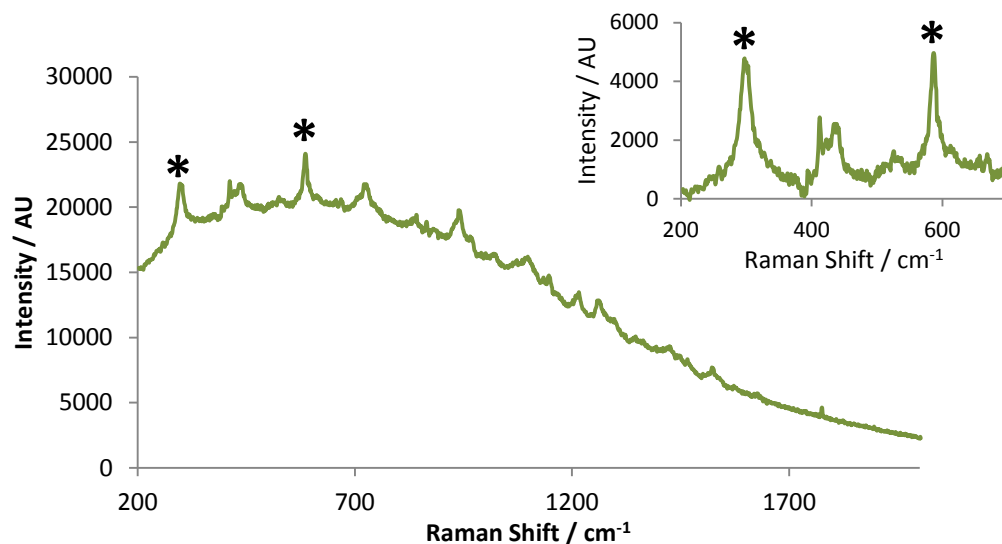
Figure 5.3 – Raman spectra of aggregated Ag-IR bulk solution. Extended scans were obtained using an excitation wavelength of 784.6 nm. Inset illustrates corrected Raman spectra over a small region and stars depict Raman peaks for potential aggregation monitoring.

5.2.2 – Point mapping of NP solutions across a microchannel

Raman signals acquired from Ag-IR solutions in a microchannel were initially investigated using point mapping. Various solutions were introduced into a microreactor and point measurements obtained from the centre of a single microchannel. Figure 5.4 illustrates the Raman spectra obtained from analysis of the different solutions along with the peak heights at 586 cm^{-1}. Raman peaks were only observed in the presence of Ag-IR verifying the absence of signal interference from buffer or aggregating agent (1 M MgSO$_4$) as expected. Fluorescence quenching in the solution of aggregated nanoparticles was evident and analysis showed a notable difference in observed peak height intensities at 586 cm^{-1} between aggregated and unaggregated samples (figure 5.4). Signal intensities for Ag-IR (~0.2 nM) were observed to be higher than for Ag-IR diluted in buffer (~0.1 nM) owing to the difference in concentration (figure 5.4).
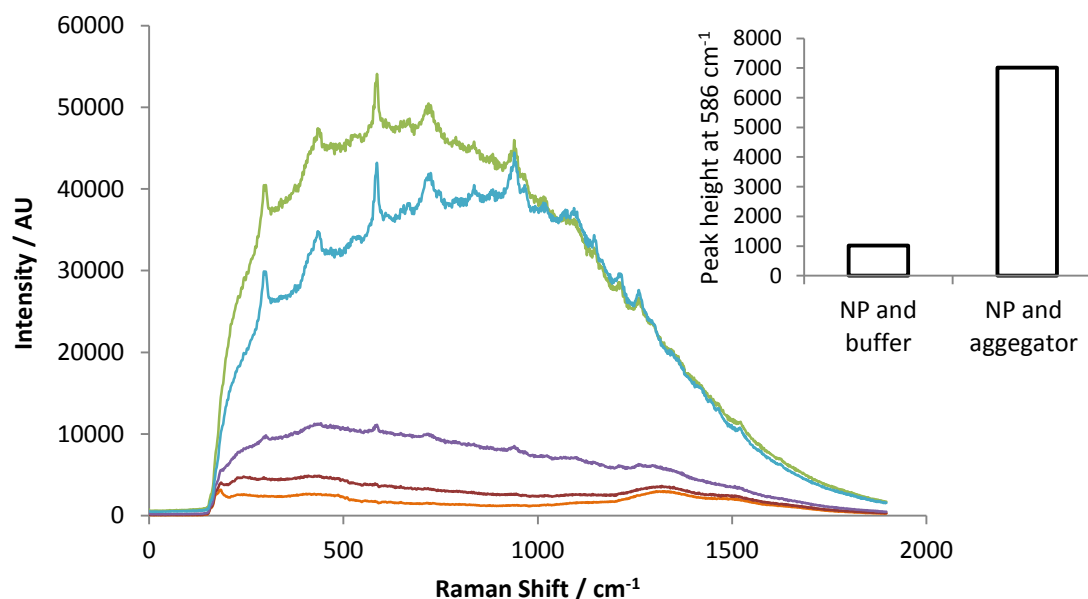
Figure 5.4 – Raw Raman spectra of 10 mM phosphate buffer (orange), aggregator (1 M MgSO$_4$) (brown), 0.2 nM NP (green), 0.1 nM NP (purple) and 1:1 NP:aggregator (blue). Final NP concentration of 0.1 nM in 1:1 NP:aggregator samples. Inset shows peak height measurements at 586 cm^{-1} for NP solutions diluted in buffer and aggregator. Raman analysis was conducted using an excitation wavelength of 784.6 nm and a 50 ms scan duration.

Point Raman mapping across the microchannel width showed signal intensities to be highest in the centre and dampening towards the edge (figure 5.5). Relative fluorescence background remained constant throughout the width of the channel. The consistency of Raman signal intensity in continuous-flow analysis was investigated by taking measurements at a central position in the microchannel every 15 seconds for 5 minutes. As demonstrated in figure 5.6, the peak height at 586 cm^{-1} remained constant over a 5 minute period, after which measurements were aborted due to a blockage which occurred at the point of the laser beam. It was theorised that under constant interrogation at the same channel position some nanoparticles became trapped or deposited under the laser focus thus creating a blockage in the channel, however this

has not been proven experimentally. Blockages of this nature can be cleared by washing the microchannels with aqua regia and should not impact on streamline Raman mapping as the laser focus will not be directed at one position for any length of time.
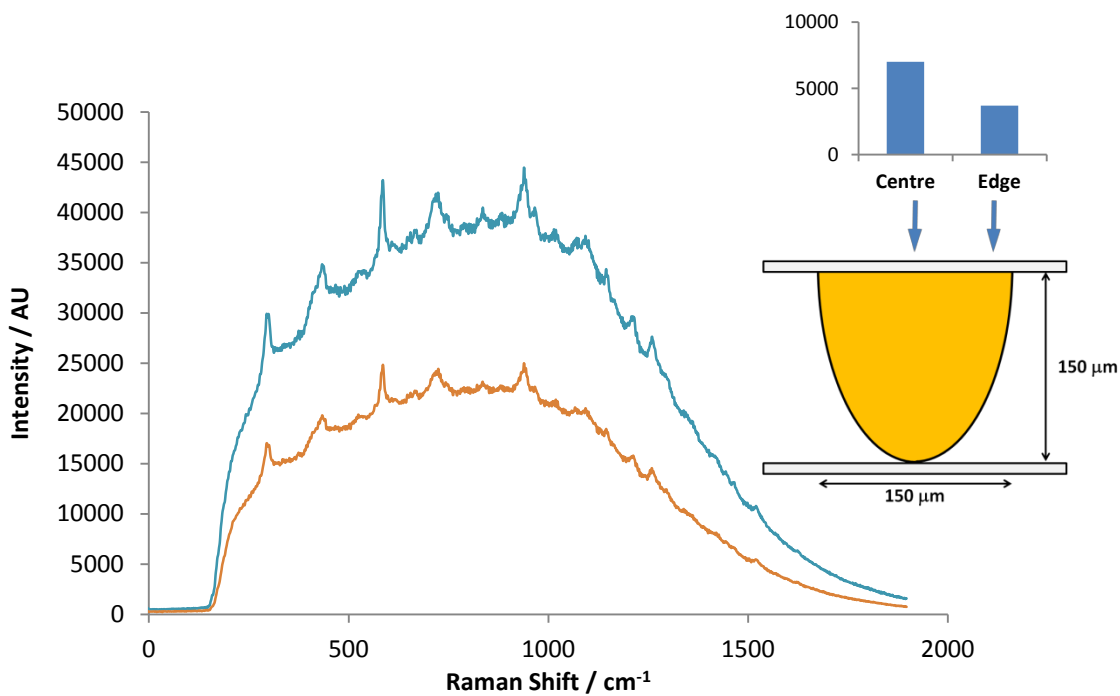
Figure 5.5 – Raw spectra obtained in point Raman analysis of unaggregated AgEDTA-NIR recorded at the centre (blue) and edge (brown) of the microchannel. Inset shows the peak intensities at 586 cm^{-1} at positions in the channel depicted by the schematic cross section. Raman analysis was conducted using an excitation wavelength of 784.6 nm and a 50 ms scan duration.
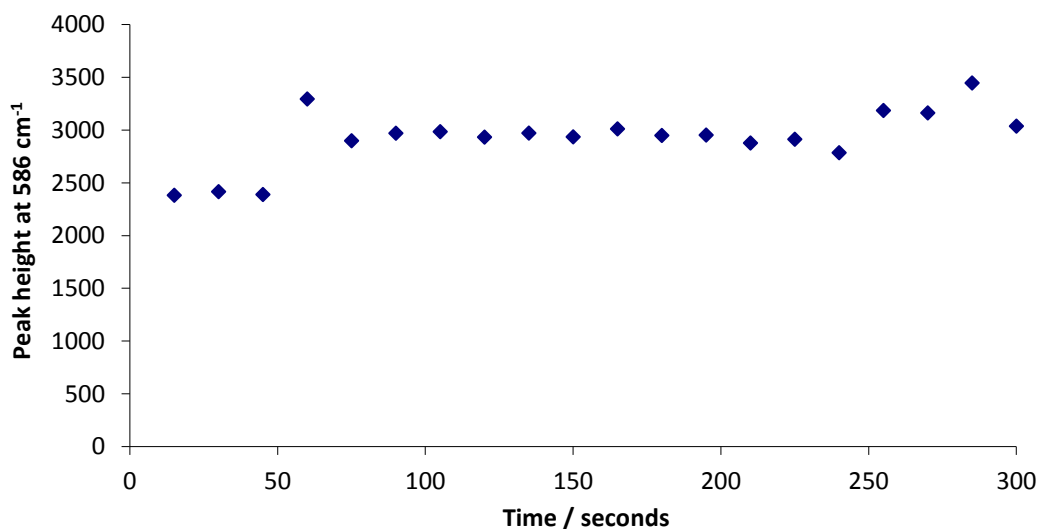
Figure 5.6 – Monitored peak height at 586 cm^{-1} over 5 minutes (1 scan (50 ms duration) was recorded every 15 seconds) for a 0.2 nM solution of Ag-IR under continuous flow (20 μL / min) using an excitation wavelength of 784.6 nm.

5.3 – Streamline Raman mapping of microchannels

Thus far, Raman analysis of Ag-IR solutions in microchannels has been carried out by recording point scans (figures 5.4 – 5.6). Streamline Raman mapping generates a large number of data points in a short period of time to produce high quality SERS map data. Owing to the large amount of collected data, spectra obtained within each data point can only monitor signal over a small spectral window. Therefore streamline Raman mapping analysis of Ag-IR in microchannels was performed with the instrument grating centred at 650 cm^{-1} to enable monitoring of the peak height at 586 cm^{-1}.

5.3.1 – Static analysis of different Ag-IR solutions

Streamline Raman mapping analysis was initially carried out on microfluidic chips containing various Ag-IR solutions in the absence of flow. False colour images were generated based on the peak area at 586 cm^{-1} for visualisation purposes. Figure 5.7 shows streamline Raman mapping of aggregated Ag-IR, 0.2 nM Ag-IR pre-aggregated with 1 M MgSO$_4$ (10 μL added to 500 μL NP). The generated false colour image, of aggregated Ag-IR, is overlaid onto the white light microscope image demonstrating Raman signal localised to the microchannels. Spectra obtained from Ag-IR solutions demonstrated two peaks at 586 cm^{-1} and 723 cm^{-1} and no SERS response was observed outside of the channels (figure 5.7).
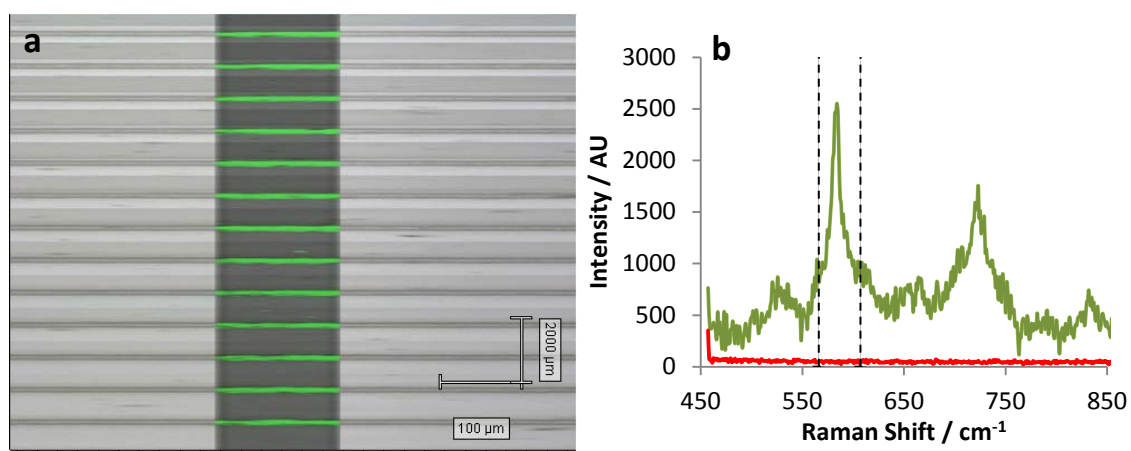
Figure 5.7 – a) False colour Raman image (LUT 0-12000) for aggregated Ag-IR (0.2 nM) in a microchannel overlaid on the white light image. b) Baseline corrected spectra collected from inside (green) and outside (red) the microchannel. Dashed lines depict the points between which signal to baseline was measured for false colour imaging. Raman spectra were obtained using an excitation wavelength of 784.6 nm.
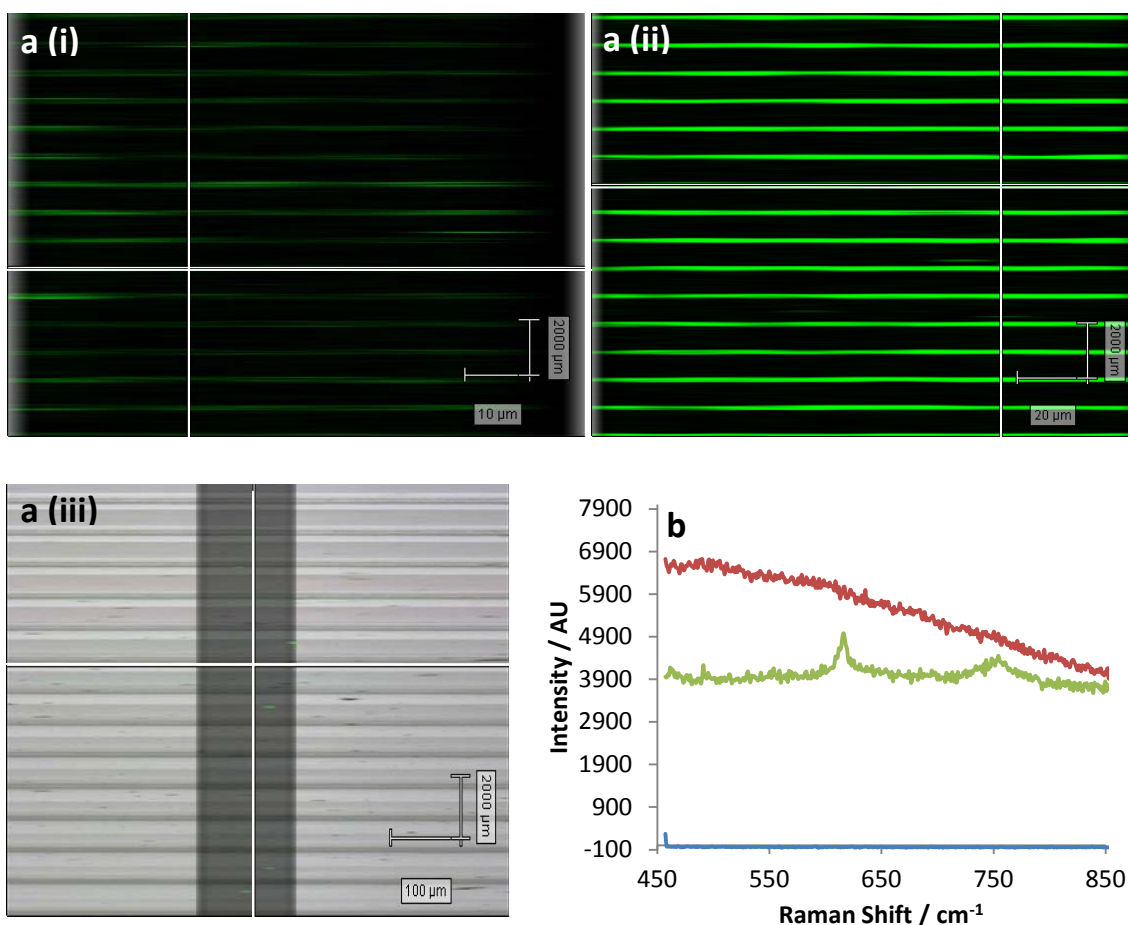
Figure 5.8 – a) False colour Raman images (LUT 0-4000) of i) Ag-IR, ii) Ag-IR aggregated with 1 M MgSO$_4$ (10 μL added to 500 μL NP) and iii) 10 mM phosphate buffer, pH 7.5 in microchannels without flow. b) Raw Raman spectra obtained at positions depicted by crosshairs in ai (red), aii (green) and aiii (blue). Raman spectra were obtained using an excitation wavelength of 784.6 nm and are offset due to a calibration error on the instrument.

The serpentine microchannel used for preliminary microfluidic experimentation documented in this chapter is made from glass and the channels created via powderblasting. The use of glass microchannel structures in this experimental set-up renders analysis susceptible to the 'memory effect'.[247] As such the microreactor was cleaned with aqua regia following each sample analysis. A Raman map of the cleaned

channel containing buffer was also obtained prior to every analysis to verify removal of all residual signal (figure 5.8). Generated false colour images representing aggregated and non-aggregated Ag-IR samples demonstrated a difference in peak intensity at 586 cm^{-1} indicating an increase in SERS response consistent with NP assembly. The false colour image for unaggregated NP solutions indicated the presence of low intensity SERS signals however this was attributed to the fluorescent background observed (figure 5.8). These results corresponded with previous results obtained using point mapping techniques in section 5.2.2.

5.3.2 – Investigating flow rates for optimimal SERS

In preparation for real-time mapping of solution mixing in microchannels, different flow rates were investigated in order to ascertain the optimal conditions for SERS analysis. Solutions of Ag-IR were introduced into the microreactor using a range of different flow rates (5 - 100 μL / minute). Raman maps were acquired subsequently from the microreactor in the in the absence of flow.

SERS spectra were initially collected following the introduction of pre-aggregated and unaggregated Ag-IR applying a flow rate of 100 μL / minute. Raman analysis of these samples showed a negligible SERS response for both unaggregated and aggregated Ag-IR (figure 5.9). At the other extreme of the range, 5 μL / minute, higher SERS signals were observed, however numerous problems with leakages were encountered (figure 5.10). The leaks were speculatively attributed to microchannel blocking due to insufficient force to push NP through the channels. The highest SERS signals, with fewest leakages, were attained when employing a flow-rate of 10 μL / minute and as such this was proposed to be optimum and was used in all subsequent studies (figure 5.12).
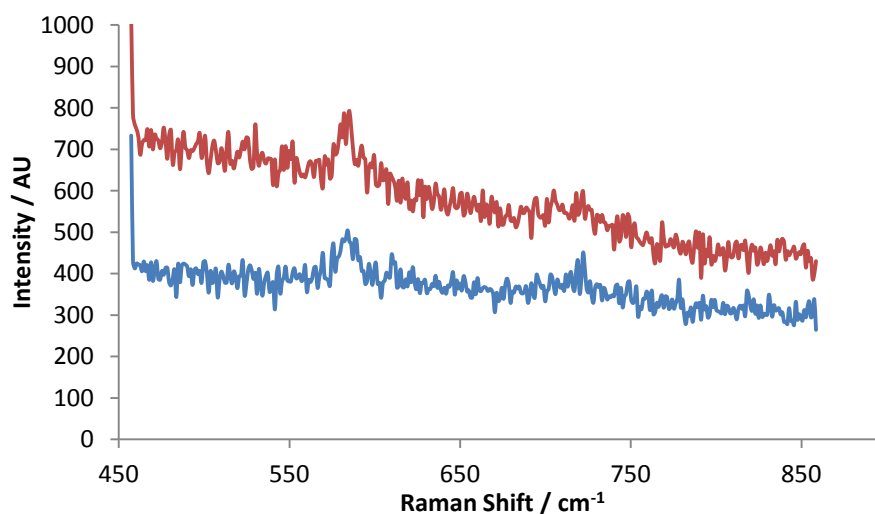
Figure 5.9 – Raw Raman spectra collected from pre-aggregated (red) and unaggregated (blue) Ag-IR (0.1nM), pumped into the microchannel at 100 μL / minute. Streamline Raman mapping was performed using an excitation wavelength of 784.6 nm.
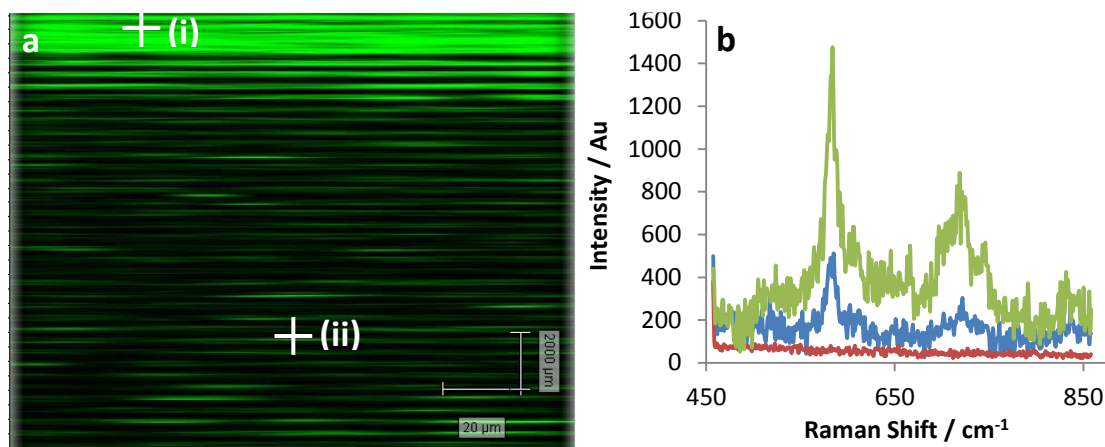
Figure 5.10 – a) False colour Raman image (LUT 0-2000) of 0.1 nM Ag-IR in 10 mM phosphate buffer pH 7.5, pre-aggregated with 1 M MgSO$_4$ (10 μL added to 500 μL NP), pumped into the microreactor using a flow rate of 5 μL / minute. b) Background corrected spectra acquired from outside the channel (red) and at crosshair positions (i (green) and ii (blue)) inside the channel indicated in a. Streamline Raman mapping was performed using an excitation wavelength of 784.6 nm.

5.3.3 – Real-time mapping of NP aggregation
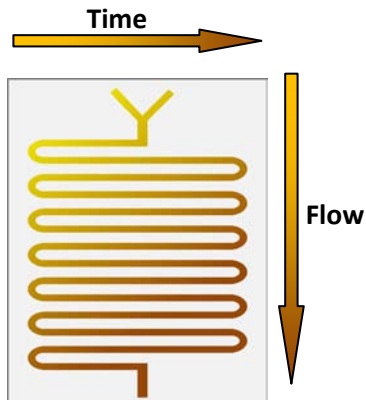
Figure 5.11 – Schematic of the microreactor illustrating the predicted Raman image resulting from streamline Raman mapping of NP assembly.

As aforementioned in section 5.1, the purpose of this chapter is to explore the potential for microfluidics in monitoring the NP assembly process using SERS. Thus far Ag-IR have been detected in microchannels using SERS and flow has been introduced into the system. Real-time mapping of Ag-IR aggregation was investigated using a 10 μL / minute flow-rate. In streamline mapping lines of data points are acquired across the microreactor from top to bottom and these data lines are progressively obtained from left to right. NP aggregation was proposed to occur increasingly from the start to end of the serpentine channel as solution mixing was increased. Taking all of these factors into consideration it was theorised that a false colour image of signal intensity would demonstrate the most intense signals in the bottom right corner due to the extent of nanoparticle mixing and the time delay associated with scanning (figure 5.11)

Solutions of Ag-IR and buffer / aggregating agent were introduced to the microchannel through separate inlets and streamline mapping was carried out of solution mixing under continual flow. Raman images obtained from mixing 0.2 nM Ag-IR in buffer with

1 M MgSO$_4$ showed higher SERS signal intensities at the top right corner of the microchannel (as viewed in figure 5.11), contradictory to theory. Increased signal intensity from left to right can be attributed to the time delay before acquisition associated with streamline mapping as previously described. The large extent of apparent aggregation, inferred by high SERS, at the start of the channel was theorised to be a result of the 'memory effect'. Previous experimentation in section 5.3.1 has demonstrated the 'memory effect' whereby nanoparticles adhere to the glass microchannel walls resulting in a need for aqua regia washings between samples. It was therefore suggested that NP deposition occurred as solutions flowed through the microchannel. If this is the case more nanoparticles will be deposited at the start of the channel which is exposed to a greater fluid volume. This effect also provides an alternative explanation for leakages observed when employing lower flow rates (figure 5.10) as slower moving particles have a greater chance of adhering to the microchannel wall.
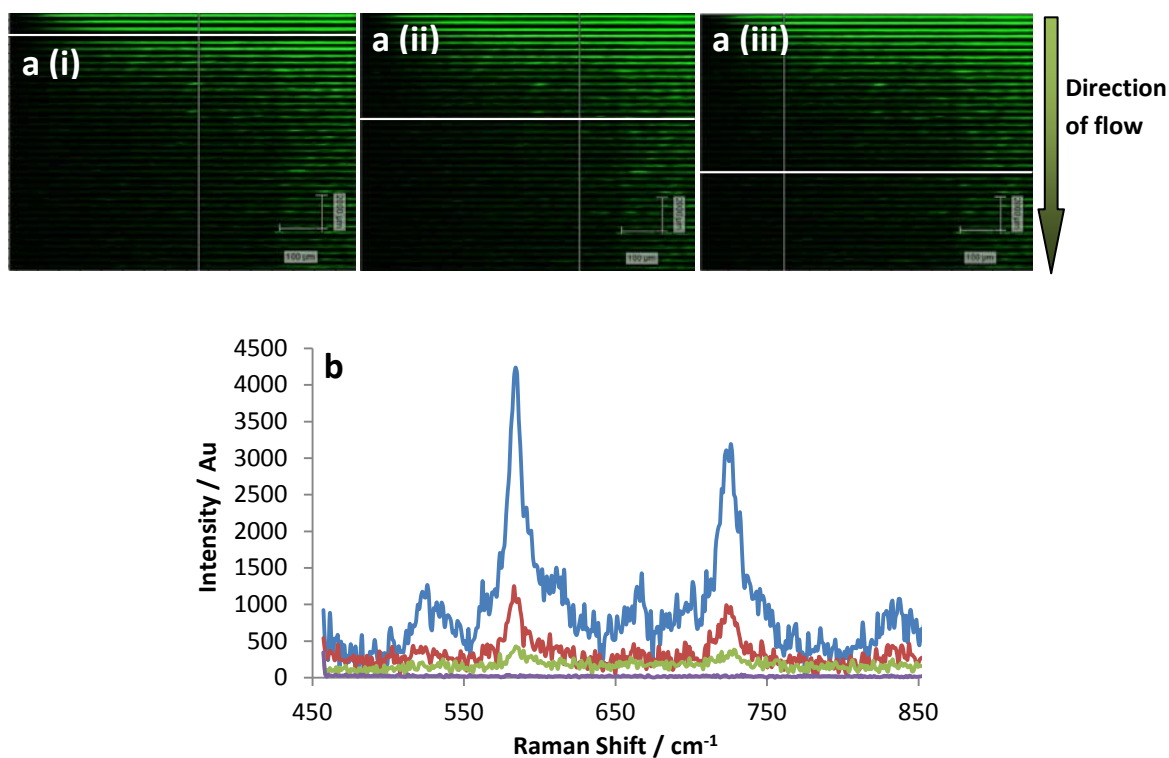
Figure 5.12 – a) False colour Raman image (LUT 0-12000) of 0.2 nM Ag-IR in buffer mixing with 1 M MgSO$_4$ at a flow rate of 10μL / minute. b) Background corrected Raman spectra taken at points indicated by cross hairs in ai (blue), aii (red) and aiii (green). Streamline Raman mapping was performed using an excitation wavelength of 784.6 nm.

5.3.4 – Preventing the 'memory effect'

To explore the contribution of the 'memory effect' to the patterns observed in Raman mapping of NP assembly (figure 5.12), the microchannels were pre-functionalised to prevent NP deposition. Various molecules were investigated to block microchannel walls and prevent the NP adherence. Tween20 is a surfactant based on a branched structure of 20 polyethylene glycols and is widely used in biology for the prevention of non-specific binding and absorption. Tween20 also physisorbs to the surface of nanoparticles and as such is used for stabilisation of nanoparticle solutions during

functionalization (section 4.2.2).[225] A solution of 0.2 % Tween20 in buffer was flowed through the microchannel prior to nanoparticle aggregation analysis. Raman mapping revealed only fluorescence signals consistent throughout the channel (figure 5.13). An explanation for this is that Tween20 may have successfully blocked the channel walls but also prevented any nanoparticles aggregating.
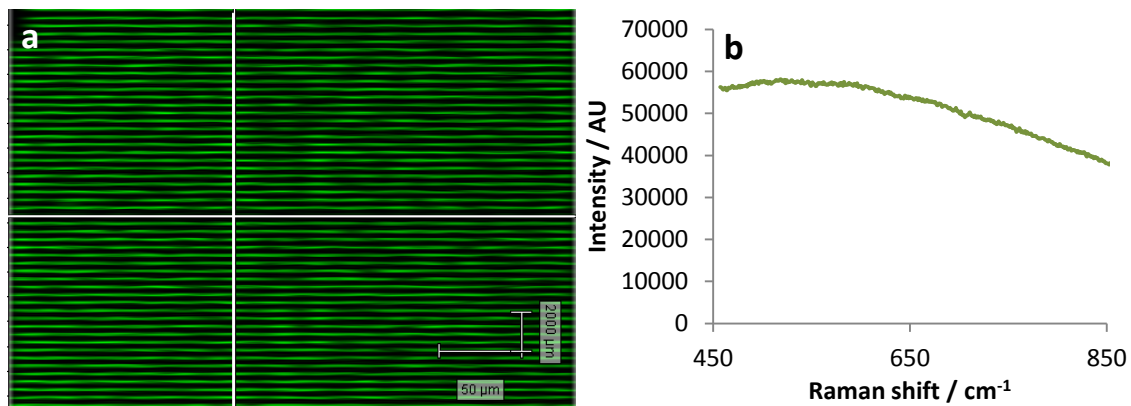

Figure 5.13 – a) False colour Raman image (LUT 0-12000) of 0.2 nM Ag-IR in buffer mixing with 1 M MgSO$_4$ at a flow rate of 10μL / minute in microchannels pre-blocked with 0.2 % Tween20. b) Raw Raman spectra obtained at the crosshair position. Streamline Raman mapping was performed using an excitation wavelength of 784.6 nm.

Bovine serum albumin (BSA) is a protein commonly used for blocking surfaces and preventing non-specific binding of biomolecules. BSA was therefore investigated as an alternative to Tween20 for blocking microchannel walls without preventing aggregation. To that end, the microreactor was pre-soaked with 2 % BSA in buffer prior to Ag-IR analysis. Figure 5.14 illustrates the results obtained from Ag-IR mixing with aggregating in the microchannel following blocking with BSA. Ag-IR aggregation was observed, demonstrated by Raman spectral peaks, however mapping results show the same pattern of Raman intensity as observed in figure 5.12. This is indicative that NP

deposition on the channel walls was not prevented following treatment with BSA (figure 5.14).
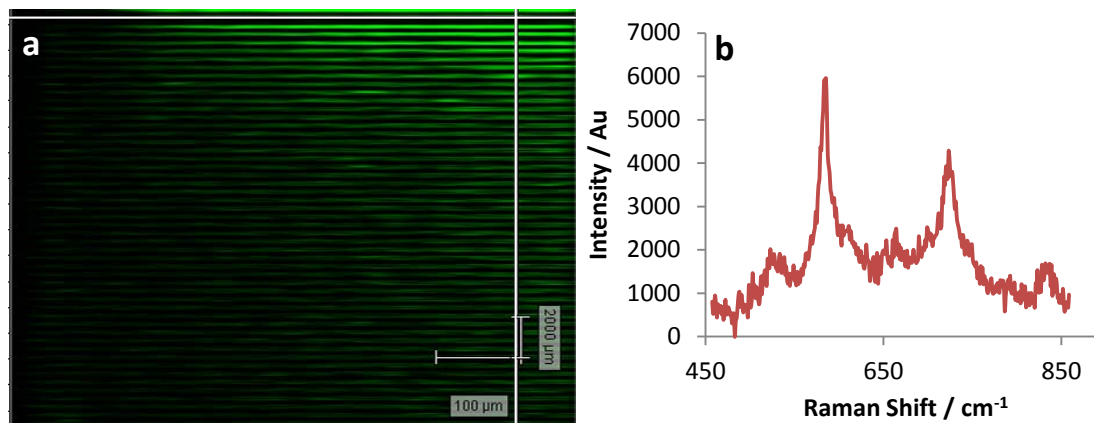
Figure 5.14 – a) False colour Raman image (LUT 0-12000) of 0.2 nM Ag-IR in buffer mixing with 1 M MgSO$_4$ at a flow rate of 10μL / minute in microchannels pre-blocked with 2 % BSA. b) Background corrected Raman spectra obtained at the crosshair position. Streamline Raman mapping was performed using an excitation wavelength of 784.6 nm.

5.4 – Aggregating agents

The experimentation in this chapter has so far focussed on SERS monitoring NP aggregation in microchannels using MgSO$_4$ as an aggregating agent. Salt is known to cause rapid and irreversible aggregation of nanoparticles. In this section different NP aggregating agents are investigated which more accurately mimic the controlled PSN assembly described in chapter 3.

Monodispersed NP solutions are maintained largely through the electrostatic repulsion of negatively charged NPs. A number of aggregating agents are available that disrupt NP surface charge, thus resulting in the formation of larger aggregates. Various salts are used that disrupt the metal surface structure resulting in the formation of large

irregular clusters. Spermine is a positively charged molecule commonly used to pre-aggregate samples prior to analysis. Spermine has an affinity to the metal surface and adheres to the nanoparticles thus disrupting the surface charge without affecting the surface structure. Aggregation in this way typically results in various nanoparticle clusters rather than the comparatively large aggregates formed by salt addition. Poly-L-lysine is another molecule, based on the positively charged amino acid (lysine), found to cause aggregation in a similar way to spermine. The destructive nature in which salt causes nanoparticle aggregation may not be accurately representative of the biologically driven aggregation described in chapter 3 and could potentially enhance nanoparticle deposition on glass channel walls. Spermine and poly-L-lysine were therefore investigated as alternative aggregating agents for microfluidic proof of concept experiments. AgEDTA-BT conjugates were prepared in HEPES-KCl buffer, as described in chapter 3, and aggregated with various amounts of different aggregating agents (figure 5.15). BT was used in this instance, rather than the near-IR linker, due to sample availability, mode of Raman analysis and for comparison to MDM2-mediated PSN assembly.
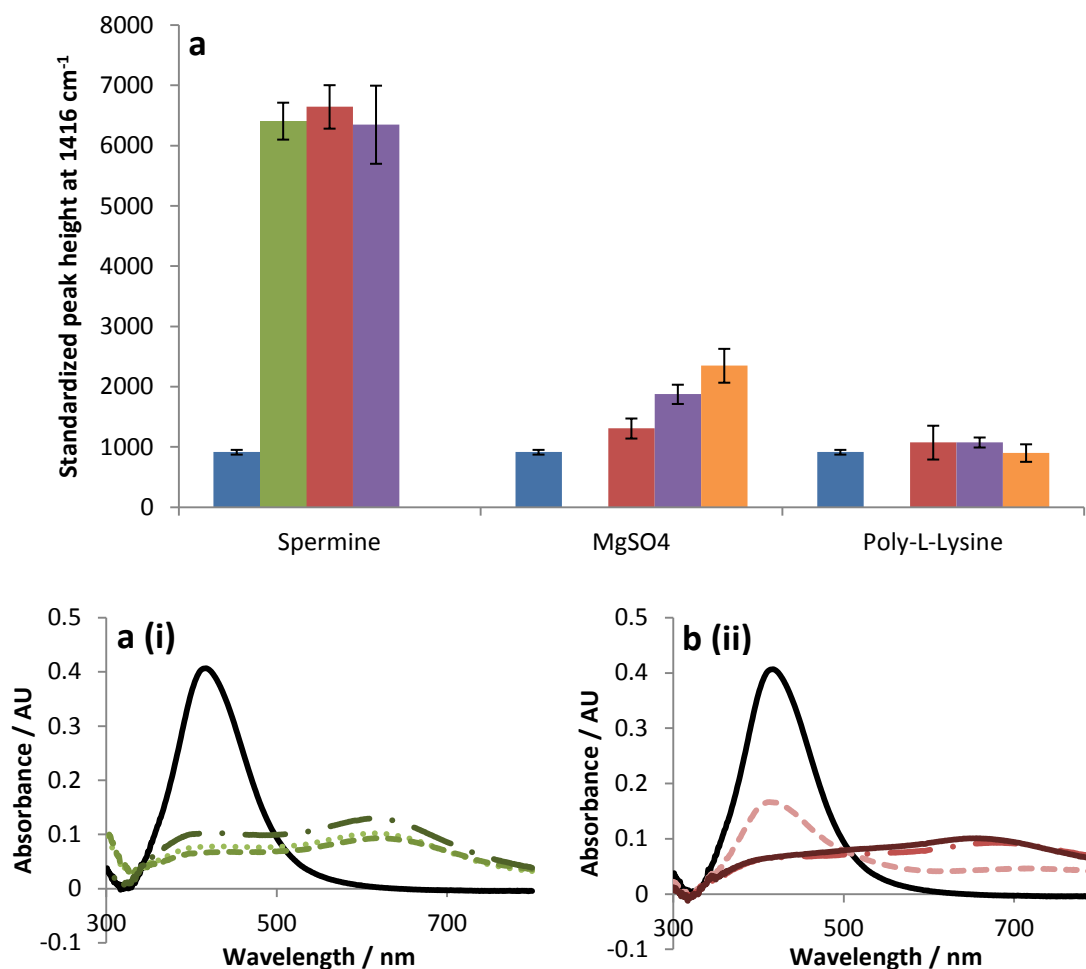
Figure 5.15 – a) Standardized peak height at 1416cm^{-1} for 70 pM AgEDTA-BT solutions with 0 (blue), 5 μL (green), 10 μL (red), 25 μL (purple) and 50 μL (orange) aggregating agent (0.1 M spermine in d$_2$H$_2$O, 1 M MgSO$_4$ in d$_2$H$_2$O or 0.01 % poly-L-lysine in d$_2$H$_2$O). b) Extinction spectra of AgEDTA-BT solutions (black) with 5 μL (dotted), 10 μL (dashed), 25 μL (dashed and dotted) and 50 μL (full line) of i) spermine and ii) MgSO$_4$.

Aggregation of AgEDTA-BT was observed following the addition of both spermine and MgSO$_4$, resulting in an increase in SERS response. No NP assembly was detected when poly-L-lysine was introduced in the quantities described (figure 5.15). This may be due to functionalisation of NP with BT, therefore poly-L-lysine was unable to alter the

surface chemistry such that aggregation would occur. Aggregation with spermine resulted in a much larger increase in SERS than was apparent in samples to which $MgSO_4$ was added (figure 5.15). It was also noted that the Raman signal intensity was constant irrespective of the quantity of spermine added whilst the SERS response recorded for AgEDTA-BT increased in correlation with $MgSO_4$ concentration. Extinction spectroscopy of AgEDTA-BT samples containing spermine and $MgSO_4$ demonstrated a decrease in the plasmon absorbance band and increased absorbance at longer wavelengths, characteristic of NP aggregation (figure 5.15). The size distribution of AgEDTA-BT aggregated with spermine showed two plasmon absorbance peaks, 400 nm and 650 nm, indicating the formation of small clusters rather than large aggregates. $MgSO_4$ aggregated samples also illustrated a decrease in the plasmon absorbance band, however the emerging absorbance band at longer wavelengths was less well defined, thus indicating a more random distribution of cluster size throughout the solution. It is documented that the highest SERS intensities are detected at an optimum interparticle distance. A explanation for high SERS intensity following spermine addition is that aggregation results in an optimal interparticle distance. Owing to the nature of spermine-induced nanoparticle aggregation it can be suggested that fewer nanoparticles would adhere to microchannel walls and this assembly is also more representative of biologically driven aggregation. Any further microfluidic studies should therefore use spermine rather than $MgSO_4$ as an aggregating agent.

5.5– Conclusions

Prelimary studies were conducted to assess the potential for SERS mapping of biologically driven NP assembly in a microfluidic channel. The proposed microfluidic set-up was aimed to attain highly sensitive detection of biologically driven nanoparticle aggregation in a smaller sample volume. Streamline Raman maps of Ag-IR in the microreactor were successfully obtained and a difference in SERS response demonstrated between unaggregated and aggregated samples. Various flow rates were investigated for the system and 10 µL / minute was found to be optimal giving the best SERS response with fewest channel leakages. SERS mapping of the nanoparticle aggregation process in real-time resulted in an unexpected signal distribution through the channel however this can be explained by the 'memory effect' resulting from NP adherance to the microchannel walls. Tween20 and BSA, were investigated to block the microchannel walls and prevent non-specific interactions, however this proved to be unsuccessful. Tween20 prevented subsequent nanoparticle aggregation and BSA was only able to lessen the extent of nanoparticle sticking. It has been suggested that the nature in which salt causes nanoparticle aggregation, by disrupting the metal surface composition, may enhance deposition at the channel edges. Spermine and poly-L-lysine induce nanoparticle aggregation by altering the surface charge whilst maintaining integrity of the metal composition. NP clustering in this manner is also more representative of that which is achieved via biological interactions such as in the MDM2 assay (chapter 3). Aggregation of AgEDTA-BT with these two agents was therefore investigated with spermine inducing the greatest extent of aggregation and associated increase in SERS response.

5.6 – Future Work

Future studies into SERS mapping of NP assembly in microfluidic platforms will investigate Spermine-induced aggregation as a model system. This will give a more accurate representation for proof of concept and hopefully reduce the 'memory effect'. Various silinization methodologies will also be explored in order to prevent nanoparticle deposition. The microchannel used for these investigations was produced via powderblasting which results in a roughened topology of the glass walls. Another avenue to investigate would be to employ a microreactor with smooth walls as this may also reduce the non-specific adherence of NP.

Chapter 6 – Conclusions

This work documents two methodologies to prepare SERS-active peptide silver nanoparticles (PSN) for use in different applications. Chapter 3 reports PSN preparation via pre conjugation of peptide and a Raman tag (BT). Peptide-BT conjugates were then directly added to AgEDTA to yield stable SERS-active and biologically functional PSN. Chapter 4 describes the preparation of PSN through mixed monolayer formation with positively charged peptides and small molecule Raman reporters. PSN created with negatively charged peptides are prepared by direct conjugation and resultant particles are not SERS-active.

Using the PSN prepared in chapter 3, a novel solution SERS-based assay was developed to investigate the allosteric interactions of full-length wild-type MDM2 in solution. The extent of PSN assembly observed was altered by pre-mixing MDM2 with various binding ligands, thus demonstrating the potential for allosteric investigations. This assay format is advantageous compared with alternative available techniques as it enables the interrogation of intricate interactions of full-length, unlabelled proteins in solution. MDM2-mediated PSN assembly was also explored for use as a screening assay to identify potential MDM2 binding partners and pilot screen of 80 natural product mixtures was carried out. The MDM2 assay demonstrates the potential of SERS as a tool for protein-protein interaction studies and drug discovery.

Chapter 4 investigated SERS detection of PSN assembly based on coiled coil heterodimerization. pH sensitive PSN assembly was observed in heterogeneous solutions using extinction spectroscopy and SERS. SERS intensities resulting from PSN assembly varied with peptide orientation on the NP surface and the extent of coiled coil based PSN aggregation was reduced by introducing inhibitor peptides. This work illustrates a step forward in the development of malleable bionanomaterials for a variety of applications.

The work completed in chapters 3 and 4 highlights AgEDTA as a valuable colloid for SERS. NP assembly, as monitored using SERS, has also shown applicability to biological studies for which current methodologies fall short. The linear correlation of SERS intensity versus time shown for MDM2-induced PSN assembly also highlights the potential for using SERS in PSN assembly rate studies.

Chapter 5 documents preliminary tests that were performed in order to assess the possibility of mapping NP assembly within a microfluidic platform. A microfluidic set-up was developed, however NP assembly studies have thus far proved unsuccessful due to NP adherence to microchannel walls.

In conclusion, this thesis presents novel applications of NP assembly and SERS. SERS-monitored NP assembly is shown as a powerful technique for investigating intricate biological interactions and as a tool for therapeutic screening. NP assembly using coiled coil peptides also demonstrates an important step towards biocompatible nanomaterials that can be manipulated using physiological environmental factors and sensitively monitored using SERS.

Chapter 7 – Future work

MDM2-directed PSN assembly has demonstrated allosteric protein activity using a small number of ligands. This study will be expanded to include various alternative MDM2 binding ligands in order to elucidate a more comprehensive understanding of protein functionality. At present this work has shown a proof of concept for a novel screening assay for MDM2 interaction inhibitors. The pilot screen highlighted a few potential inhibiting ligands but it would also be interesting to investigate natural products that were seen to enhance PSN assembly with MDM2. Once more established, the methodology described in chapter 3 could potentially be used for determining affinity constants for MDM2 binding ligands. This would involve calibration using small molecules, such as Nutlin, for which IC_{50} values have previously been determined. One experiment would be to compare affinity constants determined using the MDM2 – induced PSN assembly and those acquired using more traditional techniques, such as ELISA. This could elucidate differences in binding activity of MDM2 when in solution as opposed to on a surface. The largest factor affecting variation in the MDM2 assay was found to be protein expression and purification. In order for any further experimentation to yield valid biological information it is of utmost importance to investigate this preparative step. It may also be valuable to compare PSN assembly using MDM2 purified using different techniques. MDM2 purified using a GST (Glutathione S Transferase) tag may have a different activity in solution to untagged MDM2.

The assay format described in chapter 3 can be transferred to investigate alternative protein systems by functionalizing NP with various different peptide ligands. It is however important to take care when choosing a peptide sequence for NP modification. One rule would be to avoid cysteine residues as the formation of disulfide linkages will cause aggregation of NP. Non-specific NP assembly was also observed

when using peptide sequences with high and low pI values, therefore favouring neutral peptides for these studies.

Employing various Raman tags would give rise to multiplexing opportunities in protein interaction studies. Allosteric protein interactions could be interrogated using heterogeneous solutions of PSN, functionalized with different Raman tags and peptide ligands that bind two separate domains of the same protein. A more adventurous approach could also be to investigate the affect of MDM2 on p53 DNA binding by multiplexing DNA-NP and PSN with p53 and MDM2 in solution.

PSN assembly based on heterodimer coiled coil interactions has been demonstrated using SERS following assembly completion. Temporal analysis of heterogeneous PSN solutions will be conducted to gain a more in depth understanding of the PSN assembly process. Work described here demonstrates the potential of both extinction spectroscopy and SERS as techniques for monitoring the rate of PSN assembly. Such rate determination studies can also be applied to the MDM2 – directed PSN assembly. Chapter 4 illustrates preliminary coiled coil NP assembly studies and it is therefore difficult to gain a comprehensive understanding of the interactions taking place. Further experimentation is imperative to verify the data obtained already obtained, however a reliable method for the preparation of PSN with positively peptides has been described. As for protein interaction studies, exploration of various small molecule Raman tags will enable multiplexing studies. In this case, multiplexing would allow for coiled coil specificity studies by introducing positive coiled coil peptides to heterogeneous solutions of PSN with expressing different negatively charged peptide sequences.

Work shown here has investigated PSN assembly with coiled coil peptides that attach at differing orientations on the NP surface. These studies require further investigation, however future work will also explore coiled peptides of varying lengths and with differently positioned Cysteine residues. This will allow exploration into the effect of

peptide length and orientation on both PSN assembly and the resultant SERS intensity. Coupled with SEM studies this work has the potential to produce a peptide-based molecular ruler demonstrating the relationship between interparticle spacing an SERS intensity.

Reversible, coiled coil induced PSN assembly, if achieved, has potential uses in a number of biological applications. For example, pH induced disassociation could possibly be used in future methods of controlled drug release. Following verification and understanding of the assembly process, inhibition of coiled coil PSN assembly will also be studied in more detail. Temporal analysis of coiled coil PSN assembly inhibition would be investigated after introducing inhibitor peptides both after and during PSN preparation. Temporal analysis could also be used to explore the reversibility of coiled coil PSN assembly following either addition of inhibitor peptides or a change in the solution pH.

For all of the future experimentation previously described, close monitoring of the NP aggregation process is important. Future studies will therefore explore mapping NP assembly on a microfluidic platform further and will employ Spermine as a model aggregating agent. Difficulties experienced when using microfluidic reactors included leakages at non-secure tubing connections and the memory effect associated with NPs adhering to microchannel walls. Various glass silinization procedures will be explored to prevent NP deposition, along with the use of microreactors with smoother microchannel walls. Droplet based methodologies, using oil and water mixtures, will also be employed to avoid the memory effect. Such methodologies could also potentially allow interrogation of the interactions of a few NP in a small droplet. Developments in microfluidic technologies will also be studied to improve connections, thus preventing leakages. As technology develops there is also potential for more complex microchannel systems that would be investigated for performing the MDM2 screening assay on a chip.

Chapter 8 – Experimental

Unless otherwise stated, chemicals used for this work were purchased from Sigma Aldrich, UK.

8.1 – Peptide modification

Peptides 12.1 (SGSG-MPRFMDYWEGLN-resin) and $12.1_{W\Delta A}$ (SGSG-MPRFMDYAEGLN-resin) were obtained bound to Wang resin via the C-terminus (Almac Sciences, Edinburgh, UK) with the N-terminus deprotected. Modification of both peptides with BT was carried out via amide coupling in the solid phase and cleaved from the resin using 95 % TFA. Peptide was calculated to account for 70 % of the total peptide-resin weight and peptide-bound resin (12.14 mg 12.1, 19.4mg $12.1_{W\Delta A}$) was pre-swelled in 1 mL dimethylformamide (DMF) for a minimum of 30 minutes. 1.5 eq. (1.75 mg 12.1, 3.04 mg $12.1_{W\Delta A}$) *O*-(7-Azabenzotriazol-1-lyl)-*N,N,N,N*-tetramethyluronium hexafluorophosphate (HATU) and 3 eq. (1.70 μL 12.1, 4.40 μL $12.1_{W\Delta A}$) *N,N*-diisopropylethylamine (DIPEA) were mixed with 1 eq. BT (153.4 μL 12.1, 175.3 μL $12.1_{W\Delta A}$ of $2x10^{-2}$ M in DMF) and immediately added to the preswelled peptide-resin. The reaction mixture was left to stir at 20 °C for 6 hours. Following removal of the reaction solution, resin was washed once with DMF (1 mL), acetonitrile, MeCN (3 x 1 mL), and diethyl ether, DEE (3 x 1 mL) and dried under nitrogen. A second delivery of 1 eq. BT was pre-activated with 1.5 eq. HATU and 3 eq. DIPEA in a total volume of 1.5 mL DMF and added to the dried resin. After stirring for 16 hours the solution was discarded and resin washed with DMF (1 mL), MeCN (3 x 1 mL) and DEE (3 x 1 mL) as described above. Modified peptides were cleaved from the resin using a 2.2 mL cleavage cocktail (2 mL trifluoroacetic acid (TFA), 100 μL triisopropylsilane (TIS) and 100 μL d_2H_2O) for 4 hours in an inert atmosphere. Cleaved peptide was filtered from the resin using a 1.0

µm PTFE filter, which was washed through with MeCN (2 x 2 mL). Solvent was removed under reduced pressure and cold DEE (1 mL) was added to afford a precipitate. Following DEE removal, the precipitate was dissolved in an appropriate volume of ddH$_2$O (4 mL). Unmodified peptides 12.1 and 12.1$_{W\Delta A}$ were prepared by preswelling the resin for a minimum of 30 minutes in DMF and cleaving from resin as described for peptide – BT conjugates.

8.2 - Matrix Associated Laser Desorption Ionisation – Mass Spectroscopy (MALDI-MS)

Peptide samples were analysed using a 1:1 ratio of sample to matrix, α-cyano-4-hydroxycinnamic acid (α-cyano). Ionisation was conducted in the positive reflectron mode using an Axima CFR MALDI (Kratos / Shimadzu). A linear 3-point calibration was achieved using a pre-prepared peptide mix: 379.1 m/z (α-cyano matrix), 757.4 m/z (Bradykinin fragment) and 1046.5 m/z (Angiotensin II). To analyse nanoparticle-bound peptide samples conjugates were removed from the nanoparticles and desalted. Nanoparticle samples were treated with DTT (10 mM) for a minimum of 30 minutes to displace BT from the metal surface. Following centrifugation at 5000 rpm for 20 minutes 150 µl of supernatant was desalted using PepClean C-18 spin columns (Thermo Scientific) MALDI-MS carried out on the recovered sample.

8.3 – Circular Dichroism (CD)

46 mM and 43 mM solutions of peptide 12.1 and peptide 12.1 – BT respectively were analysed in cuvettes with a 0.1 cm path length. Measurements were recorded using a JASCO J-810 CD spectropolarimeter. The raw data collected were normalized for dilution.

8.4 – Protein preparation

Protein expression and purification was carried out by researchers at CRUK, Edinburgh and supplied in storage buffer for this work. Full-length, untagged MDM2 was expressed in *Escherichia coli* BL21 cells and purified by cationic exchange using a HiTrap-SP column. Purified full-length MDM2 was stored at -20 ^{o}C in storage buffer (25 mM HEPES pH 7.5, 10 % glycerol, 1 mM Benzamidine, 5 mM DTT, 290 mM KCl) and filtered through 10,000 Da molecular weight filters (Millipore) into assay buffer (25 mM HEPES pH 7.5, 20 mM KCl). Bovine Serum Albumin (BSA) was obtained from Sigma and dissolved in assay buffer. MDM2 and BSA stocks were prepared at a concentration of ~8×10^{-7} M in assay buffer for use in NP aggregation assays. MDM2 protein was validated in the dual site-binding assay (data not shown), that measures the ability of Nutlin to stimulate the interaction of MDM2 with the Rb1 peptide. Active MDM2 was quantified via ELISA.

8.5 - Nanoparticle synthesis

EDTA reduced silver nanoparticles (AgEDTA), with ~36 nm diameter, were produced using a method described by Fabrikanos *et al* in 1963.[254] EDTA (47.35 mg) was added to 1 L of ddH$_2$O under heat. NaOH (0.16 g in 10 mL d$_2$H$_2$O) was added just prior to the solution reached the boil. Once boiling silver nitrate, AgNO$_3$, (0.044 g in 10 mL d$_2$H$_2$O) was added in 5 mL aliquots. The solution was boiled for a further 15 minutes and allowed to cool with continuous stirring maintained throughout. Colloidal nanoparticles (NP) were resuspended in buffer (25 mM HEPES, 20 mM KCl, pH 7.5) to a final concentration of approximately 70 pM prior to functionalization.

Citrate reduced gold nanoparticles (AuNP), with ~13 nm diameter, were prepared using a protocol described by Turkevitch *et al*. in 1951.[123] 50 mg Sodium tetrachloroaurate,

NaAuCl$_4$, was dissolved in 500 mL ddH$_2$O and brought to the boil. Once boiling sodium citrate (0.075 g in 7.5 mL ddH$_2$O) was added and the solution boiled for a further 15 minutes and allowed to cool. Continuous stirring was maintained throughout.

8.6 – Nanoparticle functionalization (PSN-12.1 / PSN-12.1$_{W\Delta A}$)

AgEDTA nanoparticles, ~70 pM, were centrifuged at 5000 rpm for 20 minutes and resuspended in buffer (25 mM HEPES and 20 mM KCl, pH 7.5) before addition of BT (AgEDTA-BT) or peptide – BT (Peptide Silver Nanoparticles, PSN) at a final concentration of 10^{-6} M. After shaking for a minimum of 1 hour the conjugation solutions were centrifuged at 1900 g for 20 minutes and resuspended in buffer to remove any excess analytes. Complete PSN were characterised using extinction spectroscopy, dynamic light scattering and MALDI-MS.

8.7 – MDM2 NP aggregation assay

Purified full-length protein (MDM2 / BSA) was filtered using 10,000 Dalton molecular weight cut off filters, MWC, (Millipore, UK) to remove storage buffer components and diluted to 1 μM in assay buffer (25 mM HEPES, 20 mM KCl, pH 7.5). PSN-12.1 and PSN-12.1$_{W\Delta A}$ were quantified using extinction spectroscopy and diluted in buffer (25 mM HEPES, 20 mM KCl, pH 7.5) to a final concentration of 15 pM in the final assay volume (500 μl for extinction / Raman temporal analysis, 300 μl for screening in 96-well microtitre plates). Protein (1 mM) was added to PSN at a final concentration of 15 pM (7.5 μl in 500 μl, 4.5 μl in 300 μl) immediately prior to analysis. Volumes were adjusted accordingly for lower concentrations of MDM2. All inhibition experiments were conducted using 15 pM PSN and 15 nM MDM2. Inhibitor molecules were diluted to 0.1 mM in assay buffer (25 mM HEPES, 20 mM KCl, pH 7.5) and added to samples at a 50

fold excess to MDM2 (0.75 μM (2.25 μl in 300 μl, 3.75 μl in 500 μl)). MDM2 and inhibitor molecule were pre-mixed and incubated at room temperature (~18-22 ^{o}C) for 30 minutes before addition to PSN solutions and analysis. Volumes of inhibitor molecule were adjusted accordingly for lower concentrations used.

8.8 - Extinction spectroscopy

Absorbance readings were taken within the range of 200 - 800 nm using a Cary Eclipse extinction spectrometer. AgEDTA (chapters 3 and 5) spectra were baseline corrected using appropriate buffer (25 mM HEPES buffer pH 7.5, 20 mM KCl or 10 mM phosphate buffer pH 7.5) as a blank. NP concentrations were calculated using the the extinction co-efficient for 40 nm silver nanoparticles at λ-max (ε = 2.87x10^{10} L M^{-1} cm^{-1}). Peptide-BT concentrations were calculated using the extinction co-efficient for BT at 487 nm (ε = 12017 L M^{-1} cm^{-1}). Unmodified peptide samples were analysed in and baseline corrected using 0.1 M phosphate buffer, pH 7. Concentrations were calculated using the extinction co-efficients for Tryptophan (ε = 5379 L M^{-1} cm^{-1}), Tyrosine (ε = 1400 L M^{-1} cm^{-1}) and Phenylalanine (ε = 4 L M^{-1} cm^{-1}) in 0.1 M phosphate buffer, pH 7. AuNP and AgEDTA spectra (chapter 4) were baseline corrected using ddH$_2$O. A scanning kinetics program (Cary Eclipse) was employed for temporal analysis.

8.9 - Dynamic Light Scattering

1 mL samples were analysed via dynamic light scattering using a Malvern high performance particle sizer (HPPS) using standard disposable cuvettes.

8.10 – Raman spectroscopy

Raman spectra were collected using a Renishaw inVia microscope system (Renishaw, Wotton-under-edge, UK). Excitation at 514.5 nm was achieved via a ~6 mW Ar+ laser, at 632.8 nm via a ~30 mW HeNe laser and at 784.6 nm using a 13 mW laser diode laser attenuated using neutral density filters. Spectra were obtained using 180° backscattering with the grating centred at 1400 cm^{-1} using a 20x long-working distance objective. MDM2 assay analysis (514.5 nm excitation) of post-assay samples was conducted in disposable cuvettes recording static 3 scan measurements with a 1 second collection time per sample replicate. Raman time course analysis of samples in NMR tubes was conducted using an NMR tube spinner microscope attachment. 1 second scan durations were used and 1 spectrum acquired every 60 seconds for 30 minutes. Analysis of AuNP (632.8 nm excitation) was carried out in disposable cuvettes recording 5 scans of 30 second duration per sample. A streamline® mapping system (Renishaw, UK) was used for line mapping and SERS maps created by integration of characteristic peaks.

8.11 – Scanning Electron Microscopy

Scanning electron microscopy (SEM) was carried out of PSN solutions deposited onto poly(diallyldimethylammonium) (PDDA) coated silicon wafers. Following cleaning with methanol and oxygen plasma (Diener electronic femto oxygen plasma cleaner, 72 cm^{3}/min gas flow), silicon wafers were coated with a 10 mg/mL PDDA solution in 1 nM NaCl for 30 minutes. The coated wafers were then rinsed with deionised water and dried with N_2. 20 mL of PSN solutions were deposited on individual wafers and allowed to sit for 25 minutes, after which the samples were removed. The sample coated wafers were then washed with deionised water and dried using N_2. SEM imaging was carried out using a Sirion 200 Schottky field-emission electron microscope (FEM)

operating at an accelerating voltage of 5 kV. The samples did not require additional metallic coating before imaging.

8.12 – PNP preparation with coiled coil peptides

Peptide gold nanoparticles (PGN)

AuNP were suspended in ddH$_2$O for functionalization with charged peptide species (final concentration 10 nM AuNP, 10 μM peptide). 10 μL E / Em (0.5 mM in d$_2$H$_2$O) were diluted to 0.05 mM (0.1 mL) in ddH$_2$O and added to 0.4 mL AuNP (12.5 nM). AuNP were functionalized with K / Km using a two step protocol involving acid pre-functionalization. I mL AuNP (15 nM) was brought up to pH 11 by adding 1 M NaOH (1 μL) before addition of Thioctic acid (TA) at a final concentration of 15 μM. 1 μL 4-mercaptobenzoic (10 mM) acid (MBA) 1 mL AuNP (15 nM) at pH 7. Au-TA / Au-MBA solutions were shaken overnight, centrifuged (2250 g, 20 minutes) and resuspended in ddH$_2$O to remove any excess ligand. Au-TA / Au-MBA (0.4 mL, 12.5 nM) were adjusted to pH 11 by adding 1 M NaOH (0.5 μL) before addition of K / Km (0.1 mL, 0.05 mM). After 1 hour HCl was added (10 μL, 1 M) and solutions changed from purple to pink. Samples were then shaken overnight before centrifugation (2250 g, 20 minutes) and resuspension in 0.5 mL ddH$_2$O.

Peptide silver nanoparticles (PSN)

AgEDTA were suspended in ddH$_2$O for functionalization with charged peptide species (final concentration 0.2 nM AgNP, 2 μM peptide). 10 μL E / Em (0.5 mM in d$_2$H$_2$O) were diluted to 0.05 mM (0.1 mL) in ddH$_2$O and 20 μL added to 480 μL AgEDTA (0.2 nM). AgEDTA were functionalized with K / Km using a three step protocol involving acid pre-

functionalization. 500 μL AgEDTA (0.2 nM) was brought up to pH 11 by adding 1 M NaOH (0.5 μL) before addition of 1 μL MBA (1 mM) pH 7. AgEDTA-MBA solutions were shaken overnight, centrifuged (2250 g, 20 minutes) and resuspended in ddH$_2$O to remove any excess ligand. AgEDTA-MBA (0.5 mL, 0.2 nM) were adjusted to pH 11 by adding 1 M NaOH (0.5 μL) before addition of K / Km (20 μL, 0.05 mM). After 1 hour HCl was added (1 μL, 1 M) and solutions changed from olive green to yellow. Samples were then shaken overnight before centrifugation (2250 g, 20 minutes) and resuspension in 0.5 mL ddH$_2$O.

8.13 – Nanoparticle functionalization (IR)

AgEDTA were concentrated to ~0.3 nM and resuspended in 10 mM Phosphate buffer, pH 7.5. The near-IR stock solution (10^{-3} M) was diluted to 10^{-4} M in d$_2$H$_2$O and 0.1 mL added to 0.9 mL AgEDTA (0.3 nM). The NP solutions were shaken overnight before centrifugation (1900 g, 20 minutes) and resuspension in buffer.

8.14 – Microfluidics

Microreactor chips (FC_R150.676.2) with a 676.2 μM channel with 150 μM width and height (Micronit Microfluidics, Netherlands) were used and connections achieved using a Fluidic Connect chip holder with teflon connection tubing (Micronit Microfluidics, Netherlands). Solution flow was created using 1 mL disposable syringes, fitted with 23G 0.6 x 25 mm sterile needles (Terumo, UK), and an electrically driven mechanical syringe pump (Cole-Parmer, Vernon Hills, IL).

8.15 – pH adjustments

The AuNP solution pH range was achieved through the addition of specific volumes of 1 M HCl and 1 M NaOH. 10 mL AuNP (2 nM) in ddH$_2$O was recorded to be ~pH 7 using a

Jenway 3510 pH meter. A 0.5 ml aliquots of 1 M NaOH / 1 M HCl were then added to the AuNP solution and pH values recorded after each addition. A calibration curve was plotted and used to determine the volumes of acid / base required to adjust the pH of a 500 ml AuNP solution accordingly:

	0.05 M HCl				0.05 M NaOH		
Volume (µL)	25	2.5	1.25	-	1.25	2.5	25
pH	3	4	5	7	9	10	11

References

1. Wagner, D. E., Phillips, C. L., Ali, W. M., Nybakken, G. E., Crawford, E. D., Schwab, A. D., Smith, W. F., Fairman, R. *PNAS* (2005) **102**, 12656-12661.

2. Woolfson, D. N. & Ryadnov, M. G. *Curr. Opin. Chem. Biol*. (2006) **10**, 559-567.

3. Fruton, J. S. *Ann. N. Y. Acad. of Sci.,* 1979, **325**, 1-18.

4. Cozzone, A. J. *Encyclopedia of Life Sciences,* Macmillan Publishers Ltd., Nature Publishing Group, 2002.

5. Anfinsen, C. B., Haber, E., Sela, M. & White, F. H. *PNAS,* 1961, **47**, 1309-&.

6. Wathen, B. & Jia, Z. *Int. J. Mol. Sci.,* 2009, **10**, 1567-1589.

7. Moreland, J. L., Gramada, A., Buzko, O. V., Zhang, Q. & Bourne, P. E. *BMC Bioinformatics,* 2005, **6**, 21.

8. Kussie, P. H., Gorina, S., Marechal, V., Elenbaas, B., Moreau, J., Levine, A. J., Pavletich, N. P. *Science,* 1996, **274**, 948-953.

9. Xu, D. & Zhang, Y. *PLoS ONE,* 2009, **4**, e8140.

10. Chou, K. C. & Cai, Y. D. *Proteins: Struct., Funct., Genet.,* 2003, **53**, 282-289.

11. Yu, X. J., Wang, C. & Li, Y. X. *BMC Bioinformatics,* 2006, **7**, 187.

12. Weber, P. C., Ohlendorf, D. H., Wendoloski, J. J. & Salemme, F. R. *Science,* 1989, **243**, 85-88.

13. Park, S.-Y., Yokoyama, T., Shibayama, N., Shiro, Y. & Tame, J. R. H. *J. Mol. Biol.,* 2006, **360**, 690-701.

14. Vousden, K. H. & Lu, X. *Nat. Rev. Cancer,* 2002, **2**, 594-604.

15. Carson, D. A. & Lois, A. *Lancet ,* 1995, **346,** 1009-1011.

16. Lane, D. P. *Nature,* 1992, **358**, 15-16.

17. Wang, P., Reem, M., Wang, Y., Mayr, G., Stenger, J. E., Anderson, M. E., Schwedes, J. F., Tegtmeyer, P. *Mol. Cell. Biol.,* 1994, **14**, 5182-5191.

18. Ho, W. C., Fitzgerald, M. X. & Marmorstein, R. *J. Biol. Chem.,* 2006, **281**, 20494-20502.

19. Ceskova, P., Chichgeri, H., Wallace, M., Vojtesek, B. & Hupp, T. R. *J. Mol. Biol*., 2006, **357**, 442-456.

20. Kitayner, M., Rozenberg, H., Kessler, N., Rabinovich, D., Shaulov, L., Haran, T. E., Shakked, Z. *Mol. Cell,* 2006, **22**, 741-753.

21. Fakharzadeh, S. S., Trusko, S. P. & George, D. L. *EMBO J.*, 1991, **10**, 1565-1569.

22. Momand, J., Zambetti, G. P., Olson, D. C., George, D. & Levine, A. J. *Cell,* 1992, **69,** 1237-1245.

23. Oliner, J. D., Kinzler, K. W., Meltzer, P. S., George, D. L. & Vogelstein, B. *Nature,* 1992, **358**, 80-83.

24. Wawrzynow, B., Pettersson, S., Zylicz, A., Bramham, J., Worrall, E., Hupp, T. R., Ball, K. L. *J. Biol. Chem.,* 2009, **284**, 11517-11530.

25. Wallace, M., Worrall, E., Pettersson, S., Hupp, T. R. & Ball, K. L. *Mol. Cell,* 2006, **23**, 251-263.

26. Ding, Y., Mei, Y. & Zhang, J. Z. H. *J. Phys. Chem. B,* 2008, **112**, 11396-11401.

27. Espinoza-Fonseca, L. M. & Garcia-Machorro, *J. Biochem. Biophys. Res. Commun.*, 2008, **370**, 547-551.

28. Dastidar, S. G., Lane, D. P. & Verma, C. S. *J. Am. Chem. Soc.*, 2008, **130**, 13514-+.

29. Ding, K., Lu, Y., Nikolovska-Coleska, Z., Wang, G., Qiu, S., Shangary, S., Gao, W., Qin, D., Stuckey, J., Krajewski, K., Roller, P. P., Wang, S. *J. Med. Chem.*, 2006, **49**, 3432-3435.

30. Garcia-Echeverria, C., Chene, P., Blommers, M. J. J. & Furet, P. *J. Med. Chem.*, 2000, **43**, 3205-3208.

31. Pazgiera, M., Liu, M., Zou, G., Yuan, W., Li, C., Li, J., Monbo, J., Zella, D., Tarasov, S. G., Lu, W. *PNAS,* 2009, **106**, 4665-4670.

32. Wang, S. M., Ding, K., Lu, Y. P., Nikolovska-Coleska, Z., Qiu, S., Kumar, S., Roller, P. P., Tomita, Y., Krajewski, K., Deschamps, J. R. *Abstr. Papers Am. Chem. Soc.,* 2005, **230**, U2700-U2700.

33. Yu, S. et al., Qin, D., Shangary, S., Chen, J., Wang, G., Ding, K., McEachern, D., Qiu, S., Nikolovska-Coleska, Z., Miller, R., Kang, S., Yang, D., Wang, S. *J. Med. Chem.*, 2009 **52**, 7970-7973.

34. Shimizu, H., Burch, L. R., Smith, A. J., Dornan, D., Wallace, M., Ball, K. L., Hupp, T. R. *J. Biol. Chem.*, 2002, **277**, 28446-28458.

35. Craig, A. L., Chrystal, J. A., Fraser, J. A., Sphyris, N., Lin, Y., Harrison, B. J., Scott, M. T., Dornreiter, I., Hupp, T. R. *Mol. Cell. Biol.*, 2007, **27**, 3542-3555.

36. Qiu, W., Wu, J., Walsh, E. M., Zhang, Y., Chen, C. Y., Fujita, J., Xiao, Z. X. J. *Oncogene,* 2008, **27,** 4034-4043.

37.	Kostic, M., Matt, T., Martinez-Yamout, M. A., Dyson, H. J. & Wright, P. E. *J. Mol. Biol.*, 2006, **363**, 433-450.

38.	Mekhail, K., Khacho, M., Carrigan, A., Hache, R. R. J., Gunaratnam, L., Lee, S. *J. Cell Biol.,* 2005, **170**, 733-744.

39.	Lorick, K. L., Jenson, J. P., Fang, S. Y., Ong, A. M., Hatakeyama, S., Weissman, A. M. *PNAS*, 1999, **96**, 11364-11369.

40.	Fang, S. Y., Jensen, J. P., Ludwig, R. L., Vousden, K. H. & Weissman, A. M. *J. Biol. Chem.,* 2000, **275**, 8945-8951.

41.	Wawrzynow, B., Zylicz, A., Wallace, M., Hupp, T. & Zylicz, M. *J. Biol. Chem*, 2007, **282**, 32603-32612.

42.	Uldrijan, S., Pannekoek, W.-J. & Vousden, K. H. *EMBO J.*, 2007, **26**, 102-112.

43.	Poyurovsky, M. V., Priest, C., Kentsis, A., Borden, K. L. B., Pan, Z.-Q., Pavletich, N., Prives, C. *EMBO-J.*, 2007, **26**, 90-101.

44.	Linke, K., Mace, P. D., Smith, C. A., Vaux, D. L., Silke, J., Day, C. L. *Cell Death Differ.*, 2008, **15**, 841-848.

45.	Bailey, K. *Proc. R. Soc. B-Biol. Sci.*, 1953, **141**, 45-48.

46.	Sodek, J., Hodges, R. S., Smillie, L. B. & Jurasek, L. *PNAS,* 1972, **69**, 3800-3804.

47.	Moutevelis, E. & Woolfson, D. N. *J. Mol. Biol.*, 2009, **385**, 726-732.

48.	Wolf, E., Kim, P. S. & Berger, B. *Protein Sci.*, 1997, **6**, 1179-1189.

49.	Rose, A. & Meier, I. *Cell. Mol. Life Sci.,* 2004, **61**, 1996-2009.

50.	Kohn, W. D., Mant, C. T. & Hodges, R. S. *J. Biol. Chem.*, 1997, **272**, 2583-2586.

51.	Marsden, H. R. & Kros, A. *Angew. Chem. Int. Ed.*, 2010, **49**, 2988-3005.

52.	Bornberg-Bauer, E., Rivals, E. & Vingron, M. *Nucleic Acids Res.*, 1998, **26**, 2740-2746.

53.	Landschulz, W. H., Johnson, P. F. & McKnight, S. L. *Science,* 1988, **240**, 1759-1764.

54.	Kass, R. S., Kurokawa, J., Marx, S. O. & Marks, A. R. *Trends Cardiovas. Med.*, 2003, **13,** 52-56.

55.	Obrdlik, P., Neuhaus, G. & Merkle, T. *FEBS Lett.,* 2000, **476**, 208-212.

56.	Roig, J., Mikhailov, A., Belham, C. & Avruch, J. *Genes Dev.,* 2002, **16**, 1640-1658.

57.	Wang, W. L., Gao, R. & Lynn, D. G. *Chembiochem,* 2002, **3**, 311-317.

58.	Szilak, L., Moitra, J. & Vinson, C. *Protein Sci.*, 1997, **6**, 1273-1283.

59.	Gottschalk, K. E. *Structure,* 2005, **13**, 703-712.

60. Rose, A., Schraegle, S. J., Stahlberg, E. A. & Meier, I. *BMC Evol. Biol.*, 2005, **5**, 66.

61. Ausmees, N., Kuhn, J. R. & Jacobs-Wagner, C. *Cell,* 2003, **115**, 705-713.

62. Margolin, W. *Curr. Biol.,* 2004, **14**, R242-R244.

63. Burgess, S. A., Walker, M. L., Sakakibara, H., Knight, P. J. & Oiwa, K. *Nature,* 2003, **421**, 715-718.

64. Harborth, J., Wang, J., Gueth-Hallonet, C., Weber, K. & Osborn, M. *EMBO J.*, 1999, **18**, 1689-1700.

65. Kreplak, L., Nyland, L. R., Contompasis, J. L. & Vigoreaux, J. O. *J. Mol. Biol.*, 2009, **386**, 1403-1410.

66. Thorn, K. S., Ubersax, J. A. & Vale, R. D. *J. Cell Biol.*, 2000, **151**, 1093-1100.

67. Carr, C. M. & Kim, P. S. *Cell,* 1993, **73**, 823-832.

68. Rizo, J., Chen, X. C. & Arac, D. *Trends Cell Biol.*, 2006, **16**, 549-550.

69. Crick, F. H. C. *Acta Crystallogr.*, 1953, **6**, 689-697.

70. McLachlan, A. D., Stewart, M. & Smillie, L. B. *J. Mol. Biol.*, 1975, **98**, 281-291.

71. Walshaw, J. & Woolfson, D. N. *Protein Sci.*, 2001, **10**, 668-673.

72. Peters, J., Baumeister, W. & Lupas, A. *J. Mol. Biol.*, 1996, **257**, 1031-1041.

73. Oshea, E. K., Klemm, J. D., Kim, P. S. & Alber, T. *Science,* 1991, **254**, 539-544.

74. Oshea, E. K., Lumb, K. J. & Kim, P. S. *Curr. Biol.*, 1993, **3**, 658-667.

75. Monera, O. D., Kay, C. M. & Hodges, R. S. *Biochemistry,* 1994, **33,** 3862-3871.

76. Pagel, K., Wagner, S. C., Araghi, R. R., von Berlepsch, H., Boettcher, C., Koksch, B. *Chem.--Eur. J.*, 2008, **14**, 11442-11451.

77. Woolfson, D. N. & Alber, T. *Protein Sci.*, 1995, **4**, 1596-1607.

78. Burkhard, P., Ivaninskii, S. & Lustig, A. *J. Mol. Biol.,* 2002 **318**, 901-910.

79. Ciani, B., Hutchinson, E. G., Sessions, R. B. & Woolfson, D. N. *J. Biol. Chem.*, 2002, **277,** 10150-10155.

80. Monera, O. D., Zhou, N. E., Lavigne, P., Kay, C. M. & Hodges, R. S. *J. Biol. Chem.*, 1996, **271**, 3995-4001.

81. Son, S., Caglar Tanrikulu, I. & Tirrell, D. A. *Chembiochem,* 2006, **7**, 1251-1257.

82. Tsatskis, Y., Kwok, S. C., Becker, E., Gill, C., Smith, M. N., Keates, R. A. B., Hodges, R. S., Wood, J. M. *Biochemistry*, 2008, **47**, 60-72.

83. Litowski, J. R. & Hodges, R. S. *J. Pept. Res.*, 2001, **58**, 477-492.

84.   Diss, M. L. & Kennan, A. J. *Org. Lett*., 2008, **10**, 3797-3800.

85.   Harbury, P. B., Zhang, T., Kim, P. S. & Alber, T. *Science,* 1993, **262**, 1401-1407.

86.   Kajava, A. V. *Proteins: Struct., Funct., Genet.,* 1996, **24**, 218-226.

87.   Harbury, P. B., Kim, P. S. & Alber, T. *Nature,* 1994 **371**, 80-83.

88.   Kojima, S., Kuriki, Y., Yoshida, T., Yazaki, K. & Miura, K. *Proc. Jpn. Acad. Ser. B Phys. Biol. Sci*., 1997, **73**, 7-11.

89.   Pandya, M. J., Spooner, G. M., Sunde, M., Thorpe, J. R., Rodger, A., Woolfson, D. N. *Biochemistry,* 2000, **39**, 8728-8734.

90.   Dong, H., Paramonov, S. E. & Hartgerink, J. D. *J. Am. Chem. Soc.,* 2008, **130**, 13691-13695.

91.   Gribbon, C., Channon, K. J., Zhang, W., Banwell, E. F., Bromley, E. H. C., Chaudhuri, J. B., Oreffo, R. O. C., Woolfson, D. N. *Biochemistry,* 2008, **47**, 10365-10371.

92.   Potekhin, S. A., Melnik, T. N., Popov, V., Lanina, N. F., Vazgina, A. A., Rigler, P., Verdini, A. S., Corradin, G., Kajava, A. V. *Chem. Biol*., 2001, **8**, 1025-1032.

93.   Lazar, K. L., Miller-Auer, H., Getz, G. S., Orgel, J. & Meredith, S. C. *Biochemistry,* 2005, **44**, 12681-12689.

94.   Zhou, M., Bentley, D. & Ghosh, I. *J. Am. Chem. Soc*., 2004, **126**, 734-735.

95.   Holmstrom, S. C., King, P. J. S., Ryadnov, M. G., Butler, M. F., Mann, S., Woolfson, D. N. *Langmuir,* 2008, **24**, 11778-11783.

96.   Ryadnov, M. G. & Woolfson, D. N. *J. Am. Chem. Soc*., 2004, **126**, 7454-7455.

97.   Ryadnov, M. G. *Angew. Chem. Int. Ed*., 2007, **46**, 969-972.

98.   Wagner, S. C., Roskamp, M., Pallerla, M., Araghi, R. R., Schlecht, S., Koksch, B. *Small,* 2010, **6,** 1321-1328.

99.   Banwell, E. F., Abelardo, E. S., Adams, D. J., Birchall, M. A., Corrigan, A., Donald, A. M., Kirkland, M., Serpell, L. C., Butler, M. F., Woolfson, D. N. *Nature Materials,* 2009, **8**, 596-600.

100.   Marsden, H. R., Korobko, A. V., van Leeuwen, E. N. M., Pouget, E. M., Veen, S. J., Sommerdijk, N. A. J. M., Kros, A. *J Am. Chem. Soc.,* 2008, **130**, 9386-9393.

101.   Nakaji-Hirabayashi, T., Kato, K. & Iwata, H. *Biomacromolecules,* 2008, **9**, 1411-1416.

102.   Petka, W. A., Harden, J. L., McGrath, K. P., Wirtz, D. & Tirrell, D. A. *Science,* 1998, **281**, 389-392.

103. Wang, C., Stewart, R. J. & Kopecek, J. *Nature,* 1999, **397**, 417-420.

104. Bromley, E. H. C., Sessions, R. B., Thomson, A. R. & Woolfson, D. N. *J. Am. Chem. Soc.,* 2009, **131**, 928-+.

105. Frost, D. W. H., Yip, C. M. & Chakrabartty, A. *Biopolymers,* 2005, **80**, 26-33.

106. Almeida, A. J., Runge, S. & Muller, R. H. *Int. J. Pharm*., 1997,**149**, 255-265.

107. Li, J. K., Wang, N. & Wu, X. S. *J. Pharm. Sci*., 1997, **86**, 891-895.

108. Sakuma, S., Suzuki, N., Kikuchi, H., Hiwatari, K., Arikawa, K., Kishida, A., Akashi, M. *Int. J. Pharm*., 1997, **149**, 93-106.

109. Florence, A. T., Hillery, A. M., Hussain, N. & Jani, P. U. *J. Controlled Release,* 1995, **36**, 39-46.

110. Quinten, M. *Appl. Phys. B: Lasers Opt.,* 2001, **73**, 245-255.

111. Pitarke, J. M., Silkin, V. M., Chulkov, E. V. & Echenique, P. M. *J. Opt. A-Pure Appl. Op*., 2005, **7**, S73-S84.

112. GarciaVidal, F. J. & Pendry, J. B. *Phys. Rev. Lett*., 1996, **77**, 1163-1166.

113. Josephson, L., Tung, C. H., Moore, A. & Weissleder, R. *Bioconjugate Chem*., 1999, **10**, 186-191.

114. Slocik, J. M., Stone, M. O. & Naik, R. R. *Small,* 2005, **1**, 1048-1052.

115. Tan, Y. N., Lee, J. Y. & Wang, D. I. C. *J. Am. Chem. Soc*., 2010, **132**, 5677-5686.

116. Duchesne, L., Wells, G., Fernig, D. G., Harris, S. A. & Levy, R. *Chembiochem,* 2008, **9**, 2127-2134.

117. Graf, P., Mantion, A., Foelske, A., Shkilnyy, A., Masic, A., Thuenemann, A. E., Taubert, A. *Chemistry*, 2009, **15**, 5831-5844.

118. Levy, R., Thanh, N. T. K., Doty, R. C., Hussain, I., Nichols, R. J., Schiffrin, D. J., Brust, M., Fernig, D. G. *J. Am. Chem. Soc*., 2004, **126**, 10076-10084.

119. Duchesne, L., Gentili, D., Comes-Franchini, M. & Fernig, D. G. *Langmuir,* 2008, **24**, 13572-13580.

120. Krpetic, Z., Nativo, P., Porta, F. & Brust, M. *Bioconjugate Chem*., 2009, **20**, 619-624.

121. Mandal, H. S. & Kraatz, H.-B. *J. Am. Chem. Soc*., 2007, **129**, 6356-+.

122. Serizawa, T., Hirai, Y. & Aizawa, M. *Langmuir,* 2009, **25**, 12229-12234.

123. Turkevich, J., Stevenson, P. C. & Hillier, J. *Disc. Faraday Soc*., 1951, **11**, 55-&.

124. Lee, P. C. & Meisel, D. *J. Phys. Chem*., 1982, **86**, 3391-3395.

125. Bastus, N. G., Sanchez-Tillo, E., Pujals, S., Farrera, C., Lopez, C., Giralt, E., Celada, A., Lloberas, J., Puntes, V. *ACS Nano,* 2009, **3**, 1335-1344.

126. Hosta-Rigau, L., Olmedo, I., Arbiol, J., Cruz, L. J., Kogan, M. J., Albericio, F. *Bioconjugate Chem*., 2010, **21**, 1070-1078.

127. MacKay, J. A. & Szoka, F. C. *J. Disper. Sci. Technol*., 2003, **24,** 465-473.

128. Pujals, S., Bastus, H. G., Pereiro, E., Lopez-Iglesias, C., Punte, V. F., Kogan, M. J., Giralt, E. *Chembiochem,* 2009, **10**, 1025-1031.

129. Surujpaul, P. P., Gutierrez-Wing, C., Ocampo-Garcia, B., Ramirez, F. d. M., de Murphy, C. A., Pedraza-Lopez, M., Camacho-Lopez, M. M., Ferro-Flores, G. *Biophys. Chem*., 2008, **138**, 83-90.

130. Sun, L., Liu, D. & Wang, Z. *Langmuir,* 2008, **24**, 10293-10297.

131. Savage, A. C. & Pikramenou, Z. *Chem. Commun*., 2011, **47**, 6431-6433.

132. Coomber, D., Bartczak, D., Gerrard, S. R., Tyas, S., Kanaras, A. G., Stulz, E. *Langmuir,* 2010, **26**, 13760-13762.

133. Shim, J.-Y. & Gupta, V. K. *J. Coll. Interf. Sci.,* 2007, **316**, 977-983.

134. Si, S., Raula, M., Paira, T. K. & Mandal, T. K. *Chemphyschem,* 2008, **9**, 1578-1584.

135. Berson, S. A., Yalow, R. S., Bauman, A., Rothschild, M. A. & Newerly, K. *J. Clin. Invest*., 1956, **35**, 170-190.

136. Yalow, R. S. & Berson, S. A. *J. Clin. Invest*., 1960, **39**, 1157-1175.

37. Van Weemen, B. K. & Schuurs, A. H. W. M. *FEBS Lett*., 1971, **15**, 232-236.

138. Savchenko, A., Yurchenko, M., Snopok, B. & Kashuba, E. *Mol. Biotechnol*., 2009, **41**, 270-277.

139. Hayes, F. J., Halsall, H. B. & Heineman, W. R. *Anal. Chem*., 1994, **66**, 1860-1865.

140. Wang, G., Yuan, J., Hai, X. & Matsumoto, K. *Talanta,* 2006, **70**, 133-138.

141. Vuori, J., Rasi, S., Takala, T. & Vaananen, K. *Clin. Chem*., 1991, **37**, 2087-2092.

142. Caldwell, M. L., Moffitt, R. A., Liu, J., Parry, R. M., Sharma, Y., Wang, M. D. *Conf. proc. IEEE Eng. Med. Biol. Soc*., 2008, 1907-10.

143. Gutcho, S. & Mansbach, L. *Clin. Chem*., 1977, **23**, 1609-1614.

144. Chan, W. C. W. & Nie, S. M. *Science,* 1998, **281**, 2016-2018.

145. Engvall, E. & Perlmann, P. *Immunochemistry,* 1971, **8**, 871-&.

146. Xia, Z. & Rao, J. *Curr. Opin. Biotechnol.,* 2009, **20**, 37-44.

147. Pei, R. J., Cui, X. Q., Yang, X. R. & Wang, E. K. *Talanta,* 2000, **53**, 481-488.

148. Xu, Y. Y., Pettersson, K., Blomberg, K., Hemmila, I., Mikola, H., Lovgren, T. *Clin. Chem.*, 1992, **38**, 2038-2043.

149. Allen, S., Chen, X. Y., Davies, J., Davies, M. C., Dawkes, A. C., Edwards, J. C., Roberts, C. J., Sefton, J., Tendler, S. J. B., Williams, P. M. *Biochemistry,* 1997, **36**, 7457-7463.

150. Tang, L., Dong, C. & Ren, J. *Talanta,* 2010, **81**, 1560-1567.

151. Pihlasalo, S., Kirjavainen, J., Hanninen, P. & Harma, H. *Anal. Chem.*, 2011, **83**, 1163-1166.

152. Biswas, P., Cella, L. N., Kang, S. H., Mulchandani, A., Yates, M. V., Chen, W. *Chem. Commun.,* 2011, **47**, 5259-5261.

153. Liu, J., Yang, X., Wang, K., Yang, R., Ji, H., Yang, L., Wu, C. *Chem. Commun.*, 2011, **47,** 935-937.

154. Sehr, P., Pawlita, M. & Lewis, J. *J. Biomol. Screen.*, 2007, **12**, 560-567.

155. Lawrence, H. R., Li, Z., Yip, M. L. R., Sung, S.-S., Lawrence, N. J., McLaughlin, M. L., McManus, G. J., Zaworotko, M. J., Sebti, S. M., Chen, J., Guida, W. C. *Bioorg. Med. Chem. Lett.*, 2009, **19**, 3756-3759.

156. Ewen Smith, G. D. *Modern Raman Spectroscopy - A Practical Approach.* John Wiley and Sons Ltd., Chichester, 2005.

157. Graham, D., Faulds, K. & Smith, W. E. *Chem. Commun.*, 2006, **42**, 4363-4371.

158. Albrecht, M. G. & Creighton, J. A. *J. Am. Chem. Soc.*, 1977, **99**, 5215-5217.

159. Jeanmaire, D. L. & Vanduyne, R. P. *J. Electroanal. Chem.*, 1977, **84**, 1-20.

160. Moskovits, M. *Rev. Mod. Phys.*, 1985, **57**, 783-826.

161. McLaughlin, C., Graham, D. & Smith, W. E. *J. Phys. Chem. B,* 2002, **106**, 5408-5412.

162. Vlckova, B., Pavel, I., Sladkova, M., Siskova, K. & Slouf, M. *J. Mol. Struct.*, 2007, **834**, 42-47.

163. Faulds, K., Jarvis, R., Smith, W. E., Graham, D. & Goodacre, R. *Analyst,* 2008, **133**, 1505-1512.

164. Sabatte, G., Keir, R., Lawler, M., Black, M., Graham, D., Smith, W. E. *Anal. Chem.*, 2008, **80**, 2351-2356.

165. Weitz, D. A., Moskivits, M. and Creighton, J. A. *Chemistry and Structure at Interfaces* ed. Ellis, R. B. H. a. B. A. VCH, Deerfield Beech, 1986.

166.   Pergolese, B., Muniz-Miranda, M. & Bigotto, A. *J. Phys. Chem. B,* 2004, **108**, 5698-5702.

167.   Naumov, S., Kapoor, S., Thomas, S., Venkateswaran, S. & Mukherjee, T. *J. Mol. Struct.-Theochem,* 2004, **685**, 127-131.

168.   Graham, D., McLaughlin, C., McAnally, G., Jones, J. C., White, P. C., Smith, W. E. *Chem. Commun*., 1998, **11**, 1187-1188.

169.   Jones, J. C., McLaughlin, C., Littlejohn, D., Sadler, D. A., Graham, D., Smith, W. E. *Anal. Chem*., 1999, **71**, 596-601.

170.   McAnally, G., McLaughlin, C., Brown, R., Robson, D. C., Faulds, K., Tackley, D. R., Smith, W. E., Graham, D. *Analyst,* 2002, **127**, 838-841.

171.   Graham, D., Kennedy, A. R. & Teat, S. J. *J. Heterocycl. Chem*., 2000, **37**, 1555-1558.

172.   McHugh, C. J., Docherty, F. T., Graham, D. & Smith, W. E. *Analyst,* 2004, **129**, 69-72.

173.   Enright, A., Fruk, L., Grondin, A., McHugh, C. J., Smith, W. E., Graham, D. *Analyst,* 2004, **129**, 975-978.

174.   Grondin, A., Robson, D. C., Smith, W. E. & Graham, D. *J. Chem.Soc. Perkin Trans.,* 2001, **2**, 2136-2141.

175.   Alvarez-Puebla, R. A., Dos Santos, D. S. & Aroca, R. F. *Analyst,* 2004, **129**, 1251-1256.

176.   Gellner, M., Koempe, K. & Schluecker, S. *Anal. Bioanal. Chem*., 2009, **394**, 1839-1844.

177.   Michota, A. & Bukowska, J. *J. Raman Spectrosc.,* 2003, **34**, 21-25.

178.   Skadtchenko, B. O. & Aroca, R. *Spectrochim. Acta A Mol. Biomol. Spectrosc*., 2001, **57**, 1009-1016.

179.   Zavaleta, C. L., Smith, B. R., Walton, I., Doering, W., Davis, G., Shojael, B., Natan, M. J., Gambhir, S. S. *PNAS,* 2009, **106,** 13511-13516.

180.   Wang, G., Park, H.-Y. & Lipert, R. J. *Anal. Chem*., 2009, **81**, 9643-9650.

181.   Ni, J., Lipert, R. J., Dawson, G. B. & Porter, M. D. *Anal. Chem*., 1999, **71,** 4903-4908.

182.   Driskell, J. D., Kwarta, K. M., Lipert, R. J., Porter, M. D., Neill, J. D., Ridpath, J. F. *Anal. Chem*., 2005, **77**, 6147-6154.

183.   Grubisha, D. S., Lipert, R. J., Park, H. Y., Driskell, J. & Porter, M. D. *Anal. Chem.*, 2003, **75**, 5936-5943.

184.   Narayanan, R., Lipert, R. J. & Porter, M. D. *Anal. Chem*., 2008, **80**, 2265-2271.

185.   Yakes, B. J., Lipert, R. J., Bannantine, J. P. & Porter, M. D. *Clin. Vaccine Immunol.,* 2008, **15**, 227-234.

186. Munro, C. H., Smith, W. E., Garner, M., Clarkson, J. & White, P. C. *Langmuir,* 1995, **11**, 3712-3720.

187. Michaels, A. M., Jiang, J. & Brus, L. *J. Phys. Chem. B,* 2000, **104**, 11965-11971.

188. Lal, S., Grady, N. K., Goodrich, G. P. & Halas, N. J. *Nano Lett*., 2006, **6,** 2338-2343.

189. Zhu, Z. H., Zhu, T. & Liu, Z. F. *Nanotechnology,* 2004, **15**, 357-364.

190. Faulds, K., Littleford, R. E., Graham, D., Dent, G. & Smith, W. E. *Anal. Chem*., 2004, **76**, 592-598.

191. Campbell, F. M., Ingram, A., Monaghan, P., Cooper, J., Sattar, N., Eckersall, P. D., Graham, D. *Analyst,* 2008, **133**, 1355-1357.

192. Dou, X., Takama, T., Yamaguchi, Y., Yamamoto, H. & Ozaki, Y. *Anal. Chem*., 1997, **69**, 1492-1495.

193. Douglas, P., Stokes, R. J., Graham, D. & Smith, W. E. *Analyst,* 2008, **133**, 791-796.

194. Han, X. X., Kitahama, Y., Tanaka, Y., Guo, J., Xu, W. Q., Zhao, B., Ozaki, Y. *Anal. Chem*., 2008, **80**, 6567-6572.

195. Rohr, T. E., Cotton, T., Fan, N. & Tarcha, P. J. *Anal. Biochem*., 1989, **182**, 388-398.

196. Laing, S., Hernandez-Santana, A., Sassmannshausen, J., Asquith, D. L., McInnes, I. B., Faulds, K., Graham, D. *Anal. Chem*., 2011, **83**, 297-302.

197. Han, X. X., Cai, L. J., Cuo, J., Wang, C. X., Ruan, W. D., Han, W. Y., Xu, W. Q., Zhao, B., Ozaki, Y. *Anal. Chem*., 2008, **80**, 3020-3024.

198. Gupta, S., Huda, S., Kilpatrick, P. K. & Velev, O. D. *Anal. Chem.,* 2007, **79**, 3810-3820.

199. Han, X. X., Chen, L., Guo, J., Zhao, B. & Ozaki, Y. *Anal. Chem*., 2010, **82**, 4102-4106.

200. Huang, G. G., Hossain, M. K., Han, X. X. & Ozaki, Y. *Analyst,* 2009, **134**, 2468-2474.

201. Ingram, A., Stokes, R. J., Redden, J., Gibson, K., Moore, B., Faulds, K., Graham, D. *Anal. Chem*., 2007, **79**, 8578-8583.

202. Kim, K., Lee, H. B., Lee, Y. M. & Shin, K. S. *Biosens. Bioelectron*., 2009 **24**, 1864-1869.

203. Wang, G., Lipert, R. J., Jain, M., Kaur, S., Chakraboty, S., Torres, M. P., Batra, S. K., Brand, R. E., Porter, M. D. *Anal. Chem*., 2011, **83**, 2554-2561.

204. Li, C., Pazgier, M., Li, C., Yuan, W., Liu, M., Wei, G., Lu, W.-Y. *J. Mol. Biol*., 2010, **398**, 200-213.

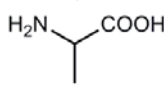205. Liu, M., Pazgier, M., Li, C., Yuan, W., Li, C., Lu, W. *Angew. Chemie Int. Ed*., 2010, **49**, 3649-3652.
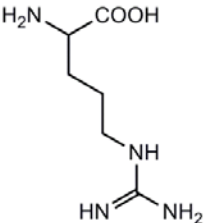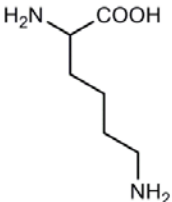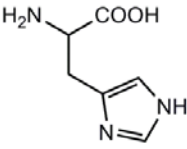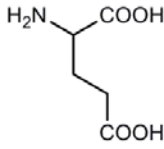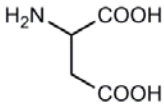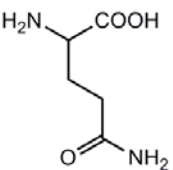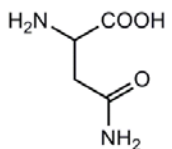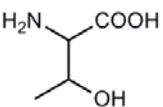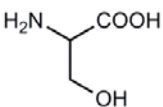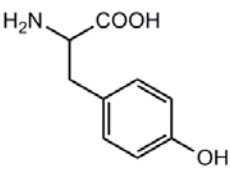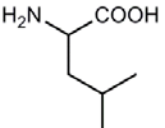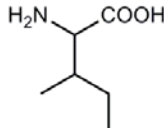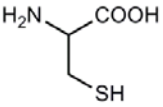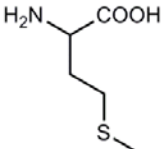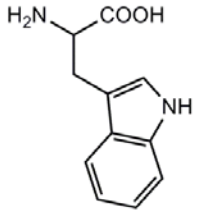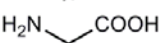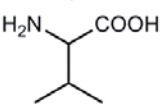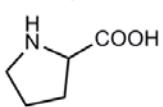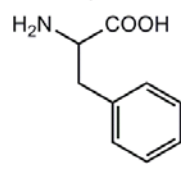
206. Bottger, V., Bottger, A., Howard, S. F., Picksley, S. M., Chene, P., GarciaEcheverria, C., Hochkeppel, H. K., Lane, D. P. *Oncogene,* 1996, **13**, 2141-2147.

207. Bucci, C. F. & Bucci, E. *Biochemistry,* 1975, **14**, 4451-4458.

208. Roccatano, D., Colombo, G., Fioroni, M. & Mark, A. E. *PNAS,* 2002, **99**, 12179-12184.

209. Ozdemir, A., Lednev, I. K. & Asher, S. A. *Biochemistry,* 2002, **41**, 1893-1896.

210. Sun, S. Q., Thompson, D., Schmidt, U., Graham, D. & Leggett, G. J. *Chem. Commun.*, 2010, **46**, 5292-5294.

211. Andresen, H., Gupta, S. & Stevens, M. M. *Nanoscale,* 2011, **3**, 383-386.

212. Gupta, S., Andresen, H. & Stevens, M. M. *Chem. Commun.*, 2011, **47**, 2249-2251.

213. Onoda, A., Ueya, Y., Sakamoto, T., Uematsu, T. & Hayashi, T. *Chem. Commun.*, 2010, **46**, 9107-9109.

214. Vassilev, L. T. *Cell Cycle,* 2004, **3**, 419-421.

215. Hsieh, J. K., Chan, F. S. G., O'Connor, D. J., Mittnacht, S., Zhong, S., Lu, X. *Mol. Cell,* 1999, **3**, 181-193.

216. Ryadnov, M. G., Ceyhan, B., Niemeyer, C. M. & Woolfson, D. N. *J. Am. Chem. Soc.,* 2003, **125**, 9388-9394.

217. Aili, D., Enander, K., Rydberg, J., Nesterenko, I., Bjoerefors, F., Baltzer, L., Liedberg, B. *J. Am. Chem. Soc.*, 2008, **130**, 5780-5788.

218. Aili, D., Enander, K., Baltzer, L. & Liedberg, B. *Nano Lett.*, 2008, **8**, 2473-2478.

219. Slocik, J. M., Tam, F., Halas, N. J. & Naik, R. R. *Nano Lett.*, 2007, **7**, 1054-1058.

220. Stevens, M. M., Flynn, N. T., Wang, C., Tirrell, D. A. & Langer, R. *Adv. Mater.*, 2004, **16**, 915-918.

221. Ernenwein, D., Ghosh, P., Rotello, V. & Chmielewski, J. *Biopolymers,* 2009, **92**, 318-318.

222. Wagner, S. C., Roskamp, M., Coelfen, H., Boettcher, C., Schlecht, S., Koksch, B. *Org. Biomol. Chem.*, 2009, **7**, 46-51.

223. Contarino, M. R., Sergi, M., Harrington, A. E., Lazareck, A., Xu, J., Chaiken, I. *J. Mol. Recognit.*, 2006, **19**, 363-371.

224. Su, J. Y., Hodges, R. S. & Kay, C. M. *Biochemistry,* 1994, **33**, 15501-15510.

225. Aslan, K. & Perez-Luna, V. H. *Langmuir,* 2002, **18**, 6059-6065.

226. Lin, S. Y., Tsai, Y. T., Chen, C. C., Lin, C. M. & Chen, C. H. *J. Phys. Chem. B,* 2004, **108**, 2134-2139.

227. Bokenkamp, D., Desai, A., Yang, X., Tai, Y. C., Marzluff, E. M., Mayo, S. L. *Anal. Chem*., 1998, **70**, 232-236.

228. Hodder, P. S., Blankenstein, G. & Ruzicka, J. *Analyst,* 1997, **122**, 883-887.

229. Dou, X. M. & Ozaki, Y. *Appl. Spectrosc*., 1998, **52**, 815-819.

230. Freeman, R. D., Hammaker, R. M., Meloan, C. E. & Fateley, W. G. *Appl. Spectrosc*., 1988, **42**, 456-460.

231. Taylor, G. T., Sharma, S. K. & Mohanan, K. *Appl. Spectrosc*., 1990, **44**, 635-640.

232. Kamholz, A. E., Weigl, B. H., Finlayson, B. A. & Yager, P. *Anal. Chem*., 1999, **71,** 5340-5347.

233. Chen, H. & Meiners, J. C. *Appl. Phys. Lett*., 2004, **84**, 2193-2195.

234. Kim, D. J., Oh, H. J., Park, T. H., Choo, J. B. & Lee, S. H. *Analyst,* 2005, **130**, 293-298.

235. Liu, R. H., Stremler, M. A., Sharp, K. V., Olsen, M. G., Santiago, J. G., Adrian, R. J., Aref, H., Beebe, D. J. *J. Microelectromech. Syst*., 2000, **9**, 190-197.

236. Mengeaud, V., Josserand, J. & Girault, H. H. *Anal. Chem*., 2002, **74**, 4279-4286.

237. Stroock, A. D., Dertinger, S. K. W., Ajdari, A., Mezic, I., Stone, H. A., Whitesides, G. M. *Science,* 2002, **295**, 647-651.

238. Park, T., Lee, M., Choo, J., Kim, Y. S., Lee, E. K., Kim, D. J., Lee, S. H. *Appl. Spectrosc*., 2004, **58**, 1172-1179.

239. Salmon, J. B., Ajdari, A., Taberling, P., Servent, L., Talaga, D., Joanicot, M. *Appl. Phys. Lett*., 2005, **86**, 094106.

240. Ackermann, K. R., Henkel, T. & Popp, J. *Chemphyschem,* 2007, **8**, 2665-2670.

241. Fortt, R., Wootton, R. C. R. & de Mello, A. J. *Org. Process Res. Dev.,* 2003, **7,** 762-768.

242. Lee, M., Lee, J. P., Rhee, H., Choo, J., Chai, Y. G., Lee, E. K. *J. Raman Spectrosc*., 2003, **34**, 737-742.

243. Monaghan, P. B., McCarney, K. M., Ricketts, A., Littleford, R. E., Docherty, F., Smith, W. E., Graham, D., Cooper, J. M. *Anal. Chem*., 2007, **79,** 2844-2849.

244. Keir, R., Igata, E., Arundell, M., Smith, W. E., Graham, D. McHugh, C., Cooper, J. M. *Anal. Chem*., 2002, **74**, 1503-1508.

245. Docherty, F. T., Monaghan, P. B., Keir, R., Graham, D., Smith, W. E., Cooper, J. M. *Chem. Commun*., 2004, **1**, 118-119.

246. Park, T., lee, S., Seong, G. H., Choo, J., Lee, E. K., Kim, Y. S., Ji, W. H., Hwang, S. Y., Gweon, D. G., Lee, S. Lab Chip, 2005, **5**, 437-442.

247. Strehle, K. R., Cialla, D., Rosch, P., Henkel, T., Kohler, M., Popp, J. *Anal. Chem.*,2007, **79**, 1542-1547.

248. Walter, A., Marz, A., Schumacher, W., Rosch, P. & Popp, J. Lab Chip, 2011, **11**, 1013-1021.

249. Chiriaco, M. S., Primiceri, E., D'Amone, E., Ionescu, R. E., Rinaldi, R., Maruccio, G. *Lab Chip,* 2011, **11**, 658-663.

250. Herr, A. E., Hatch, A. V., Throckmorton, D. J., Tran, H. M., Brennan, J. S., Giannobile, W. V., Singh, A. K. *PNAS* , 2007, **104**, 5268-5273.

251. Lee, N. Y., Yang, Y., Kim, Y. S. & Park, S. *Bull. Korean Chem. Soc.*, 2006, **27**, 479-483.

252. Lin, F. Y. H., Sabri, M., Alirezaie, J., Li, D. Q. & Sherman, P. M. *Clin. Diagn. Lab. Immun.*, 2005, **12**, 418-425.

253. Lin, F. Y. H., Sabri, M., Erickson, D., Alirezaie, J., Li, D. Q., Sherman, P. M. *Analyst*, 2004, **129**, 823-828.

254. Heard, S. M., Grieser, F., Barraclough, C. G. & Sanders, J. V. *J. Colloid Interf. Sci.*, 1983 **93**, 545-555.

Appendix A – Amino acid structures

HYDROPHILIC BASIC

Arginine
Arg, R

Lysine
Lys, K

Histidine
His, H

HYDROPHILIC ACIDIC

Glutamic Acid
Glu, E

Aspartic Acid
Asp, D

HYDROPHILIC NEUTRAL

Glutamine
Gln, Q

Asparagine
Asn, N

Threonine
Thr, T

Serine
Ser, S

HYDROPHILIC AROMATIC

Tyrosine
Tyr, Y

HYDROPHOBIC

Leucine
Leu, L

Isoleucine
Iso, I

Cysteine
Cys, C

Methionine
Met, M

HYDROPHOBIC AROMATIC

Tryptophan
Trp, W

Glycine
Gly, G

Alanine
Ala, A

Valine
Val, V

Proline
Pro, P

Phenylalanine
Phe, F

Appendix B – Scanning electron microscopy

Part (i) - MDM2-mediated PSN assembly

Additional images from SEM analysis of PSN-12.1 and PSN-12.1$_{W\Delta A}$ with and without MDM2 (Figure 3.21, section 3.4.3.4, page 69)

15 pM PSN-12.1 without MDM2. PSN are monodispersed in solution.
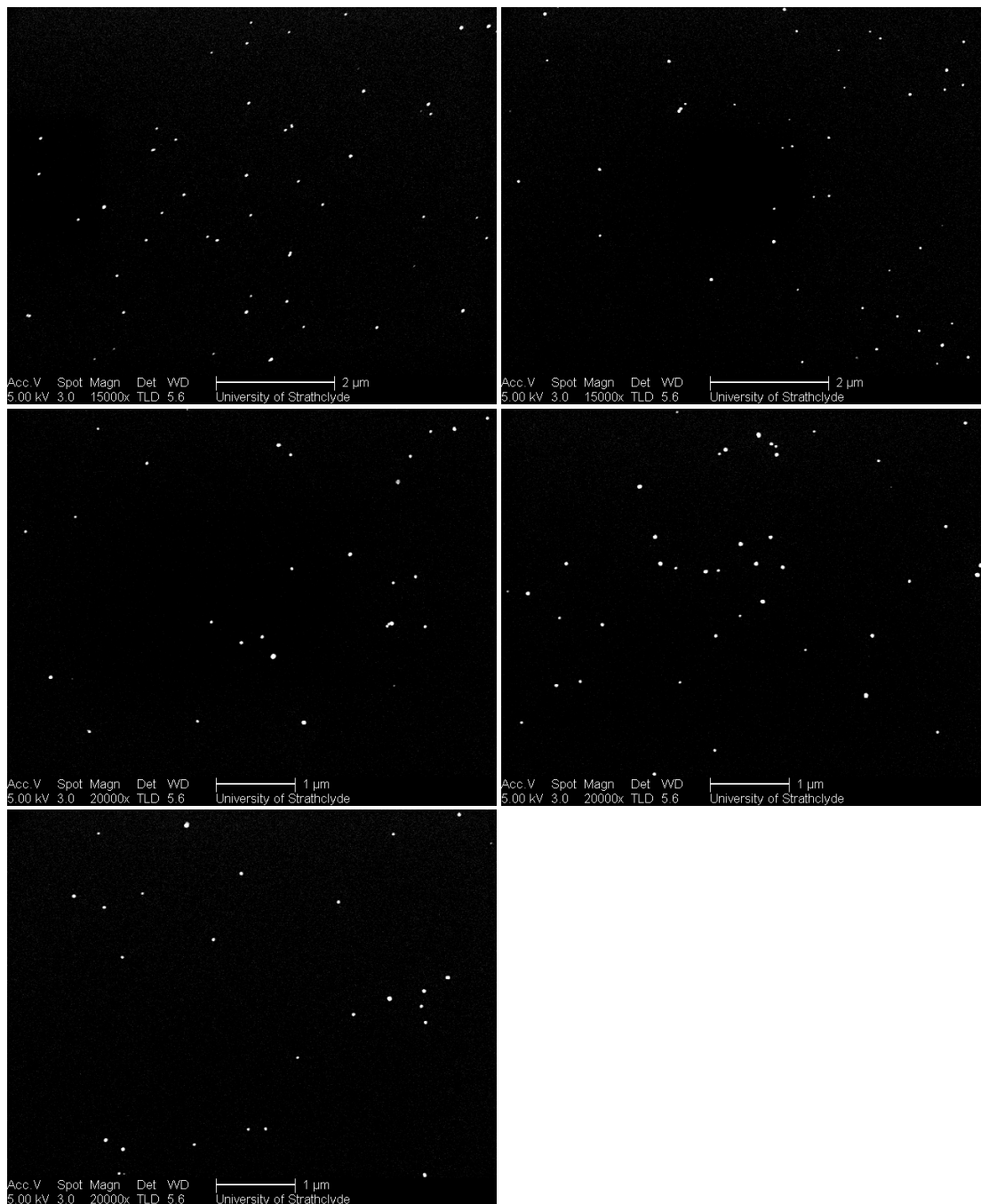
Appendix B – Scanning electron microscopy

15 pM PSN-12.1 following the addition of 15 nM MDM2. MDM2 – induced PSN assembly is observed as illustrated by the appearance of small clusters.
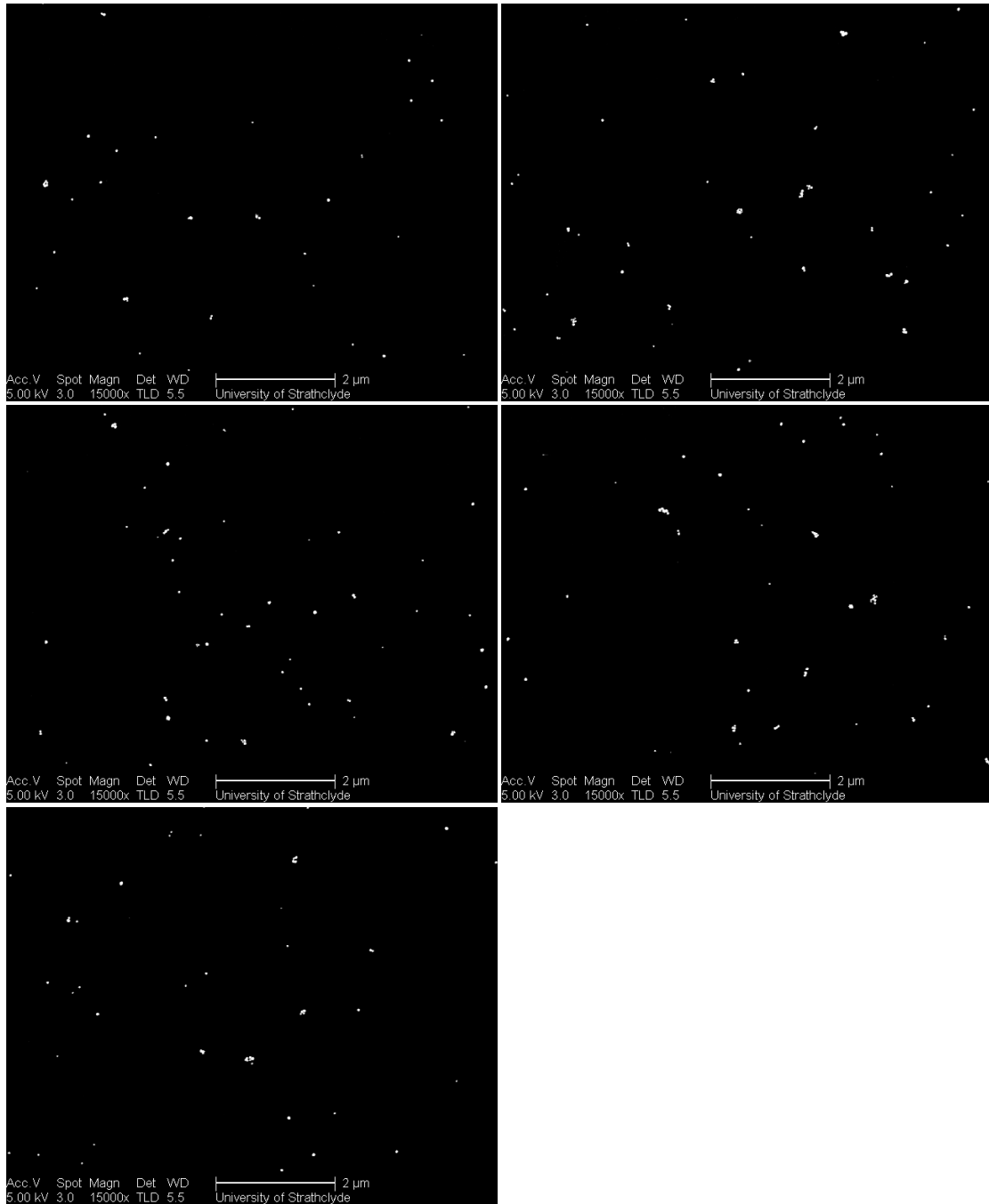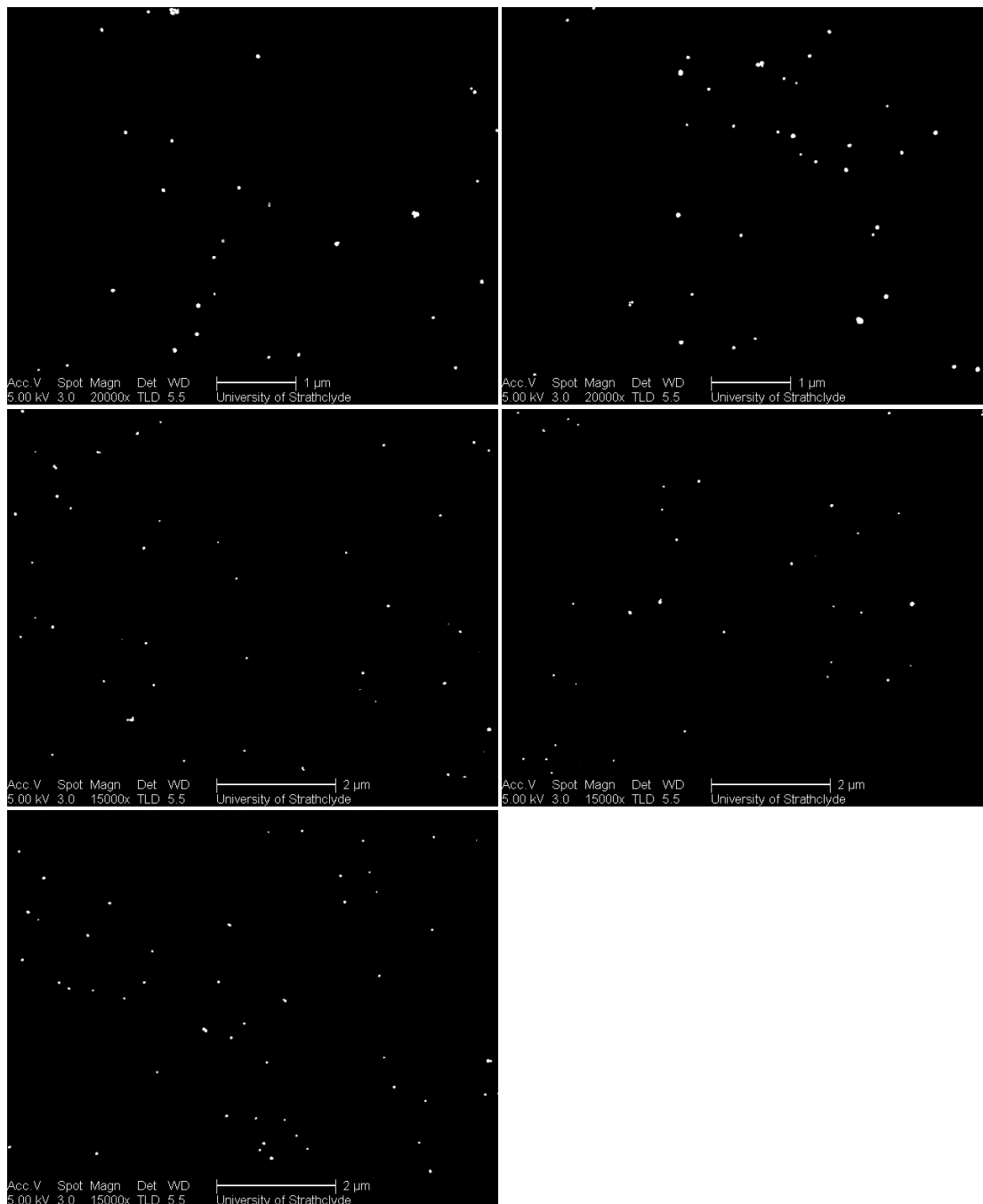
Appendix B – Scanning electron microscopy

15 pM PSN-12.1$_{W\Delta A}$ without MDM2. PSN are monodispersed in solution.
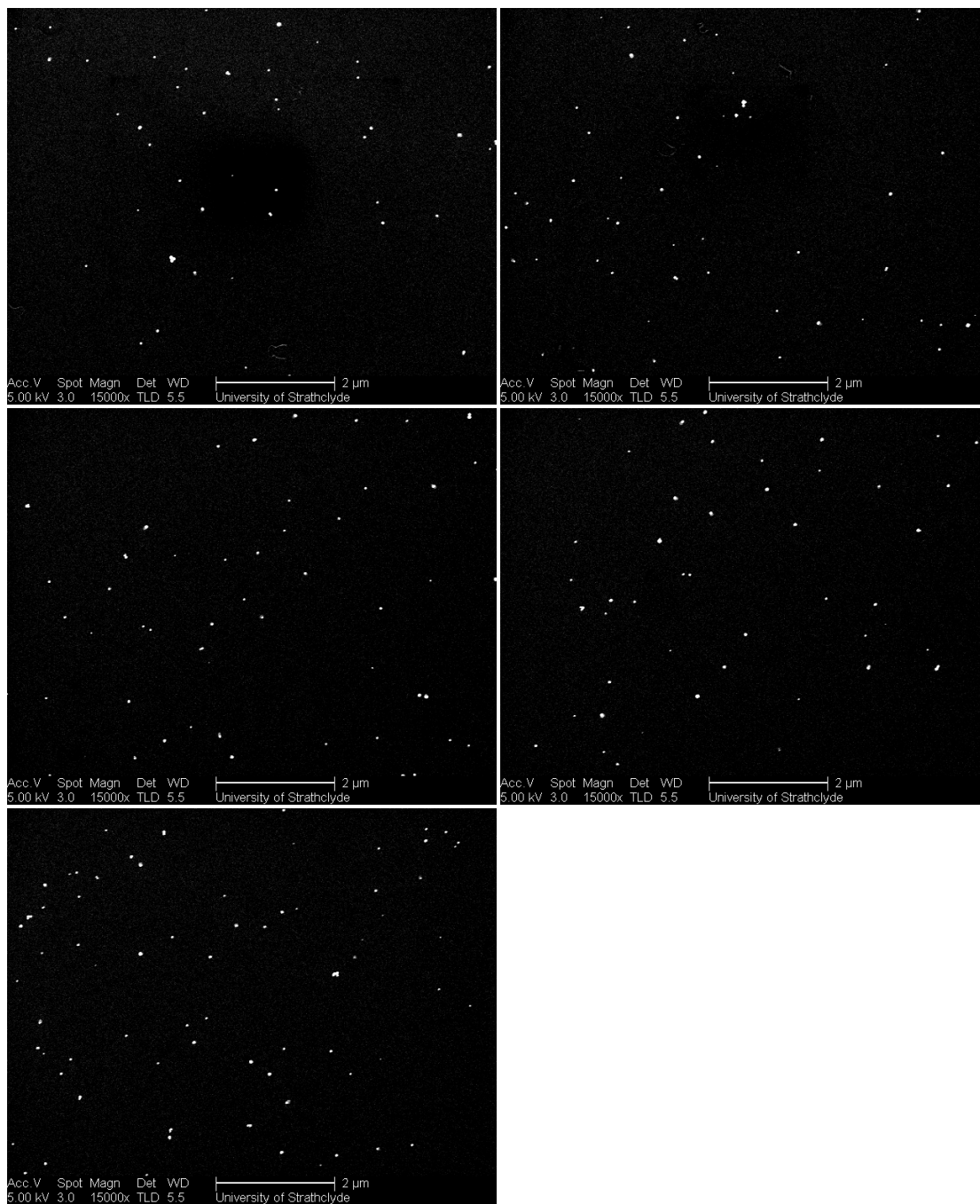
Appendix B – Scanning electron microscopy

15 pM PSN-12.1$_{W\Delta A}$ following the addition of 15 nM MDM2. Partial MDM2 – induced assembly is observed, as illustrated by the appearance of small clusters. Aggregation is not evident to the same extent as observed for PSN-12.1 with MDM2. (Figure 3.21b page 69)
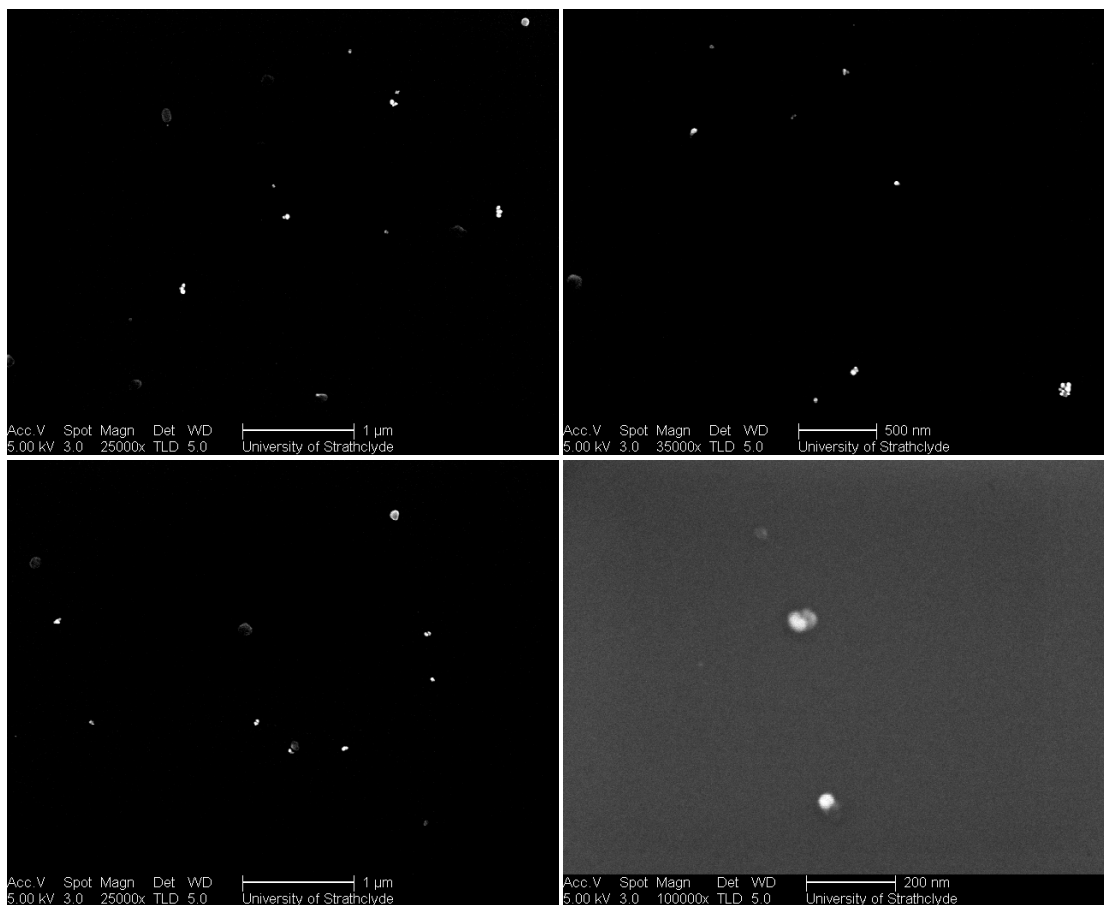
Appendix B – Scanning electron microscopy

## Part (ii) - PSN assembly with MDM2 and natural products P35 and P80

Additional SEM images from PSN samples used in natural product screening. Images recorded following temporal SERS analysis (Figure 3.44, section 3.6.3, page 102)

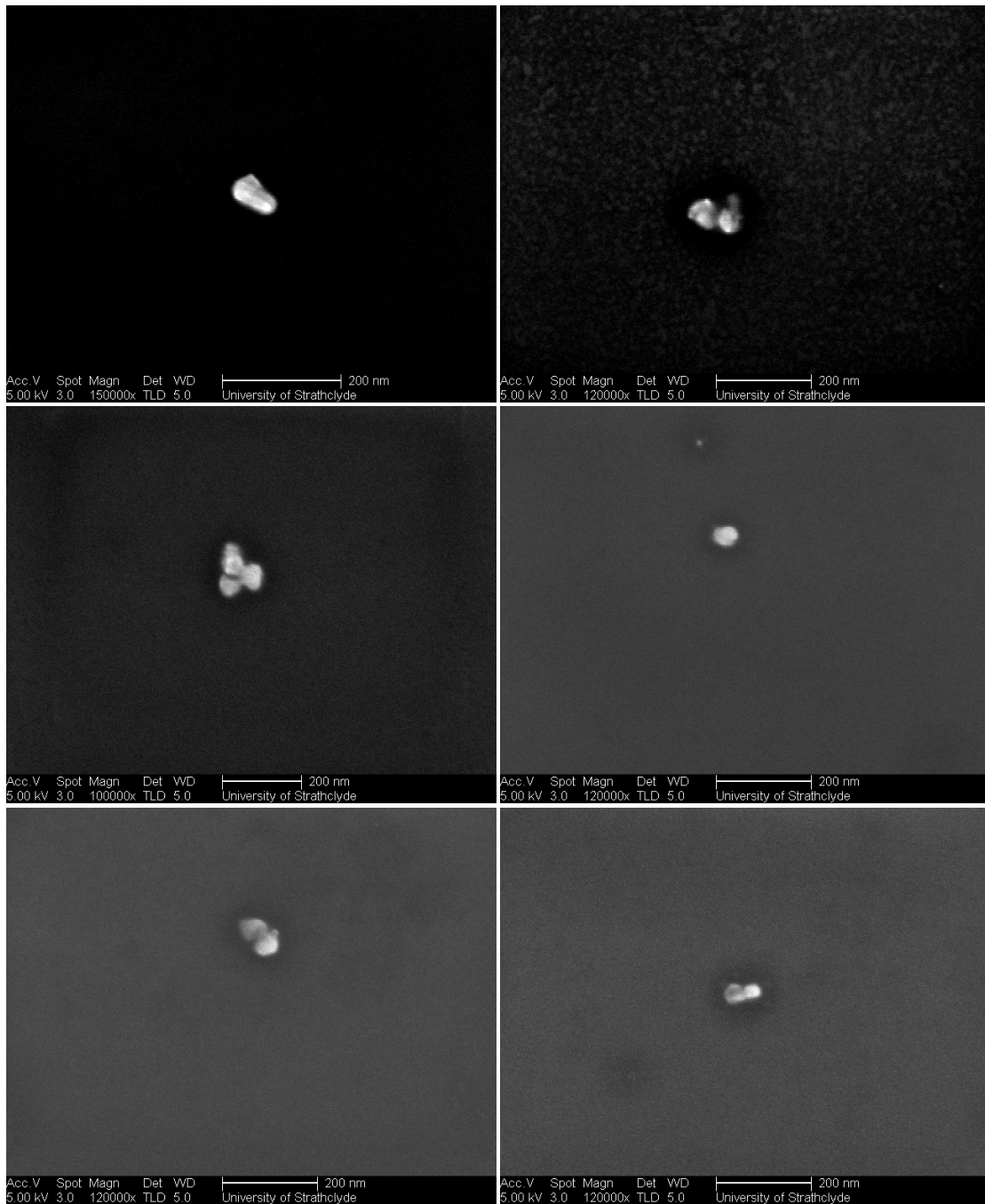### (A) 15 pM PSN-12.1 without MDM2. PSN are monodispersed in solution.

Appendix B – Scanning electron microscopy

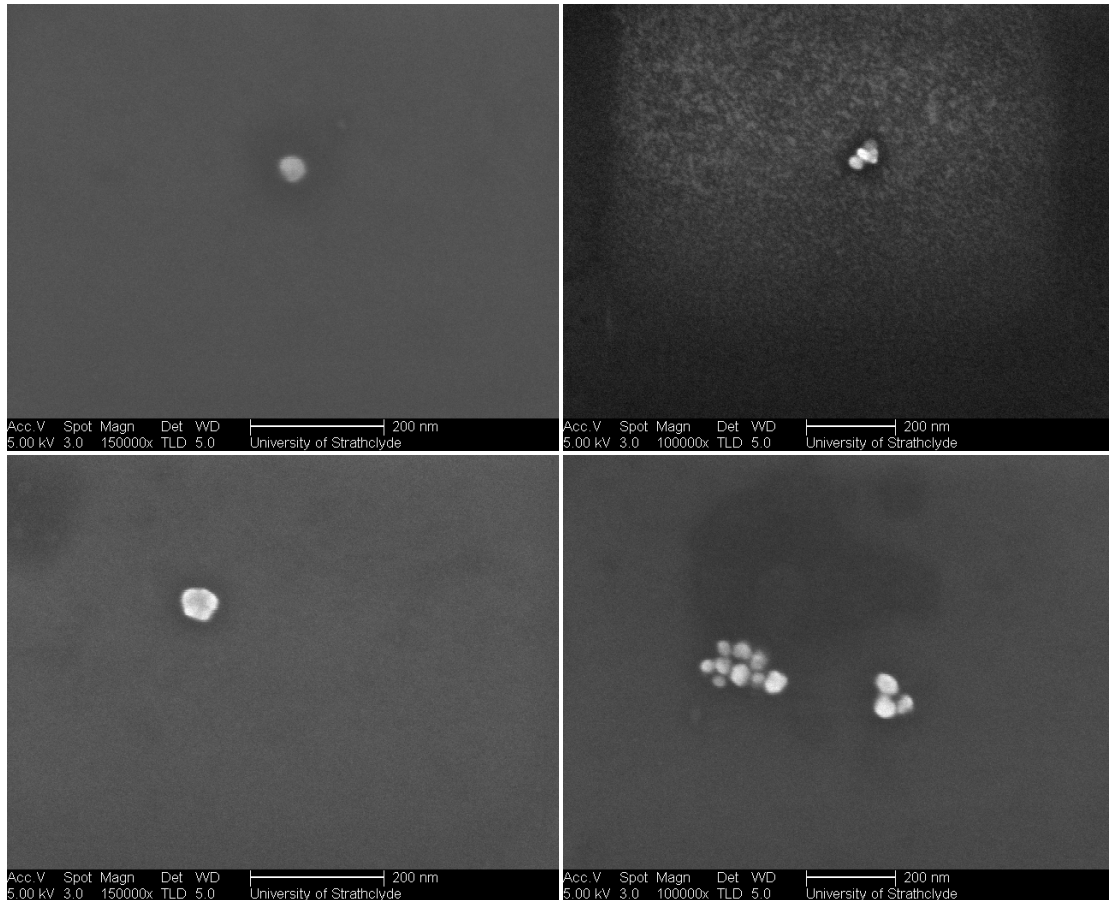**Continued... 15 pM PSN-12.1 without MDM2. PSN are monodispersed in solution.**
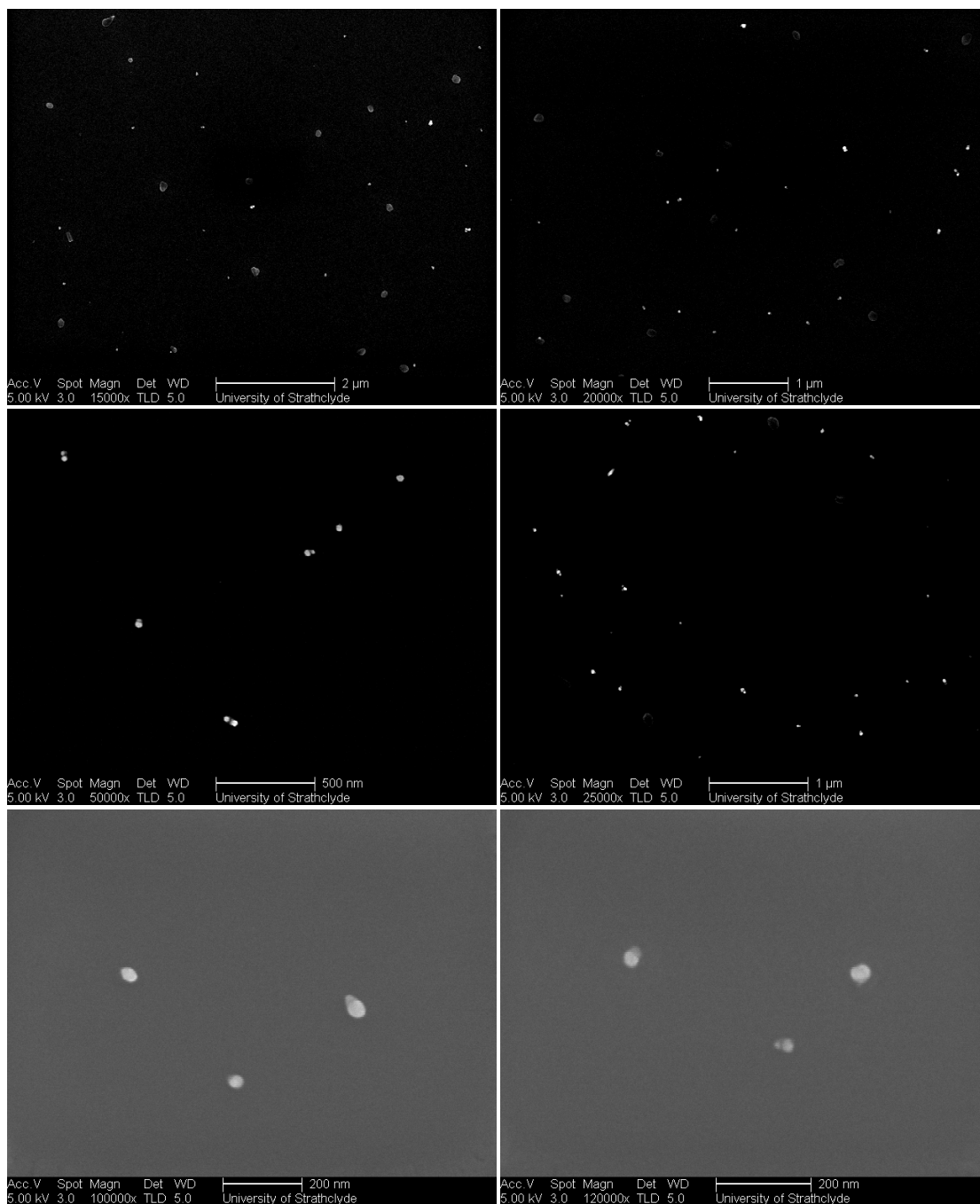
Appendix B – Scanning electron microscopy

(B) 15 pM PSN-12.1 following the addition of 15 nM MDM2. MDM2 – induced PSN assembly is obserbed, as illustrated by the appearance of small clusters.

Appendix B – Scanning electron microscopy

Continued… 15 pM PSN-12.1 following the addition of 15 nM MDM2. MDM2 – induced PSN assembly is obserbed, as illustrated by the appearance of small clusters.
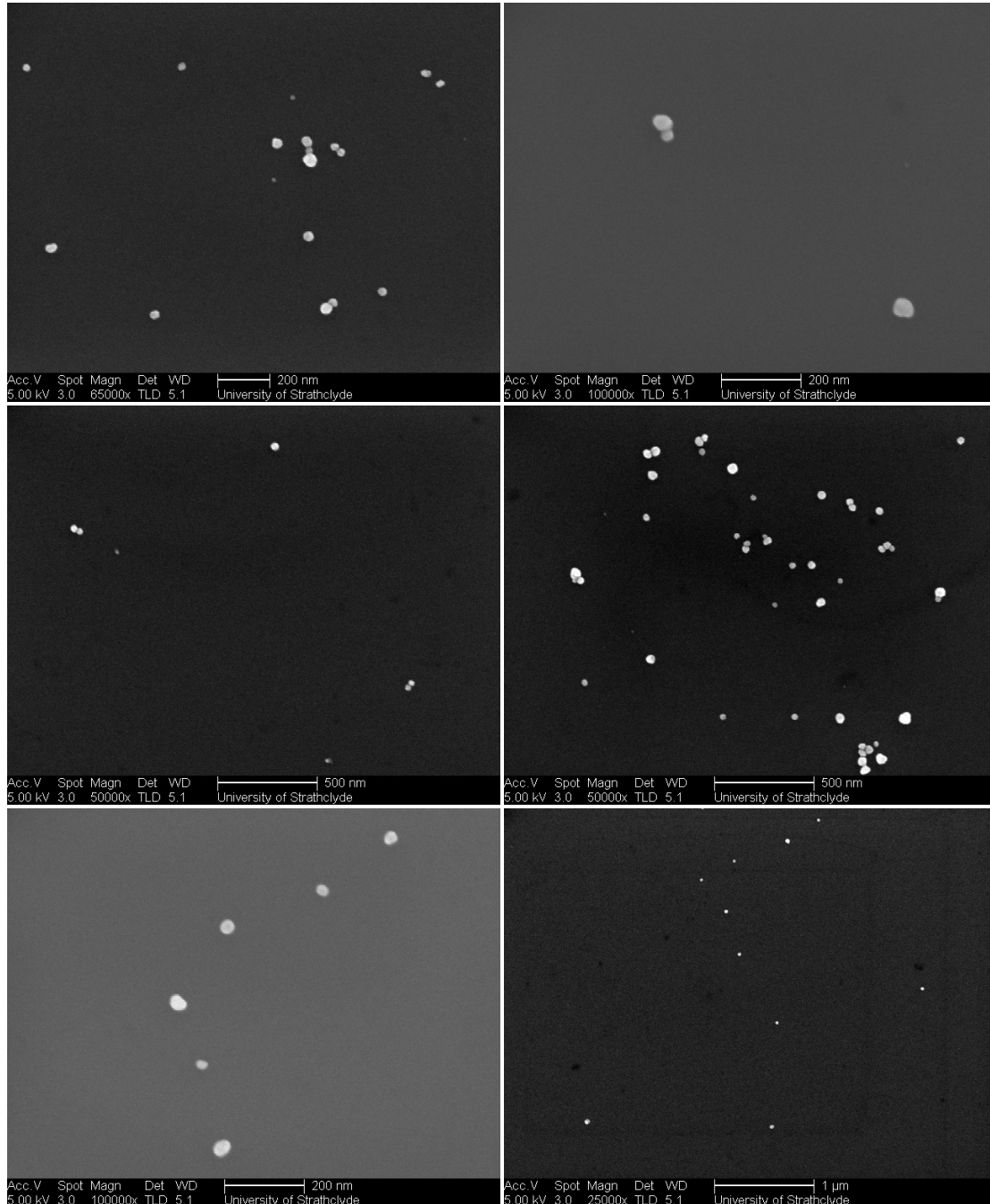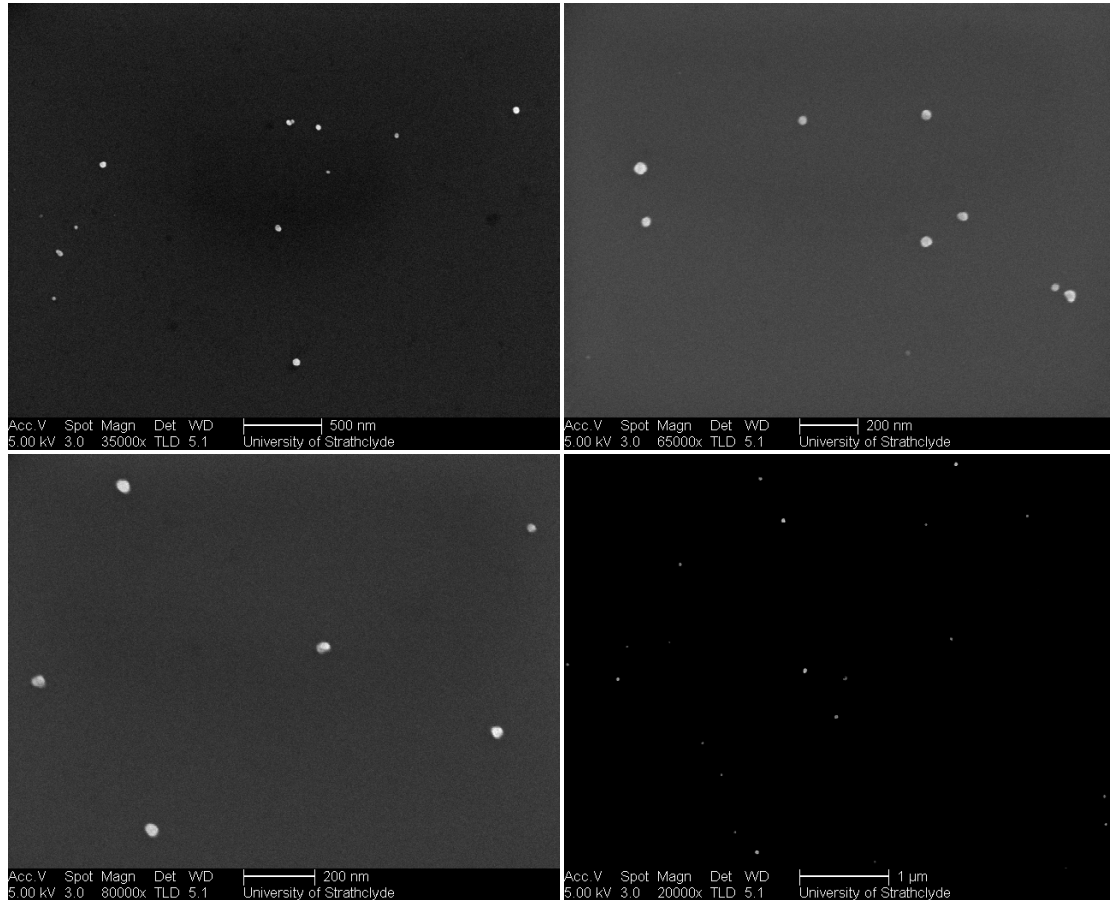
Appendix B – Scanning electron microscopy

(C) **15 pM PSN-12.1 following the addition of 15 nM MDM2 pre-incubated with an excess of P35. PSN distribution is similar to that observed in (A) indicating inhibition of MDM2 – induced PSN assembly by P35, resulting in a monodispersed solution**

Appendix B – Scanning electron microscopy

Continued … 15 pM PSN-12.1 following the addition of 15 nM MDM2 pre-incubated with an excess of P35. PSN distribution is similar to that observed in (A) indicating inhibition of MDM2 – induced PSN assembly by P35, resulting in a monodispersed solution
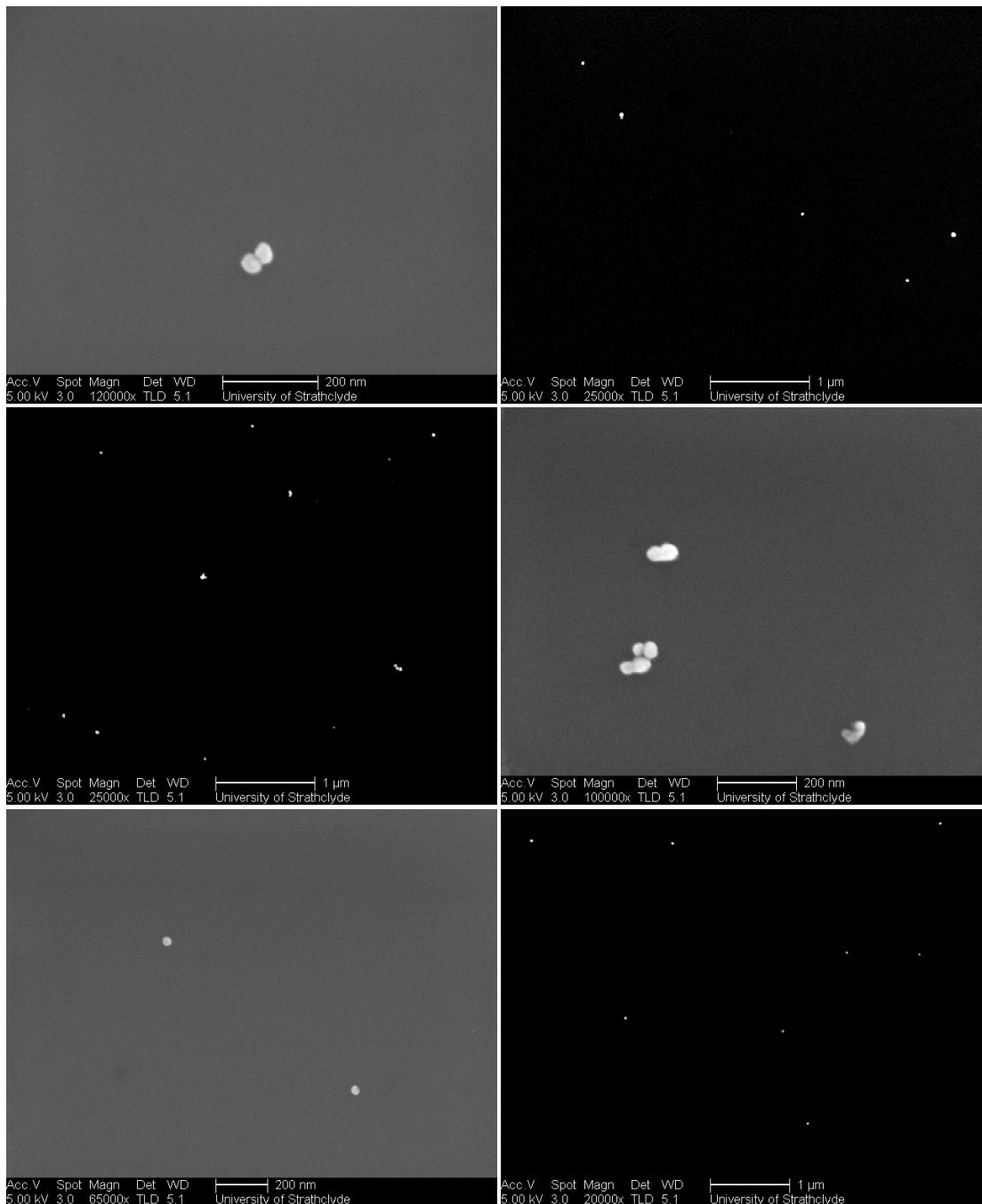
Appendix B – Scanning electron microscopy

(D) **15 pM PSN-12.1 following the addition of 15 nM MDM2 pre-incubated with an excess of P80. PSN distribution is similar to that observed in (A) indicating inhibition of MDM2 – induced PSN assembly by P80, resulting in a monodispersed solution**

Appendix B – Scanning electron microscopy

15 pM PSN-12.1 following the addition of 15 nM MDM2 pre-incubated with an excess of P80. PSN distribution is similar to that observed in (A) indicating inhibition of MDM2 – induced PSN assembly by P80, resulting in a monodispersed solution
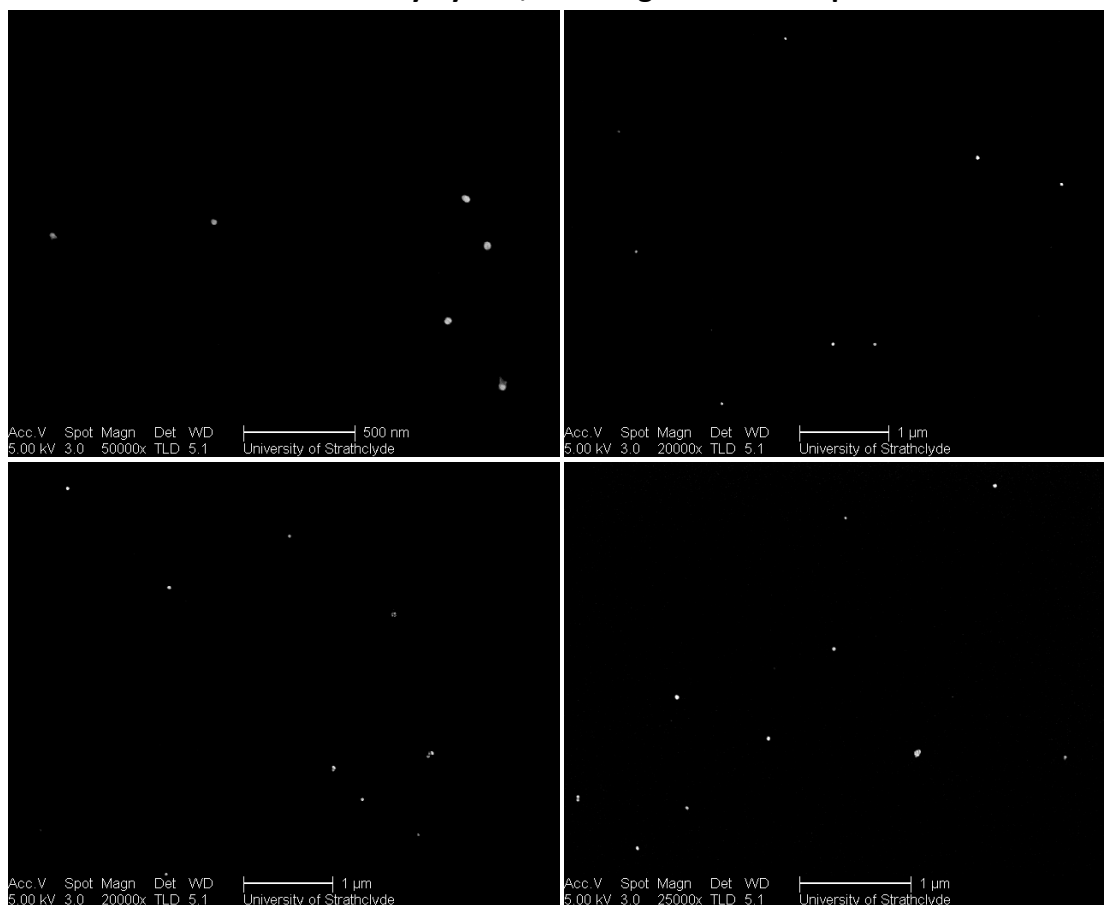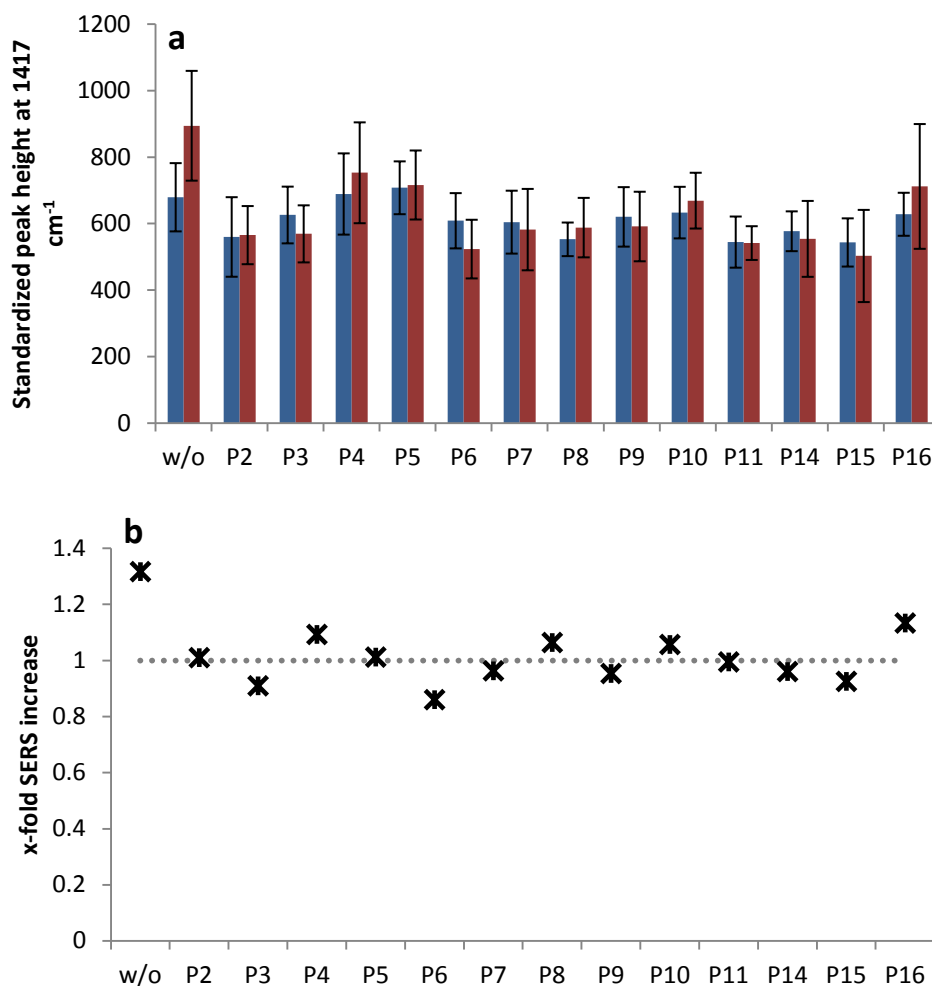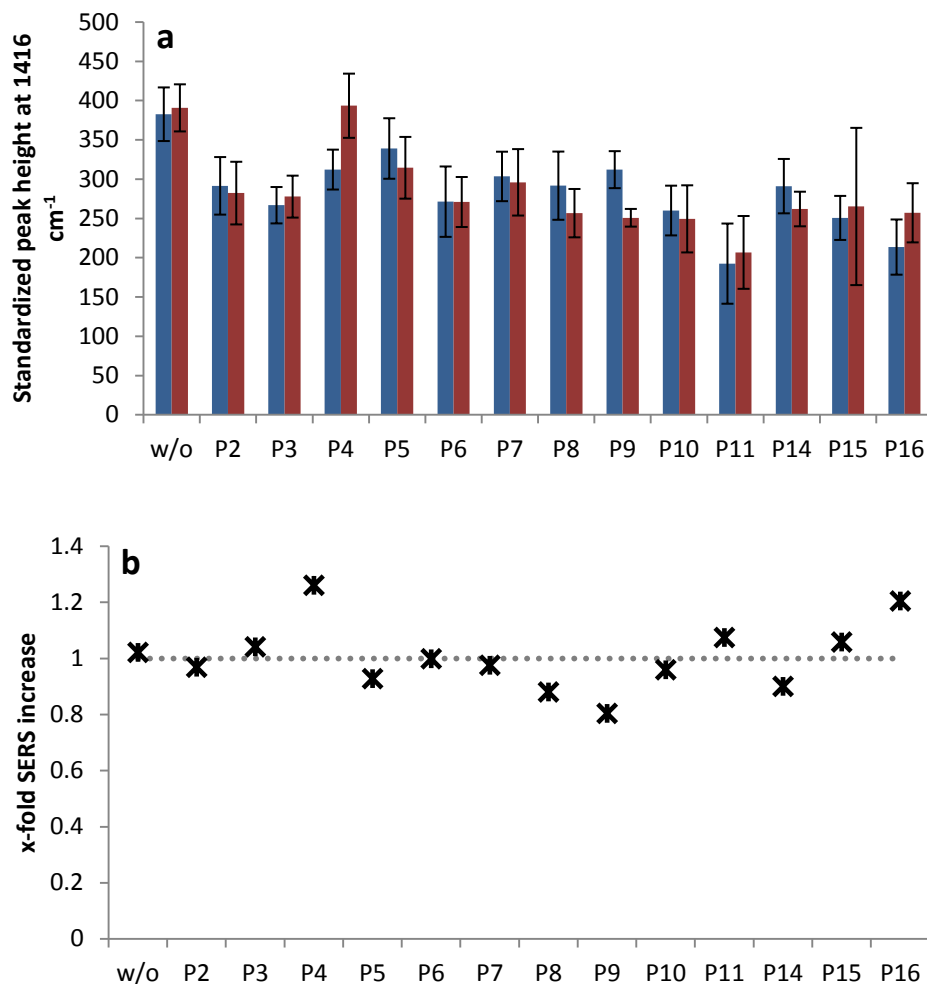
Appendix C – Pilot screen of natural products

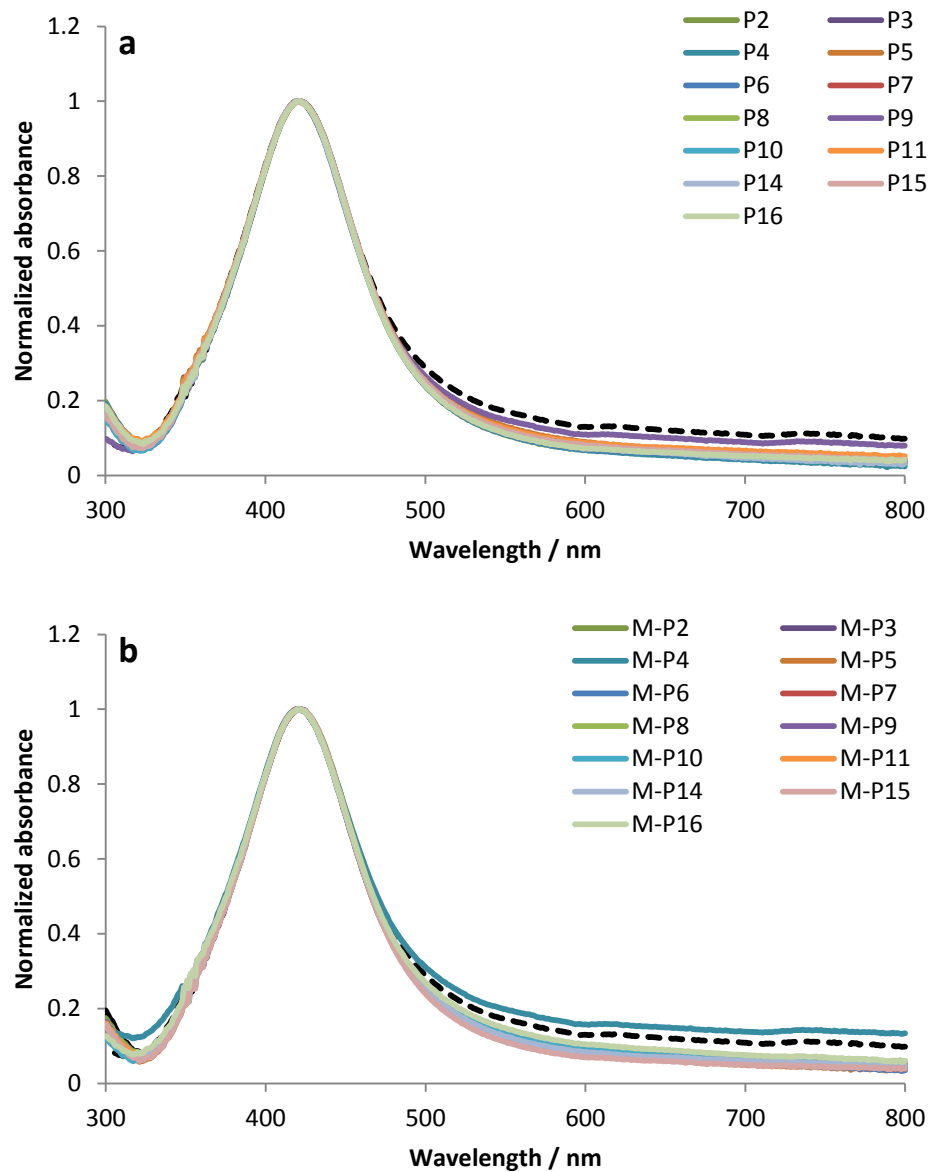## Plate 1 – Natural products P2-P16

Figure 1.1 – Day 1 SERS analysis. a) Peak height measurements at 1417 cm^{-1} recorded in SERS analysis of PSN-12.1 samples with natural products in the absence (blue) and presence (red) of MDM2. Five replicate scans with, one second time duration, acquired for each sample replicate using 100 % laser power and an excitation wavelength of 514.5 nm. Error bars indicate the standard deviation in peak heights standardized against cyclohexane. b) Calculated x-fold increase in SERS for PSN-12.1 with natural product and MDM2 compared to samples with natural product only. Grey dotted line represents the SERS response for PSN-12.1 without MDM2 or natural product. Red circles indicate natural products taken forward for further analysis.

Appendix C – Pilot screen of natural products

Figure 1.2 – Day 2 SERS analysis. a) Peak height measurements at 1416 cm^{-1} recorded in SERS analysis of PSN-12.1 samples with natural products in the absence (blue) and presence (red) of MDM2. Five replicate scans with, one second time duration, acquired for each sample using 100 % laser power and an excitation wavelength of 514.5 nm. Error bars indicate the standard deviation in peak heights standardized against cyclohexane. b) Calculated x-fold increase in SERS for PSN-12.1 with natural product and MDM2 compared to samples with natural product only. Grey dotted line represents the SERS response for PSN-12.1 without MDM2 or natural product. Red circles indicate natural products taken forward for further analysis.
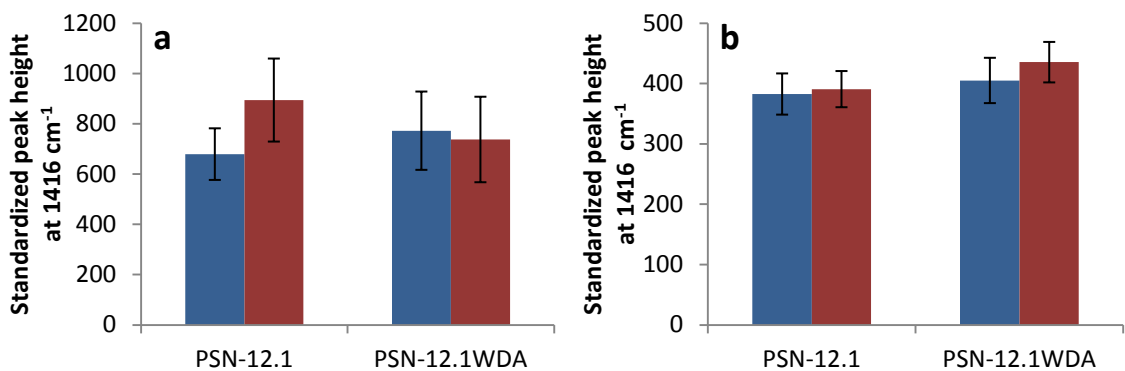
Appendix C – Pilot screen of natural products

Figure 3.1 – Normalized extinction spectra of PSN-12.1 with a) natural product and b) MDM2 and natural product. PSN-12.1 samples before (black solid line) and after (black dashed) addition of MDM2 are added for reference purposes.

Appendix C – Pilot screen of natural products

|	Day 1	Day 2
PSN-12.1	1.316481	1.021178
PSN-12.1$_{W\Delta A}$	0.954766	1.074797

Figure 1.4 – a) Peak height measurements at 1416 cm^{-1} recorded in SERS analysis of PSN-12.1 and PSN-12.1$_{W\Delta A}$ in the absence (blue) and presence (red) of MDM2 on a) day one and b) day two. Five replicate scans with, one second time duration, acquired for each sample using 100 % laser power and an excitation wavelength of 514.5 nm. Error bars indicate the standard deviation in peak heights standardized against cyclohexane. Table shows the calculated x-fold increase in SERS for PSN samples with MDM2 on both days.

P4 – Positive effect on PSN assembly. Enhanced PSN assembly evident in SERS and extinction spectroscopy on day two.

P9 – Negative effect on PSN assembly. Low SERS on day one and the lowest x-fold change in SERS on day two. No partial assembly evident in extinction spectroscopy.
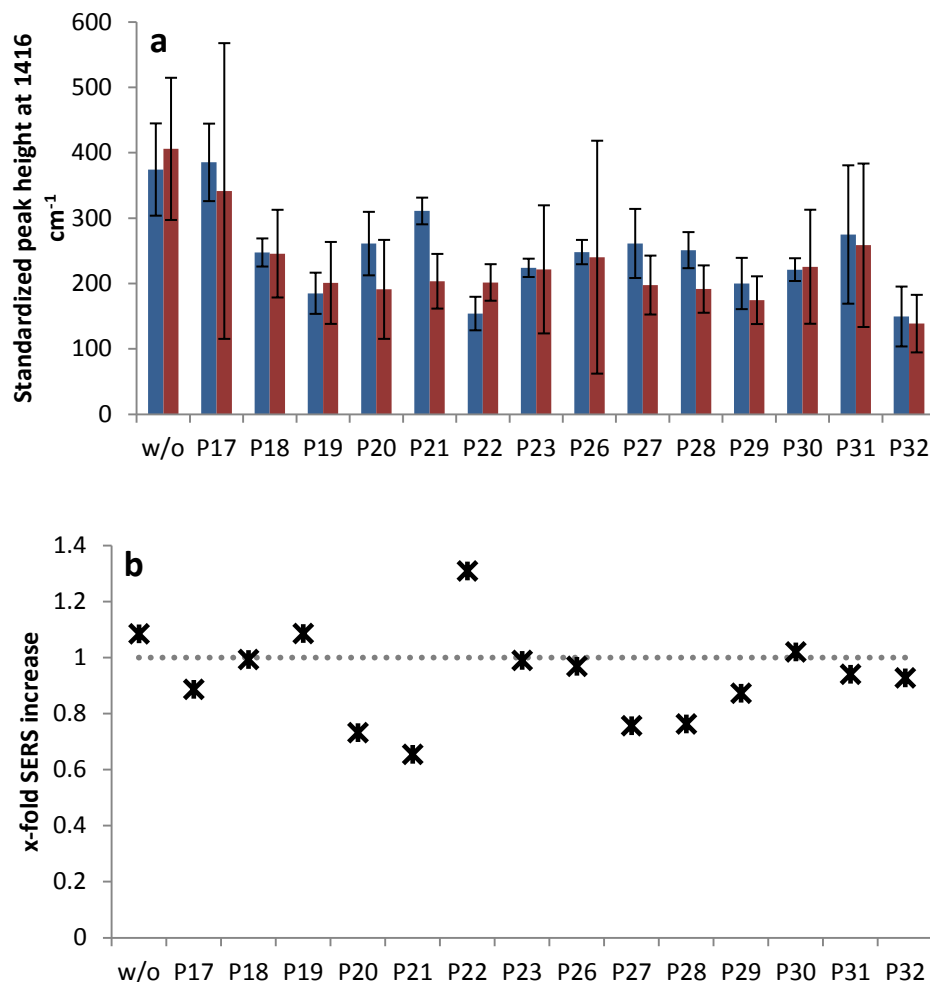
Appendix C – Pilot screen of natural products

Plate 2 – Natural products P17-P32
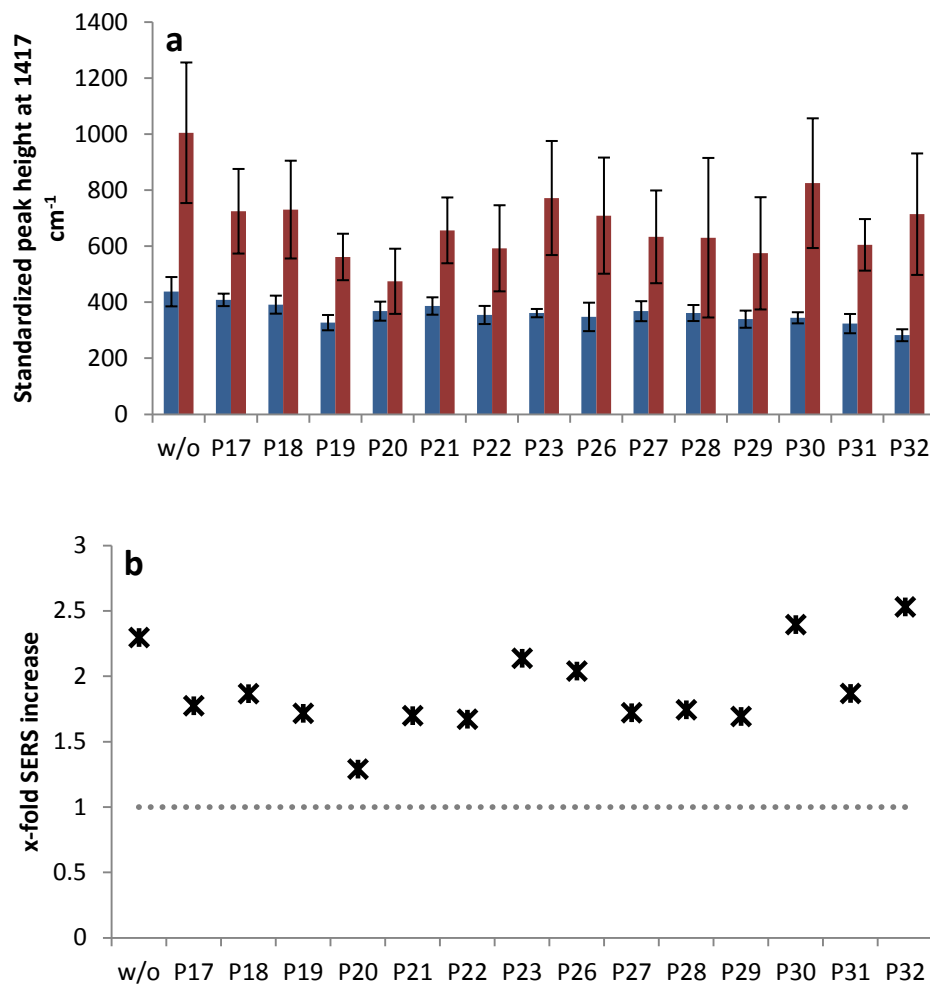
Figure 2.1 – Day 1 SERS analysis. a) Peak height measurements at 1417 cm^{-1} recorded in SERS analysis of PSN-12.1 samples with natural products in the absence (blue) and presence (red) of MDM2. Five replicate scans with, one second time duration, acquired for each sample replicate using 100 % laser power and an excitation wavelength of 514.5 nm. Error bars indicate the standard deviation in peak heights standardized against cyclohexane. b) Calculated x-fold increase in SERS for PSN-12.1 with natural product and MDM2 compared to samples with natural product only. Grey dotted line represents the SERS response for PSN-12.1 without MDM2 or natural product. Red circles indicate natural products taken forward for further analysis.

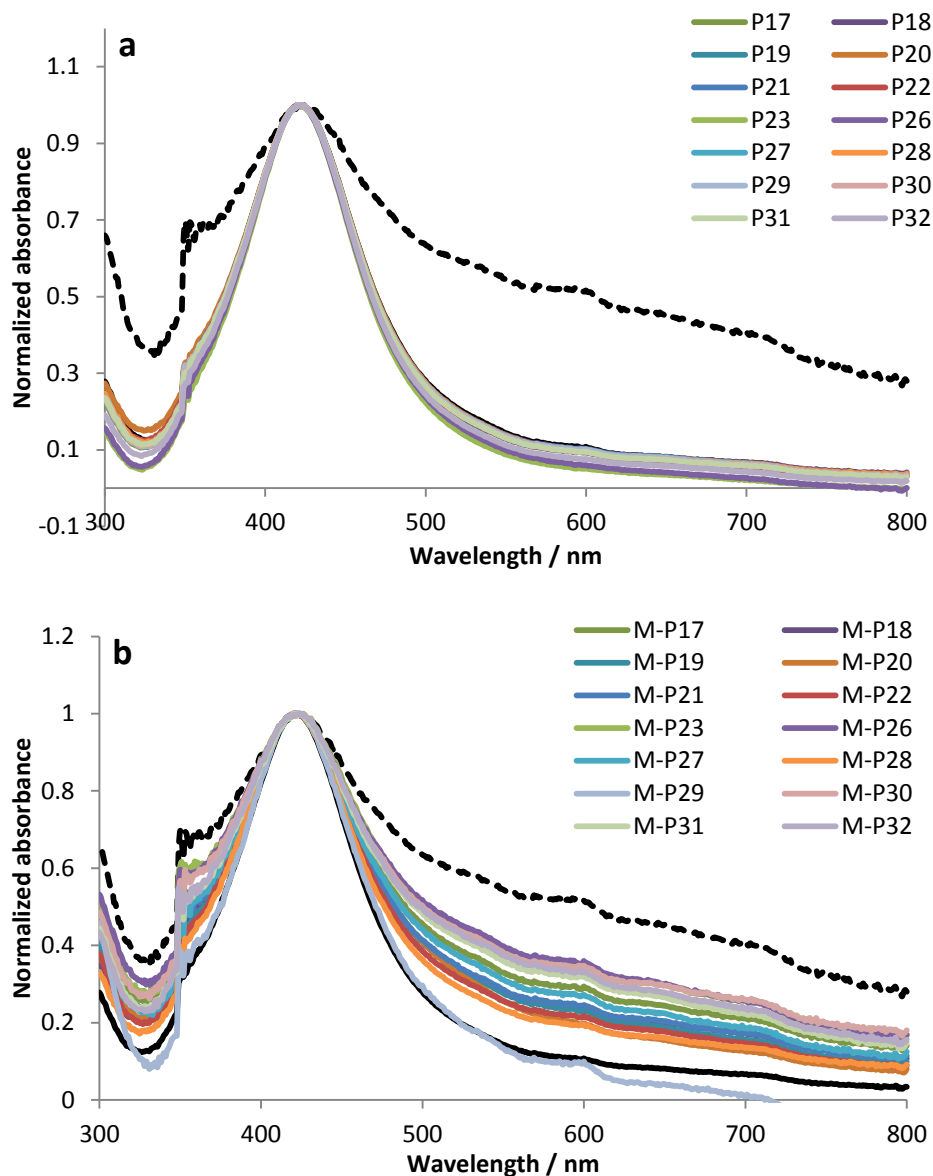# Appendix C – Pilot screen of natural products

Figure 2.2 – Day 2 SERS analysis. a) Peak height measurements at 1416 cm^{-1} recorded in SERS analysis of PSN-12.1 samples with natural products in the absence (blue) and presence (red) of MDM2. Five replicate scans with, one second time duration, acquired for each sample using 100 % laser power and an excitation wavelength of 514.5 nm. Error bars indicate the standard deviation in peak heights standardized against cyclohexane. b) Calculated x-fold increase in SERS for PSN-12.1 with natural product and MDM2 compared to samples with natural product only. Grey dotted line represents the SERS response for PSN-12.1 without MDM2 or natural product. Red circles indicate natural products taken forward for further analysis.

Appendix C – Pilot screen of natural products
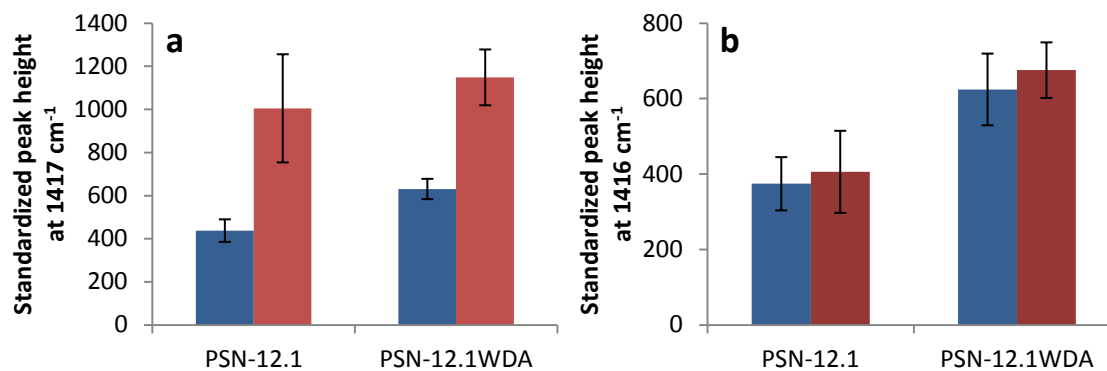

Figure 3.2 – Normalized extinction spectra of PSN-12.1 with a) natural product and b) MDM2 and natural product. PSN-12.1 samples before (black solid line) and after (black dashed) addition of MDM2 are added for reference purposes.

Appendix C – Pilot screen of natural products

	Day 1	Day 2
PSN-12.1	2.29615	1.08443
PSN-12.1$_{W\Delta A}$	1.820872	1.08192

Figure 2.4 – a) Peak height measurements at 1416 cm^{-1} recorded in SERS analysis of PSN-12.1 and PSN-12.1$_{W\Delta A}$ in the absence (blue) and presence (red) of MDM2 on a) day one and b) day two. Five replicate scans with, one second time duration, acquired for each sample using 100 % laser power and an excitation wavelength of 514.5 nm. Error bars indicate the standard deviation in peak heights standardized against cyclohexane. Table shows the calculated x-fold increase in SERS for PSN samples with MDM2 on both days.

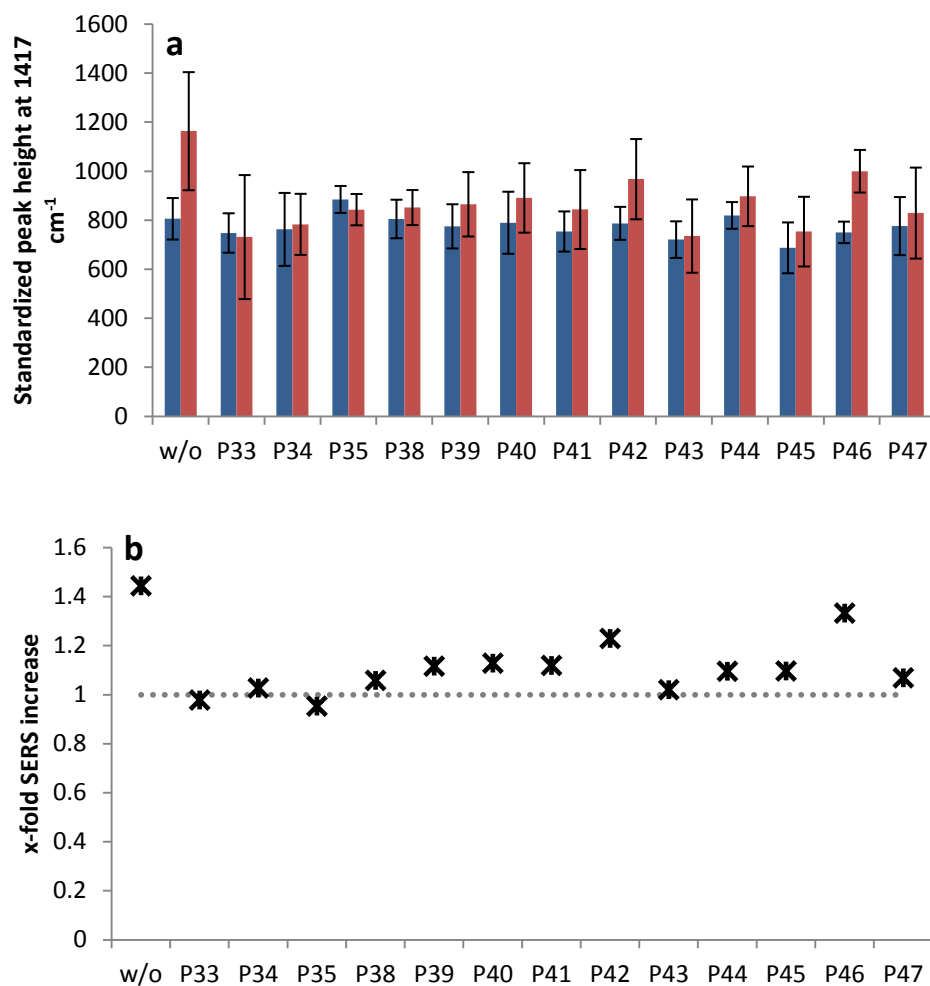**P20 –** Negative effect on PSN assembly. Lowest x-fold change on day 1 and minimal aggregation in extinction spectroscopy.

P29 – Negative effect on PSN assembly. Low SERS on both days and lowest aggregation evident in extinction spectroscopy.

Appendix C – Pilot screen of natural products

Plate 3 – Natural products P33-P47

Figure 3.1 – Day 1 SERS analysis. a) Peak height measurements at 1417 cm^{-1} recorded in SERS analysis of PSN-12.1 samples with natural products in the absence (blue) and presence (red) of MDM2. Five replicate scans with, one second time duration, acquired for each sample replicate using 100 % laser power and an excitation wavelength of 514.5 nm. Error bars indicate the standard deviation in peak heights standardized against cyclohexane. b) Calculated x-fold increase in SERS for PSN-12.1 with natural product and MDM2 compared to samples with natural product only. Grey dotted line represents the SERS response for PSN-12.1 without MDM2 or natural product. Red circles indicate natural products taken forward for further analysis.

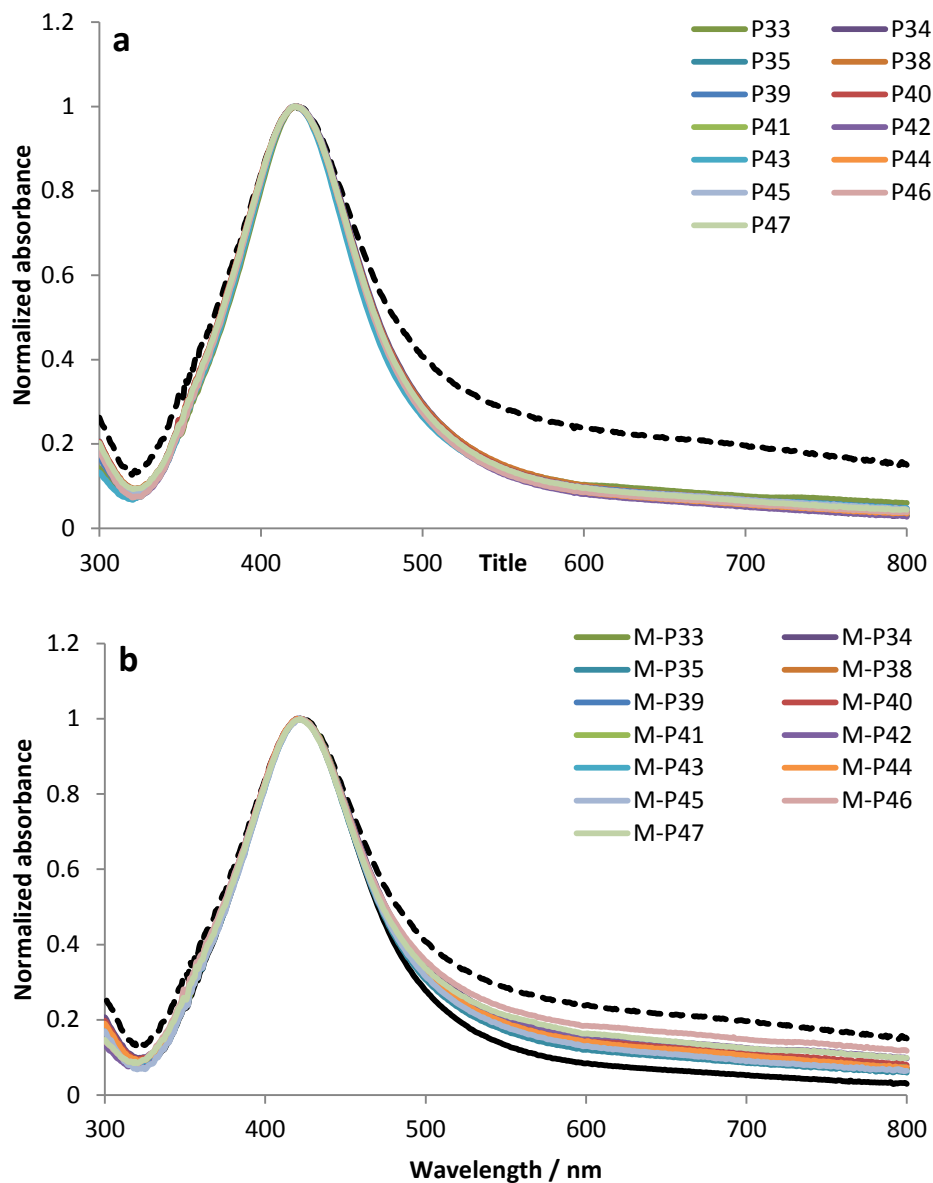# Appendix C – Pilot screen of natural products

Figure 3.2 – Day 2 SERS analysis. a) Peak height measurements at 1416 cm^{-1} recorded in SERS analysis of PSN-12.1 samples with natural products in the absence (blue) and presence (red) of MDM2. Five replicate scans with, one second time duration, acquired for each sample using 100 % laser power and an excitation wavelength of 514.5 nm. Error bars indicate the standard deviation in peak heights standardized against cyclohexane. b) Calculated x-fold increase in SERS for PSN-12.1 with natural product and MDM2 compared to samples with natural product only. Grey dotted line represents the SERS response for PSN-12.1 without MDM2 or natural product. Red circles indicate natural products taken forward for further analysis.

Appendix C – Pilot screen of natural products
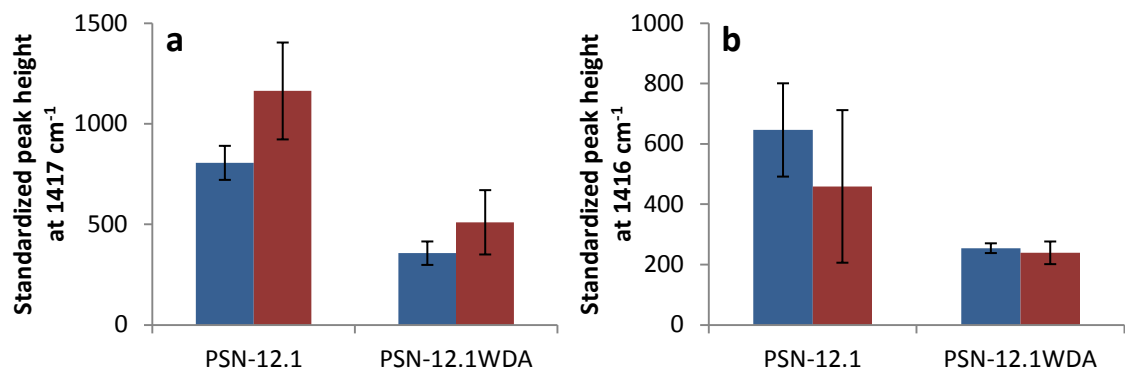

Figure 3.3 – Normalized extinction spectra of PSN-12.1 with a) natural product and b) MDM2 and natural product. PSN-12.1 samples before (black solid line) and after (black dashed) addition of MDM2 are added for reference purposes.

Appendix C – Pilot screen of natural products

	Day 1	Day 2
PSN-12.1	1.443546	0.710459
PSN-12.1$_{W\Delta A}$	1.4302	0.93974

Figure 3.4 – a) Peak height measurements at 1416 cm^{-1} recorded in SERS analysis of PSN-12.1 and PSN-12.1$_{W\Delta A}$ in the absence (blue) and presence (red) of MDM2 on a) day one and b) day two. Five replicate scans with, one second time duration, acquired for each sample using 100 % laser power and an excitation wavelength of 514.5 nm. Error bars indicate the standard deviation in peak heights standardized against cyclohexane. Table shows the calculated x-fold increase in SERS for PSN samples with MDM2 on both days.

P35 – Negative effect on PSN assembly. Lowest x-fold change in SERS on both days and lowest partial assembly evident in extinction spectroscopy.

Appendix C – Pilot screen of natural products

Plate 4 – Natural products P50-P64
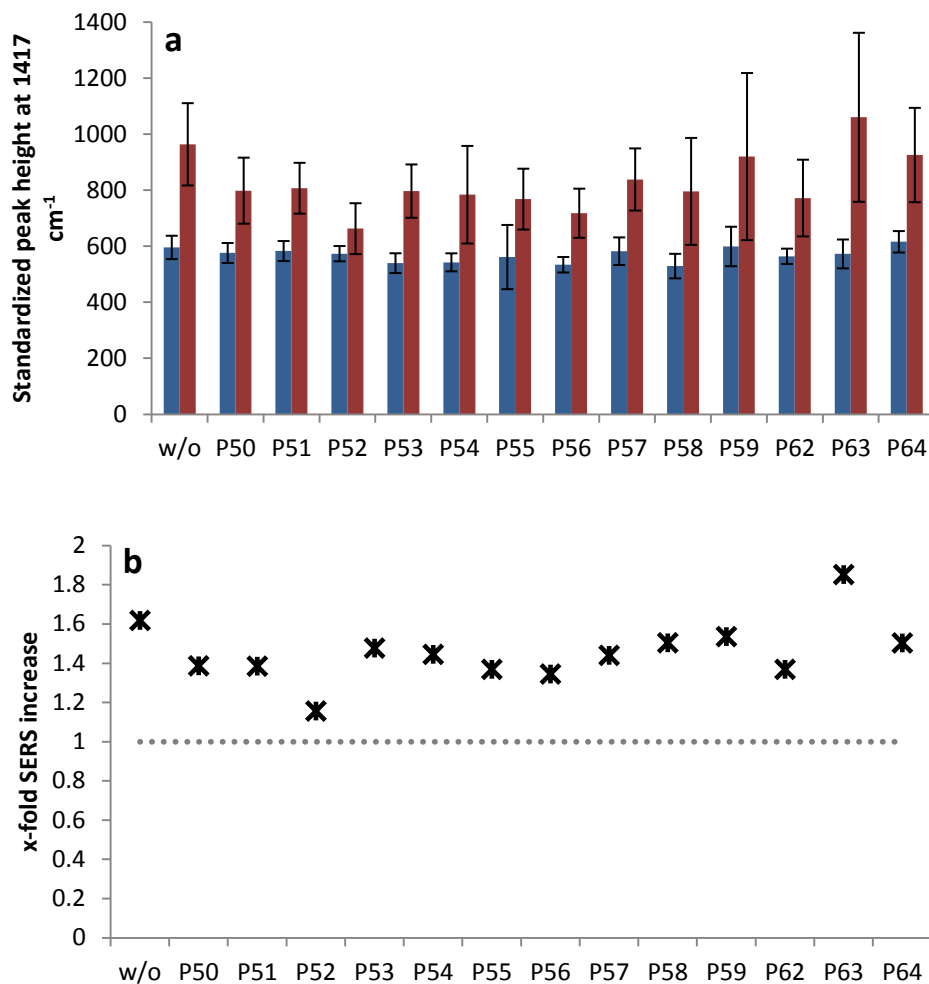
Figure 4.1 – Day 1 SERS analysis. a) Peak height measurements at 1417 cm^{-1} recorded in SERS analysis of PSN-12.1 samples with natural products in the absence (blue) and presence (red) of MDM2. Five replicate scans with, one second time duration, acquired for each sample replicate using 100 % laser power and an excitation wavelength of 514.5 nm. Error bars indicate the standard deviation in peak heights standardized against cyclohexane. b) Calculated x-fold increase in SERS for PSN-12.1 with natural product and MDM2 compared to samples with natural product only. Grey dotted line represents the SERS response for PSN-12.1 without MDM2 or natural product. Red circles indicate natural products taken forward for further analysis.

Appendix C – Pilot screen of natural products

Figure 4.2 – Day 2 SERS analysis. a) Peak height measurements at 1416 cm^{-1} recorded in SERS analysis of PSN-12.1 samples with natural products in the absence (blue) and presence (red) of MDM2. Five replicate scans with, one second time duration, acquired for each sample using 100 % laser power and an excitation wavelength of 514.5 nm. Error bars indicate the standard deviation in peak heights standardized against cyclohexane. b) Calculated x-fold increase in SERS for PSN-12.1 with natural product and MDM2 compared to samples with natural product only. Grey dotted line represents the SERS response for PSN-12.1 without MDM2 or natural product. Red circles indicate natural products taken forward for further analysis.

Appendix C – Pilot screen of natural products

Figure 4.3 – Normalized extinction spectra of PSN-12.1 with a) natural product and b) MDM2 and natural product. PSN-12.1 samples before (black solid line) and after (black dashed) addition of MDM2 are added for reference purposes.

Appendix C – Pilot screen of natural products

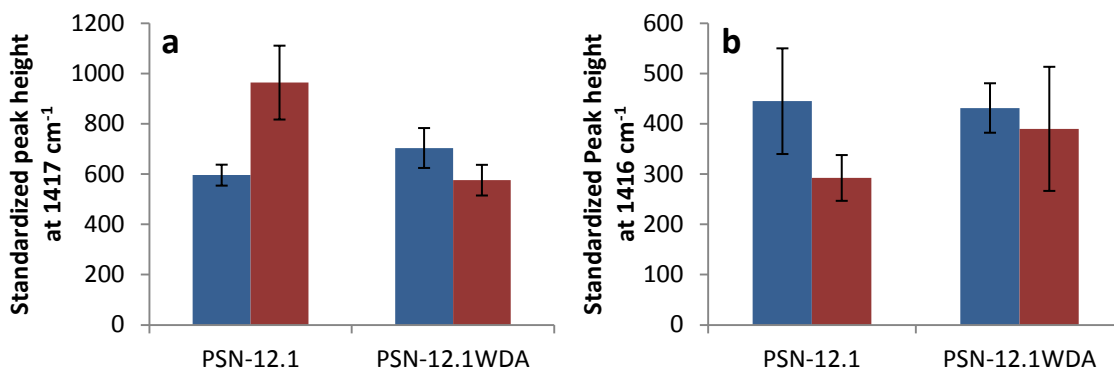|	Day 1	Day 2
PSN-12.1	1.617799	0.656984
PSN-12.1$_{W\Delta A}$	0.818238	0.903875

Figure 4.4 – a) Peak height measurements at 1416 cm^{-1} recorded in SERS analysis of PSN-12.1 and PSN-12.1$_{W\Delta A}$ in the absence (blue) and presence (red) of MDM2 on a) day one and b) day two. Five replicate scans with, one second time duration, acquired for each sample using 100 % laser power and an excitation wavelength of 514.5 nm. Error bars indicate the standard deviation in peak heights standardized against cyclohexane. Table shows the calculated x-fold increase in SERS for PSN samples with MDM2 on both days.

P52 – Negative effect on PSN assembly. Lowest SERS on day one, one of the lowest on day two and least aggregation evident in extinction spectroscopy.

P63 – Positive effect on PSN assembly. Highest SERS on day one and most aggregation evident in extinction spectroscopy.

Appendix C – Pilot screen of natural products

Plate 5 – Natural products P65-P80
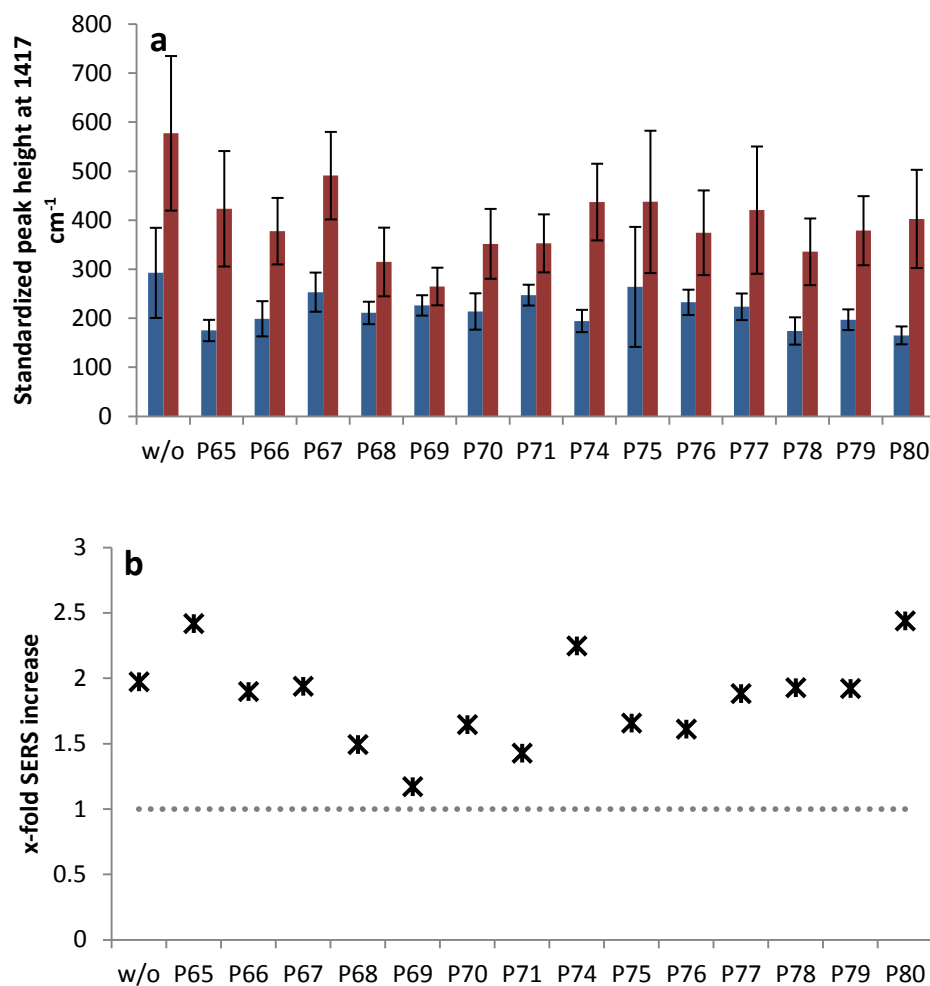
Figure 5.1 – Day 1 SERS analysis. a) Peak height measurements at 1417 cm^{-1} recorded in SERS analysis of PSN-12.1 samples with natural products in the absence (blue) and presence (red) of MDM2. Five replicate scans with, one second time duration, acquired for each sample replicate using 100 % laser power and an excitation wavelength of 514.5 nm. Error bars indicate the standard deviation in peak heights standardized against cyclohexane. b) Calculated x-fold increase in SERS for PSN-12.1 with natural product and MDM2 compared to samples with natural product only. Grey dotted line represents the SERS response for PSN-12.1 without MDM2 or natural product. Red circles indicate natural products taken forward for further analysis.

Appendix C – Pilot screen of natural products

Figure 5.2 – Day 2 SERS analysis. a) Peak height measurements at 1416 cm^{-1} recorded in SERS analysis of PSN-12.1 samples with natural products in the absence (blue) and presence (red) of MDM2. Five replicate scans with, one second time duration, acquired for each sample using 100 % laser power and an excitation wavelength of 514.5 nm. Error bars indicate the standard deviation in peak heights standardized against cyclohexane. b) Calculated x-fold increase in SERS for PSN-12.1 with natural product and MDM2 compared to samples with natural product only. Grey dotted line represents the SERS response for PSN-12.1 without MDM2 or natural product. Red circles indicate natural products taken forward for further analysis.

Appendix C – Pilot screen of natural products

Figure 5.3 – Normalized extinction spectra of PSN-12.1 with a) natural product and b) MDM2 and natural product. PSN-12.1 samples before (black solid line) and after (black dashed) addition of MDM2 are added for reference purposes.

Appendix C – Pilot screen of natural products
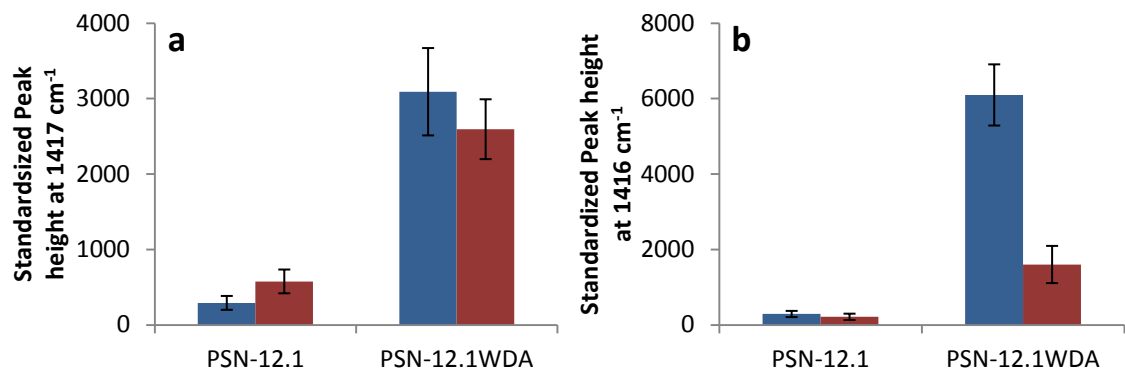
	Day 1	Day 2
PSN-12.1	1.972889	0.739842
PSN-12.1$_{W\Delta A}$	0.839323	0.262835

Figure 5.4 – a) Peak height measurements at 1416 cm^{-1} recorded in SERS analysis of PSN-12.1 and PSN-12.1$_{W\Delta A}$ in the absence (blue) and presence (red) of MDM2 on a) day one and b) day two. Five replicate scans with, one second time duration, acquired for each sample using 100 % laser power and an excitation wavelength of 514.5 nm. Error bars indicate the standard deviation in peak heights standardized against cyclohexane. Table shows the calculated x-fold increase in SERS for PSN samples with MDM2 on both days.

P65 – Positive effect on PSN assembly. High SERS on day one and aggregation higher than standard evident in extinction spectroscopy.

P69 – Questionable effect on PSN assembly. Lowest SERS on day one, highest SERS on day two. Aggregation akin to standards evident in extinction spectroscopy.

P74 – Positive effect on PSN assembly. High SERS on both days compared with other products. Most aggregation evident in extinction spectroscopy.

P80 – Questionable effect on PSN assembly. High SERS on day one but similar to other samples on day two. Low aggregation evident in extinction spectroscopy.

Appendix C – Pilot screen of natural products
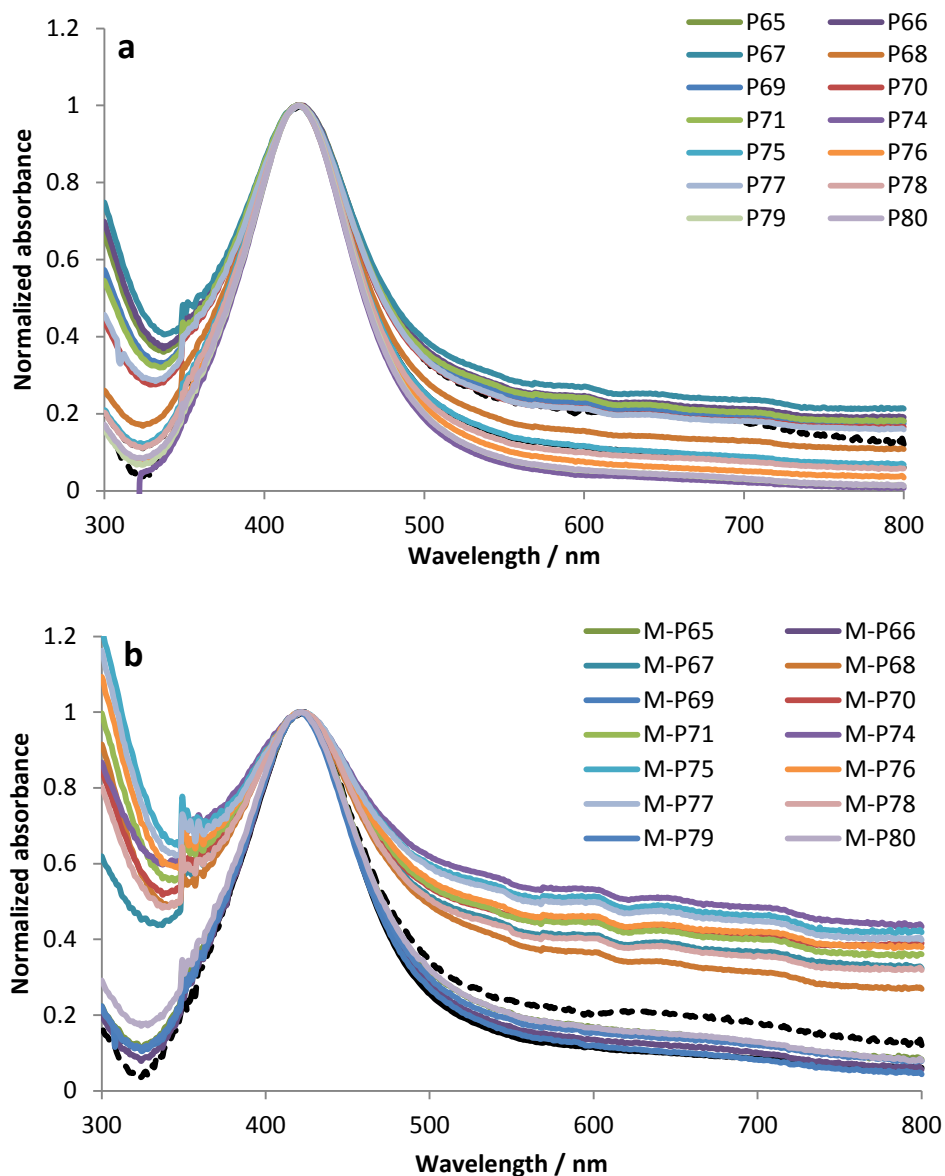
Plate 6 – Natural products P81-P95
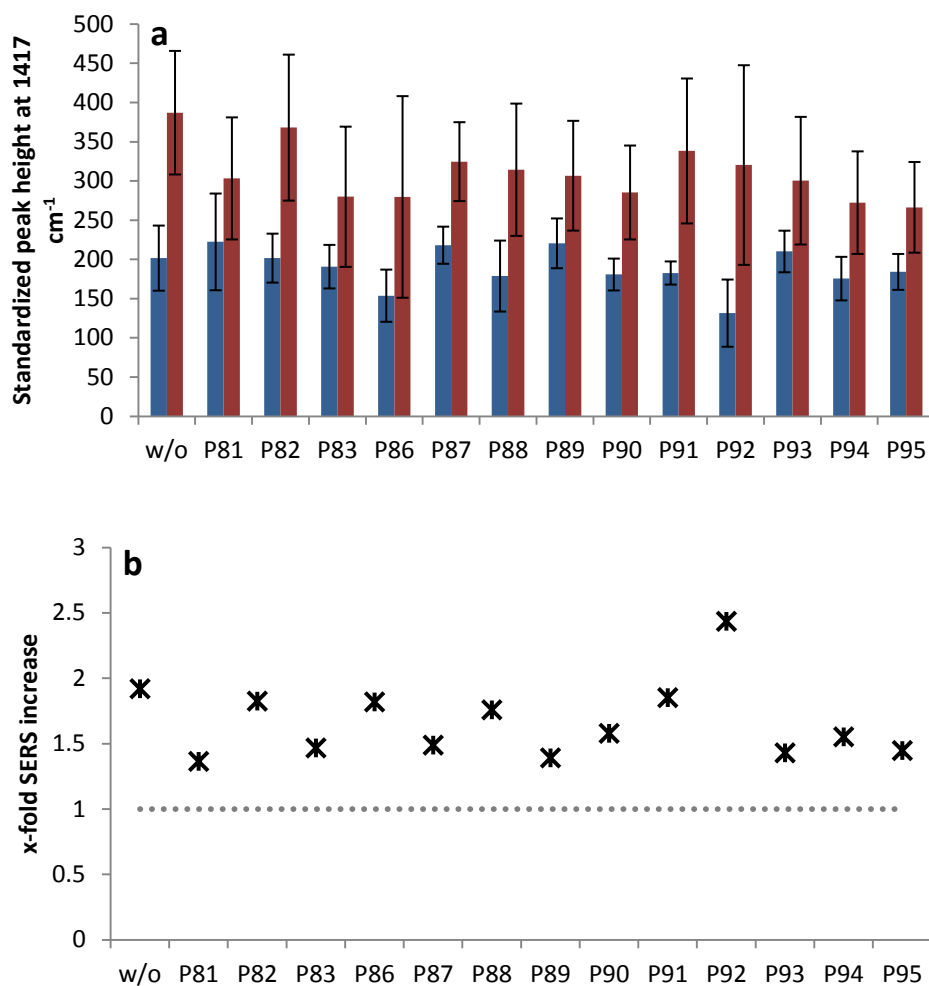
Figure 6.1 – Day 1 SERS analysis. a) Peak height measurements at 1417 cm⁻¹ recorded in SERS analysis of PSN-12.1 samples with natural products in the absence (blue) and presence (red) of MDM2. Five replicate scans with, one second time duration, acquired for each sample replicate using 100 % laser power and an excitation wavelength of 514.5 nm. Error bars indicate the standard deviation in peak heights standardized against cyclohexane. b) Calculated x-fold increase in SERS for PSN-12.1 with natural product and MDM2 compared to samples with natural product only. Grey dotted line represents the SERS response for PSN-12.1 without MDM2 or natural product. Red circles indicate natural products taken forward for further analysis.

Appendix C – Pilot screen of natural products

Figure 6.2 – Day 2 SERS analysis. a) Peak height measurements at 1416 cm⁻¹ recorded in SERS analysis of PSN-12.1 samples with natural products in the absence (blue) and presence (red) of MDM2. Five replicate scans with, one second time duration, acquired for each sample using 100 % laser power and an excitation wavelength of 514.5 nm. Error bars indicate the standard deviation in peak heights standardized against cyclohexane. b) Calculated x-fold increase in SERS for PSN-12.1 with natural product and MDM2 compared to samples with natural product only. Grey dotted line represents the SERS response for PSN-12.1 without MDM2 or natural product. Red circles indicate natural products taken forward for further analysis.

Appendix C – Pilot screen of natural products

Figure 6.3 – Normalized extinction spectra of PSN-12.1 with a) natural product and b) MDM2 and natural product. PSN-12.1 samples before (black solid line) and after (black dashed) addition of MDM2 are added for reference purposes.

Appendix C – Pilot screen of natural products
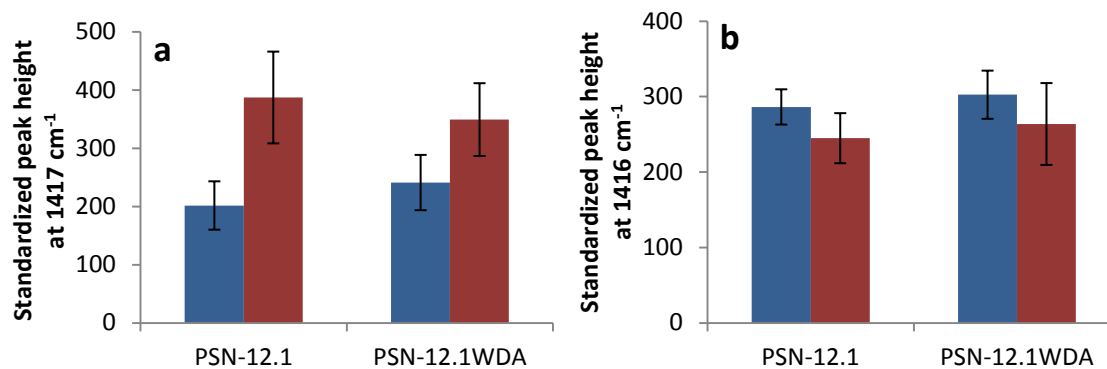
	Day 1	Day 2
PSN-12.1	1.919489	0.855346
PSN-12.1$_{W\Delta A}$	1.448342	0.871631

Figure 6.4 – a) Peak height measurements at 1416 cm^{-1} recorded in SERS analysis of PSN-12.1 and PSN-12.1$_{W\Delta A}$ in the absence (blue) and presence (red) of MDM2 on a) day one and b) day two. Five replicate scans with, one second time duration, acquired for each sample using 100 % laser power and an excitation wavelength of 514.5 nm. Error bars indicate the standard deviation in peak heights standardized against cyclohexane. Table shows the calculated x-fold increase in SERS for PSN samples with MDM2 on both days.

P81 – Negative effect on PSN assembly. Low SERS on day one and lowest aggregation evident in extinction spectroscopy.

P86 – Positive effect on PSN assembly. High SERS on day one, highest SERS on day two and most aggregation evident in extinction spectroscopy.

P92 – Negative effect on PSN assembly. Low SERS on both days and low aggregation evident in extinction spectroscopy.

Nanosensing protein allostery using a bivalent mouse double minute two (MDM2) assay

Anna F. Robson[a], Ted R. Hupp[b,1], Fiona Lickiss[b], Kathryn L. Ball[b], Karen Faulds[a], and Duncan Graham[a,1]

[a]Centre for Molecular Nanometrology, WestCHEM, Department of Pure and Applied Chemistry, University of Strathclyde, Glasgow G1 1XL, United Kingdom; and [b]Edinburgh Cancer Research Centre, Cell Signaling Unit, Institute of Genetics and Molecular Medicine, University of Edinburgh, Edinburgh EH4 2XU, United Kingdom

The tumor suppressor protein, p53, is either mutated or absent in >50% of cancers and is negatively regulated by the mouse double minute (MDM2) protein. Understanding and inhibition of the MDM2-p53 interaction are, therefore, critical for developing novel chemotherapeutics, which are currently limited because of a lack of appropriate study tools. We present a nanosensing approach to investigate full-length MDM2 interactions with p53, thus providing an allosteric assay for identifying binding ligands. Surface-enhanced Raman scattering (SERS)-active nanoparticles, functionalized with a p53 peptide mimic (peptide 12.1), display biologically specific aggregation following addition of MDM2. Nanoparticle assembly is competitively inhibited by the N-terminal MDM2-binding ligands peptide 12.1 and Nutlin-3. This study reports nanoparticle assembly through specific protein–peptide interactions that can be followed by SERS. We demonstrate solution-based MDM2 allosteric interaction studies that use the full-length protein.

assay system | biosensing | nano-assembly | protein interaction studies | Raman spectroscopy

The p53 tumor suppressor protein is often referred to as the "guardian of the genome" owing to its key role in cell-cycle regulation and its activity in a number of different cancer pathways (1–3). The antiproliferative action of p53 arises from the induction of cell-cycle arrest and apoptosis in cells subjected to DNA damage in response to stress. As such, p53 is central to protecting cells from uncontrolled growth and malignant transformation with inactivation or mutation of p53 found in over 50% of human cancers (1–3). Under nonstressed conditions, mouse double minute (MDM)2 negatively regulates p53, primarily through the ubiquitin degradation pathway but also via transrepression (4, 5). Studies have shown up-regulation of MDM2 in malignancies where p53 is fully functional, making the MDM2-p53 feedback loop of great interest in chemotherapeutic studies (6, 7).

MDM2 is a multidomain protein that exerts E3-ligase activity on a number of proteins, including p53 (5, 8, 9). The ubiquitination activity of MDM2 is a multisubunit process whereby the N-terminal hydrophobic pocket and central acidic domain of MDM2 are used in p53 binding, to the N-terminal and central domains of p53, respectively (10). The complexity of this multisubunit interaction makes it relatively difficult to investigate the allosteric nature of MDM2. This is made more difficult by the problems in acquiring a structure of full-length MDM2 because of intrinsically disordered regions on the protein that reduce likelihood of crystallization. Focus solely on the N-terminal domain of MDM2 has identified Nutlin-3-type molecules that activate p53 in cells; however, these also act as allosteric agonists that stimulate rather than inhibit p53 ubiquitination (10–15). The putative dimerization of MDM2 through the C-terminal really interesting new gene (RING) domain is reported to be critical for E3-ligase activity; however, molecular reasoning for this is not fully understood (8, 16–18). To date, studies on MDM2 structure have been conducted with purified domain constructs, which is not representative of full-length protein activity in nature.

Using full-length MDM2, which has the capacity to exhibit allosteric interactions (19, 20), would provide an assay for the screening of MDM2 ligands. Domain construct studies have investigated the multiple binding interactions of MDM2, but few, thus far, have used unlabeled full-length protein to simultaneously interrogate two binding events. The assay described in this report monitors both N-terminal and C-terminal activities of MDM2 simultaneously using full-length protein, which is critical to understanding the biological action of the native protein. The methodology provides a step forward in the capability for investigating such intricate interactions, and a unique insight is provided into the allosteric nature of native MDM2 that cannot be observed using other techniques.

Current methodologies used to probe interactions in biological systems commonly use readout tools such as fluorescence (21–23). This technique is subject to a high background from biological media and is limited by broad emission bands and the inability to probe interactions over distances of more than 10 nm. Surface-enhanced Raman scattering (SERS) is a vibrational spectroscopy that can provide similar sensitivity to fluorescence, but narrower spectral peaks allow for simultaneous detection of multiple species (24, 25). SERS interrogates an analyte, adsorbed onto a roughened metal surface, from which further Raman signal enhancement is achieved by coinciding the laser excitation wavelength with the analyte absorbance maxima (26, 27). SERS can also be enhanced or "turned on" by aggregation of nanoparticles (NPs) in solution because of "hot spots" of higher electromagnetic fields at NP junctions (26–28). Cotton et al. pioneered the use of NP and SERS for proteomic investigations and developed the first SERS-based enzyme immunoassay in 1989 (29). Subsequently, a number of SERS-based immunoassays have been documented (30–39). Assembly of functionalized NPs via protein–ligand interactions has been previously demonstrated using techniques such as extinction spectroscopy, transmission electron microscopy, and gel electrophoresis, all of which lack the sensitivity of SERS (40–44). Such interactions have been detected via SERS on metal surfaces, where binding events are compromised by protein orientation and conformation at the surface. Solution-based studies allow structural integrity of the full-length protein to be maintained, thus providing accurate information about complex interactions: however, such investigations have yet to be reported (36).

In this report, we outline a method for NP assembly through the interaction of full-length MDM2 with an N-terminal-domain peptide ligand. By exploiting the sensitivity and selectivity of SERS, we provide insight into the allosteric nature of MDM2 in

solution, which is not achievable by current methodologies, which only monitor one binding interaction, involve protein labeling, or require surface immobilization.

Results

Protein–Peptide Nanoparticle Assembly. We propose a solution-based approach to investigate the interaction of full-length MDM2 with a p53 peptide mimic exploiting the sensitivity and selectivity of SERS. p53 is known to bind the N-terminal hydrophobic pocket of MDM2 by forming an ampipathic helix containing the peptide motif, FxxxWxxL (45). Peptide 12.1 (MPRFMDYWEGLN) originates from a library of p53 peptide mimics and demonstrates high-affinity binding to the MDM2 hydrophobic cleft (46). Tryptophan, a key residue involved in aromatic-aromatic interactions with MDM2 (47, 48), was replaced with alanine to create the

mutant peptide $12.1_{W\Delta A}$, which provided a negative control to ensure biological specificity of the interaction. In theory, putative dimerization of full-length MDM2 (through its RING domain) would present two N-terminal hydrophobic pockets free (per dimer) to interact with ligands such as peptide 12.1. N-terminal interactions with peptide ligand, therefore, allow the MDM2 dimer to bring together two peptide 12.1 functionalized silver NP, peptide silver nanoparticle (PSN)-12.1, in solution (Fig. 1A, i). An alternative model for PSN-12.1 assembly, via a secondary peptide 12.1-binding site, is also illustrated (Fig. 1A, ii). The latter is unlikely because there is no evidence for two different peptide 12.1-binding sites on MDM2, and cell based studies suggest MDM2 is oligomeric in solution (16). MDM2-induced aggregation can be monitored over time by extinction spectroscopy and premodifying peptide 12.1 with a benzotriazole Raman tag, BT, enables the
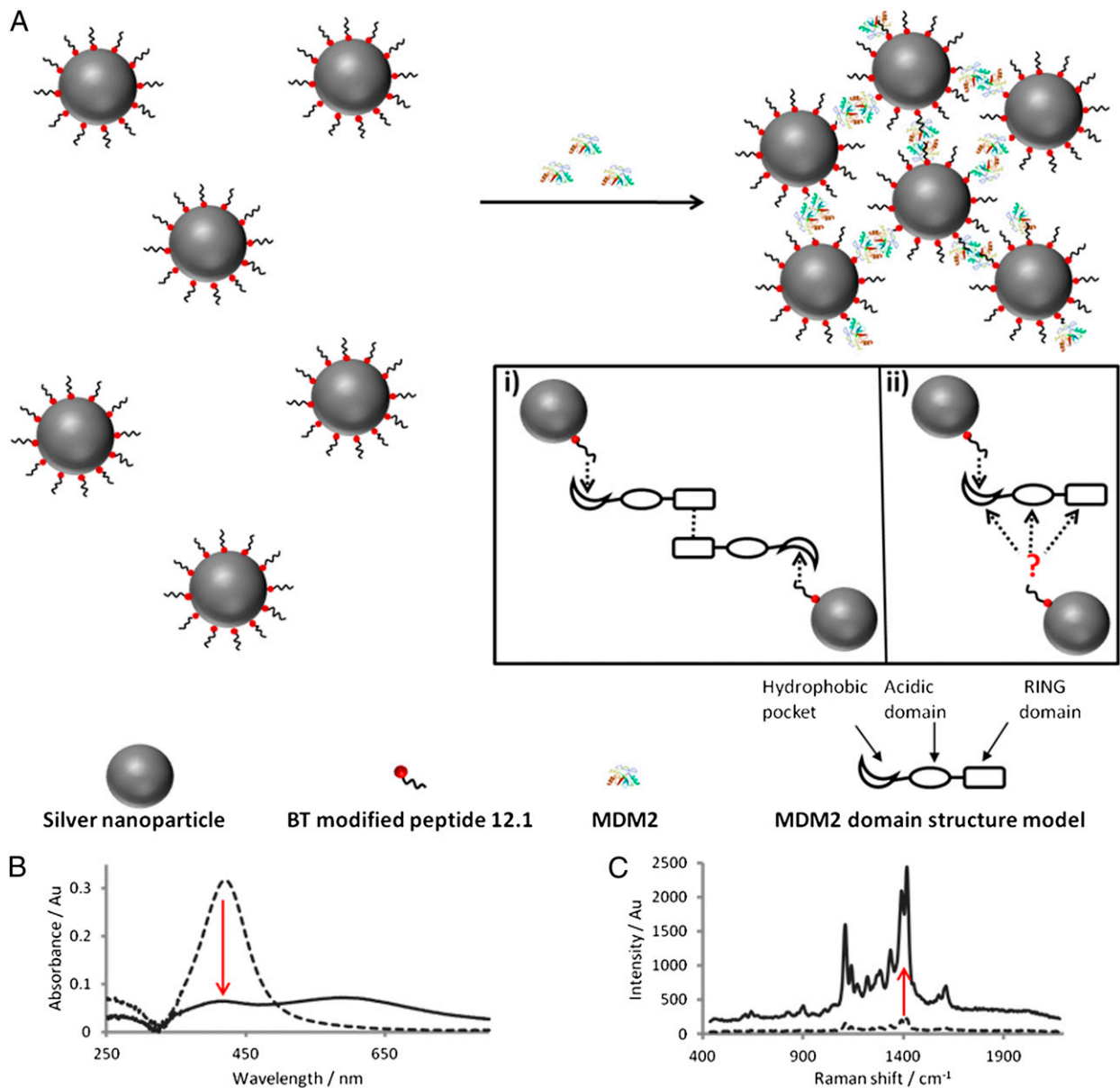
Fig. 1. (A) Schematic of the proposed assembly of PSN through specific interactions between MDM2 and peptide 12.1 (not to scale). *Inset* shows two proposed models for MDM2 bivalency resulting in PSN aggregation from a MDM2 dimerization (e.g., "oligomeric") conformation (*i*) and monomeric MDM2 (*ii*) have two distinct binding sites with the known and an alternative peptide 12.1 binding site (not to scale). (B and C) Extinction spectroscopy (B) and SERS analysis (C) before (dashed) and after (solid line) addition of MDM2 to PSN-12.1.

process to be explored using SERS. Both extinction and SERS intensity can be monitored over time to investigate the biological interactions driving this NP-assembly process.

Peptide Silver Nanoparticles. Reproducibility of spectra from Raman reporters used in SERS-based immunoassays is extremely important to obtain reliable results. Benzotriazole dyes adsorb onto silver nanoparticle surfaces in the same orientation irrespective of concentration, resulting in reproducible Raman spectral intensities (49). This is attributable to steric hindrance presented by covalent interactions between N_1 and N_3 lone electron pairs with the silver surface (50, 51). BT has an absorbance λ_{max} of 487 nm and, as such, is close in resonance when using an excitation wavelength of 514 nm. The most prominent peak in the BT Raman spectrum occurs at a shift of 1,416 cm^{-1} (Fig. 1*C*) and can be attributed to the azo stretch in the dye structure (Fig. S1).

Peptide 12.1 and mutant peptide 12.1$_{W\Delta A}$ were modified with BT and directly conjugated to EDTA-reduced silver NP (AgEDTA) in a one-step reaction. BT consists of a triazole moiety with an affinity for silver surfaces, a Raman active chromophore, and a stabilizing polyethylene glycol spacer (Fig. S1). Circular dichroism (CD) analysis of peptide 12.1 and BT-modified peptide 12.1 showed the modification to have no inhibitory effect on the peptide adopting a helical conformation (Fig. S2). BT-modified peptide 12.1 and mutant peptide 12.1$_{W\Delta A}$ displayed high- and low-level binding, respectively, to MDM2 in ELISA competition assays (Fig. S3). Successful PSN formation was shown by an increase in particle size through extinction spectroscopy, and matrix-associated laser desorption ionization–mass spectroscopy (MALDI-MS) analysis was used to identify BT-peptide molecules anchored on the nanoparticle surface (Figs. S4 and S5).

MDM2-Induced PSN Aggregation. Unlabeled full-length MDM2 was added to PSN solutions at various concentrations based on a molar excess of protein to PSN. This is in line with previously published data using streptavidin for controlled assembly of biotin-functionalized gold NP (40). Aggregation of 15 pM PSN-12.1 in solution was observed following the addition of MDM2 in a concentration-dependent manner, as shown by the plasmon band decrease monitored by extinction spectroscopy (Figs. 2 and 3). A dampening in the band at 419 nm and an increase at longer wavelengths are indicative of aggregate formation, verified by the change in NP size distribution shown by dynamic light scattering (Fig. 2*B*). Biological specificity of the MDM2–peptide 12.1

interaction was confirmed by using mutant PSN-12.1$_{W\Delta A}$ samples in which aggregation was observed to a much lesser extent at MDM2 concentrations up to a NP: protein ratio of 1:1,000 (15 pM PSN, 15 nM MDM2) (Figs. 2 and 4 and *SI Text*). This confirms the importance of specific amino acid residues in the binding event between MDM2 and NP-bound peptide. At protein concentrations higher than this, the extent of aggregation between PSN-12.1 and PSN-12.1$_{W\Delta A}$ solutions cannot be distinguished by extinction spectroscopy or dynamic light scattering (Figs. 2 and 3). At these concentrations, MDM2 is present in such excess that binding to the mutant peptide 12.1$_{W\Delta A}$ is comparable to that of peptide 12.1, indicating a saturation point to the assay. Extinction spectroscopic measurements of samples taken 96 h after MDM2 addition show a much greater distinction in aggregation extent between PSN-12.1 and the mutant PSN-12.1$_{W\Delta A}$ up to the saturation concentration of 15 nM MDM2 (Fig. 2*A*); however, such a time duration for an immunoassay is impractical. The PSN assembly process can be monitored over time by measuring the extinction change at the λ-max, and aggregation was seen to plateau within the first 30 min (Fig. 3*A*). These data correlate with previous literature describing binding of p53 BOX-I to the MDM2 hydrophobic cleft to be a stable, high-affinity interaction. PSN-12.1 assembly can be interpreted through either of the models proposed in Fig. 1*A*; however, because there is no evidence to support the latter, the most likely explanation for the observed PSN aggregation is an active MDM2-dimer (or "oligomer").

MDM2-Induced Aggregation "Turns On" SERS. Initial SERS studies involved analysis of PSN samples after completion of aggregate assembly monitored by extinction spectroscopy. SERS enhancement was measured by comparing the standardized peak height at 1,416 cm^{-1} (Fig. 1*B*) for each sample in relation to unaggregated PSN solutions. Raman signal intensity increased in a positive correlation with MDM2 concentration up to a molar ratio of 1:1,000 PSN:MDM2 (15 pM PSN, 15 nM MDM2) (Fig. 4). This corresponds with previous extinction spectroscopy investigations indicating assay saturation at this concentration. When MDM2 was present at a larger molar excess than 1:1,000, a decrease in SERS intensity was observed (Fig. 4*A*). At these concentrations, protein can form almost monolayer coverage on the PSN surface, thus dampening Raman signals associated with BT but still allowing aggregation, as seen by extinction spectroscopy (Fig. 3*B*). Another possibility is that large aggregates
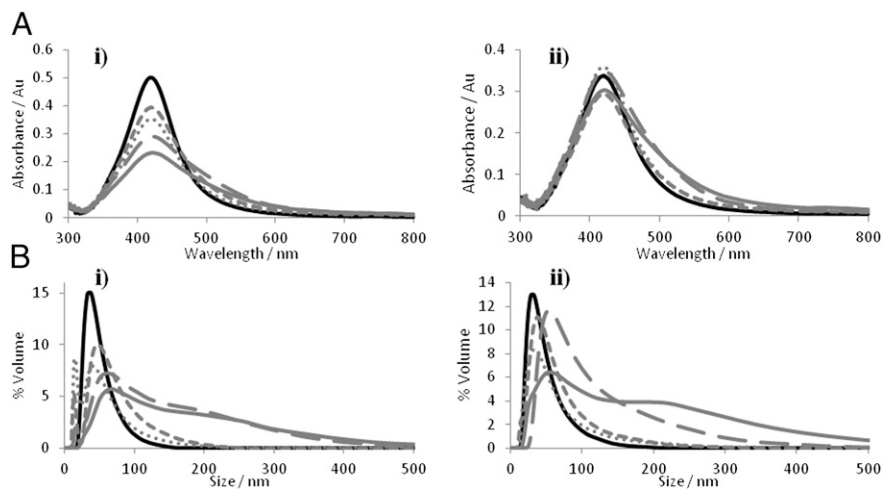
Fig. 2. Extinction spectroscopy and particle size analysis of PSN solutions before and after addition of MDM2. (*A* and *B*) Extinction profiles (*A*) and particle size distributions (*B*) of PSN-12.1 (*i*) and PSN-12.1$_{W\Delta A}$ (*ii*) samples without MDM2 (black) and 96 h after addition of 300 (dotted gray), 500 (short dashed gray), 1,000 (long dashed gray), and 2,000 (solid gray) MDM2 monomers per PSN.
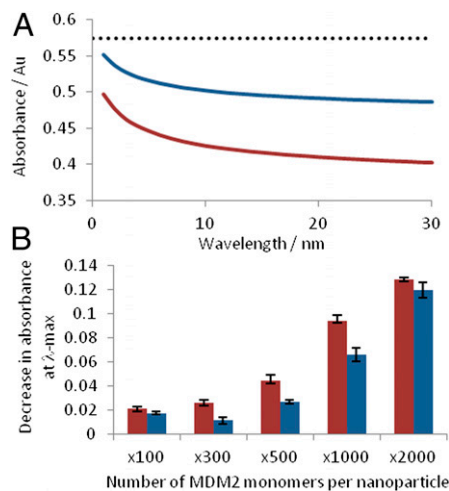
Fig. 3. Extinction spectroscopy analysis of PSN aggregation. (*A*) Extinction spectroscopy monitored for a 30-min duration following MDM2 addition to PSN-12.1 (red) and PSN-12.1$_{W\Delta A}$ (blue) at a PSN:MDM2 molar ratio of 1:1,000. Dotted line indicates the average plasmon band intensity before MDM2 addition. (*B*) Change in the plasmon band monitored from the 1–30 min after MDM2 addition. Error bars illustrate the SD.

Fig. 4. SERS analysis of PSN aggregation. (*A*) Calculated x-fold increase in SERS intensity following MDM2 addition to PSN-12.1 (red) and PSN-12.1$_{W\Delta A}$ (blue). (*B*) Peak height at 1416 cm^{-1} monitored every 60 seconds for 30 min following addition of varying amounts of MDM2 to PSN-12.1 (red) and PSN-12.1$_{W\Delta A}$ (blue). X-value represents the excess of MDM2 monomers per PSN. Dotted line indicates PSN samples when MDM2 is absent. Error bars illustrate the SD.

form that fall out of solution; however, this explanation is contradicted by the partial aggregation observed in scanning electron microscopy (SEM) (Fig. S6). At a molar ratio of 1:1,000 PSN: MDM2 (15 pM PSN, 15 nM MDM2), an eightfold increase in peak height was observed compared with samples where protein was absent. No such signal enhancement was apparent for PSN-12.1$_{W\Delta A}$ samples or when MDM2 was replaced with a control protein, BSA (Fig. 4*A* and Fig. S7). This demonstrated the high biological specificity of the interaction, further validated by additional MDM2 binding studies (Fig. S8). SERS analysis of MDM2-induced PSN aggregation enables protein detection at a molar excess of 100 MDM2 per PSN (15 pM PSN, 1.5 nM MDM2), demonstrating a lower limit of detection than was achievable using extinction spectroscopy (Figs. 3*B* and 4*A*). Comparable results for PSN-12.1 and PSN-12.1$_{W\Delta A}$ samples were also more distinguishable when applying SERS rather than extinction spectroscopy (Figs. 3 and 4). These data indicate that SERS presents a more sensitive analysis technique than extinction spectroscopy for NP assembly controlled by biological interactions.

Temporal SERS Analysis of Aggregation. Our findings show that the assembly of PSN-12.1 with MDM2 is a time- and concentration-dependent process (Fig. 3). To this end, SERS analysis was investigated to monitor the PSN assembly process over time. To minimize SERS signal variations, PSN preparation and final solution concentrations were optimized. Focus of the laser through the bulk of the solution and continuous sample rotation ensured consistent sampling of the components throughout the duration of the experiment.

The rate at which SERS intensity reached saturation was seen to increase with MDM2 concentration, and it can be interpreted from the data that the formation of PSN assemblies approaches completion within 11, 9, and 7 min for PSN:MDM2 ratios of 1:300, 1:500, and 1:1,000, respectively (15 pM PSN, 4.5–15 nM MDM2) (Fig. 4*B*). This is quicker than observed in extinction spectroscopy (Fig. 3*A*), demonstrating the higher sensitivity of SERS as an analytical tool for monitoring NP aggregation. These data demonstrate that SERS can be used as a viable tool for monitoring time-dependent NP assembly, although it must be realized that it does not represent the system found in nature owing to PSN solution kinetics.
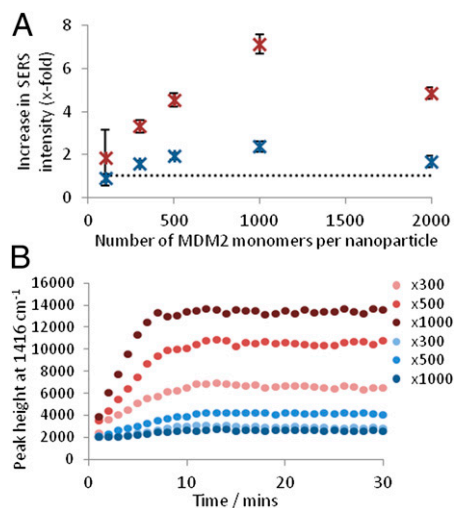
Inhibition of the MDM2-PSN Interaction. To test the potential for development of the assay for investigating MDM2 interactions with small molecules, we exposed MDM2 to N-terminal-binding ligands to competitively inhibit the aforementioned PSN-12.1 assembly. MDM2 is likely to exhibit a higher binding affinity to free peptide 12.1 (inhibitor 12.1) than to NP-bound peptide 12.1, because of the solution kinetics. Nutlin-3 is a potent and well studied small molecule inhibitor of the MDM2-p53 interaction (15). For all inhibition experiments, a molar ratio of 1:1,000 PSN: MDM2 (15 pM PSN, 15 nM MDM2) was used owing to the large extent of the aggregation observed (Figs. 2–4). MDM2 was preincubated with a 100-fold molar excess of inhibitor (0.96 mM MDM2, 96 mM inhibitor) before mixing with PSN-12.1 solutions (6.25 mL added to 400 mL of 15 pM PSN), and temporal analysis was carried out using extinction spectroscopy. A lesser decrease in the plasmon band was observed for PSN-12.1 solutions treated with MDM2 preincubated with either inhibitor 12.1 or Nutlin-3 than was evident following the addition of native MDM2 (Fig. 5). A much greater enhancement in Raman signal was also observed in the presence of native MDM2 compared with MDM2 preincubated with inhibitor (Fig. 5*B*). Inhibitor 12.1 and Nutlin-3 were able to bind the MDM2 hydrophobic cleft, thus blocking the binding site for peptide 12.1 molecules on PSN-12.1 and disallowing MDM2-mediated PSN assembly. Signal changes in SERS and extinction spectroscopy associated with PSN aggregation were, therefore, not observed to the same extent (Fig. 5*B*). It was subsequently observed that lowering the excess of inhibitor resulted in a decrease in inhibition efficiency by extinction spectroscopy and SERS (Fig. 5*C*). Varying the molar excess of inhibitor 12.1 prebound to MDM2 in this way demonstrates PSN-assembly inhibition in a dose-dependent manner. The extinction spectroscopy and SERS data, together, demonstrate a competitive inhibition of MDM2–peptide 12.1-driven NP assembly by inhibitor 12.1 and Nutlin-3. A 1.4× increase in SERS response was detected at the highest concentration of inhibitor 12.1, suggesting that some PSN assembly occurred (Fig. 5*C*). Depletion in extinction plasmon band for the same sample in extinction spectroscopy is negligible (Fig. 5*C*), thus identifying SERS as the superior technique to investigate inhibitor potency. SERS analysis also provides a positive response for NP assembly that is
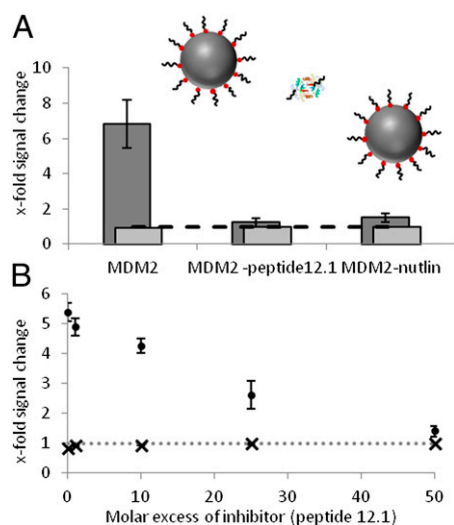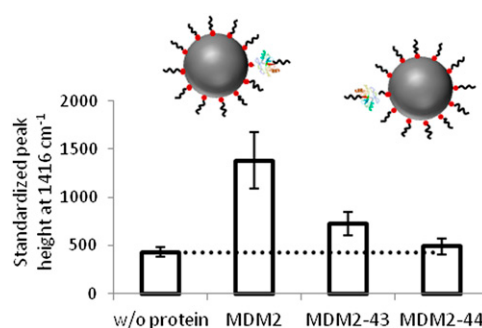
Fig. 5. Competitive inhibition of MDM2-induced PSN aggregation. Schematic illustrates proposed MDM2-induced PSN aggregation inhibition with inhibitor peptide 12.1 and Nutlin-3. (*A* and *B*) X-fold decrease in the plasmon band monitored by extinction spectroscopy [light gray (*A*) and X (*B*)] and x-fold SERS intensity change following 30 min incubation of MDM2 with varying concentrations of inhibitor molecule [dark gray (*A*) and circle (*B*)].

advantageous over extinction spectroscopy where a decrease in signal is monitored.

Disruption of the Dimerization Interface. To further test the assay capabilities for investigating MDM2 and verify the requirement for MDM2 oligomerization in PSN assembly, MDM2 was premixed with self-peptides from one linear motif that stabilizes the MDM2/MDMX heterodimer at the N-terminal junction of the C-terminal RING domain (amino acids 430-LPLNAI-435) (8) at a molar ratio of 1:100 MDM2:peptide (0.96 mM MDM2, 96 mM peptide). SERS analysis of PSN solutions (15 pM) was carried out following the addition of MDM2 preincubated with peptides 43 (DKEESVESSLPLNAI) and 44 (PLNAIEPCVICQGRP) (6.25 mL added to 400 mL), which represent overlapping sequences from the dimerization interface (Fig. S9). Preincubation of MDM2 with peptides 43 and 44 resulted in a decrease in PSN-12.1 assembly, as monitored using SERS (Fig. 6). Despite both dimerization-motif peptides demonstrating an inhibitory effect on PSN-12.1 assembly, a 1.69-fold increase in SERS was observed in the presence of peptide 43 compared with a 1.14-fold increase with peptide 44. The difference in PSN-12.1 assembly inhibition potency of these two ligands indicates a positional effect of peptide-ligand binding to the MDM2 dimerization interface in preventing dimerization. As a control, the binding of peptides 43 and 44 to MDM2 using ELISA demonstrated no affect on N-terminal-binding activity (Fig. S9B). These data highlight the difference between a standard ligand-binding assay that does not distinguish between the oligomeric or monomeric nature of the target protein (Fig. S9) and a SERS-based ligand-binding assay that requires target protein "oligomerization" (Fig. 6; PSN assembly model illustrated in Fig. 1*A, i* and *ii*).

Discussion

A number of SERS-based immunoassays have been developed for the detection of biological interactions; however, few NP–protein aggregation studies have been published. This report presents the use of protein–peptide interactions as a controlled NP-assembly template capable of "turning on" SERS. Furthermore, the protein interactions investigated are of particular biological interest owing to the critical role of MDM2 in cancer progression. PSN assembly

Fig. 6. Competitive inhibition of MDM2-induced PSN aggregation. Schematic illustrates proposed MDM2-induced PSN assembly inhibition with dimerization-motif self-peptides 43 and 44. Data show SERS peak height measurements, at 1,416 cm^{-1}, recorded for PSN-12.1 samples after completion of temporal analysis. Dotted line indicates PSN samples when MDM2 is absent. Error bars illustrate the SD.

and associated SERS enhancement were successfully inhibited by preincubating MDM2 with small-molecule-binding ligands.

We have demonstrated that full-length MDM2 is able to successfully aggregate PSN-12.1, suggesting that the MDM2 protein is in dimeric (oligomeric) state in solution, while maintaining biological activity of the hydrophobic pocket. These studies present an innovative method for interrogating the allosteric interactions of full-length unlabeled MDM2 using biologically driven NP assembly. We also demonstrate a proof-of-concept with which to use SERS-based ligand-binding assays to investigate other allosteric proteins that undergo complex conformational interactions.

Methods

Peptide–BT Conjugation. Peptides 12.1 (SGSG-MPRFMDYWEGLN-resin) and 12.1$_{W\Delta A}$ (SGSG-MPRFMDYAEGLN-resin) were obtained bound to Wang resin via the C terminus (Almac Sciences), with the N terminus deprotected. Modification with BT was carried out via amide coupling in the solid phase and cleaved from the resin using 95% TFA (*SI Methods*).

Nanoparticle Bioconjugation. AgEDTA nanoparticles were synthesized with a 40-nm diameter using the method described by Heard et al. in 1983 (52). Nanoparticles were centrifuged at 1,900 × g for 20 min and resuspended in buffer [25 mM Hepes and 20 mM KCl (pH 7.5)] before addition of BT or peptide–BT at a final concentration of 10^{-6} M. After shaking for a minimum of 1 h, the conjugation solutions were centrifuged at 5,000 rpm for 20 min and resuspended in buffer (×3) to remove any excess analytes. Complete BT–peptide conjugates were characterized using extinction spectroscopy, dynamic light scattering, and MALDI-MS.

Dynamic Light Scattering. One-milliliter samples were analyzed via dynamic light scattering using a Malvern high-performance particle sizer (HPPS) using standard disposable cuvettes.

Extinction Spectroscopy. Absorbance readings were taken from 250–650 nm using a Cary Eclipse extinction spectrometer. All spectra were baseline corrected using 25 mM Hepes buffer (pH 7.5), 20 mM KCl, as a blank. NP concentrations were calculated using the extinction coefficient for 40-nm silver nanoparticles at λ-max (ε = 2.87 × 10^{10}). Peptide–BT concentrations were calculated using the extinction coefficient for BT at 487 nm (ε = 12017).

MALDI-MS. Peptide samples were analyzed using a 1:1 ratio of sample to matrix, α-cyano-4-hydroxycinnamic acid (α-cyano). Ionization was conducted in the positive reflectron mode. A linear three-point calibration was achieved using a preprepared peptide mixture: 379.1 *m/z* (α-cyano matrix), 757.4 *m/z* (Bradykinin fragment), and 1,046.5 *m/z* (angiotensin II). To analyze nanoparticle-bound peptide samples, conjugates were removed from the nanoparticles and desalted. Nanoparticle samples were treated with DTT (10 mM) for a minimum of 30 min to displace BT from the metal surface. Following centrifugation at 5,000 rpm for 20 min, 150 μL of supernatant was desalted using PepClean C-18 spin columns (Thermo Scientific) MALDI-MS carried out on the recovered sample.

Protein Preparation. MDM2 was purified as indicated in *SI Methods*. Purified full-length MDM2 was stored at −20 °C in storage buffer [25 mM Hepes (pH 7.5), 10% (vol/vol) glycerol, 1 mM benzamidine, 5 mM DTT, 290 mM KCl], and buffer exchange into assay buffer [25 mM Hepes (pH 7.5), 20 mM KCl] was performed using a concentrator with a 10-kDa molecular mass cutoff filter (Millipore). BSA was obtained from Sigma and dissolved in assay buffer. MDM2 and BSA stocks were prepared at a concentration of $\sim 8 \times 10^{-7}$ M in assay buffer for use in NP aggregation assays. MDM2 protein was validated in the dual-site-binding assay that measures the ability of Nutlin to stimulate the interaction of MDM2 with the Rb1 peptide (10). Rb1 peptide binds to the acidic domain of MDM2 and mimics the interaction of MDM2 with the p53 central DNA-binding domain (10).

SERS Analysis. SERS spectra were collected using a Renishaw inVia microscope system. Excitation at 514.5 nm was achieved via an Ar$^+$ laser attenuated using neutral density filters. Spectra were obtained using 180° backscattering with the grating centered at 1400 cm^{-1} using a 20× long-working distance objective. Static scans with a 2-s collection time were obtained for analysis of postassay samples in disposable cuvettes. Temporal SERS analysis of samples was conducted using an NMR tube spinner microscope attachment. A 1-s scan duration was used, and one spectrum was acquired every 60-s for 30 min.

1. Carson DA, Lois A (1995) Cancer progression and p53. *Lancet* 346:1009–1011.
2. Lane DP (1992) Cancer. p53, guardian of the genome. *Nature* 358:15–16.
3. Vousden KH, Lu X (2002) Live or let die: The cell's response to p53. *Nat Rev Cancer* 2:594–604.
4. Arva NC, et al. (2005) A chromatin-associated and transcriptionally inactive p53-Mdm2 complex occurs in mdm2 SNP309 homozygous cells. *J Biol Chem* 280:26776–26787.
5. Fang SY, Jensen JP, Ludwig RL, Vousden KH, Weissman AM (2000) Mdm2 is a RING finger-dependent ubiquitin protein ligase for itself and p53. *J Biol Chem* 275:8945–8951.
6. Momand J, Zambetti GP, Olson DC, George D, Levine AJ (1992) The mdm-2 oncogene product forms a complex with the p53 protein and inhibits p53-mediated trans-activation. *Cell* 69:1237–1245.
7. Oliner JD, Kinzler KW, Meltzer PS, George DL, Vogelstein B (1992) Amplification of a gene encoding a p53-associated protein in human sarcomas. *Nature* 358:80–83.
8. Linke K, et al. (2008) Structure of the MDM2/MDMX RING domain heterodimer reveals dimerization is required for their ubiquitylation in trans. *Cell Death Differ* 15:841–848.
9. Pettersson S, Kelleher M, Pion E, Wallace M, Ball KL (2009) Role of Mdm2 acid domain interactions in recognition and ubiquitination of the transcription factor IRF-2. *Biochem J* 418:575–585.
10. Wallace M, Worrall E, Pettersson S, Hupp TR, Ball KL (2006) Dual-site regulation of MDM2 E3-ubiquitin ligase activity. *Mol Cell* 23:251–263.
11. Dastidar SG, Lane DP, Verma CS (2008) Multiple peptide conformations give rise to similar binding affinities: Molecular simulations of p53-MDM2. *J Am Chem Soc* 130:13514–13515.
12. Ding K, et al. (2005) Structure-based design of potent non-peptide MDM2 inhibitors. *J Am Chem Soc* 127:10130–10131.
13. Ding K, et al. (2006) Structure-based design of spiro-oxindoles as potent, specific small-molecule inhibitors of the MDM2-p53 interaction. *J Med Chem* 49:3432–3435.
14. García-Echeverría C, Chène P, Blommers MJJ, Furet P (2000) Discovery of potent antagonists of the interaction between human double minute 2 and tumor suppressor p53. *J Med Chem* 43:3205–3208.
15. Vassilev LT, et al. (2004) In vivo activation of the p53 pathway by small-molecule antagonists of MDM2. *Science* 303:844–848.
16. Poyurovsky MV, et al. (2007) The Mdm2 RING domain C-terminus is required for supramolecular assembly and ubiquitin ligase activity. *EMBO J* 26:90–101.
17. Uldrijan S, Pannekoek WJ, Vousden KH (2007) An essential function of the extreme C-terminus of MDM2 can be provided by MDMX. *EMBO J* 26:102–112.
18. Kostic M, Matt T, Martinez-Yamout MA, Dyson HJ, Wright PE (2006) Solution structure of the Hdm2 C2H2C4 RING, a domain critical for ubiquitination of p53. *J Mol Biol* 363:433–450.
19. Worrall EG, Worrall L, Blackburn E, Walkinshaw M, Hupp TR (2010) The effects of phosphomimetic lid mutation on the thermostability of the N-terminal domain of MDM2. *J Mol Biol* 398:414–428.
20. Wawrzynow B, et al. (2009) A function for the RING finger domain in the allosteric control of MDM2 conformation and activity. *J Biol Chem* 284:11517–11530.
21. Huang SX, Chen Y (2008) Ultrasensitive fluorescence detection of single protein molecules manipulated electrically on Au nanowire. *Nano Lett* 8:2829–2833.
22. Tang L, Dong C, Ren J (2010) Highly sensitive homogenous immunoassay of cancer biomarker using silver nanoparticles enhanced fluorescence correlation spectroscopy. *Talanta* 81:1560–1567.
23. Xia ZY, Rao JH (2009) Biosensing and imaging based on bioluminescence resonance energy transfer. *Curr Opin Biotechnol* 20:37–44.
24. Faulds K, Jarvis R, Smith WE, Graham D, Goodacre R (2008) Multiplexed detection of six labelled oligonucleotides using surface enhanced resonance Raman scattering (SERRS). *Analyst (Lond)* 133:1505–1512.
25. Sabatté G, et al. (2008) Comparison of surface-enhanced resonance Raman scattering and fluorescence for detection of a labeled antibody. *Anal Chem* 80:2351–2356.
26. Graham D, Faulds K, Smith WE (2006) Biosensing using silver nanoparticles and surface enhanced resonance Raman scattering. *Chem Commun (Camb)* 42:4363–4371.
27. Cunningham D, et al. (2006) Practical control of SERRS enhancement. *Faraday Discuss* 132:135–145, discussion 147–158.
28. Faulds K, Littleford RE, Graham D, Dent G, Smith WE (2004) Comparison of surface-enhanced resonance Raman scattering from unaggregated and aggregated nanoparticles. *Anal Chem* 76:592–598.
29. Rohr TE, Cotton T, Fan N, Tarcha PJ (1989) Immunoassay employing surface-enhanced Raman spectroscopy. *Anal Biochem* 182:388–398.
30. Campbell FM, et al. (2008) SERRS immunoassay for quantitative human CRP analysis. *Analyst (Lond)* 133:1355–1357.
31. Dou X, Takama T, Yamaguchi Y, Yamamoto H, Ozaki Y (1997) Enzyme immunoassay utilizing surface-enhanced Raman scattering of the enzyme reaction product. *Anal Chem* 69:1492–1495.
32. Douglas P, Stokes RJ, Graham D, Smith WE (2008) Immunoassay for P38 MAPK using surface enhanced resonance Raman spectroscopy (SERRS). *Analyst (Lond)* 133:791–796.
33. Driskell JD, et al. (2005) Low-level detection of viral pathogens by a surface-enhanced Raman scattering based immunoassay. *Anal Chem* 77:6147–6154.
34. Grubisha DS, Lipert RJ, Park HY, Driskell J, Porter MD (2003) Femtomolar detection of prostate-specific antigen: An immunoassay based on surface-enhanced Raman scattering and immunogold labels. *Anal Chem* 75:5936–5943.
35. Han XX, et al. (2008) Fluorescein isothiocyanate linked immunoabsorbent assay based on surface-enhanced resonance Raman scattering. *Anal Chem* 80:3020–3024.
36. Han XX, et al. (2008) Simplified protocol for detection of protein-ligand interactions via surface-enhanced resonance Raman scattering and surface-enhanced fluorescence. *Anal Chem* 80:6567–6572.
37. Narayanan R, Lipert RJ, Porter MD (2008) Cetyltrimethylammonium bromide-modified spherical and cube-like gold nanoparticles as extrinsic Raman labels in surface-enhanced Raman spectroscopy based heterogeneous immunoassays. *Anal Chem* 80:2265–2271.
38. Ni J, Lipert RJ, Dawson GB, Porter MD (1999) Immunoassay readout method using extrinsic Raman labels adsorbed on immunogold colloids. *Anal Chem* 71:4903–4908.
39. Wang G, Park H-Y, Lipert RJ, Porter MD (2009) Mixed monolayers on gold nanoparticle labels for multiplexed surface-enhanced Raman scattering based immunoassays. *Anal Chem* 81:9643–9650.
40. Aslan K, Luhrs CC, Perez-Luna VH (2004) Controlled and reversible aggregation of biotinylated gold nanoparticles with streptavidin. *J Phys Chem B* 108:15631–15639.
41. Andresen H, Gupta S, Stevens MM (2011) Kinetic investigation of bioresponsive nanoparticle assembly as a function of ligand design. *Nanoscale* 3:383–386.
42. Du BA, Li ZP, Cheng YQ (2008) Homogeneous immunoassay based on aggregation of antibody-functionalized gold nanoparticles coupled with light scattering detection. *Talanta* 75:959–964.
43. Gupta S, Andresen H, Stevens MM (2011) Single-step kinase inhibitor screening using a peptide-modified gold nanoparticle platform. *Chem Commun (Camb)* 47:2249–2251.
44. Onoda A, Ueya Y, Sakamoto T, Uematsu T, Hayashi T (2010) Supramolecular hemoprotein-gold nanoparticle conjugates. *Chem Commun (Camb)* 46:9107–9109.
45. Kussie PH, et al. (1996) Structure of the MDM2 oncoprotein bound to the p53 tumor suppressor transactivation domain. *Science* 274:948–953.
46. Böttger V, et al. (1996) Identification of novel mdm2 binding peptides by phage display. *Oncogene* 13:2141–2147.
47. Li C, et al. (2010) Systematic mutational analysis of peptide inhibition of the p53-MDM2/MDMX interactions. *J Mol Biol* 398:200–213.
48. Liu M, et al. (2010) A left-handed solution to peptide inhibition of the p53-MDM2 interaction. *Angew Chem Int Ed Engl* 49:3649–3652.
49. Graham D, et al. (1998) Synthesis of novel monoazo benzotriazole dyes specifically for surface enhanced resonance Raman scattering. *Chem Commun* 11:1187–1188.
50. Naumov S, Kapoor S, Thomas S, Venkateswaran S, Mukherjee T (2004) SERS of benzotriazole on Ag colloid: Surface structure characterization using the DFT approach. *Theochem. J Mol Struct* 685:127–131.
51. Pergolese B, Muniz-Miranda M, Bigotto A (2004) Study of the adsorption of 1,2,3-triazole on silver and gold colloidal nanoparticles by means of surface enhanced Raman scattering. *J Phys Chem B* 108:5698–5702.
52. Heard SM, Grieser F, Barraclough CG, Sanders JV (1983) The characterization of Ag Sols by electron-microscopy, optical-absorption, and electrophoresis. *J Colloid Interface Sci* 93:545–555.